Garwood, Gerri

From: Cathe Kalisz <kaliszc@api.org>
Sent: Wednesday, April 01, 2015 1:36 PM
To: Garwood, Gerri
Cc: Schaffner, Karen S.; Gary Mueller; Scott Evans (sevans@cleanair.com); vschmid@cleanair.com
Subject: Additional Flare NOx Information
Attachments: IFC Results Report Jan 2012.pdf; IFC April 2010 Flare Test Facility - Equipment and Calculations.pdf; torres_NOx_emis_Zink_flare.pdf; NOX_QA-QC_acp-9-2499-2009.pdf; Copy of EF_Dataset_Export_V10 (2).xlsx

Gerri,

Attached are the following additional supporting information requested by EPA:

- Copy of IFC January 2012 Final Test Results report
- Copy of IFC April 2010 Equipment and Calculations report (includes information on the NOx instrument used for the testing)
- Copy of CAE spreadsheet used for factor development. This spreadsheet contains the raw data for the IFC testing; as I mentioned to Karen Schaffner yesterday, the TCEQ data is taken from TCEQ reports.
- A paper on the TCEQ flare NOx testing (Torres et al 2012) along with a paper referred to for the NOX QA/QC (see page 2501).

Please let us know if you have any questions.

Cathe

Cathe Kalisz, P.E.
Policy Advisor
Regulatory and Scientific Affairs
American Petroleum Institute
1220 L Street NW
Washington, DC 20005
PH: (202) 682-8318
FAX: (202) 682-8270
kaliszc@api.org

Natural Resources Canada | Ressources naturelles Canada

CanmetENERGY

Leadership in ecoInnovation

Flare Test Facility – Results

P. Gogolek, A.Caverly, C. Balderson

CanmetENERGY- Ottawa

R. Schwartz

John Zink Company LLC

J. Seebold

Consultant

J. Pohl

Energy International

Prepared for the International Flaring Consortium

January 2012

Funding provided by members of the International Flaring Consortium

BP	ExxonMobil	Saudi Aramco
Chevron	John Zink Company LLC	Shell
DuPont	NOVA Chemicals	Total

Canada

DISCLAIMER

This report was prepared by CanmetENERGY as an account of work funded by the International Flaring Consortium. CanmetENERGY has made all reasonable efforts to ensure the exactness of the information provided in this report and the opinions expressed herein are those of CanmetENERGY solely. However, neither CanmetENERGY, the International Flaring Consortium, nor any person acting on behalf of them;

a. Makes any warranty or representation, expressed or implied with respect to the accuracy, completeness, or usefulness of the information contained in this report, or that the use of any information, apparatus, method, or process disclosed in this report may not infringe privately-owned rights, or

b. Assumes any liability with respect to the use of, or for damages resulting from the use of, any information, apparatus, method, or process disclosed in this report.

Reference to specific commercial products in this report does not represent or constitute an endorsement, recommendation, or favoring by CanmetENERGY, the International Flaring Consortium, nor any person acting on behalf of them, of the specific manufacturer or commercial product. The involvement by CanmetENERGY in this project is not to be used for promotional purposes beyond being identified as an independent third party evaluator.

TABLE OF CONTENTS

1.0 Introduction 1

1.1 Overview of CFR40 Requirements 3

2.0 Baseline, Scale-Up and Regime Transition Tests 6

2.1 Introduction 6

2.2 Test Plan 7

2.2.1 Scaling Tests 7

2.2.2 FRR Tests 8

2.2.3 Fuel Modification Tests 9

2.2.4 Transition Testing 10

2.3 Results and Discussion 11

2.3.1 Scale-up Tests 11

2.3.2 Fuel Modification Tests 23

2.3.3 Transition Testing 25

2.4 Conclusion 29

3.0 Simple Fuel Gas Tests 31

3.1 Introduction 31

3.2 Test Plan 31

3.3 Results 32

3.4 Discussion 34

3.5 Conclusion 35

4.0 Steam-assist Tests 37

4.1 Introduction 37

4.2 Test Plan 37
4.3 Results 38
4.4 Discussion 43
4.5 Conclusion 58
5.0 Dilution testing 60
5.1 Introduction 60
5.2 Test Plan 60
5.3 Results and Discussion 61
5.4 Conclusion 66
6.0 Trace emissions 68
6.1 Introduction 68
6.2 Carbon Monoxide 69
6.3 Nitrogen Oxides 71
6.4 Hydrocarbons 73
6.5 Conclusion 78
7.0 Conclusion 80
7.1 Experimental studies of the flare efficiency in the transition between jetting and wake-stabilized regimes. 81
7.2 Experimental studies of the effect of wind on steam-assisted flares. 81
7.3 Experimental studies on the limiting hydrogen concentration for steam-assisted flares and wind blown flares. 82
7.4 Experimental measurements of HRVOC and NOx measurements for flares with and without steam-assist. 82

7.5 Correlation of fuel properties to correlate the flare efficiency with flare gas composition, particularly accounting for the special case of hydrogen, and the inert gases nitrogen and carbon dioxide. 83

7.6 Correlation of flare efficiency with steam-assist rate that includes the flare gas composition, perhaps unifying steam with the handling of nitrogen and carbon dioxide dilution. 83

7.7 Gaps remaining or identified 84

8.0 References 86

9.0 Appendix 87

LIST OF FIGURES

Figure 1 - Baseline testing results for 2.5 cm (1") basic pipe firing natural gas. 12

Figure 2 - Baseline testing results for 5.1 cm (2") basic pipe firing natural gas. 12

Figure 3 - Baseline testing results for 7.6 cm (3") basic pipe firing natural gas. 13

Figure 4 - Baseline testing results for 10.2 cm (4") basic pipe firing natural gas. 13

Figure 5 - Baseline testing results for 15.2 cm (6") basic pipe firing natural gas. 14

Figure 6 - Results of all baseline tests firing natural gas. 14

Figure 7 - Results for all pipe sizes, with results reported by the University of Alberta, correlated with the Power Factor. The solid line is equation (2-2) fit to the results for 7.6 cm (3"), 10.2 cm (4") and 15.2 cm (6") pipes. 16

Figure 8 - Replotting Figure 7 as a semi-log plot, to better display the spread of the data. 17

Figure 9 - Replotting Figure 7 with only the results for pipes 7.6 cm (3") or larger. 18

Figure 10 - Replotting Figure 9 as a semi-log plot to better display the spread of the data. 19

Figure 11 - Fraction of inefficiency due to the emission of methane correlated with the Power Factor. 20

Figure 12 - Destruction efficiency for methane for the tests with natural gas and the basic pipe. 21

Figure 13 - Conversion inefficiency for 7.6 cm (3") and 15.2 cm (6") pipes fitted with FRR, plotted against the Power Factor. The solid line is the fit to the basic pipes 7.6 cm (3") and larger, equation (2-2). 22

Figure 14 - Destruction efficiency for 7.6 cm (3") and 15.2 cm (6") pipes fitted with FRR, plotted against the Power Factor. The solid line is the fit to the basic pipes 7.6 cm (3") and larger, equation (2-3). 23

Figure 15 - Results for tests with 7.6 cm (3") and 15.2 cm (6") basic pipes firing a mixture of 85%-v natural gas with 15%-v propane. The solid line is the fit to the natural gas results (equation 2-2), the dashed black line is equation (2-4). 24

Figure 16 - Results for 7.6 cm (3") basic pipe firing a mixture of 40%-v natural gas with 60%-v nitrogen. The solid line is the fit to the natural gas data. 25

Figure 17 - Results for 7.6 cm (3") pipe for transition testing versus fuel Reynolds number. Changing the fuel rate has a very small effect. 27

Figure 18 - Results for 7.6 cm (3") pipe for transition testing versus wind speed. The change in fuel rate at 1.1 m/s has a much smaller effect than the increase of wind speed. 27

Figure 19 - Results for transition testing of 7.6 cm (3") pipe correlated with the Power Factor. 28

Figure 20 - Transition test results with 7.6 cm (3”) pipes versus wind speed. 29

Figure 21 - Conversion inefficiency for unassisted flaring of ethylene and propylene in 7.6 cm (3”) FRR tip. 32

Figure 22 - Destruction efficiency for unassisted flaring of ethylene and propylene in 7.6 cm (3") FRR tip. 33

Figure 23 - Solid carbon emission as a percentage of the total carbon for unassisted flaring of ethylene and propylene in 7.6 cm (3") FRR flare tip. 34

Figure 24- Comparison of destruction efficiency of unassisted flaring of ethylene and propylene with that of natural gas in a 7.6 cm (3") FRR flare tip. The solid line is equation 2-3, the DE curve for natural gas flared with 7.6 cm, 10.2 cm or 15.2 cm (3”, 4” or 6”) basic pipe. 35

Figure 25 - Conversion inefficiency versus steam-to-fuel mass ratio for steam-assisted flaring of natural gas, indexed on nominal wind speed. The zero SFR points did have steam flowing, but the correction of the flow rate produced a negative value. 39

Figure 26 - Destruction efficiency versus steam-to-fuel mass ratio for steam-assisted flaring of natural gas, indexed on nominal wind speed in m/s. The zero SFR points did have steam flowing, but the correction of the flow rate produced a negative value..... 40

Figure 27 - Conversion inefficiency versus steam-to-fuel mass ratio for steam-assisted flaring of ethylene, indexed on nominal wind speed. The circled point appears to be anomalous. 41

Figure 28 - Destruction efficiency versus steam-to-fuel mass ratio for steam-assisted flaring of ethylene, indexed on nominal wind speed. The circled point appears to be anomalous. 41

Figure 29 - Conversion inefficiency versus steam-to-fuel mass ratio for steam-assisted flaring of propylene, indexed on wind speed in m/s. 42

Figure 30 - Destruction efficiency versus steam-to-fuel mass ratio for steam-assisted flaring of propylene, indexed on wind speed. 43

Figure 31 - Conversion inefficiency for steam-assisted flaring of natural gas versus Power Factor, for SFR < 1. 44

Figure 32 - Destruction efficiency versus Power Factor for steam-assisted flaring of natural gas, for SFR < 1. 44

Figure 33 - Conversion inefficiency versus Power Factor for steam-assisted flaring of ethylene, indexed on wind speed. All steam levels included. 46

Figure 34 – Destruction efficiency versus Power Factor for steam-assisted flaring of ethylene, indexed on wind speed. All steam levels included. 47

Figure 35 - Conversion inefficiency versus Power Factor for steam-assisted flaring of ethylene, indexed on wind speed, SFR < 1. 47

Figure 36 - Destruction efficiency versus Power Factor for steam-assisted flaring of ethylene, indexed on wind speed, SFR < 1. 48

Figure 37 - Destruction efficiency versus Power Factor for unassisted and steam-assisted flaring of ethylene, with Steam-to-Fuel Ratio up to 2. 48

Figure 38 - Conversion inefficiency versus Power Factor for steam-assisted flaring of propylene, indexed on wind speed. All steam levels included. 49

Figure 39 - Destruction efficiency versus Power Factor for steam-assisted flaring of propylene, indexed on wind speed. All steam levels included. 50

Figure 40 - Conversion inefficiency versus Power Factor for steam-assisted flaring of propylene, indexed on wind speed, SFR < 1. 50

Figure 41 - Destruction efficiency versus Power Factor for steam-assisted flaring of propylene, indexed on wind speed, SFR < 1. 51

Figure 42 - Destruction efficiency results for flaring propylene, both steam-assisted and unassisted. The CMA/EPA data for steam-assisted flaring with SFR < 1 is included. ... 52

Figure 43 - Destruction efficiency for steam-assisted flaring versus the reduced steam volume fraction. The possibly anomalous data are circled. Recommended maximum is RSVF = 0.8. 54

Figure 44 - Destruction efficiency versus Power Factor for steam-assisted trials with RSVF < 0.8. 55

Figure 45 - Destruction Efficiency results for steam-assisted flaring of natural gas, ethylene and propylene, including the CMA/EPA data. All data are restricted to RSVF < 0.8. The Fuel Factor is given in equation 4-4. 56

Figure 46 - Destruction Efficiency results for steam-assisted flaring of ethylene and propylene, including the CMA/EPA data. All data are restricted to RSVF < 0.8. The Fuel Factor is given in equation 4-4. 57

Figure 47 - Conversion inefficiency versus heat content of flare gas. 62

Figure 48 - Destruction efficiency versus heat content, volume basis. 63

Figure 49 - Destruction efficiency versus heat content, mass basis. 64

Figure 50 - Destruction efficiency for diluted flare gases versus Reduced Volume Fraction of Inert. 66

Figure 51- Conversion of fuel-carbon to carbon monoxide for all tests. 70

Figure 52 - Log-log plot of the conversion to CO against the conversion inefficiency. The solid line indicates 25% of the inefficiency is due to carbon monoxide. 71

Figure 53 - Emission factor for NO_x plotted against conversion inefficiency for all tests. 72

Figure 54 - Emission factor for NO_x for steam-assisted trials. 73

Figure 55 - Emission factors for ethylene plotted against Power Factor for tests with natural gas and propylene. 74

Figure 56 - Emission factors for ethylene plotted against SFR for steam-assisted flaring of natural gas and propylene. 75

Figure 57 - Emission factor for ethylene for tests with dilution of natural gas, propane and propylene with carbon dioxide..... 76

Figure 58 - Emission factor for 1-butene against SFR for steam-assisted flaring of propylene..... 77

Figure 59 - Emission factor for 1-butene plotted against the emission factor for ethylene for the steam-assisted flaring of propylene. The solid square symbols are the emission factors at the detection limit for these trials. 78

Figure 60 - Minimum exit velocities for steam-assisted flaring of ethylene and propylene based on RSVF<0.8 and maximum Power Factor (x 100) of 2 for propylene and 3 for ethylene. 82

Figure 61 - Baseline testing results for 1" basic pipe firing natural gas. 89

Figure 62- Baseline testing results for 2" basic pipe firing natural gas. 90

Figure 63 - Baseline testing results for 3" basic pipe firing natural gas. 90

Figure 64 - Baseline testing results for 4" basic pipe firing natural gas. 91

Figure 65 - Baseline testing results for 6" basic pipe firing natural gas. 91

Figure 66 - Results of all baseline tests firing natural gas. 92

Figure 67 - Results for 3" pipe for transition testing versus wind speed. The change in fuel rate at 2.5 miles/h has a much smaller effect than the increase of wind speed. 92

Figure 68 - Transition test results with 3” pipes versus wind speed. 93

Figure 69 - Conversion inefficiency for unassisted flaring of ethylene and propylene in 3” FRR tip. 94

Figure 70 - Destruction efficiency for unassisted flaring of ethylene and propylene in 3" FRR tip. 94

Figure 71 - Solid carbon emission as a percentage of the total carbon for unassisted flaring of ethylene and propylene in 3" FRR flare tip. 95

Figure 72 - Conversion inefficiency versus heat content of flare gas. 95

Figure 73 - Destruction efficiency versus heat content, volume basis. 96

Figure 74 - Destruction efficiency versus heat content, mass basis. 96

Figure 75 - Emission factor for NO_x plotted against conversion inefficiency for all tests. 97

Figure 76 - Emission factor for NO_x for steam-assisted trials. 98

Figure 77 - Emission factors for ethylene plotted against Power Factor for tests with natural gas and propylene. 99

Figure 78 - Emission factors for ethylene plotted against SFR for steam-assisted flaring of natural gas and propylene. 100

Figure 79 - Emission factor for ethylene for tests with dilution of natural gas, propane and propylene with carbon dioxide. 101

Figure 80 - Emission factor for 1-butene against SFR for steam-assisted flaring of propylene. 102

Figure 81 - Emission factor for 1-butene plotted against the emission factor for ethylene for the steam-assisted flaring of propylene. The solid square symbols are the emission factors at the detection limit for these trials. 103

Figure 82 - Minimum exit velocities for steam-assisted flaring of ethylene and propylene based on RSVF<0.8 and maximum Power Factor (x 100) of 2 for propylene and 3 for ethylene. 104

LIST OF TABLES

Table 1 - Test matrix for scale-up tests with natural gas. 8

Table 2 - Test matrix for tests with FRR firing natural gas. 9

Table 3 - Test matrix for the fuel modification tests, augmented with propane and diluted with nitrogen. 10

Table 4 - Test matrix for the simple fuel flaring tests..... 31

Table 5 - Overall test matrix for the steam-assisted trials. 38

Table 6 - Critical volume fraction (equation 4-2) for fuel gases. 53

Table 7 - Maximum dilution for flammable operation, with energy content and exit velocity..... 61

Table 8 - Critical volume fraction for gas mixtures with nitrogen and carbon dioxide.... 65

Table 9 - Test matrix for tests with FRR firing natural gas. 87

Table 10 - Test matrix for the fuel modification tests, augmented with propane and diluted with nitrogen. 87

Table 11 - Test matrix for the simple fuel flaring tests..... 88

Table 12 - Overall test matrix for the steam-assisted trials. 88

Table 13 - Maximum dilution for flammable operation, with energy content and exit velocity..... 88

NOMENCLATURE

δ	Destruction efficiency.
ε_{CH_4}	Error in stack methane concentration (ppm).
ε_{CO}	Error in stack carbon monoxide concentration (ppm).
$\varepsilon_{CO_2,in}$	Error in inlet carbon dioxide concentration (ppm).
$\varepsilon_{CO_2,out}$	Error in stack carbon dioxide concentration (ppm).
η	Carbon conversion efficiency.
λ	Stoichiometric air to fuel volume ratio.
ρ_a	Density of air (kg/m^3).
ρ_f	Density of fuel gas (kg/m^3).
σ_c	Reciprocal of increase of carbon in stack gas, summed over all species, ppm^{-1}.
$x^c_{CO_2,f}$	Mole fraction of carbon as carbon dioxide in fuel.
$x^c_{CO_2,out}$	Mole fraction of carbon as carbon dioxide in stack gas.
$\{x_i\}_{allcompounds}$	Composition of gas, the mole fraction of all species.
x_Σ	Volume fraction of species Σ.
X_{st}	Volume fraction of steam in the flare gas/steam mixture.
X^*_{st}	Critical volume fraction of steam, estimated maximum steam dilution for flammable mixture (equation 4-2).
A_p	Open area of flare pipe (m^2).
BMS	Burner Management System.

BTEX	Benzene, toluene, ethylbenzene, and xylenes.
CB	Carbon Balance (%).
CCE	Carbon Conversion Efficiency - the conversion of fuel-bound carbon to carbon dioxide, expressed as a percentage of the mass of carbon as carbon dioxide in the stack gas relative to mass of fuel-bound carbon.
CCI	Carbon Conversion Inefficiency - the failure to convert fuel-bound carbon to carbon dioxide, CCI = 100% - CCE.
DE	Destruction Efficiency - the percentage of a species in the flare gas that is converted into any other species. DE = 100% - FS.
D_p	Diameter of flare pipe (m).
EF_Σ	Emission factor for species Σ.
FRR	Flame Retention Ring.
FS	Fuel Slip, percentage of mass of carbon as fuel species in stack gas relative to the mass of fuel-bound carbon (%) $FS = 100\% - DE$
HV_m	Lower Heating Value, mass basis (J/kg); =1,000,000x LHV_m.
HRVOC	Highly reactive volatile organic compounds (eg. ethylene, propylene, 1-butene, cis/trans-2-butene, 1,3-butadiene).
I^*	Apex flammability curve when plotted as fuel % against inert %.
LHV_m	Lower Heating Value, mass basis (MJ/kg).
M_a	Molecular mass of air.
$\dot{m}_{air}$	Mass flow of air (kg/h).
$\dot{m}_{bucket}$	Mass flow of steam measured by the bucket (kg/h).
$\Delta\dot{m}^c{}_{CO}$	Net mass flow of carbon as carbon monoxide (kg/h).
$\Delta\dot{m}^c{}_{CO_2}$	Net mass flow of carbon as carbon dioxide (kg/h).
M_f	Molecular weight of flare gas.
$\dot{m}_f$	Mass flow of fuel (kg/h).

$\Delta \dot{m}^{c}{}_{HC}$	Net mass flow of carbon as hydrocarbon (kg/h).
$\dot{m}_{meter}$	Mass flow as measured by the steam flow meter (kg/h).
M_{Σ}	Molecular mass of species Σ.
P	Pressure (kPa).
PF	Power Factor (dimensionless).
RH	% Relative Humidity.
RSVF	Reduced Steam Volume Fraction.
RVFI	Reduced Volume Fraction Inert.
SDE	Specific Destruction Efficiency (%).
SFR	Steam to Fuel Mass Ratio, the mass ratio of steam-assist to flare gas (kg/kg).
T	Temperature (ºC).
U_f	Exit speed of fuel gas (m/s).
U_w	Mean crosswind speed, (m/s).
$y_{CO_2,in}$	Mole fraction of carbon dioxide in the inlet air (ppm).
$y_{CO_2,out}$	Mole fraction of carbon dioxide in the stack gas (ppm).

1.0 INTRODUCTION

Flares are the primary technology used for the safe and economical disposal of combustible gases at production sites and refineries. Flare performance and associated emissions are current environmental issues in some jurisdictions. This is partly because of genuine gaps in the flare research literature, as identified in a recent literature review (Gogolek et al., 2009). Also, there is confusion about the applicability of some published results to industrial scale flares. The literature review provides some structure and clarity regarding applicability of the various published data. Firstly, we distinguish the jetting and wake-stabilized regimes as distinct limiting modes of operation for flares. The research results from one regime may not be applicable to flares operating in other regimes. For example, the continuous decrease of efficiency with increasing cross-wind speed, which is well-established for the wake-stabilized production flares, may not apply to jetting refinery flares. Secondly, there is a minimum flare pipe size, around 7.5 cm (3 inches), for results to be scalable to industrial-scale flares. This means that some results in the literature are not representative of full-scale operating flares.

The International Flaring Consortium (IFC) was formed to review and address crucial gaps in the science of flares. The first objective of the IFC is to produce a method of predicting flare efficiency from operating variables: flare gas composition and flow rate; steam-assist rate; and wind speed. The method developed will rely upon original experimental work as well as published data. The second objective is to measure the emissions of: NO_x; the most important HRVOCs (ethylene, propylene, 1-3 butadiene, 1-butene and combined cis/trans-2-butene) and BTEX (benzene, toluene, ethylbenzene, and the xylenes); and to attempt to predict emission factors for these compounds based on the same set of operating variables. The third objective is to identify optimal operating conditions and identify the operating envelope for flares.

Based upon the literature review, we focused on the following six areas of flare performance which need to be addressed:

1. Experimental studies of the flare efficiency in the transition between jetting and wake-stabilized regimes.

2. Experimental studies of the effect of wind on steam-assisted flares.
3. Experimental studies on the limiting hydrogen concentration for steam-assisted flares, pilots, and wind blown flares.
4. Experimental studies of HRVOC and NO_x emissions, with and without steam-assist.
5. Correlation of flare efficiency with fuel properties and flare gas composition, particularly the inert gases nitrogen and carbon dioxide, and the impact of hydrogen.
6. Correlation of flare efficiency with steam-assist rate that considers flare gas composition, perhaps unifying steam with the approach used for correlating the effect of nitrogen and carbon dioxide dilution.

These are specific research areas that formed the general objectives of the IFC.

The technical background of the IFC experimental programs can be found in separate reports (Gogolek et al. 2009b, Caravaggio and Caverly 2008). Therein we described the equipment, procedures, quality analysis and control, and uncertainty of the derived measures. Herein we report the results of the experiments and analyze the data to obtain predictive expressions for performance and emission factors based on the operating conditions. Over 400 tests were run.

The report is organized as follows. The baseline tests with natural gas, scale-up testing with natural gas, the effect of the flame retention ring, and the transition from jetting to wake-stabilized operation are all in Chapter 2. Chapter 3 has the tests for unassisted flaring of ethylene and propylene. Chapter 4 has the tests for steam-assisted flaring of natural gas, ethylene and propylene. Chapter 5 covers the flaring limits for dilution with nitrogen or carbon dioxide. The trace emissions, NO_x, CO, HRVOCs and BTEX, for all the tests are reported in Chapter 6.

Note on terminology: We use the following definitions of performance measures.

- **Carbon Conversion Efficiency (CCE)**:= the conversion of fuel-bound carbon to carbon dioxide, expressed as a percentage of the mass of carbon as carbon dioxide in the stack gas relative to mass of fuel-bound carbon.

- **Carbon Conversion Inefficiency (CCI)**:= the failure to convert fuel-bound carbon to carbon dioxide, CCI = 100% - CCE.
- **Fuel Slip (FS)**:= percentage of mass of carbon as original fuel species in stack gas relative to the mass of fuel-bound carbon.
- **Destruction Efficiency (DE)**:= the destruction of a particular combustible species, expressed as percentage of 100% minus the mass of carbon of the combustible species in the stack gas relative to the mass of fuel-bound carbon of that combustible species. For a single hydrocarbon species, DE = 100% - FS.

1.1 Overview of CFR40 Requirements

Landmark studies sponsored by the United States Environmental Protection Agency (EPA) in the early 1980s (Pohl et al. [1984], Pohl and Solberg [1985, 1986]) demonstrated that properly designed and operated industrial flares are highly efficient. These EPA-sponsored studies led EPA to the codification of the conditions that ensure the proper operation of industrial flares.

> "EPA determined the destruction efficiency of flares combusting volatile organic emissions in the early 1980s and developed the existing flare specifications as a result of this work."

The Control Device Requirements of 40CFR60.18 were issued by EPA as a final rule on January 21, 1986.

The requirements of 40CFR60.18 apply to control devices including flares that are used to comply with New Source Performance Standards (NSPS) promulgated by EPA under Section 111 of the Clean Air Act (CAA) and the National Emission Standards for Hazardous Air Pollutants (NESHAP) issued under the authority of Section 112 prior to the CAA Amendments of 1990.

The Control Device Requirements of 40CFR63.11 were issued by EPA as a final rule on March 16, 1994. The requirements of 40CFR63.11 apply to control devices including flares that are used to comply with NESHAP issued under the authority of the CAA Amendments of 1990 for the control of hazardous air pollutants (HAP).

Operating conditions for flares are specified at 40CFR60.18(b) through (d); and 40CFR 63.11(b).

> "Flares operating in accordance with these specifications destroy volatile organic compounds (VOC) or volatile hazardous air pollutants (HAP) with a destruction efficiency of 98 percent or greater."

The flare specifications originally contained in 40 CFR 60.18 and 40 CFR 63.11 were based upon experience with waste streams containing organic substances. The rules mandate that flares be designed for, and operated with, no visible emissions, except for periods not to exceed a total of five minutes during any two consecutive hours. In addition, the flare specifications require that the flare must be operated with a flame present at all times. The presence of a flare pilot flame is to be monitored to ensure that a flame is present at all times. The minimum net heating value of the flared gas and the maximum exit velocity of steam-assisted, air-assisted, and non-assisted flares are specified in a table.

The table lists the allowable velocities for the possible heat contents and an equation is provided to calculate the net heating value of the flared gas. Air-assisted flares must operate with an exit velocity less than a specified maximum allowable velocity which is calculated from an equation that is provided. Also, an equation is provided to calculate the maximum exit velocity for non-assisted and steam-assisted flares.

Additionally, at 40CFR60.18(c)(3)(ii), EPA specified the minimum net heating value (Btu/scf) of the flared gas to assure flame stability and high destruction efficiency. However, E.I. DuPont de Nemours and Company (DuPont), among others, recognized that the net heating value (Btu/scf) of the flared gas hardly told the whole flame stability story.

In particular, DuPont and others recognized that the requirement to enrich the flared gas by injecting a higher-energy gas such as natural gas should be unnecessary when flaring a gaseous mixture that, merely by virtue of the presence of hydrogen, has a heating value that is less than that required by 40CFR60.18(c)(3)(ii).

DuPont (EER [1997]) carried out a comprehensive testing program that led EPA to conclude that

> "... hydrogen-fueled flares achieve greater than 98 percent destruction efficiency."

Subsequently, in the only substantive change in the operating condition requirements to this day, EPA amended the 40CFR60.18 and 40CFR63.11 specifications to allow compliance by adhering either to the heat content specifications that had already been set out for organic-mixture flares; or, in the case of hydrogen-mixture flares having a hydrogen content of 8.0 percent (by volume) or greater, by utilizing flares with a diameter of 3 inches or greater that are designed for and operated with an exit velocity less than 37.2 m/s.

Today's provisions can be found at the following links:

40CFR60.18: http://edocket.access.gpo.gov/cfr_2009/julqtr/pdf/40cfr60.18.pdf
40CFR63.11: http://edocket.access.gpo.gov/cfr_2009/julqtr/pdf/40cfr63.11.pdf

2.0 BASELINE, SCALE-UP AND REGIME TRANSITION TESTS

2.1 Introduction

These tests are preliminary to the main objectives of the IFC. The primary objective of these tests was to test the suitability of the 7.5 cm (3 inch) pipe, with respect to scale-up of results, and to see if smaller pipes can be used. While the "Three Inch Rule" is well established for the jetting regime [see Gogolek et al., 2009a and references therein], it was not clear that such a size limit applied in the strong wind situation that produces the wake-stabilized regime. Pipes with nominal diameters of 2.54 cm, 5.08 cm, 7.62 cm, 10.16 cm, and 15.24 cm (1", 2", 3", 4", and 6") were used to test for the lower limit (*Scaling Tests*). While the two larger pipe sizes (4" and 6") can be full-scale for flaring associated gas, industrial flares at refineries, petrochemical and chemical plants are orders of magnitude larger. A dimensionless parameter is developed to correlate the results, which is the prerequisite for successful scale-up of the results.

Natural gas is the baseline fuel for the program because it has several attractive features. Natural gas is easy to handle and low cost because it is provided as a utility and it is directly relevant for purge-and-pilot operation and upstream flaring of associated gas. Additionally, natural gas has been used in other research, notably by the University of Alberta, allowing comparison of the results from the CanmetENERGY Flare Test Facility with other published data (see the Literature Review [Gogolek et al, 2009a]). Average composition for natural is given in the Appendix of the Facility Report (Gogolek et al., 2010b), Table A1.

The effect of a Flame Retention Ring (FRR) in a cross-wind was tested with 3" and 6" tips (*FRR Tests*). The FRR is a standard appurtenance for industrial flares and provides improved performance with strong jets.

The transition from a vertical jet flame to a wake-stabilized flame was investigated (*Transition Testing*). The question was whether there would be a discontinuous change of performance as the wake-stabilized operation was established. This transition occurs as the wind begins to dominate the jet, either by strengthening of the wind or weakening of the jet. Both transitions were tested and compared.

The momentum flux ratio has been used in the literature for stacks to predict downwash, where the plume is pulled down by the low pressure wake of the stack. The wake-stabilized flare behaviour is similar, with the flame stabilized in the wake of the flare tip. The utility of this dimensionless parameter is tested both for the transition to wake-stabilized operation and correlating the combustion performance.

Some preliminary testing of flare gas composition effects was done (*Fuel Modification*), to provide guidance on how fuel composition affects performance. One level of dilution of natural gas with nitrogen was tested. One level of enrichment of natural gas with propane, a more reactive fuel, was tested.

2.2 Test Plan

2.2.1 SCALING TESTS

The scaling test matrix is given in Table 1. The flare tips were all basic pipes, Schedule 40 for the nominal size in inches. The flare gas flow, given as fuel mass rate, was at three levels – 10, 20 and 30 kg/h (22, 44 and 66 lb/h). This gave different exit velocities for the flare gas for the pipes with different diameters. The maximum wind speed was the same for all the pipe sizes. However, the minimum wind speed was not the same. For the smaller pipes, Nominal 2.5 cm (1") and 5.1 cm (2"), the minimum wind speed was determined by the flame rise – the flame would touch the ceiling of the working section of the wind tunnel when the wind speed was lower. For the Nominal 15.2 cm (6") pipe, the flame would touch the walls at lower wind speeds. A total of 258 tests were run.

Table 1 - Test matrix for scale-up tests with natural gas.

Pipe Size		Fuel Rate	Exit Velocity	Wind Speed	Number of tests
(Nom. inches)	(Nom. mm)	kg/h	m/s	m/s	
1”	25	10 - 30	7.3 – 22.2	3.1 - 12	12
2”	50	10 - 30	1.8 – 5.4	3.1 - 12	50
3”	80	10 - 30	0.8 – 2.5	2.0 - 12	66
4”	100	10 - 30	0.5 – 1.4	2.0 - 12	94
6”	150	10 - 30	0.2 – 0.6	3.5 - 12	36

2.2.2 FRR TESTS

Two flare tips were equipped with FRR. These were provided by John Zink LLC. Both were fabricated using Schedule 80 stainless steel pipe, one 7.6 cm (3”) Nominal and the other 15.2 cm (6”) Nominal. The FRR is composed of S-shaped segments each with 3 holes (see “Equipment & Calculation Report” [Gogolek et al, 2009b] section 2.2). The segments direct the main portion of the flare gas flow into the centre. The holes and the slots between segments allow a small amount of the flare gas to flow into the relative calm above the segments. This helps to stabilize the flame at high exit velocities. The open area of the 7.6 cm (3”) FRR tip is 21.7 cm^2 (3.36 in^2), equivalent to a 5.1 cm (2”) open pipe. Similarly the open area of the 15.2 cm (6”) FRR tip is 81.1 cm^2 (12.73 in^2), equivalent to a 10.2 cm (4”) open pipe. Since the FRR is a standard feature on many industrial flare tips, the FRR was selected as the base tip configuration for this test study. These tests were conducted to characterize the effect of low exit velocity and wind on the

performance of the flare tip and how the FRR flare tip results compare to basic pipe flare tips.

Table 2 - Test matrix for tests with FRR firing natural gas.

Pipe Size		Fuel Rate	Exit Velocity	Wind Speed	Number of tests
(Nom. inches)	(Nom. mm)	kg/h	m/s	m/s	
3”	80	10 - 30	1.9 – 5.5	2.0 - 12	43
6”	150	10 - 30	0.5 – 1.5	2.0 - 12	43

2.2.3 FUEL MODIFICATION TESTS

These tests were intended to provide guidance on the effect of combustion properties on flare performance. Two mixtures were tested. The first was natural gas with a small amount of propane added to increase reactivity. The mixture was 70%-mass natural gas with 30%-mass propane, which is 85%-vol natural gas and 15%-vol propane. Twenty tests were performed with this mixture flared to a 7.6 cm (3”) basic pipe; nine tests were performed with a 15.2 cm (6”) basic pipe. The mass flow rate of the flare gas was at the baseline values of 10, 20 and 30 kg/h (22, 44 and 66 lb/h).

The second mixture tested was natural gas with substantial nitrogen dilution. The mixture composition was 40%-vol natural gas with 60%-vol nitrogen. The mass flow of natural gas was at the baseline rates of 10, 20 and 30 kg/h (22, 44 and 66 lb/h), so that the total flow rate of flare gas was much higher, as shown in Table 3. This means the heat input rate, or the power of combustion was kept approximately the same as for the baseline tests with natural gas.

Table 3 - Test matrix for the fuel modification tests, augmented with propane and diluted with nitrogen.

Fuel	Pipe Size		Fuel Rate	Exit Velocity	Wind Speed	Number of tests
	(Nom. Inches)	(Nom. mm)	kg/h	m/s	m/s	
NG/propane	3”	80	10 - 30	0.6 – 1.8	3.5 – 9.5	20
NG/propane	6”	150	10, 20	0.15, 0.3	3.5 – 9.5	9
NG/N_2	3”	80	35 - 105	2 - 6	3.5 – 9.5	24

2.2.4 TRANSITION TESTING

The transition to wake-stabilized operation was addressed. The two questions being tested were:

- Is there a continuous or discontinuous transition for flare performance during the transition to wake-stabilized operation?
- Is the momentum flux ratio useful for correlating the performance during the transition?

Three flare tips were used: 5.1 cm (2") basic pipe, 7.6 cm (3") basic pipe, and the 7.6cm (3") FRR tip. Natural gas was used in all tests. Each test started at low wind and high fuel rate, producing a vertical flame a minimum of 10 cm (3.9”) above the flare tip. From this initial state, there are two ways of achieving the wake-stabilized mode – by increasing the wind speed and by decreasing the flare gas rate. Each path was followed. Three different flare gas rates of 20, 25, and 30 kg/h (44, 55 and 66 lb/h) were used for the 5.1 cm (2”) pipe. Only one flare gas rate (30 kg/h or 66 lb/h) was used for the 7.6 cm (3”) basic pipe and 7.6 cm (3”) FRR tip.

2.3 Results and Discussion

To study and evaluate a flare, two main criteria are introduced in this Section (and they are later used in the entire Report): "conversion inefficiency", and "destruction efficiency".

In general, to characterize a process, the "efficiency" (and not "inefficiency") is the primary criterion to consider. Therefore, the use of "conversion inefficiency" should be justified. Specially, using the term "conversion efficiency" would be more consistent with the use of "destruction efficiency", as both criteria aim towards as high values as possible (100%) in a well burning flare. Also, they should likely have similar trends as the functions of variables such as power factor, wind speed, Reynolds number or (for steam assisted flares) steam-to-fuel ratios. However, since the efficiencies are quite high, it is easier to demonstrate the dependence of operating variables by using inefficiency.

2.3.1 SCALE-UP TESTS

The inefficiencies for the individual pipe sizes are presented in Figures 1 through 5, plotted against wind speed. In all cases the inefficiency of carbon conversion increases with increasing wind speed. However, the inefficiency for the 5.1 cm (2") pipe appears to be almost constant for 5 m/s to 12 m/s (16 ft/s to 39 ft/s) wind speeds. Figure 6 brings all the results together in one chart, showing the large spread.

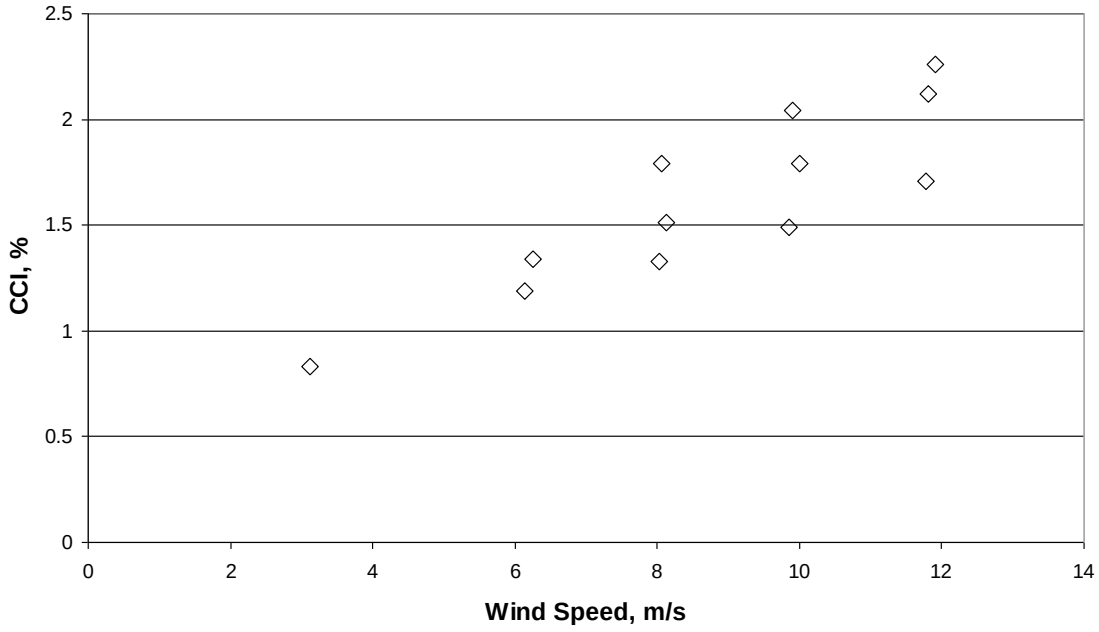

Figure 1 - Baseline testing results for 2.5 cm (1") basic pipe firing natural gas.

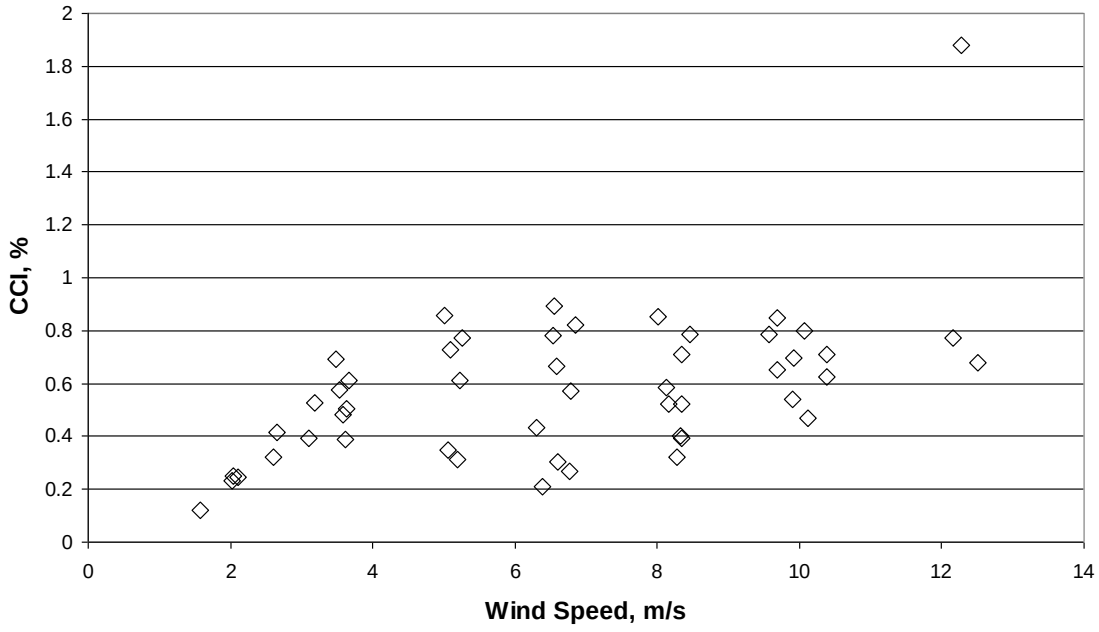

Figure 2 - Baseline testing results for 5.1 cm (2") basic pipe firing natural gas.

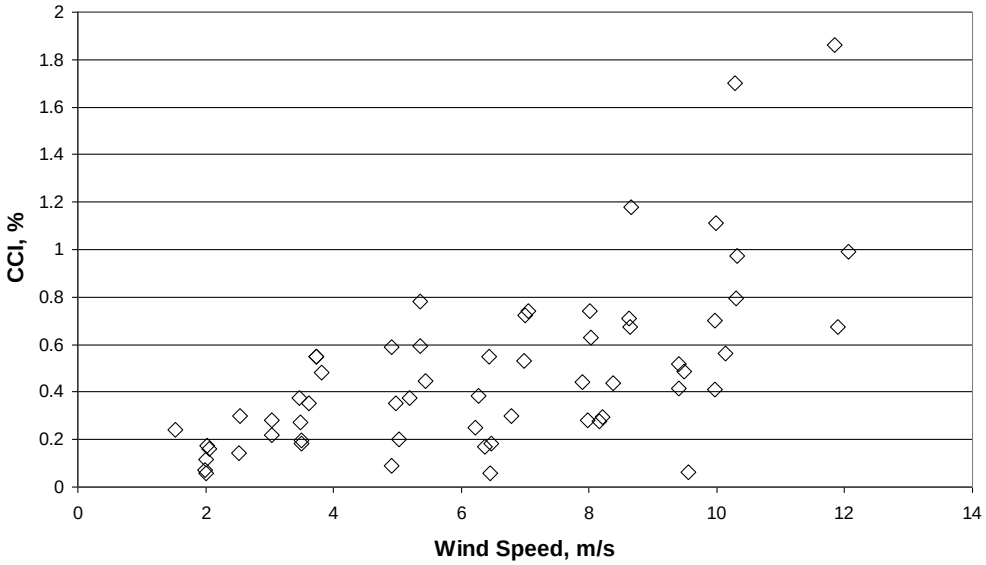

Figure 3 - Baseline testing results for 7.6 cm (3") basic pipe firing natural gas.

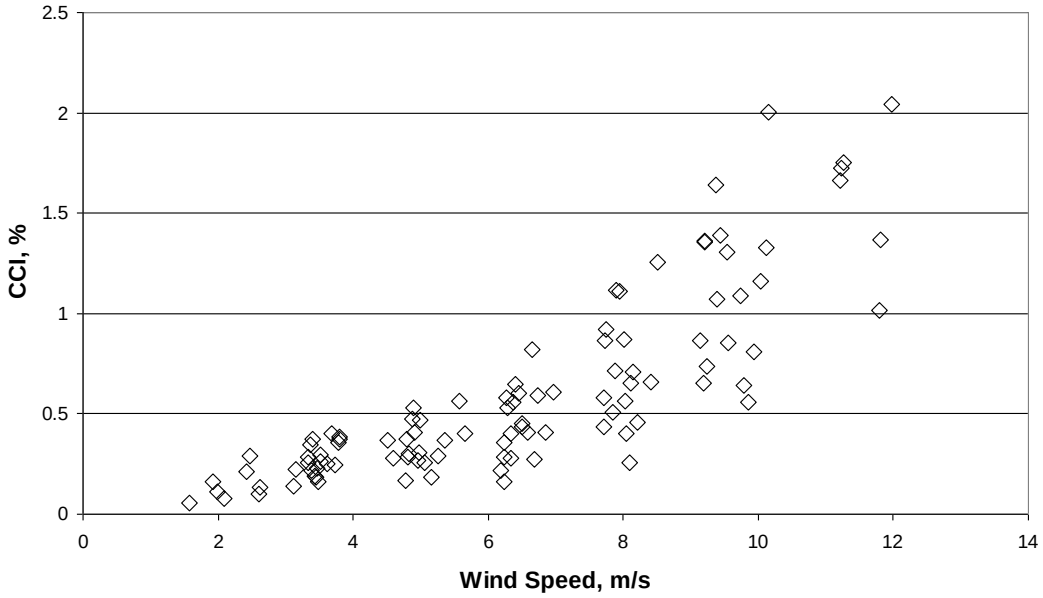

Figure 4 - Baseline testing results for 10.2 cm (4") basic pipe firing natural gas.

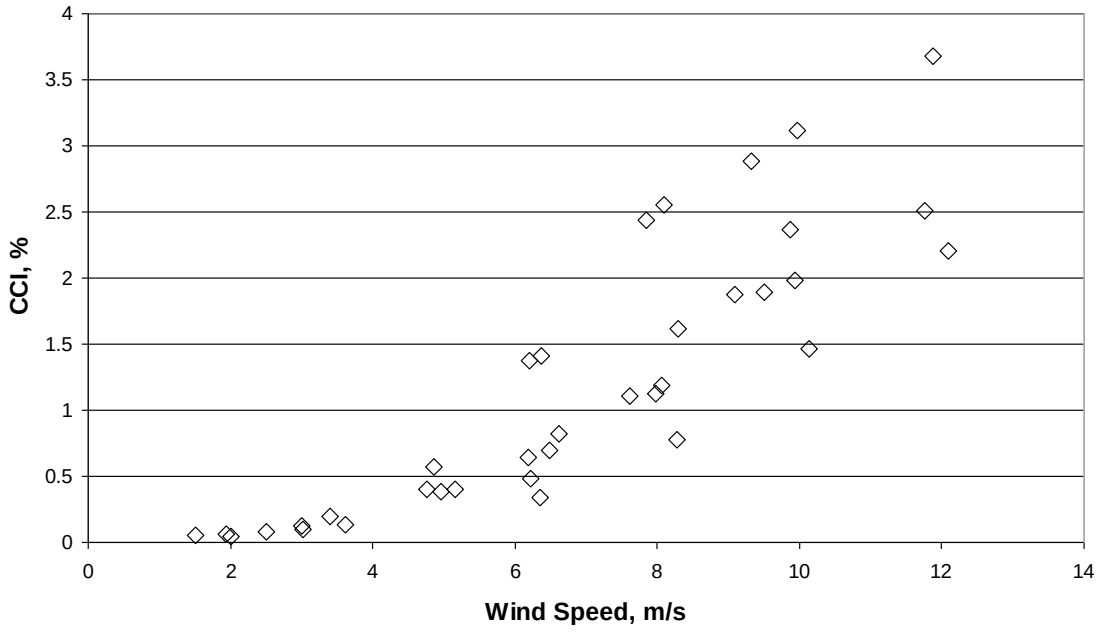

Figure 5 - Baseline testing results for 15.2 cm (6") basic pipe firing natural gas.

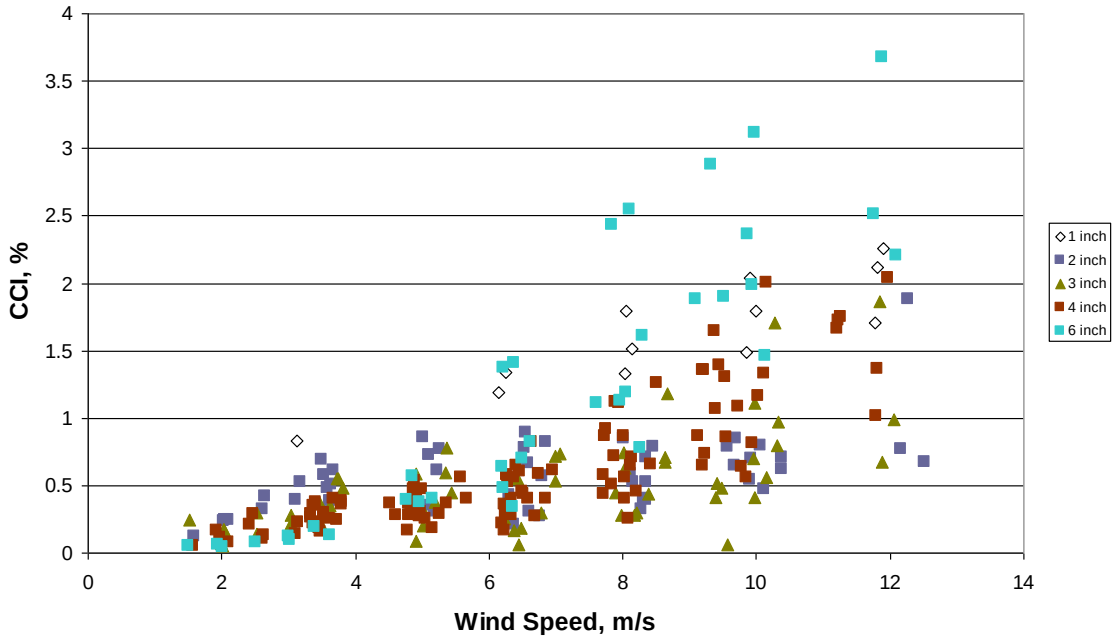

Figure 6 - Results of all baseline tests firing natural gas.

The independent variables for these tests are the wind speed, flare gas rate, and pipe diameter. In our literature review [Gogolek et al., 2009a], we showed that the Buoyant Plume dimensionless parameter[1] developed by the University of Alberta failed to correlate their data from 2.5 cm, 5.1 cm and 10.2 cm (1", 2" and 4") pipes. We developed our own dimensionless parameter from the ratio of the cross-wind power to the power of combustion of the flare gas. The cube root of this ratio gives the Power Factor.

$$PF = \left(\frac{\rho_a U_w^3 D_p^2}{\dot{m}_f HV_m} \right)^{1/3} = \left(\frac{\rho_a U_w^3 D_p^2}{\rho_f A_p U_f HV_m} \right)^{1/3} \qquad (2\text{-}1)^2$$

This factor is linear in the wind speed. If the scaling of the flare operation is according to the exit velocity of the flare gas, the Power Factor is independent of flare tip diameter. Figure 7 has the scale-up data with the data from the University of Alberta plotted against the Power Factor. It is clear that the 2.5 cm (1") pipe data diverges significantly from the rest, giving much higher inefficiency at lower values of Power Factor. The dashed line for the "U of A fit" is their correlation calculated for a 15.2 cm (6") pipe. Notice how the exponential dependence gives unrealistically high values of inefficiency compared to our experimental values. Figure 8 uses a semi-log plot to display the spread of the data. Here it is easier to see that the inefficiency for the 5.1 cm (2") pipes also diverges from the grouping for the larger pipe sizes. This demonstrates that results from pipes smaller than 7.5 cm (3") are not scalable to larger diameter pipes.

---

[1] Buoyant plume parameter is $BP = \frac{U_w}{\sqrt[3]{gD_p U_f}}$. The "U of A fit" is a simple exponential of the Buoyant Plume parameter. See Gogolek et al. (2009a) for details.

[2] At first glance, the Power Factor is not obviously dimensionless. In the second form, the units of the density terms cancel, as do the units of diameter squared with the open area of the pipe. The units of the heating value (mass basis) are J/kg = N m/kg = (kg m/s^2) m/kg = m^2/s^2, which are the same units as for velocity squared. So it is dimensionless.

Figures 9 and 10 show the results for only the 7.6 cm, 10.2 cm and 15.2 cm (3", 4" and 6") pipe sizes. There is a good correlation with the Power Factor. The 10.2 cm (4") pipe data from the University of Alberta are included and also show reasonable correlation with the Power Factor. The solid line fit to the data is equation 2-2.

$$CCI = 0.1 + \frac{100PF}{1 + \left(\frac{0.06}{PF}\right)^2} \qquad (2\text{-}2)$$

This form of equation is better suited for extrapolation, since as the Power Factor gets large the predicted inefficiency increases linearly with Power Factor.

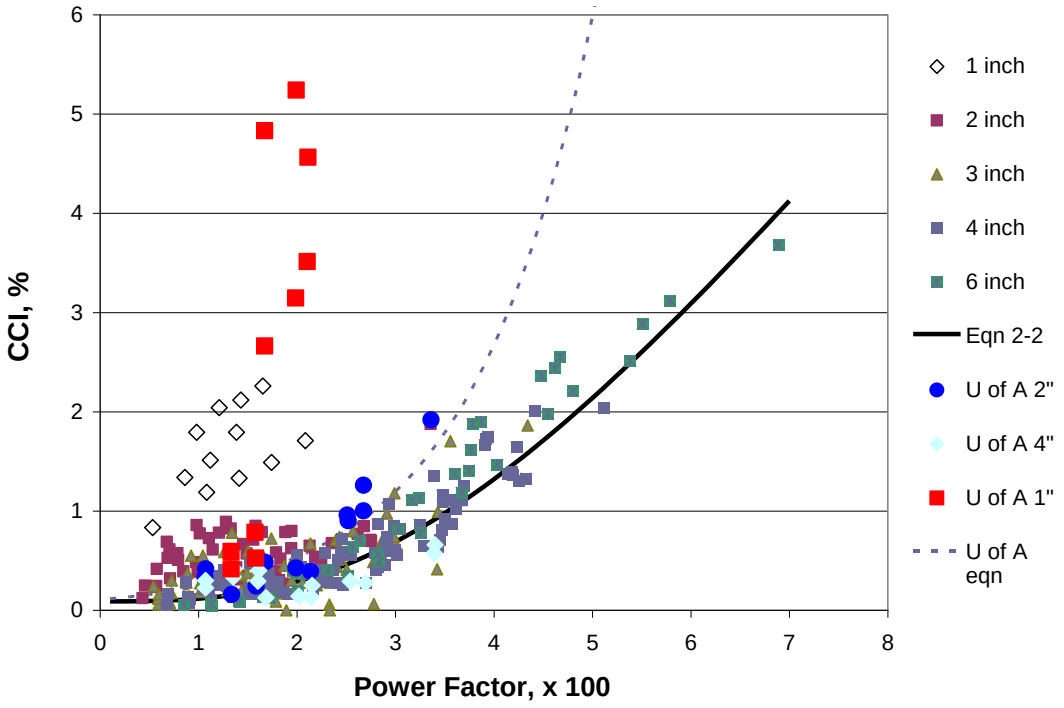

Figure 7 - Results for all pipe sizes, with results reported by the University of Alberta, correlated with the Power Factor. The solid line is equation (2-2) fit to the results for 7.6 cm (3"), 10.2 cm (4") and 15.2 cm (6") pipes.

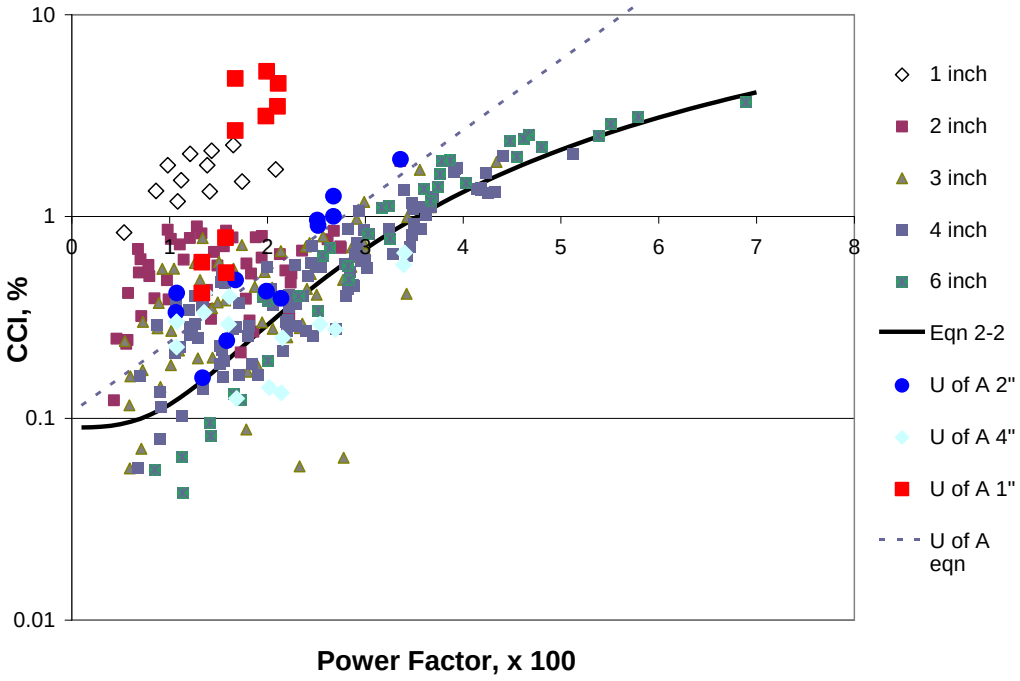

Figure 8 - Replotting Figure 7 as a semi-log plot, to better display the spread of the data.

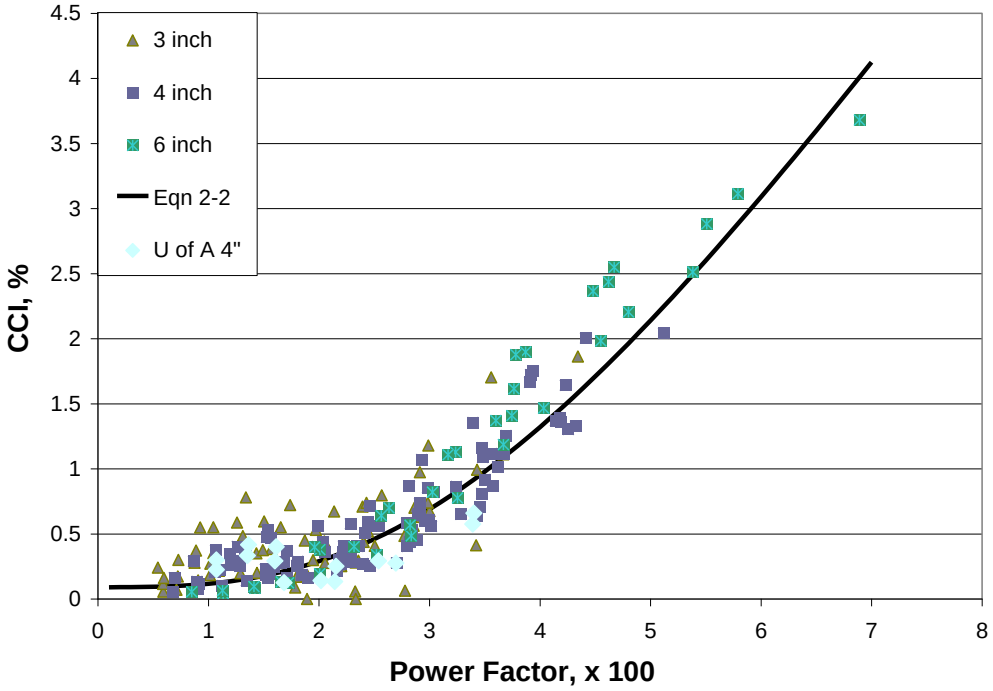

Figure 9 - Replotting Figure 7 with only the results for pipes 7.6 cm (3") or larger.

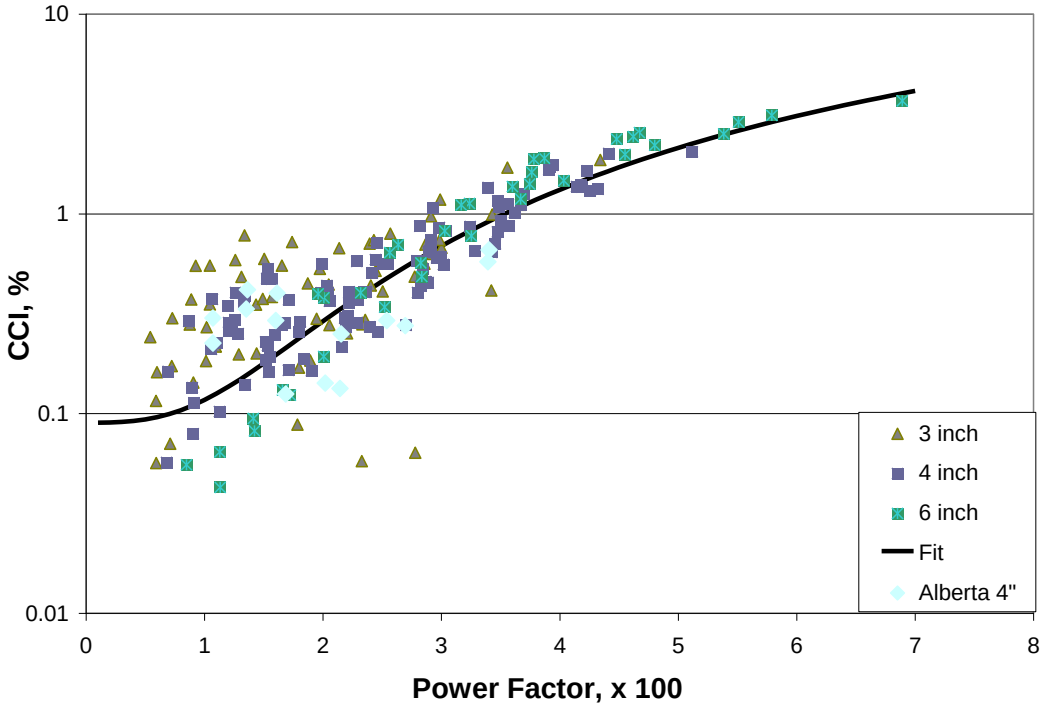

Figure 10 - Replotting Figure 9 as a semi-log plot to better display the spread of the data.

The conversion inefficiency measures the failure of the flare to convert the natural gas to carbon dioxide. The two mechanisms that contribute to the CCI are incomplete combustion, producing carbon monoxide, and fuel stripping, emitting methane. Figure 11 shows the percentage of conversion inefficiency due to fuel stripping, i.e. emitting methane, correlated with the Power Factor. Fuel stripping accounts for 60% to 80% of the inefficiency, the balance is production of carbon monoxide. The destruction efficiency data for these tests with the basic pipe are plotted against the Power Factor in Figure 12. The DE data have more scatter than the corresponding CCI data. The Power Factor is a useful correlating parameter.

$$DE = 99.9 - \frac{40PF}{1 + \left(\frac{0.035}{PF}\right)^4} \qquad (2\text{-}3)$$

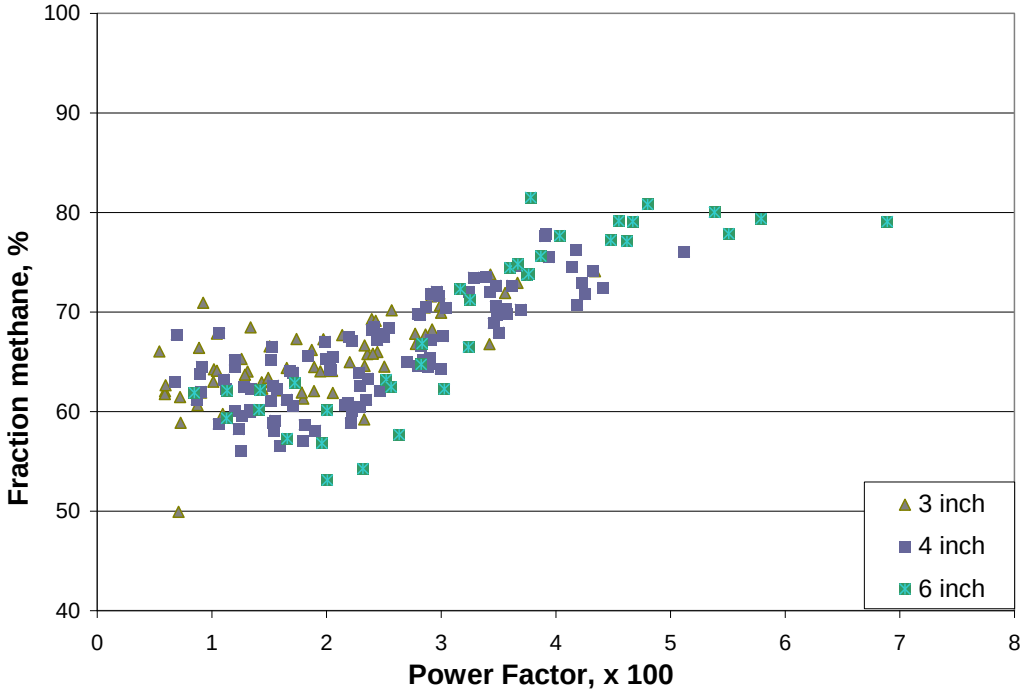

Figure 11 - Fraction of inefficiency due to the emission of methane correlated with the Power Factor.

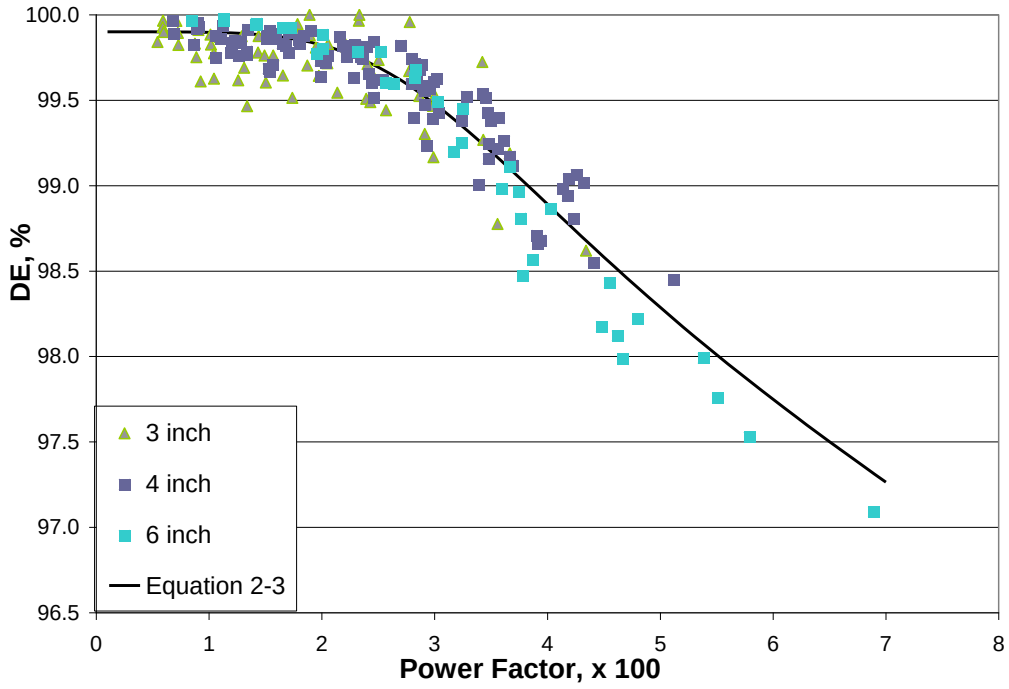

Figure 12 - Destruction efficiency for methane for the tests with natural gas and the basic pipe.

Figure 13 shows the conversion inefficiency for 7.6 cm and 15.2 cm (3" and 6") pipes equipped with the Flame Retention Ring (FRR). The solid line is equation (2-2), the fit to the inefficiency data for basic pipes. While there is a great deal more spread than for the basic pipe data, the FRR data are in moderate agreement. For the rest of the work, it is important to note that the 3" FRR data displays higher inefficiency than the basic pipes and the 15.2 cm (6") FRR tip. This means that the results with the 7.6 cm (3") FRR over-predict the inefficiency of larger tips which impacts the scalability of 3" test results

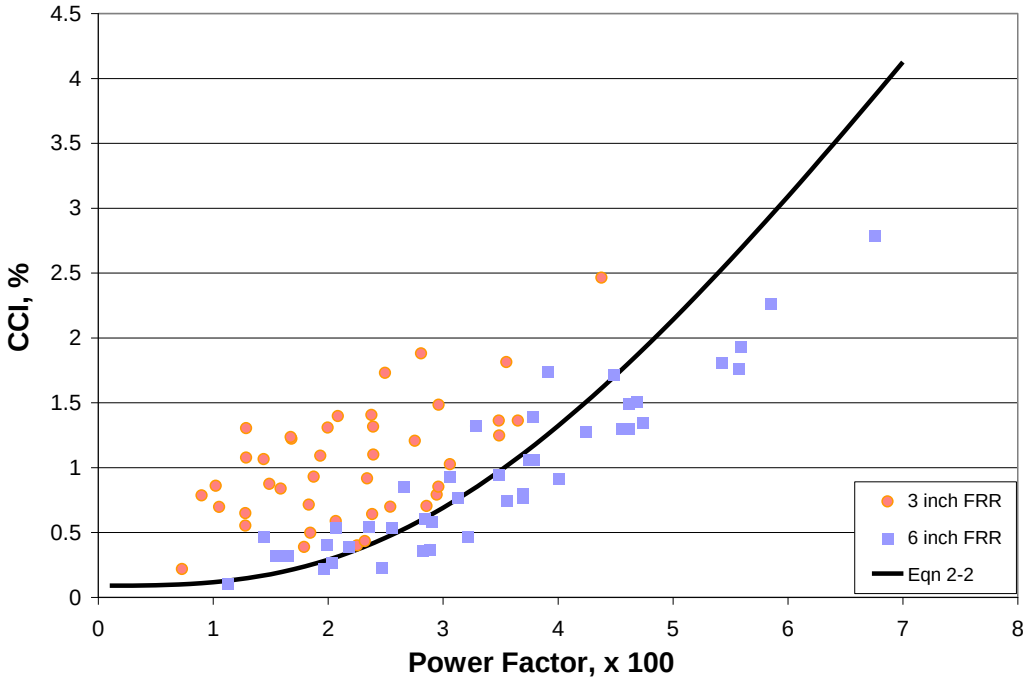

Figure 13 - Conversion inefficiency for 7.6 cm (3") and 15.2 cm (6") pipes fitted with FRR, plotted against the Power Factor. The solid line is the fit to the basic pipes 7.6 cm (3") and larger, equation (2-2).

The DE data for these tests are plotted in Figure 14. Only a couple of points are slightly below the 98% threshold efficiency often assumed. The equation fit to the data for the basic pipe is plotted here. The DE for the 7.6 cm (3") pipe with FRR is lower, and the DE for the 15.2 cm (6") pipe with FRR is larger.

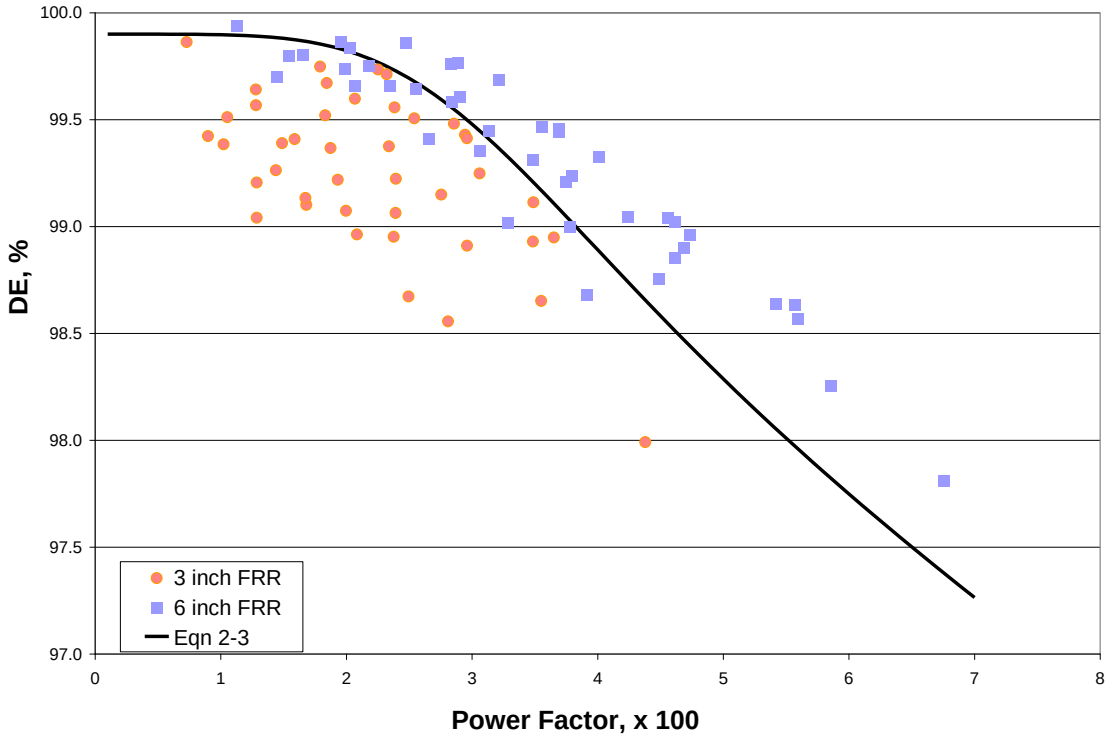

Figure 14 - Destruction efficiency for 7.6 cm (3") and 15.2 cm (6") pipes fitted with FRR, plotted against the Power Factor. The solid line is the fit to the basic pipes 7.6 cm (3") and larger, equation (2-3).

2.3.2 FUEL MODIFICATION TESTS

These tests considered natural gas enriched with 15%-vol propane and natural gas diluted with 60%-vol nitrogen. These tests were intended to provide relative effects of fuel composition, providing guidance for subsequent tests.

Figure 15 shows the results for the propane-enriched tests. The blue solid line indicates equation 2-2. The data are well correlated with the Power Factor, in the same form as equation 2-2 but with a 0.5 multiplier on the Power Factor (Eq. 2-4).

$$CCI = 0.1 + \frac{50PF}{1 + \left(\frac{0.06}{PF}\right)^2} \qquad (2\text{-}4)$$

This indicates that for low values of the Power Factor, the effect of fuel composition is small. As the Power Factor increases (> 2), the effect of the enrichment with 15%-vol propane is to decrease the conversion inefficiency.

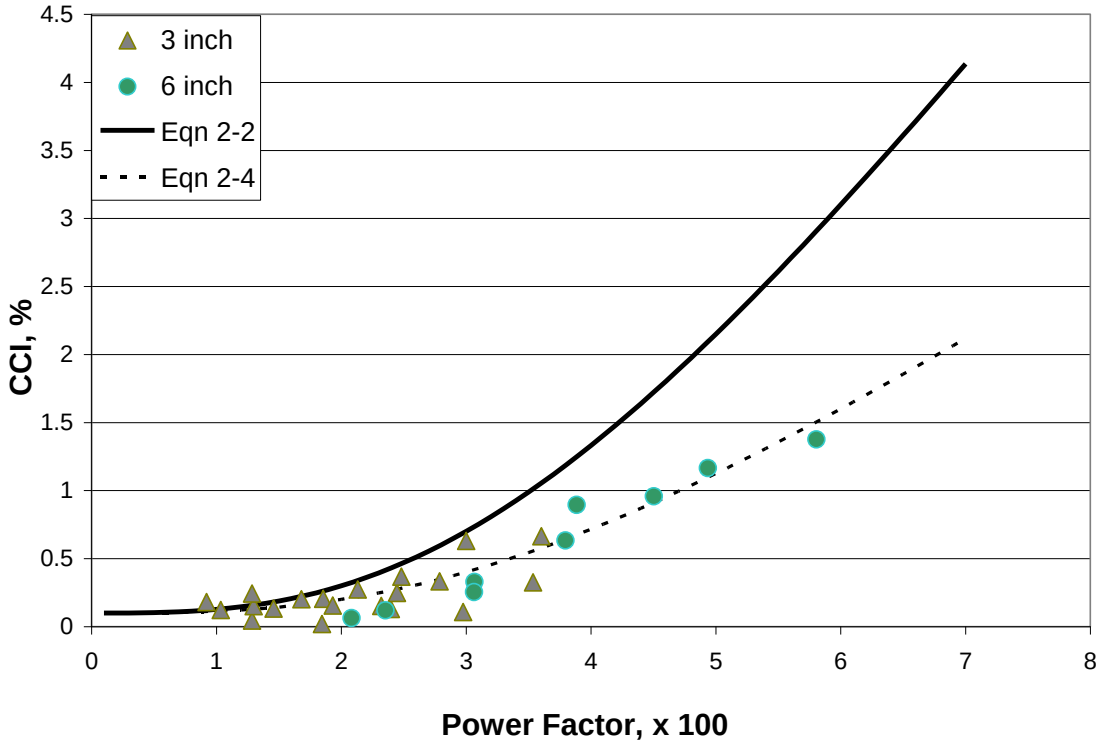

Figure 15 - Results for tests with 7.6 cm (3") and 15.2 cm (6") basic pipes firing a mixture of 85%-v natural gas with 15%-v propane. The solid line is the fit to the natural gas results (equation 2-2), the dashed black line is equation (2-4).

Figure 16 shows the conversion inefficiency results for natural gas diluted with 60%-vol nitrogen. Comparison with Figure 9 should convince the reader that the nitrogen dilution at this level produced no significant change in conversion inefficiency.[3] Note that in the range of Power Factor covered (1<PF<3), the conversion inefficiency is relatively flat.

[3] The only visible change in the flame was that it was paler, more blue and less yellow.

These two figures pose a difficult question on modelling the fuel effects. The nitrogen dilution produces a much bigger change in the combustion properties of the mixture (such as laminar burning rate or adiabatic flame temperature) than the enrichment with 15%-vol propane. However, the effect of the propane addition is substantial while the nitrogen dilution has no noticeable effect.

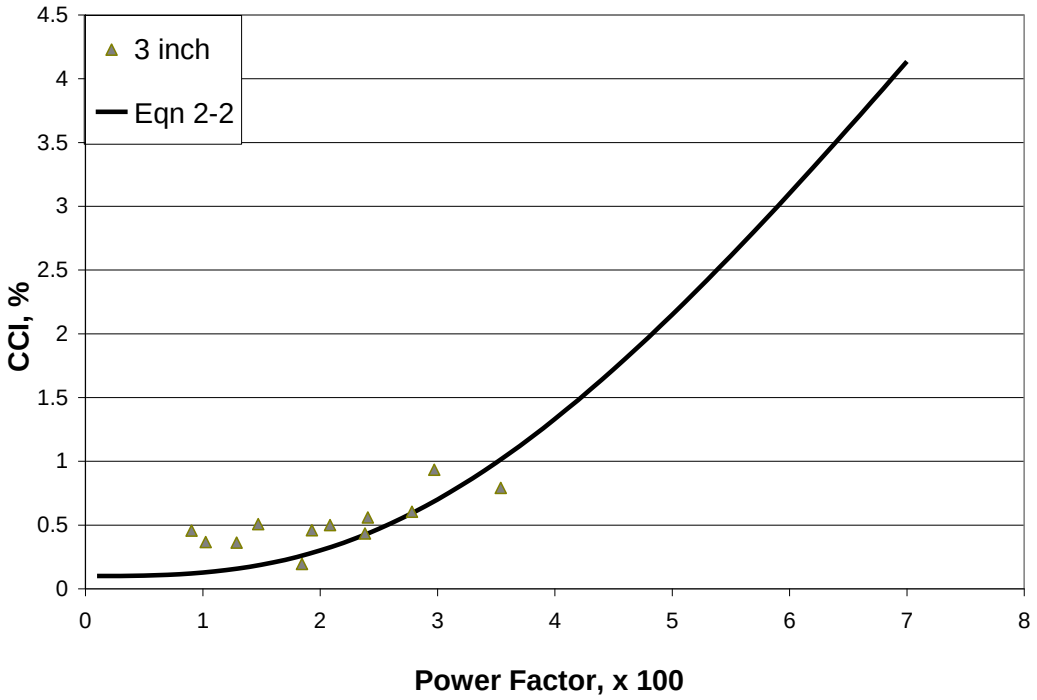

Figure 16 - Results for 7.6 cm (3") basic pipe firing a mixture of 40%-v natural gas with 60%-v nitrogen. The solid line is the fit to the natural gas data.

2.3.3 TRANSITION TESTING

The transition to wake-stabilized operation was tested with 5.1 cm and 7.6 cm (2", 3") basic tips and 7.6 cm (3") FRR flare tips. Since the results for the 5.1 cm (2") pipe has been shown not to scale to larger sizes, we will concentrate on the 7.6 cm (3") pipe results. Figure 17 shows conversion inefficiency for the 7.6 cm (3") pipe in the two paths to wake stabilized operation. The pipe Reynolds number is proportional to the flare gas

flow rate[4]. Changing the flare gas flow rate produces very little change in the inefficiency, as indicated by the nearly horizontal line. However, increasing the wind speed produces a marked increase in the inefficiency, as shown by the vertical line in Figure 17 and the curved line in Fig 18. Figure 19 plots the inefficiency against the Power Factor. The correlation is reasonable. However, all the transition data are plotted in Figure 20 against the wind speed and display a good correlation with that single operating variable for these transition tests. From this figure the 7.6 cm (3") FRR performs significantly different than the 7.6 cm (3") basic flare. Data curve fits have significantly different slopes.

That the fuel ramping and wind ramping produce drastically different inefficiency with the same momentum flux ratio indicates that the momentum flux ratio has limits for correlating the performance of flares. However, the transition to wake-stabilized operation, determined visually, occurred at momentum flux ratio of around 3 for all three pipes. This agrees with the downdraft literature for smoke stacks as we described in the literature review [Gogolek et al., 2009]. Although smoke stacks are non-reacting flows and flares are strongly reacting, this coincidence may be worth further investigation and may indicate that 3 is a good boundary for the transition to wake-stabilized operation.

---

[4] The pipe Reynolds number is $D_{pi}U_f/\nu_f$ where D_{pi} is the inner diameter of the pipe, U_f is the exit velocity of the flare gas, and ν_f is the kinematic viscosity of the flare gas. For the FRR flare tips, the inner diameter and exit velocity are based on the open area of the flare tip.

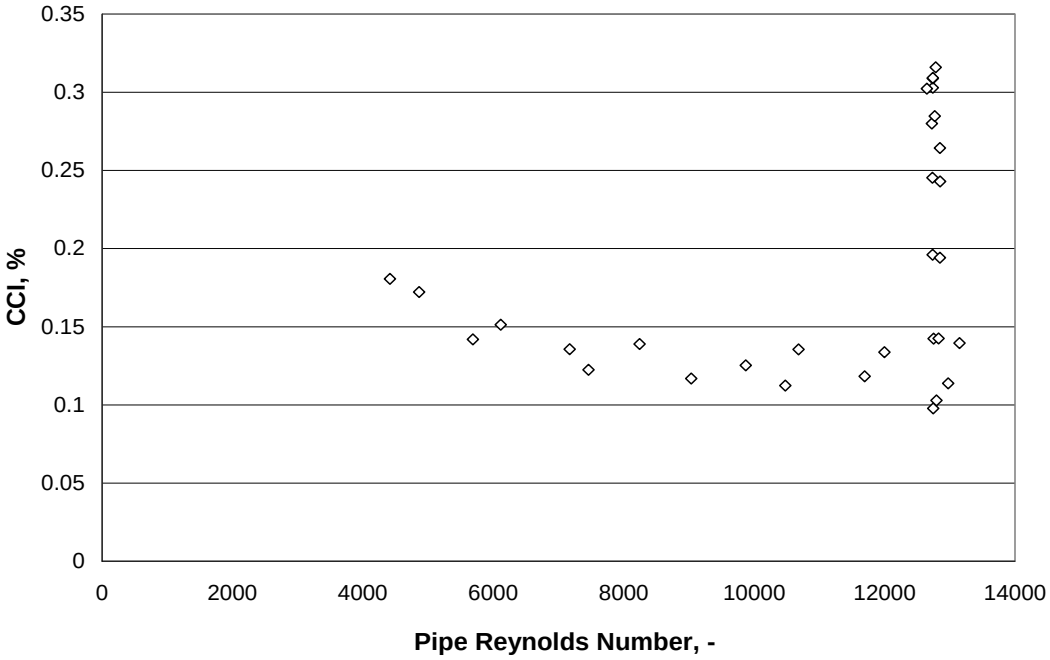

Figure 17 - Results for 7.6 cm (3") pipe for transition testing versus fuel Reynolds number. Changing the fuel rate has a very small effect.

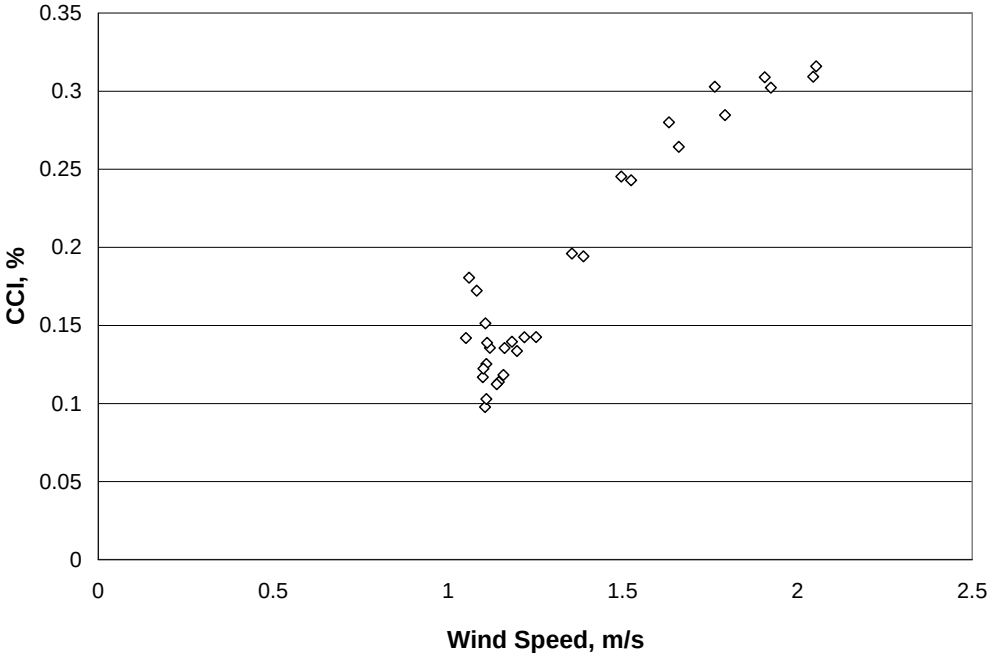

Figure 18 - Results for 7.6 cm (3") pipe for transition testing versus wind speed. The change in fuel rate at 1.1 m/s has a much smaller effect than the increase of wind speed.

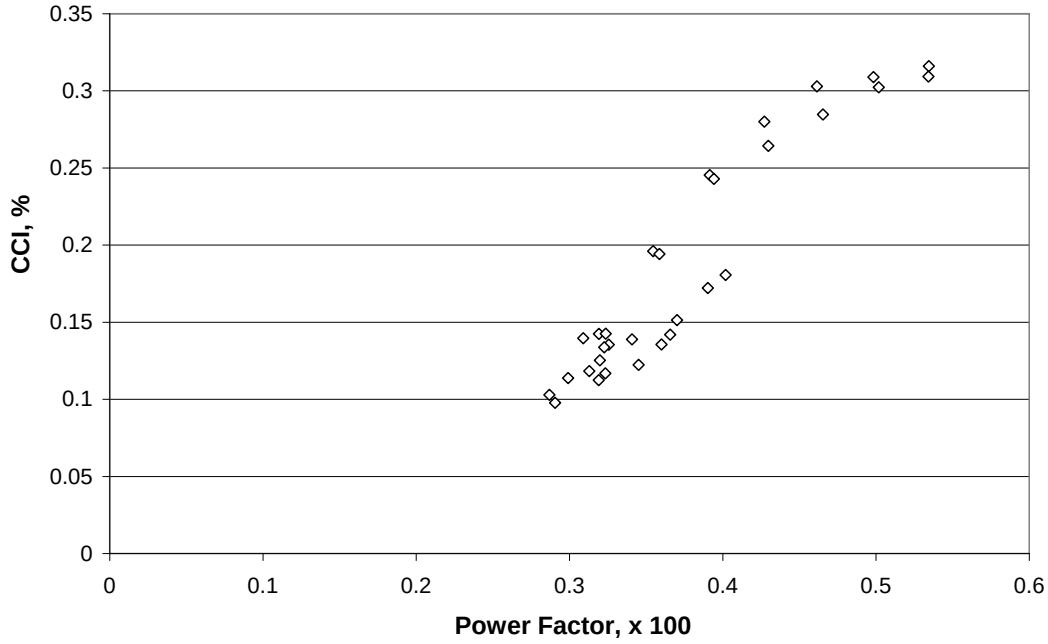

Figure 19 - Results for transition testing of 7.6 cm (3") pipe correlated with the Power Factor.

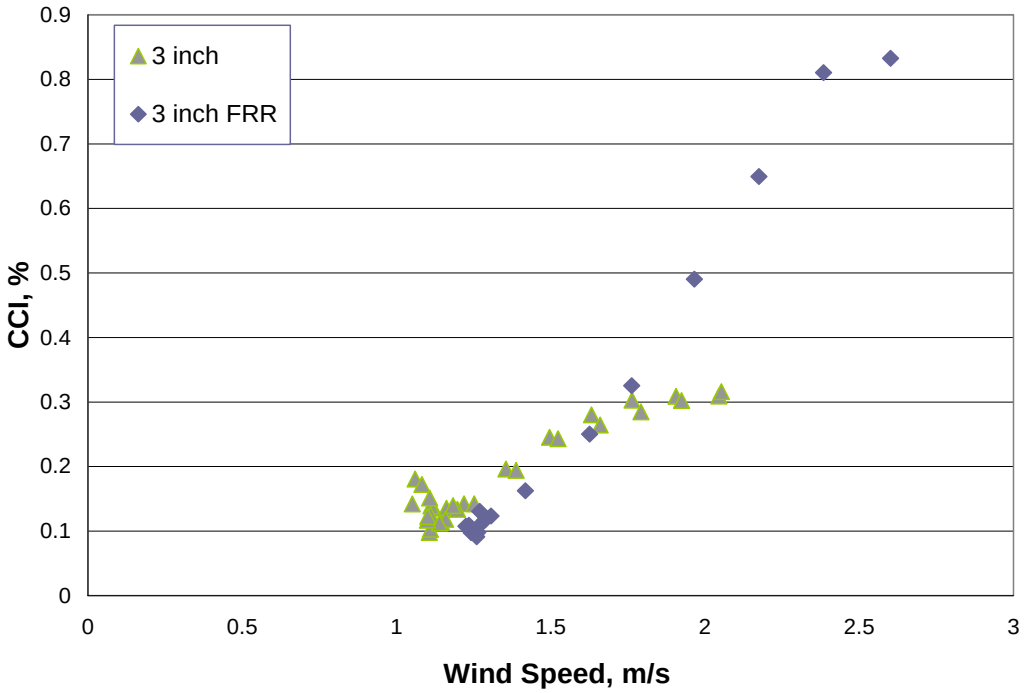

Figure 20 - Transition test results with 7.6 cm (3") pipes versus wind speed.

2.4 Conclusion

These baseline tests with natural gas have produced several results useful for the further work on flare performance.

- It is conclusively shown that there is a "Three Inch Rule" for the wake-stabilized operation of flares with wind, as there is for jetting (no wind) operation. This means that results for pipes smaller than 7.6 cm (3") do not scale-up to larger pipes. This is important to keep in mind when small pipe results are used for guiding operating practice. Whether the results for 3" to 6" pipes can be successfully applied to full-scale industrial flares has not been established and is beyond the scope of this work.

- The Power Factor (equation 2-1) appears to be a useful dimensionless parameter for correlating flare performance data. It incorporates the effects of wind speed, flare gas rate, and pipe diameter. This indicates the potential for results correlated with the Power Factor to apply to larger diameter flares. However, the PF does

not contain information about the combustion properties of the flare gases and was only tested on natural gas in this chapter. It would have to be augmented to correlate performance of different flare gases and gas mixtures.

- Equation 2-2 is a correlation of the CCI with the Power Factor for results with 7.6 cm, 10.2 cm and 15.2 cm (3", 4" and 6") pipes flaring natural gas (see Figure 9). This correlation should be useful for solution gas flaring relative to flaring only natural gas.
- Augmentation of natural gas with 15%-vol propane produced a significant reduction in inefficiency. Equation 2-4 is the correlation of the CCI with the Power Factor for this flare gas (see Figure 15); it is a simple modification of equation 2-2.
- Dilution of natural gas with 60%-vol nitrogen produced no noticeable change in inefficiency (see Figure 16).
- The Flame Retention Ring (FRR) does have an effect on the performance of the flare compared to the basic pipe. It gives slightly worse performance for the 3" pipe and slightly better performance for the 15.2 cm (6") pipe (see Figures 13 and 14). Physical change to flare tip configuration affect flare emissions. Results from this test work apply to small pipe flares that have and don't have flare retention rings, such as production flares. Based on the comparison of CEs for the 3" and 6" pipes in this chapter, actual CEs for larger diameter flares will be higher than those reported in subsequent chapters for the 3" FRR tip.
- Transition testing shows that there is a continuous change in the performance of the flare as the wake-stabilized regime is established. When the transition is accomplished by reducing the flare gas rate, there is negligible change in the inefficiency. When the transition is accomplished by increasing the wind speed, the inefficiency is increased.

3.0 SIMPLE FUEL GAS TESTS

3.1 Introduction

These tests investigated the effect of wind on the carbon conversion inefficiency and destruction efficiency (DE) for unassisted operation. All the tests were performed using the 7.6 cm (3") FRR tip. The two gases flared were ethylene and propylene. Unassisted flaring of these gases produces significant soot, and particulate sampling was performed for all these tests to measure the emission rate. The results of these tests are compared to our baseline results for natural gas from Chapter 2.

3.2 Test Plan

The variables investigated are the fuel rate and wind speed for each fuel. The test matrix is given in Table 4. The mass rate of flare gas was the same for both fuels.

Table 4 - Test matrix for the simple fuel flaring tests.

Fuel	Rate (kg/h)	Exit velocity (m/s)	Wind Speed (m/s)	Number of Tests
Ethylene	10, 30	1.2, 3.4	3.8, 7.0, 10.3	10
Propylene	10, 30	0.75, 2.2	3.8 – 10.8	7

The tests with ethylene had three levels of wind speed. The tests with propylene had 5 levels of wind speed, covering the same range. There is an overlap of the ranges of exit velocity for each gas. This isolated the effects, if any, of the gas properties. A total of 17 tests were performed.

3.3 Results

The conversion inefficiency results for all the tests with ethylene and propylene are plotted against wind speed in Figure 21. The results for propylene show high conversion inefficiency and non-monotonic behaviour with wind speed. The inefficiency results for ethylene are lower and basically monotonic with wind speed.

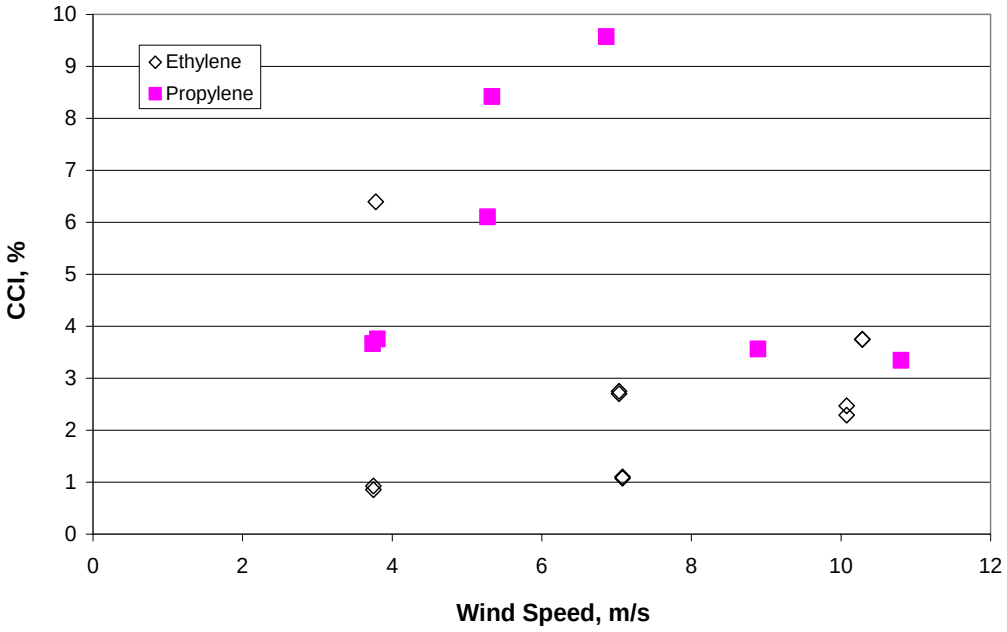

Figure 21 - Conversion inefficiency for unassisted flaring of ethylene and propylene in 7.6 cm (3") FRR tip.

The DE results are shown in Figure 22. Better than 98% DE is achieved for all wind speeds for ethylene flaring without assist. The DE for propylene drops below 98% above 8 m/s (26 ft/s) wind, but remains better than 97% and monotonically increases with wind speed. The difference between the CCI and DE is due primarily to the formation and emission of particulate carbon, soot.

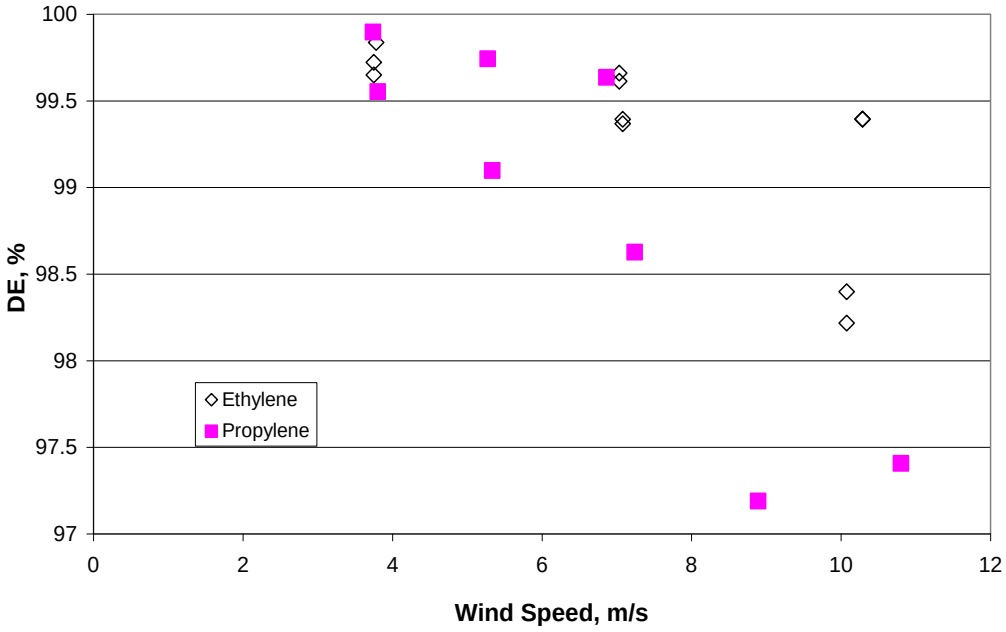

Figure 22 - Destruction efficiency for unassisted flaring of ethylene and propylene in 7.6 cm (3") FRR tip.

The soot emission, solid carbon emitted as percent of total carbon flared, is shown in Figure 23. The behaviour of the two fuels is markedly different. Soot emission goes to zero for wind speed above 8 m/s (26 ft/s) for propylene. This is possibly due to increased entrainment of air reducing the flame temperature. The soot emission for ethylene displays no pattern, a random scattering, with respect to wind speed.

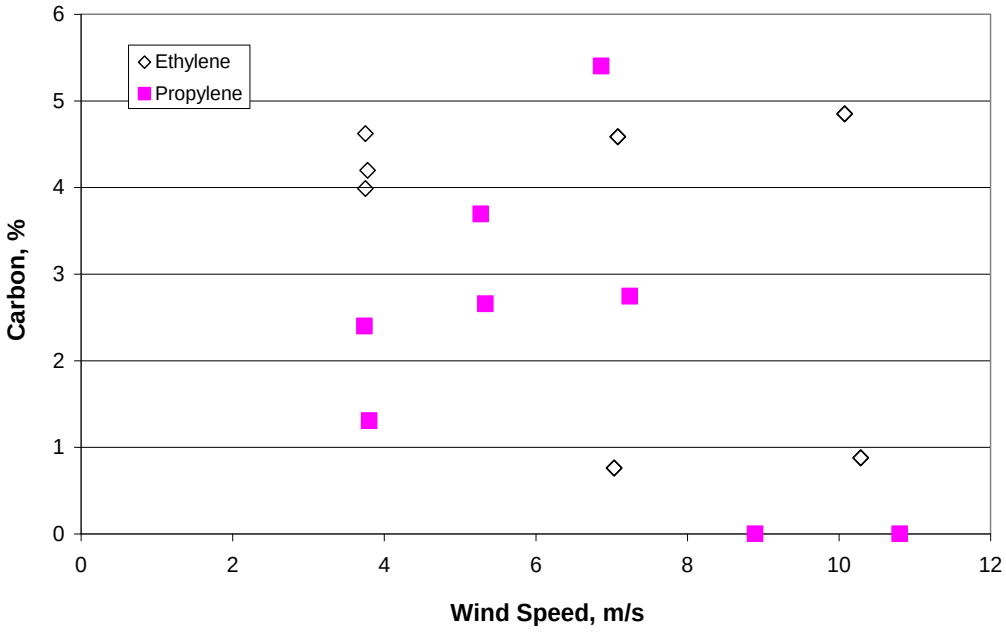

Figure 23 - Solid carbon emission as a percentage of the total carbon for unassisted flaring of ethylene and propylene in 7.6 cm (3") FRR flare tip.

3.4 Discussion

The simple fuel results show that high destruction efficiencies (above 98%) are obtained even at very high wind speeds for these two fuels. Figure 24 plots these results against the Power Factor, together with equation (2-2) for natural gas flared in a basic pipe and the data for the natural gas flared with the 7.6 cm (3") FRR tip. The basic pipe fit has higher DE. There is a large amount of scatter (around 1%) for the natural gas DE with the 7.6 cm (3") FRR tip. This covers the data points for ethylene and propylene. However, it does appear that the Power Factor can correlate the DE results for ethylene and propylene.

Ethylene has higher DE than propylene, which is to be expected from its combustion properties – wider flammability limits and higher laminar flame speed. As seen with the enrichment of natural gas with propane, the differences in fuel properties become evident only at the higher values of Power Factor. When the Power Factor is small all the fuels have high DE.

The correlation using the Power Factor indicates that these results should be scalable to large flare pipes, as shown in the previous chapter.

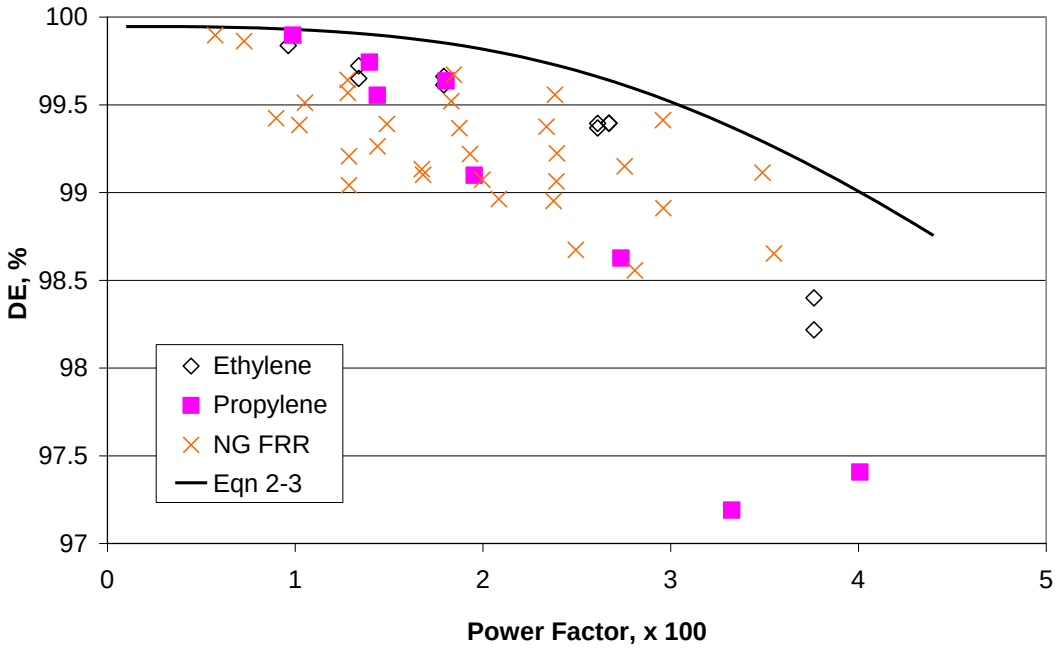

Figure 24- Comparison of destruction efficiency of unassisted flaring of ethylene and propylene with that of natural gas in a 7.6 cm (3") FRR flare tip. The solid line is equation 2-3, the DE curve for natural gas flared with 7.6 cm, 10.2 cm or 15.2 cm (3", 4" or 6") basic pipe.

3.5 Conclusion

Tests of the unassisted flaring of ethylene and propylene established the following:

- Particulate carbon makes a significant contribution to the carbon conversion inefficiency (CCI). It does not affect the Destruction Efficiency. For ethylene, it is around 5% of total carbon, independent of wind speed. For propylene, particulate carbon emissions increase with wind speed to a maximum around 6% at 7 m/s (23 ft/s). Carbon emission dropped below the measurement threshold of 0.1% of fuel carbon at higher winds for propylene.

- Destruction Efficiency decreases with wind speed but remains better than 98% for ethylene even at the highest wind speed tested (11 m/s or 36 ft/s).
- DE for propylene decreases more with wind speed, falling below 98% above 8 m/s (26 ft/s). DE is above 97% for all winds for propylene.
- DE for unassisted flaring of ethylene and propylene is correlated with the Power Factor. The scale-up results in the previous chapter indicate that these DE results for ethylene and propylene have the potential to scale-up to large flare tip sizes.

4.0 STEAM-ASSIST TESTS

4.1 Introduction

Here we test the effects of steam-assist on the flaring of natural gas, ethylene and propylene. Flaring natural gas generally does not require steam-assist. However, a steam-assisted flare may have a purge flow of natural gas and the steam nozzles with stand-by flow. Some of the tests with natural gas are therefore with low flow rates for both the flare gas and the steam.

The tests with the model gases ethylene and propylene are intended to demonstrate more normal operation of the flare. There was no measureable soot for the steam rates used in this study.

These results are presented against the standard measure of level of steam-assist, the steam-to-fuel mass ratio (SFR). The Power Factor is also used to correlate the data, with some success. A new measure of the steam-assist rate, the Reduced Steam Volume Fraction (RSVF), is derived in equation 4-3 to assist the analysis.

The CMA/EPA tests (McDaniel, 1983) on the steam-assisted flaring of propylene had little or no wind. As a result, those results are not directly comparable to ours. However, they will be used as a possible extrapolation of our results to the condition of low wind speed. The steam-assisted tests by EER (Pohl et al. 1984, Pohl and Soelberg 1985, Pohl and Soelberg 1986) found a maximum combustion efficiency with SFR = 0.7. However, those tests used propane as the flare gas, which again is not directly comparable to our tests.

4.2 Test Plan

All tests used the 7.6 cm (3") FRR tip, with the steam-ring provided by John Zink LLC. See the report on the experimental facility for a description of the equipment [Gogolek et al, 2009b]. Three wind speeds were tested. The test matrix is given in Table 5.

Table 5 - Overall test matrix for the steam-assisted trials.

Fuel	Fuel Rate (kg/h)	Exit Velocity (m/s)	Wind Speed (m/s)	SFR (kg/kg)
Natural gas	7 - 30	1.2 – 5.8	3.5 – 9.5	<0.3 – 2.2
Ethylene	10, 30	1.1 – 3.3	3.5 – 9.5	0.24 – 3.4
Propylene	10, 20, 30	0.7, 1.4, 2.2	3.5 – 9.5	0.3 – 1.2

There are 6 tests with natural gas that had steam flow but the measurement of the steam flow was faulty. These were low flow tests and hence the steam rate was set to zero.

There was only one test with ethylene at the high flare gas rate of 30 kg/h (66 lb/h).

The maximum SFR for propylene was 1.2. The flame was quenched at higher steam rates. Published work, particularly the CMA/EPA study [McDaniel, 1983], indicated that propylene can have an SFR up to 3.5 before performance is significantly degraded. The difference in these measurements is addressed in the Discussion section.

4.3 Results

The conversion inefficiency and DE results for steam-assisted flaring of natural gas are presented in Figures 25 and 26, plotted against the SFR and indexed by the wind speed. Wind clearly has a strong negative impact on the performance of the flare. Natural gas test results for destruction efficiency and combustion inefficiency are much degraded compared to the mid-1980's CMA/EPA [McDaniel, 1983] and EPA test results [Pohl et al. 1985, Pohl and Soelberg 1985, 1986]. IFC results do not produce 98-99% destruction efficiency as the CMA/EPA and EPA tests did. Instead, the IFC test results have 90-95% destruction efficiency. For SFR > 1.0, CCI increases significantly whereas the CMA/EPA and EPA tests experienced such degradation when SFR > 3.5.

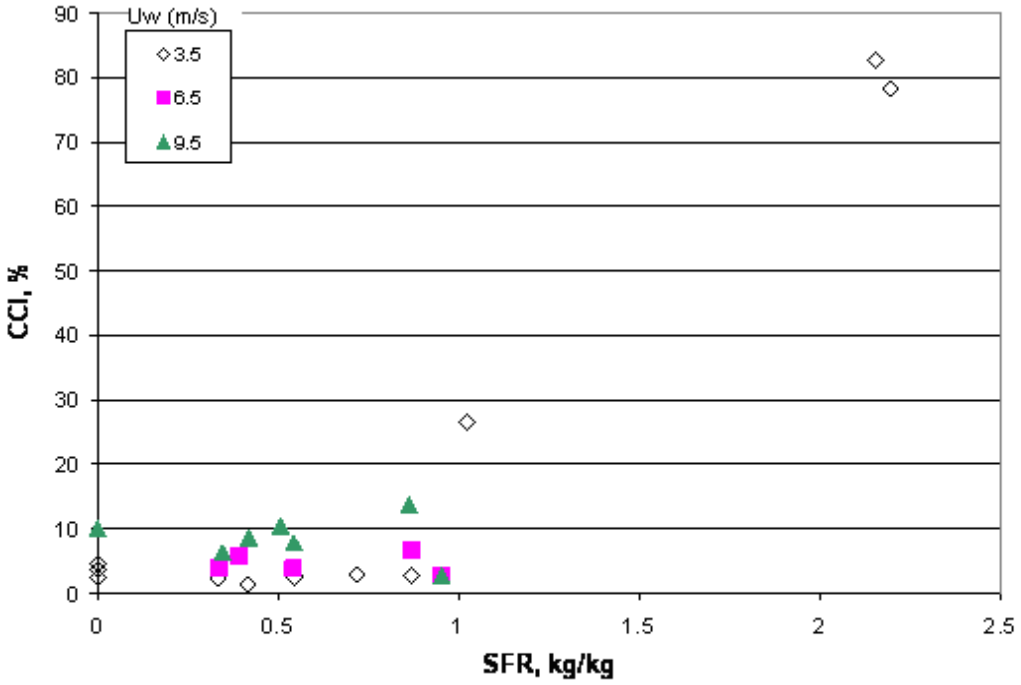

Figure 25 - Conversion inefficiency versus steam-to-fuel mass ratio for steam-assisted flaring of natural gas, indexed on nominal wind speed. The zero SFR points did have steam flowing, but the correction of the flow rate produced a negative value.

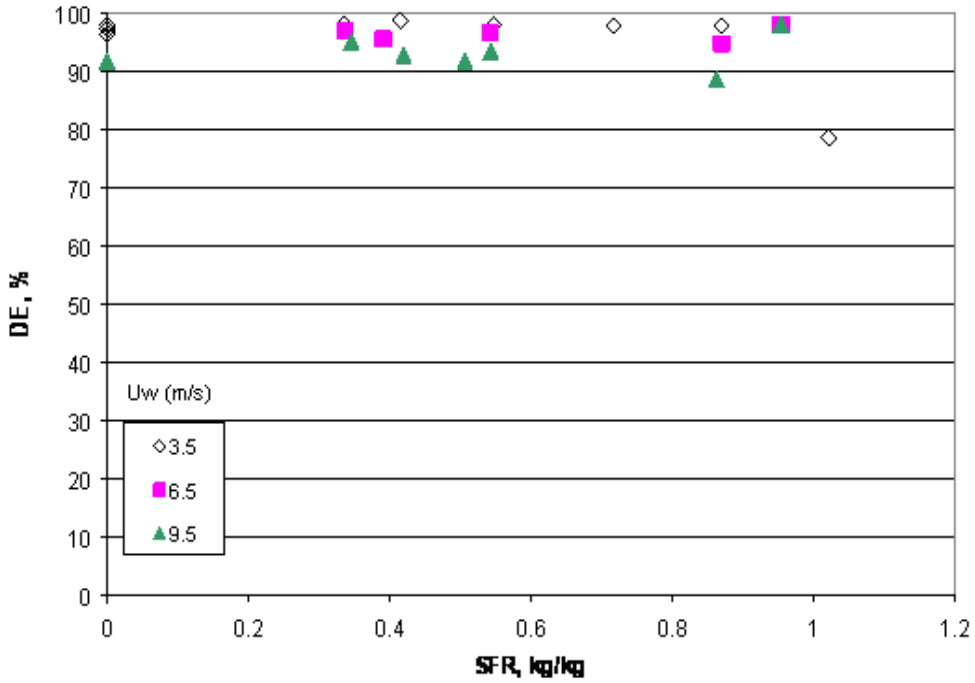

Figure 26 - Destruction efficiency versus steam-to-fuel mass ratio for steam-assisted flaring of natural gas, indexed on nominal wind speed in m/s. The zero SFR points did have steam flowing, but the correction of the flow rate produced a negative value.

The conversion inefficiency and DE for steam-assisted flaring of ethylene are presented in Figures 27 and 28, plotted against SFR and indexed by wind speed. The test with SFR=1.5 appears to be anomalous, giving a very high inefficiency. Ethylene test results for destruction efficiency and combustion inefficiency are degraded compared to the mid-1980's CMA/EPA [McDaniel, 1983] and EPA test results [Pohl et al. 1985, Pohl and Soelberg 1985, 1986]. IFC results do not produce 99.91% destruction efficiency as the CMA/EPA tests did in the flare screening facility. IFC test results have 95-99% destruction efficiency. IFC test results extend only to Steam-to-fuel ratio of 0.8 before severe degradation of destruction efficiency happens. CMA/EPA and EPA test results experienced such degradation when SFR > 3.5.

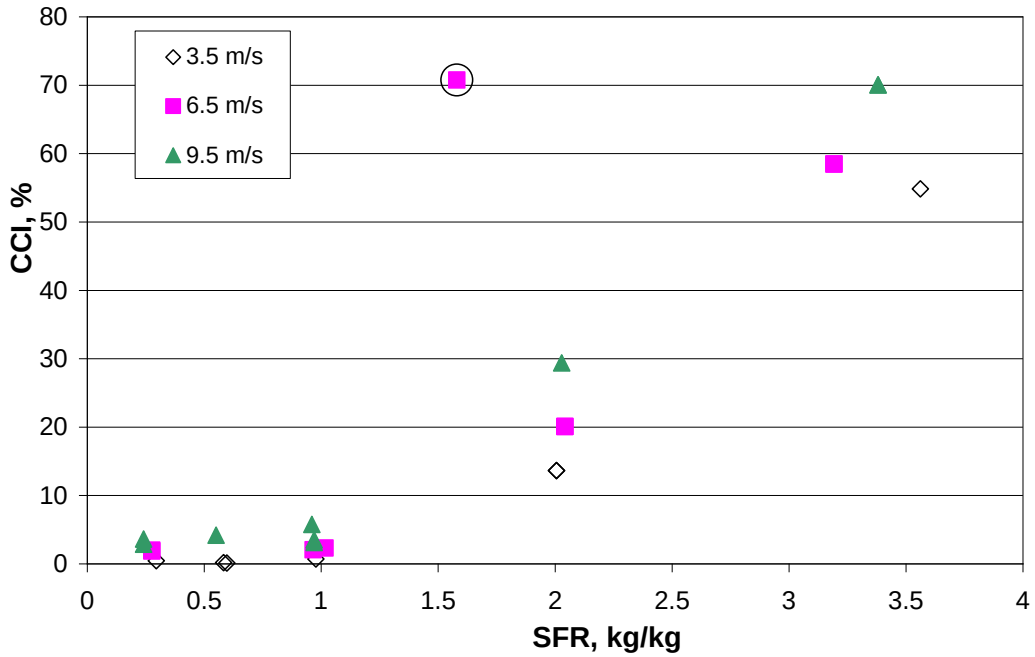

Figure 27 - Conversion inefficiency versus steam-to-fuel mass ratio for steam-assisted flaring of ethylene, indexed on nominal wind speed. The circled point appears to be anomalous.

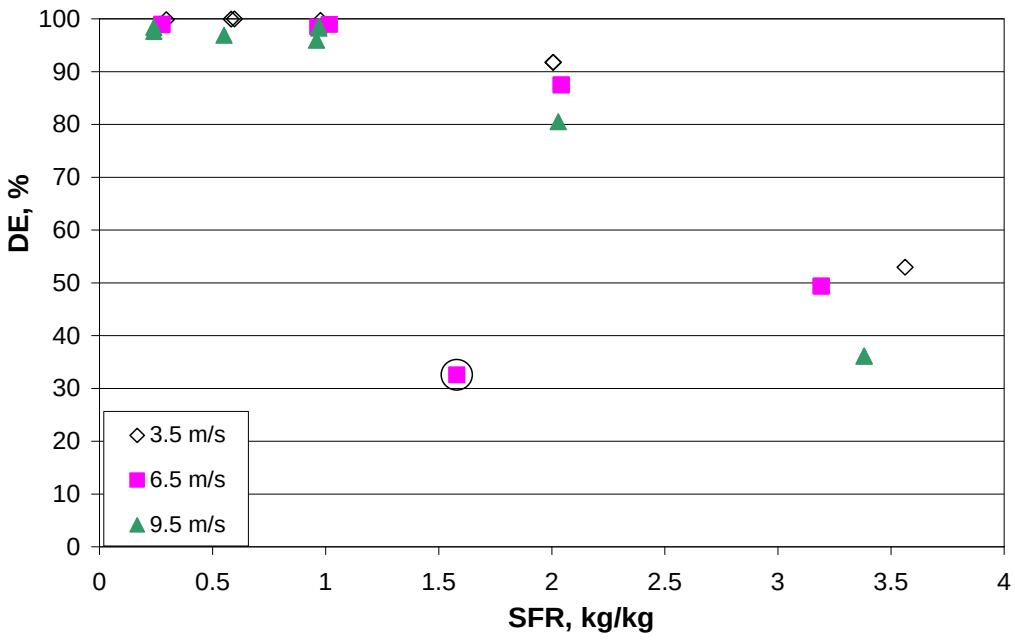

Figure 28 - Destruction efficiency versus steam-to-fuel mass ratio for steam-assisted flaring of ethylene, indexed on nominal wind speed. The circled point appears to be anomalous.

Figures 29 and 30 present the conversion inefficiency and DE for steam-assisted flaring of propylene, plotted against SFR and indexed on wind speed. The test results for SFR = 0.8 appear to be anomalously low. There may be a maximum DE around SFR = 0.7 as found in the EER reports on steam-assisted flaring of propane. Propylene test results for destruction efficiency and combustion inefficiency are degraded compared to the mid-1980's CMA/EPA and EPA test results. IFC results do not produce 99.98% destruction efficiency as the CMA/EPA tests did in the flare screening facility. IFC test results have 88-98% destruction efficiency. IFC test results for Steam-to-fuel ratio above 0.6 show severe degradation of destruction efficiency. CMA/EPA and EPA test results experienced such degradation when SFR > 3.5. We analyse these data further in the next section.

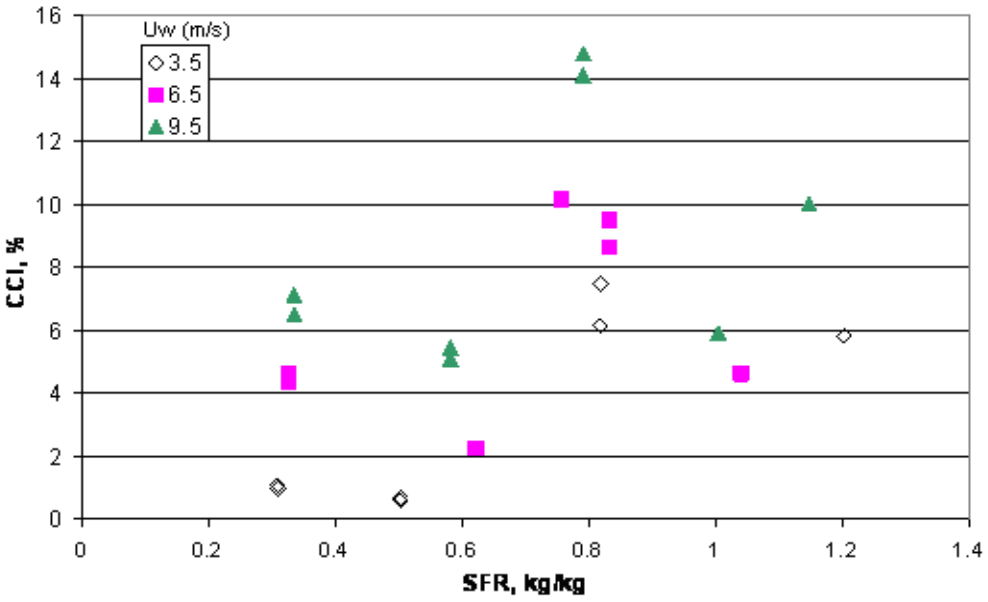

Figure 29 - Conversion inefficiency versus steam-to-fuel mass ratio for steam-assisted flaring of propylene, indexed on wind speed in m/s.

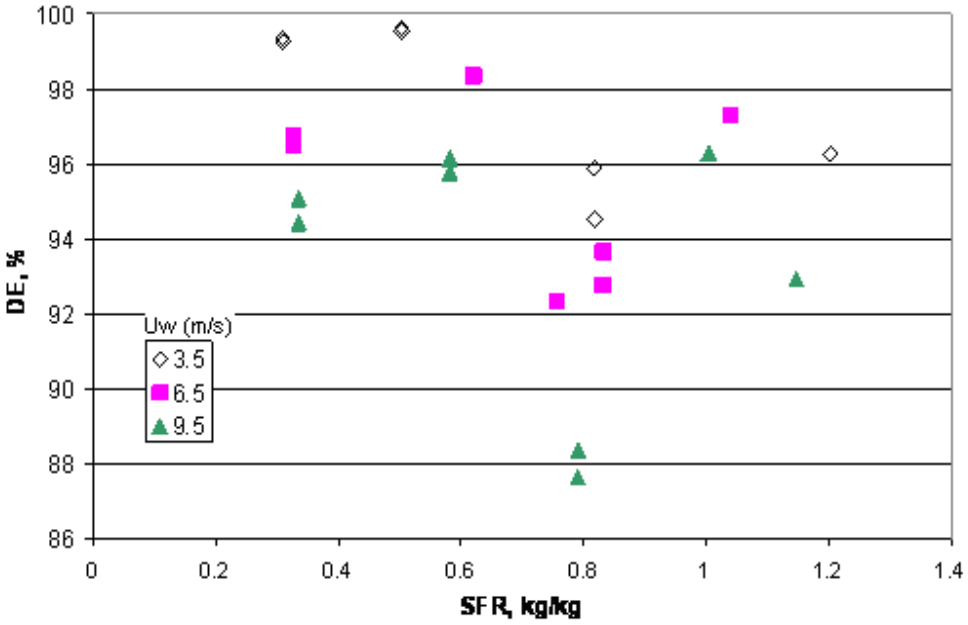

Figure 30 - Destruction efficiency versus steam-to-fuel mass ratio for steam-assisted flaring of propylene, indexed on wind speed.

4.4 Discussion

The first level of analysis is to use the Power Factor to correlate the performance measures. Figures 31 and 32 show the conversion inefficiency and DE for the natural gas tests with SFR < 1 plotted against the Power Factor. These show that a Power Factor less than 0.013 is needed to get DE better than 98%, when flaring natural gas.

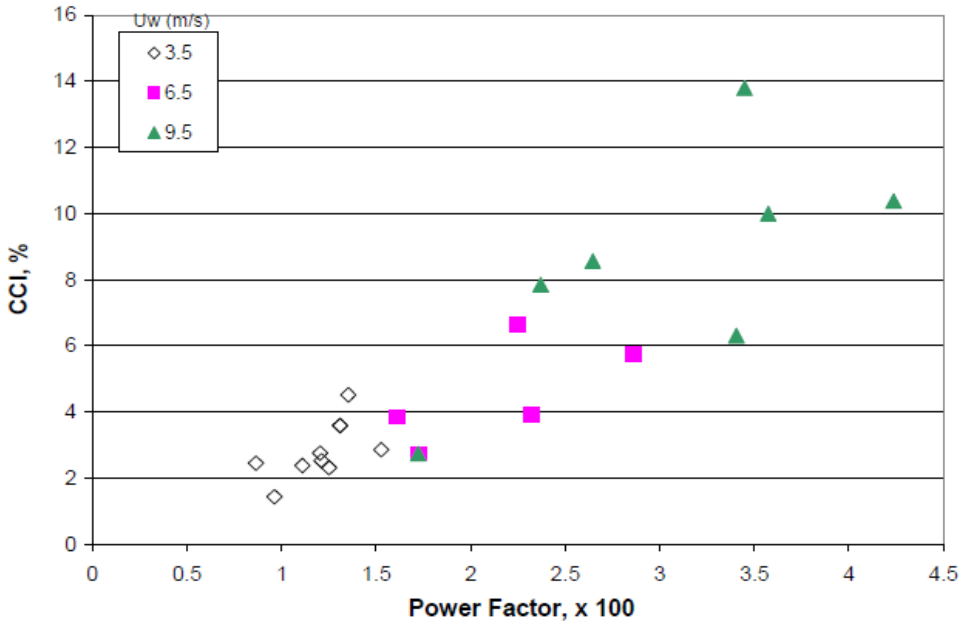

Figure 31 - Conversion inefficiency for steam-assisted flaring of natural gas versus Power Factor, for SFR < 1.

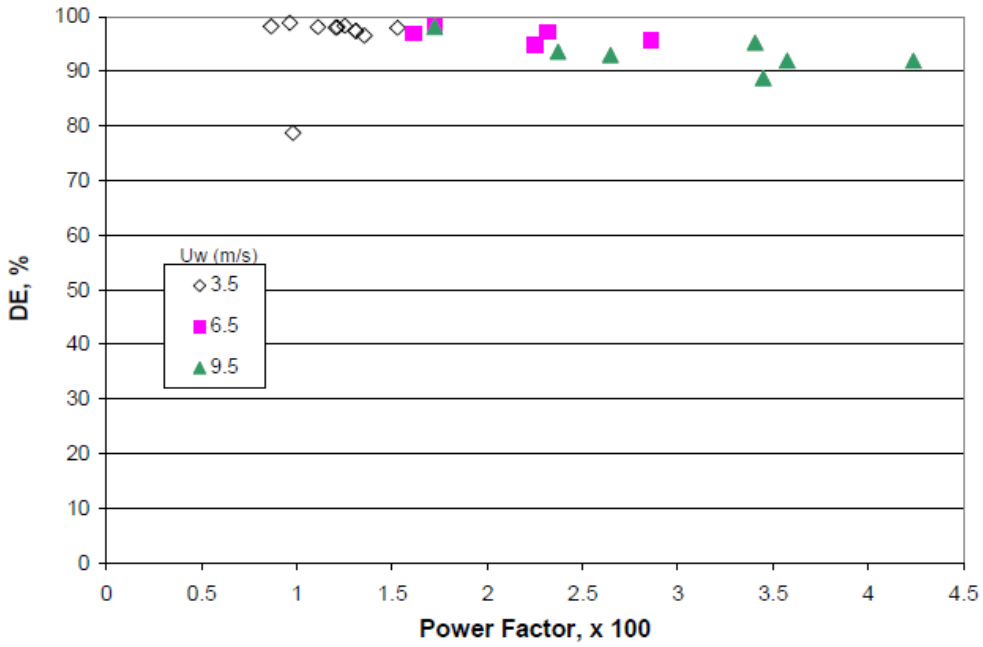

Figure 32 - Destruction efficiency versus Power Factor for steam-assisted flaring of natural gas, for SFR < 1.

Figures 33 and 34 show the conversion inefficiency and DE for ethylene plotted against Power Factor, for all values of SFR. There are clearly three separate divisions between the data, corresponding to the three different values of SFR. One can extrapolate the data separation to the point of zero Power Factor, corresponding to no wind. The middle DE data, with SFR = 2, extrapolates to better than 98% DE with no wind, as may be expected from earlier flaring studies. This shows the sensitivity of the case of low fuel flow to the cross-wind. For SFR values tested (<1, =2. =3.5), all test results show lower combustion and destruction efficiencies with wind speeds greater than zero than the 1980's EPA and CMA test results.

Figures 35 and 36 present only the results with SFR < 1. The Power Factor correlates the results and the figure shows that the DE > 98% is obtained when the Power Factor is less than 0.03. However, these figures show that the wind can have a very strong effect on the performance of steam-assisted flares.

In Figure 37 we have included the DE results for unassisted flaring of ethylene. There is a clear decrease in destruction efficiency as the SFR is increased. The dependence on the Power Factor, which combines the effects of wind speed and flare gas rate, is clear for the different steam-assist rates.

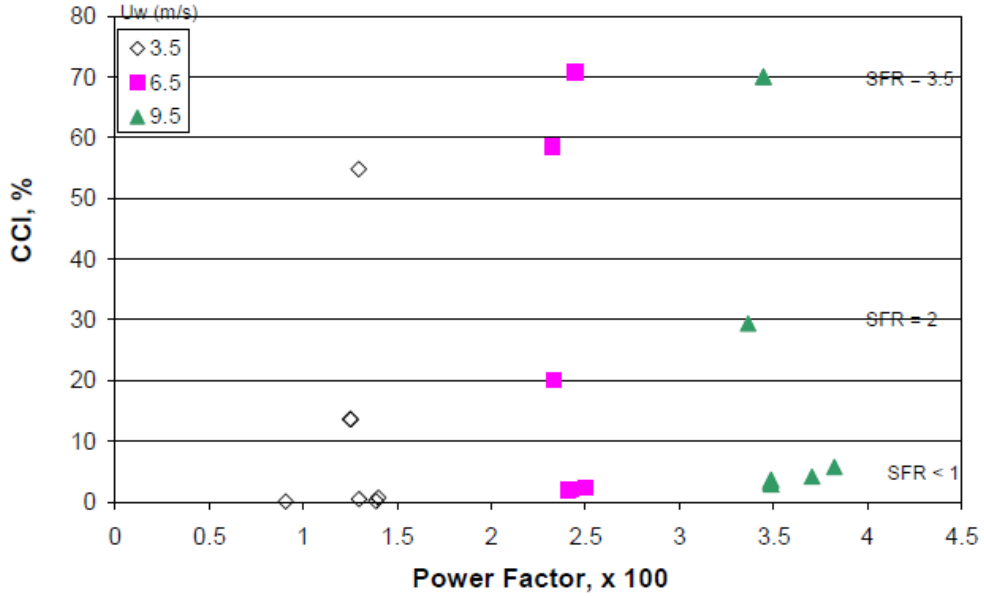

Figure 33 - Conversion inefficiency versus Power Factor for steam-assisted flaring of ethylene, indexed on wind speed. All steam levels included.

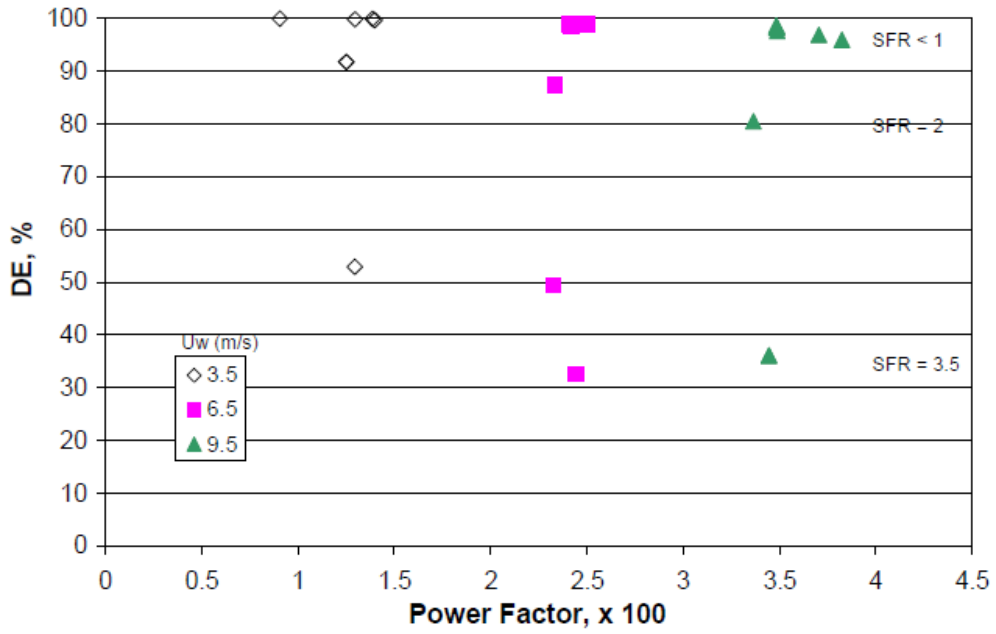

Figure 34 – Destruction efficiency versus Power Factor for steam-assisted flaring of ethylene, indexed on wind speed. All steam levels included.

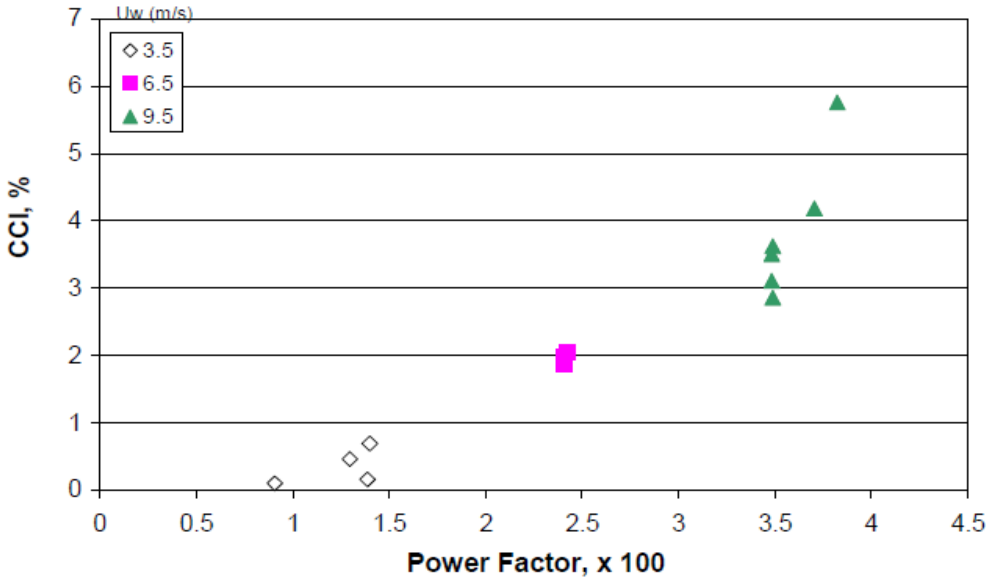

Figure 35 - Conversion inefficiency versus Power Factor for steam-assisted flaring of ethylene, indexed on wind speed, SFR < 1.

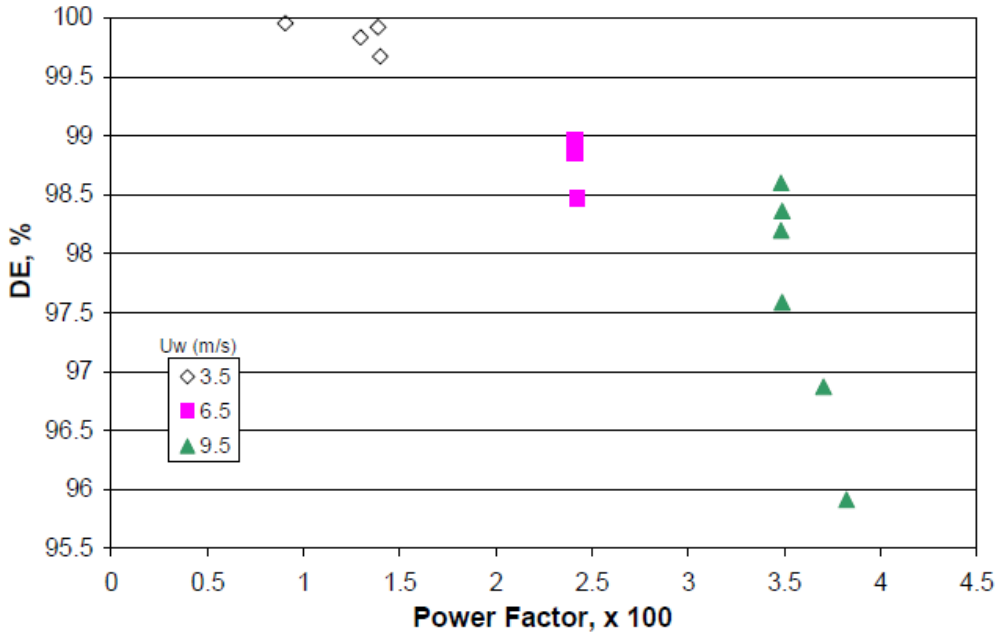

Figure 36 - Destruction efficiency versus Power Factor for steam-assisted flaring of ethylene, indexed on wind speed, SFR < 1.

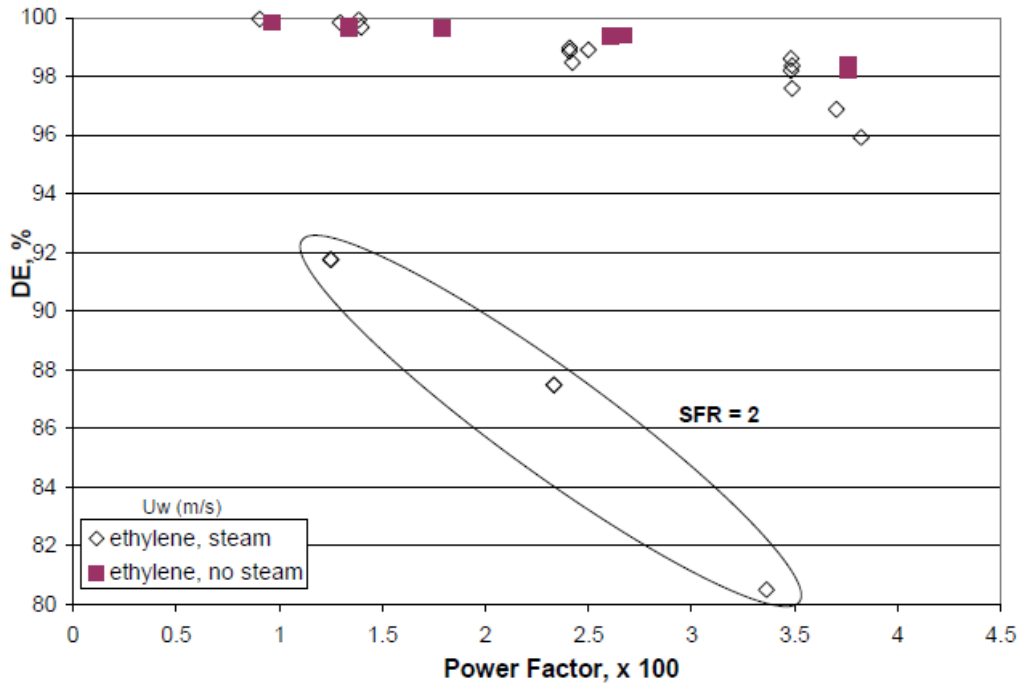

Figure 37 - Destruction efficiency versus Power Factor for unassisted and steam-assisted flaring of ethylene, with Steam-to-Fuel Ratio up to 2.

The conversion inefficiency and DE results for propylene are plotted against the Power Factor in Figures 38 through 42. These display two separate divisions of the data. However, these propylene test results are unlike the ethylene test results; this separation does not correspond to different SFR values. Close inspection of the run data did not identify any particular problems with those tests, though there is clearly something peculiar about the results. IFC does not have an explanation to reconcile these ethylene and propylene test results for combustion and destruction efficiency. Figures 39 and 40 show that the lower data include points with SFR > 1. The points in the upper data division are from two particular test days, March 19 and March 25, 2008. These are the data for SFR = 0.8 noted above. If we neglect those data, the remaining results show that a Power Factor less than 0.02 is needed to have DE > 98%.

Figure 42 collects the DE results for our steam-assisted and unassisted tests and the steam-assisted DE from the CMA/EPA tests. The anomalous data for SFR = 0.8 are circled. The CMA/EPA data, which were tests with low wind speed, are the extrapolation to low wind speed of our data.

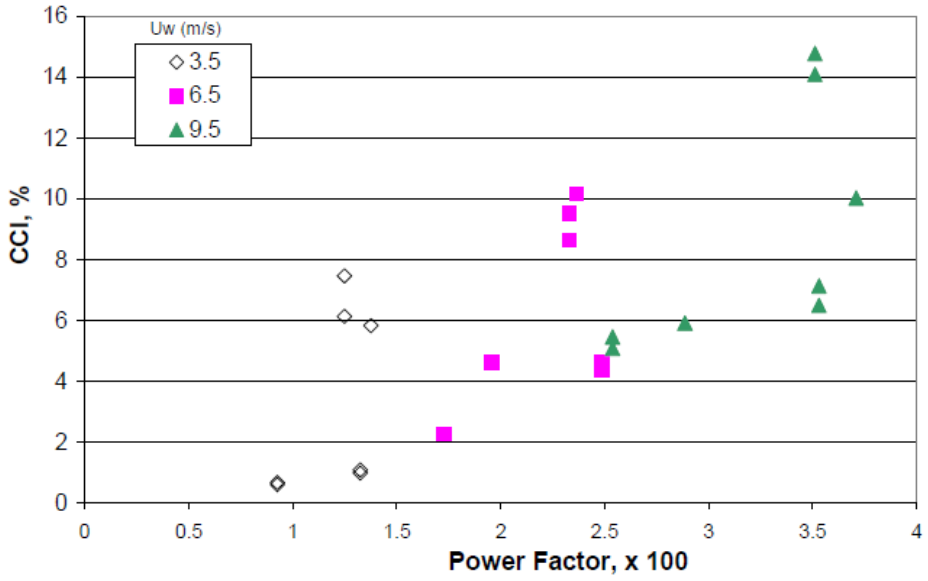

Figure 38 - Conversion inefficiency versus Power Factor for steam-assisted flaring of propylene, indexed on wind speed. All steam levels included.

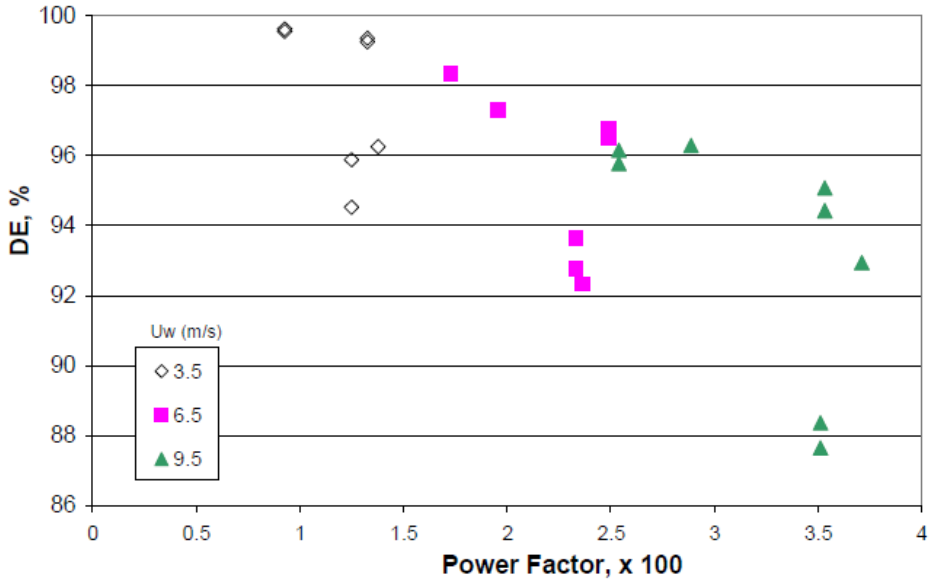

Figure 39 - Destruction efficiency versus Power Factor for steam-assisted flaring of propylene, indexed on wind speed. All steam levels included.

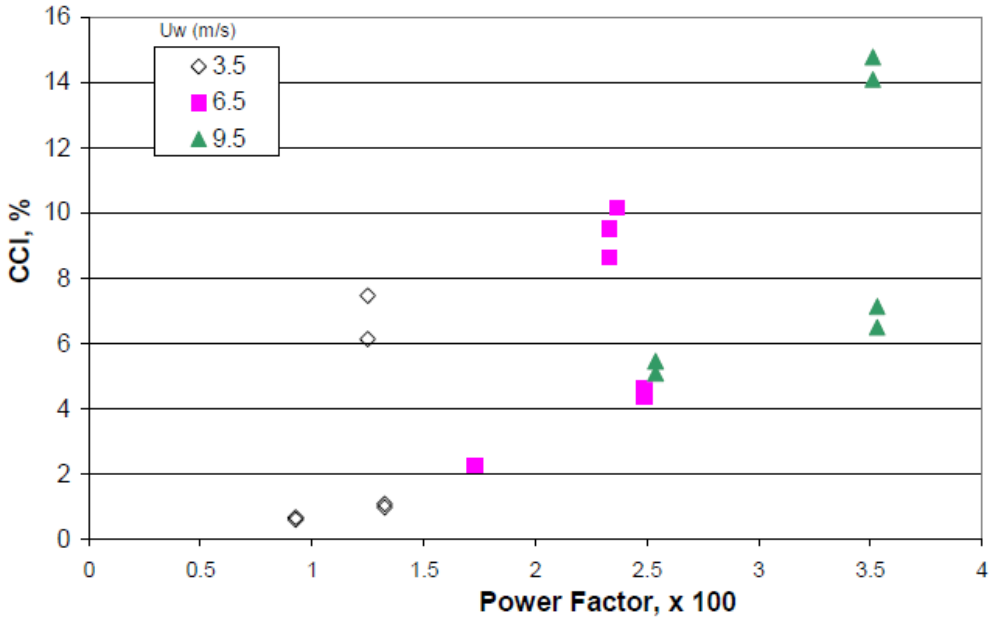

Figure 40 - Conversion inefficiency versus Power Factor for steam-assisted flaring of propylene, indexed on wind speed, SFR < 1.

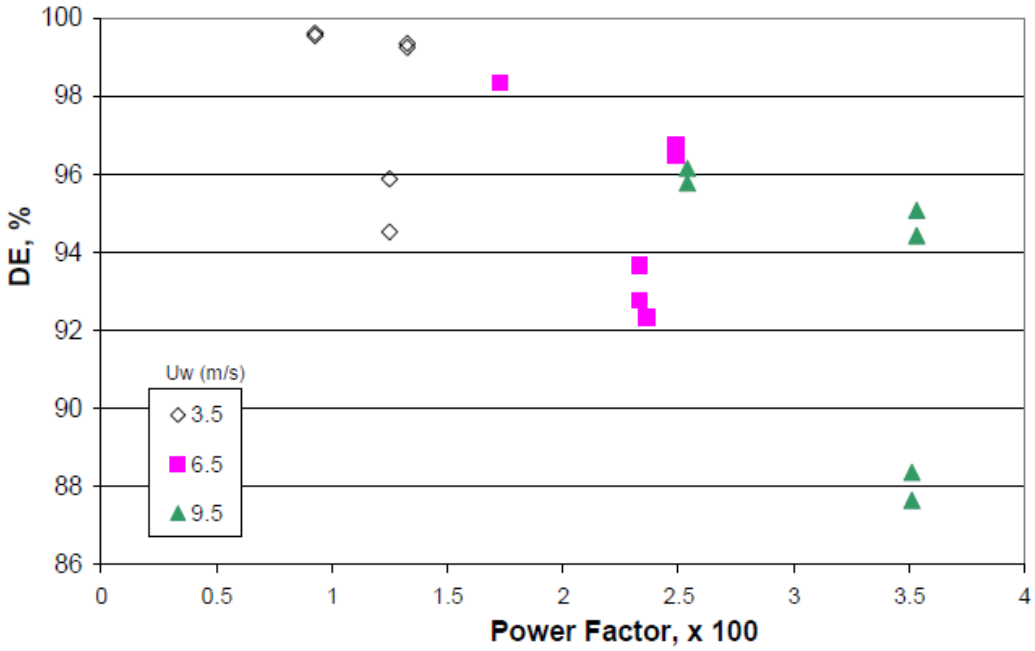

Figure 41 - Destruction efficiency versus Power Factor for steam-assisted flaring of propylene, indexed on wind speed, SFR < 1.

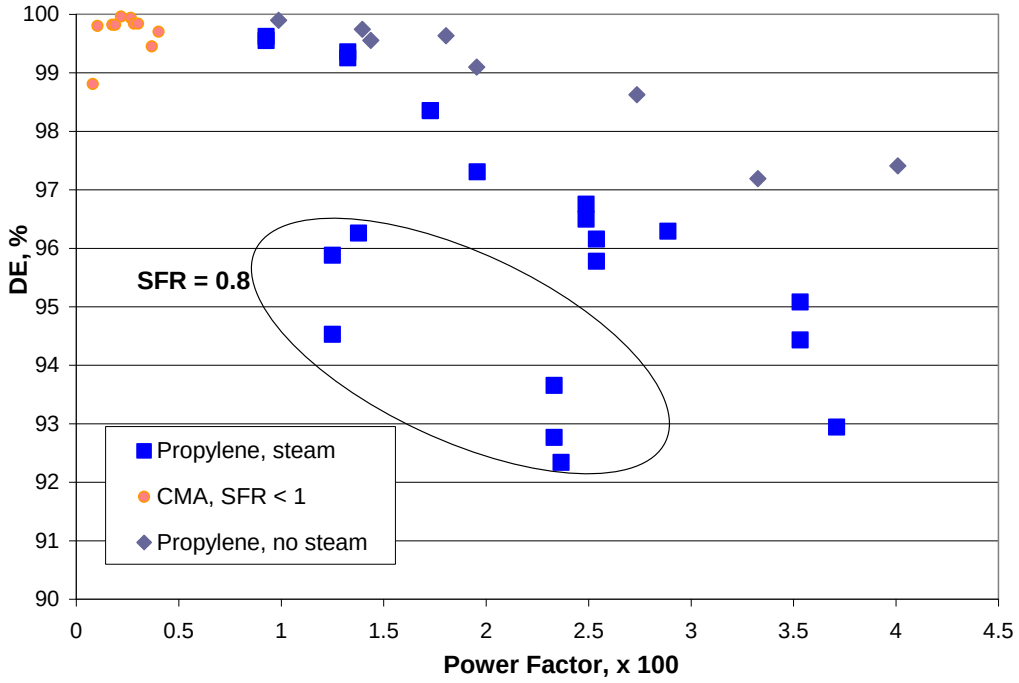

Figure 42 - Destruction efficiency results for flaring propylene, both steam-assisted and unassisted. The CMA/EPA data for steam-assisted flaring with SFR < 1 is included.

The results for the different fuels can be brought together by correlating with the steam volume fraction. Assume that the flare gas and steam are well-mixed. The volume fraction of the steam in the mixture is given by

$$X_{st} = \frac{SFR}{18/M_f + SFR} \tag{4-1}$$

Here M_f is the molecular weight of the flare gas.

The volume fraction of steam (or any inert compound) has an upper limit determined from the flammability limits (I^*). Above this limit, the mixture is no longer flammable. For the gases used in this work the apex of the flammability diagrams was tabulated in the Literature Review (Table 6) [Gogolek et al, 2009a] for nitrogen and carbon dioxide. The apex for steam was taken to be midway between those two values. Using this apex

value for steam I^* together with the stoichiometric air:fuel volume ratio λ, the critical volume fraction of steam, above which the mixture is not flammable, is

$$X^*_{st} = \frac{(1+\lambda)I^*/100}{\lambda I^*/100+1} \tag{4-2}$$

This critical volume fraction is used to normalize the actual volume fraction of steam as calculated by (4-1).

$$RSVF = \frac{X_{st}}{X^*_{st}} \tag{4-3}$$

This gives the Reduced Steam Volume Fraction (RSVF), which is the ratio of the actual steam volume fraction relative to the theoretical maximum. This number is calculable for any combustible gas or mixture of combustible gases for which the stoichiometry and flammability limits can be calculated. The critical volume fraction for steam for the three gases of interest calculated using equation 4-2 is given in Table 6.

Table 6 - Critical volume fraction (equation 4-2) for fuel gases.

	I*	λ	Critical Volume Fraction Steam
Methane	34	9.55	0.845
Ethylene	42.5	14.32	0.919
Propylene	34	21.48	0.921

Figure 43 presents all the steam-assisted flare results for DE plotted against the RSVF. This collapses the data almost onto a single curve. The CMA/EPA data for flaring undiluted propylene is included in this figure. In the low wind situation for those tests, we see that the RSVF is slightly above 1, the 'theoretical' limit, for the test with high SFR (SFR of 5.7 and 6.7). The fact that the flare flame was not extinguished in those cases is due to the difference between the perfect and instant mixing assumed in the

analysis and the imperfect and delayed mixing with actual steam injection. It does show, however, that the simplified analysis does provide useful guidance. The previously noted anomalous data points are circled in the figure. If these points are ignored, then the DE for steam-assisted flaring of ethylene and propylene in the FTF starts to degrade when the RSVF is above 0.8. This is significantly less than the 'theoretical' maximum RSVF of 1, and the difference can be attributed to the effect of wind on the flare gas flame diluted with steam.

In Figure 44, we have plotted the DE data with RSVF < 0.8 against the Power Factor, including the CMA/EPA data for propylene. There is a good correlation for each of the different fuels used. The CMA/EPA data fit as the extrapolation of our propylene data to low Power Factor conditions. It should be possible to further collapse these data onto a single curve through a judicious selection of combustion properties of the fuels.

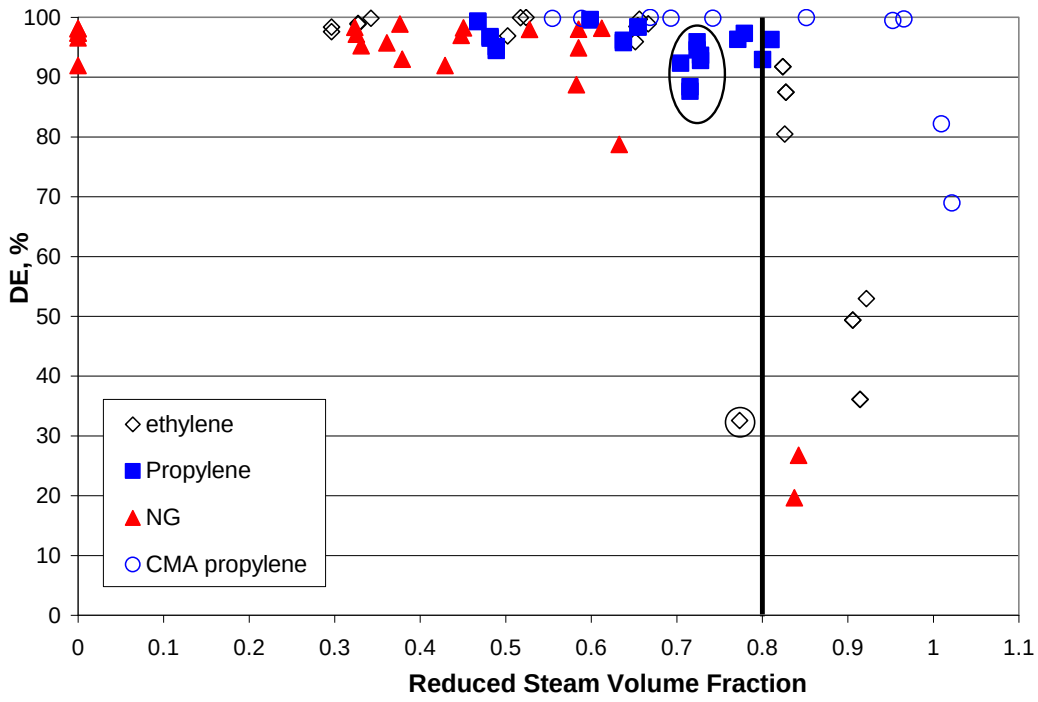

Figure 43 - Destruction efficiency for steam-assisted flaring versus the reduced steam volume fraction. The possibly anomalous data are circled. Recommended maximum is RSVF = 0.8.

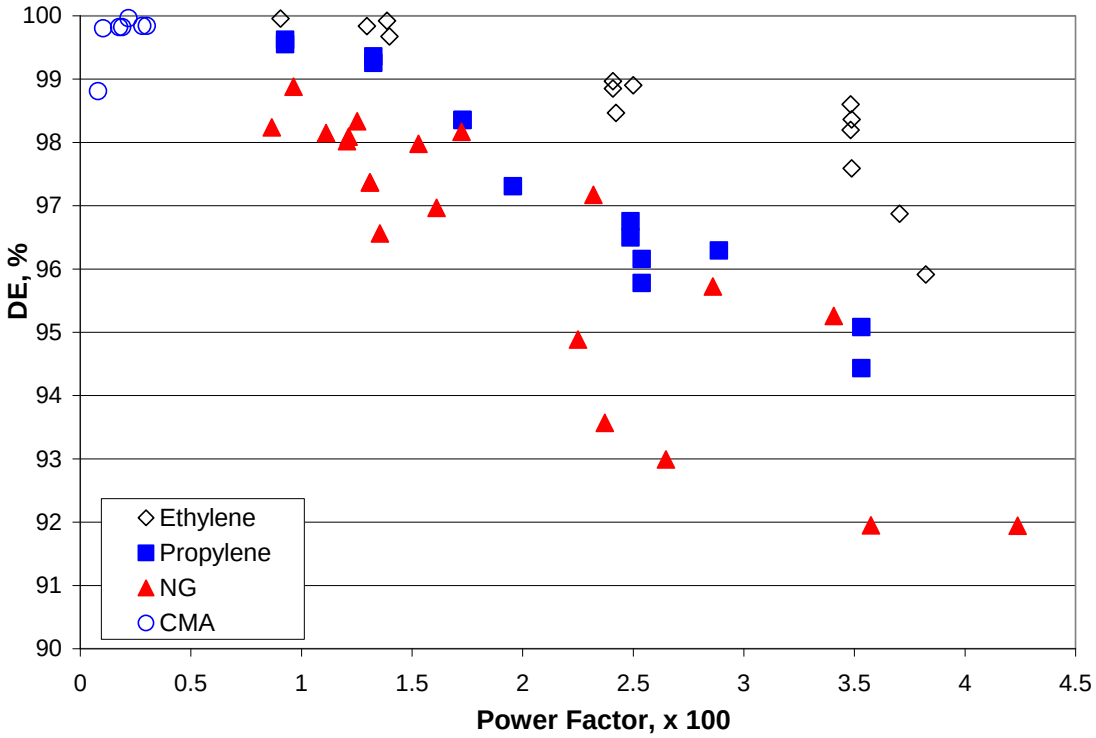

Figure 44 - Destruction efficiency versus Power Factor for steam-assisted trials with RSVF < 0.8.

A first step at a suitable Fuel Factor uses the flammability limits. A simple conceptual model of the mixing of flare gas with air considers the gases as packets that coalesce and divide. A flammable packet has fuel content between the upper and lower flammability limits. A rough measure of the amount of mixing that can be endured by the packets while remaining flammable is the flammability spread divided by the lower flammability limit. This measure is larger for more reactive gases. Our Fuel Factor is the reciprocal of this, so that larger Fuel Factor means a less reactive gas and lower efficiency.

$$\text{Fuel Factor} = \frac{LFL}{UFL - LFL} \tag{4-4}$$

The DE data for RSVF < 0.8 for natural gas, ethylene, propylene and the CMA/EPA study (McDaniel 1983) are plotted against the product of the Fuel Factor and the Power Factor in Figure 45. This fuel factor does not fit the data for natural gas very well. This

may be because there are kinetic limitations for natural gas flaring while the Fuel Factor addresses only mixing. The data for natural gas are removed in Figure 46.

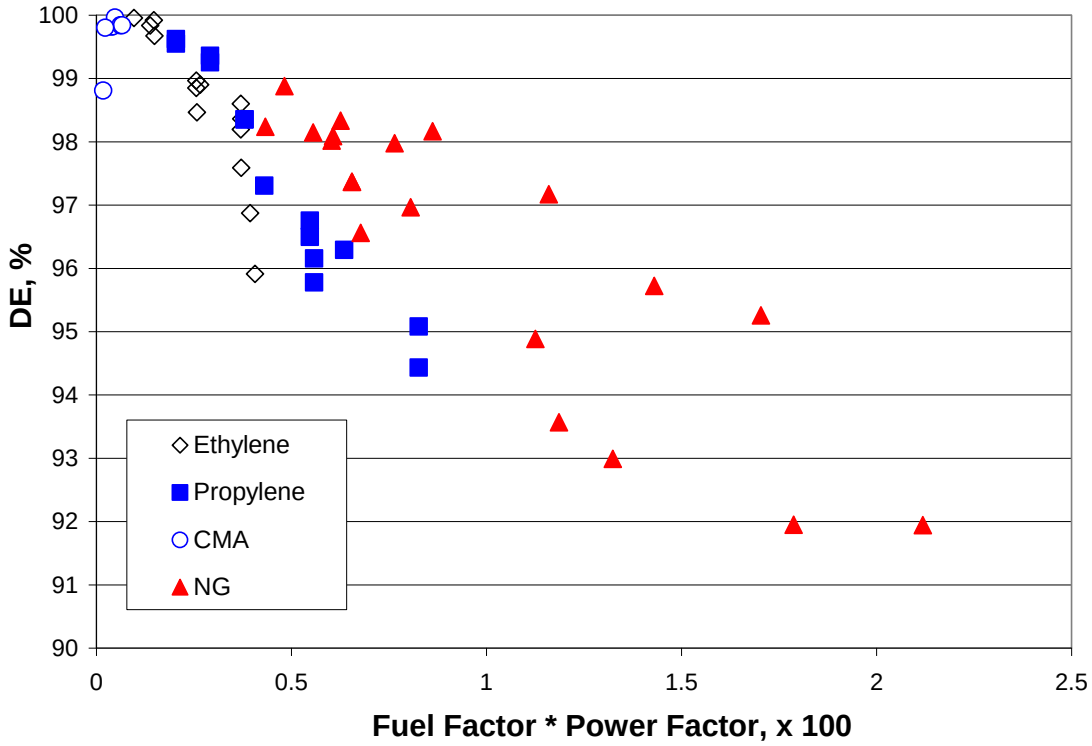

Figure 45 - Destruction Efficiency results for steam-assisted flaring of natural gas, ethylene and propylene, including the CMA/EPA data. All data are restricted to RSVF < 0.8. The Fuel Factor is given in equation 4-4.

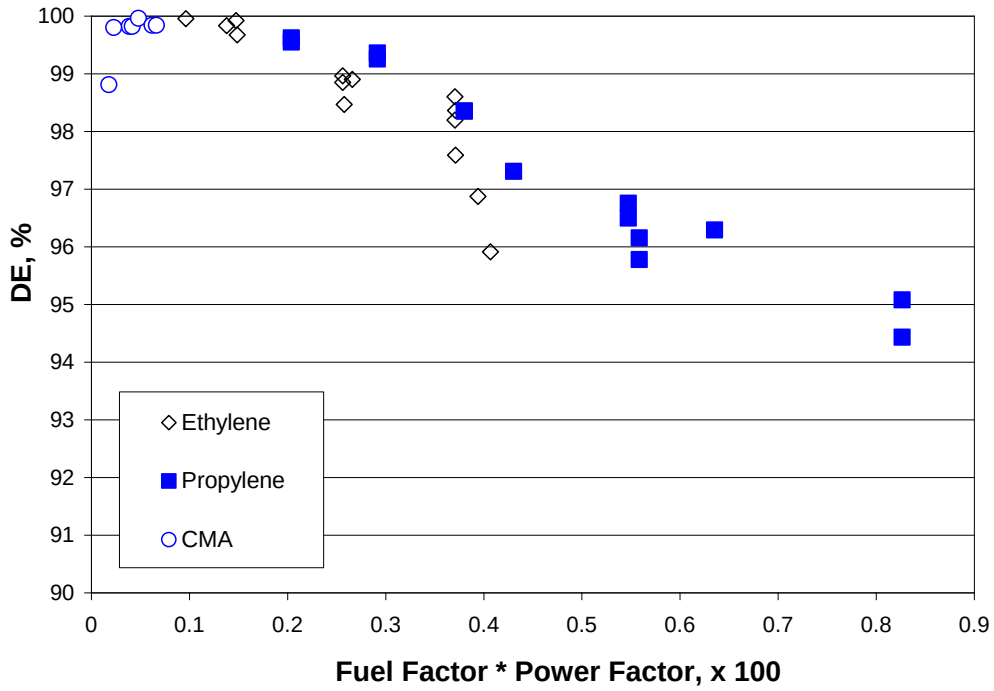

Figure 46 - Destruction Efficiency results for steam-assisted flaring of ethylene and propylene, including the CMA/EPA data. All data are restricted to RSVF < 0.8. The Fuel Factor is given in equation 4-4.

The product of the Fuel Factor and Power Factor is put forward as an attempt at a predictive formula incorporating the effects of flare gas combustion properties, wind speed, and flare gas flow rate. It appears to work for two of the three pure gases tested with steam assist. In section 2.3.2, we presented data showing the effect of nitrogen addition and propane addition on the unassisted flaring of natural gas. Recall that the results posed a difficult question on the how to treat the composition of the flare gas; the nitrogen addition, at 60%-v, had little effect while 15%-v propane produced a halving of the combustion inefficiency. The Fuel Factor for natural gas is 0.33, for 85% natural gas/15% propane is 0.42, and for 40% natural gas/60% nitrogen is 0.5. The Fuel Factor does not explain those results. The explanation may be that natural gas and its mixtures require a treatment of kinetics and the Fuel Factor is only mixing based.

The previous study for the effect of steam-assist rate was the CMA/EPA study (McDaniel, 1983). That study showed little degradation of DE up to SFR of 3.5 while flaring raw propylene. Those tests were conducted with a fixed steam flow rate and

increasing the fuel flow rate and low wind speed. Our tests are primarily with a fixed fuel rate and increasing the steam flow rate and wind speeds at and above the average.

The two studies used different methods to increase the SFR. The CMA tests kept the steam rate fixed and decrease the flare gas rate. This produces a fixed entrainment of air and penetration depth for the steam/air jet into the flare gas volume. Our tests have fixed flare gas rate and increasing steam flow rate. The increasing steam flow rate gives an increase in air entrainment and jet penetration into the fixed flare gas volume. Each method can give the same range of SFR, but different effects on flare efficiency. If that is the case, then the SFR is not a good parameter for predicting flare efficiency.

However, there is another possibility to explain the difference between our results and the CMA/EPA results (McDaniel, 1983). The CMA/EPA study used a 20.3 cm (8") flare and a different design of steam ring. The steam effect may be sensitive to the design of the steam ring (number of nozzles, position of nozzles) for smaller flare diameters. This could imply that the minimum scalable flare for steam-assisted flare studies is larger than the 7.6 cm (3") pipe used here. Also, the commercial 20.3 cm (8") flare tip, with commercial pilot burners, may be more resistant to the effect of wind than our 7.6 cm (3") pilot-scale flare tip.

Finally, possibly the most significant difference is the inclusion of the effect of fairly strong wind in these tests. The wind speeds used in our wind tunnel ranged from 3.5 m/s to 9.5 m/s (11.5 ft/s to 31 ft/s). These winds speeds are greater than the median for most locations, meaning that wind speeds are less than our range more than half the time. The CMA/EPA data are a reasonable extrapolation of our results to low Power Factor conditions (low wind speed or high exit velocity). We have shown that keeping the Power Factor low enough, the DE can be kept above 98%. This threshold Power Factor is somewhere around 0.02 for propylene, around 0.03 for ethylene.

4.5 Conclusion

The steam-assisted flaring of natural gas, ethylene and propylene was carried out. There are significant differences in the findings compared to the benchmark CMA/EPA study (McDaniel, 1983) and the explanation of the differences is not readily available.

The main findings of this chapter are:

• Wind has a strong negative impact on the performance of steam-assisted flares.

• The effect of the wind increases with increased SFR, particularly if SFR > 1.0. For SFR values tested (<1, =2. =3.5), all test results show lower combustion and destruction efficiencies with wind speeds greater than zero than the 1980's EPA and CMA test results.

• The propylene test results are unlike the ethylene test results; this separation does not correspond to different SFR values. Close inspection of the run data did not identify any particular problems with those tests, though there is clearly something peculiar about the results. IFC does not have an explanation to reconcile these ethylene and propylene test results for combustion and destruction efficiency.

• The Reduced Steam Volume Fraction (RSVF) was derived as the ratio of the steam volume fraction to the theoretical maximum steam dilution for continued flammability. This parameter was used to bring together all the steam-assist tests for natural gas, ethylene and propylene only. It is put forward as an alternative for the SFR for controlling the steam-assist rate. The exact "critical volume fraction of steam" is a function of the flare tip design configuration and where/when the steam is mixed with the flare gases

• The data with RSVF < 0.8 correlate well with the Power Factor for each fuel gas. A simple Fuel Factor (equation 4-4) based on a mixing argument was derived that successfully collapses the data for ethylene and propylene onto a single curve for the product of the Fuel Factor and the Power Factor. The natural gas data are not well correlated.

• With RSVF < 0.8, the maximum Power Factor to have DE > 98% is around 0.02 for propylene and around 0.03 for ethylene.

• The CMA data for flaring propylene fits as an extrapolation of our results to low Power Factor conditions (low wind speed or high exit velocity). However, it may be that the pilot-scale flare tip used in our tests was too small and that larger commercial flare tips are more resistant to the effect of wind.

5.0 DILUTION TESTING

5.1 Introduction

An important part of the flaring EPA regulations is the control of the heat content of the flare gas. The minimum energy content for the flare gas is required to be at least 7.5 MJ/m^3 (200 Btu/scf) for unassisted flares and 11.2 MJ/m^3 (300 Btu/scf) for steam- and air-assisted flares (EPA 40CFR 60). These requirements arose from an interpretation of the landmark studies by Pohl and co-workers [Pohl et al, 1986].

Subsequently, questions were raised about the adequacy of the energy content. DuPont had an exemption to the regulation for the cases of unassisted flaring of hydrogen-containing flare gases, based on work by EER [1997] in the jetting regime. Gogolek and Hayden showed that mixtures of natural gas with nitrogen or carbon dioxide with the same energy content have different conversion efficiency when flared in the wake-stabilized mode [Gogolek and Hayden, 2003]. Wake-stabilized operation is common for low momentum solution gas flares and high turndown operation of industrial flares when the wind is blowing.

The aim of the tests reported in this chapter is to investigate the effect of nitrogen and carbon dioxide dilution with the model flare gases (natural gas, ethylene and propylene). Nitrogen can be found in flare gas at refineries and chemical plants. Carbon dioxide is generally not found in the flare gas of refineries, but can be found in the flare gas at chemical plants and at some upstream oil processing facilities.

5.2 Test Plan

The following is the procedure for the tests:

- Set the initial fuel rate at 10 kg/h (22 lb/h).
- Set the initial diluent rate to give a 50%-vol hydrocarbon/inert mixture.
- Increase the diluent rate in 10 kg/h (22 lb/h) increments until flare extinction or until maximum inert gas flow rate is achieved.

- If maximum inert gas flow rate is achieved, then decrease the hydrocarbon flow rate in 1 kg/h (2.2 lb/h) increments until extinction.

The exit velocity from the pipe increases at the same time as the inert gas supply rate increases. The wind speed was kept low, at 2.5 m/s (8 ft/s). As for all the other tests, the flare tip was the 7.6 cm (3") FRR.

5.3 Results and Discussion

The results for conversion inefficiency and destruction efficiency for these tests plotted against the energy content are presented in Figures 47 and 48. There is a clear difference in the performance for nitrogen dilution and carbon dioxide dilution – carbon dioxide shows a higher reduction in performance. Table 7 gives the maximum dilution for flammable operation for these tests, with the exit velocity of the flare gas mixture. Here is also tabulated the estimated energy content threshold for 98% DE. Note that with nitrogen dilution the threshold is around 3.9 MJ/m^3 (105 Btu/scf), almost half of the minimum level promulgated by the U.S. EPA (EPA 40CFR 60). For dilution with carbon dioxide, the threshold is much higher than the recommended level for unassisted flares, even above the level of 11.2 MJ/m^3 (300 Btu/scf) set for assisted flares. Destruction efficiency for N_2 dilution is >99% for NG and ethylene when heat content exceeds 5 MJ/m^3 (134 Btu/scf). Refineries and petrochemical plant flares have N_2 rather than CO_2 in the flare gases. So the flares at these facilities would be operating with DE above 98% with low heat content gases because the diluent is nitrogen.

Table 7 - Maximum dilution for flammable operation, with energy content and exit velocity.

Mixture	LHV	Fraction inert (Volume basis)	Exit Velocity	Estimated 98% DE Threshold
	MJ/m^3	%	m/s	MJ/m^3
NG/N_2	3.8	89.7	17.1	3.8
NG/CO_2	10.9	70.4	6.2	11.8
$Ethylene/N_2$	3.7	93.4	16.7	3.9

Ethylene/CO_2	9.1	83.7	7.2	12.0
Propylene/CO_2	16.2	80.1	3.9	20.0

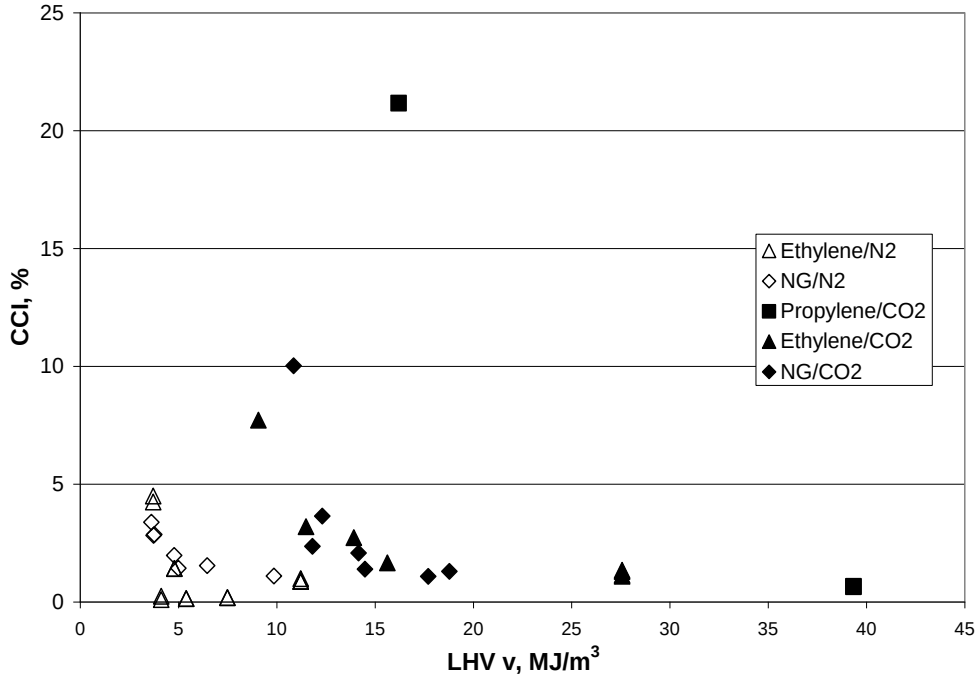

Figure 47 - Conversion inefficiency versus heat content of flare gas.

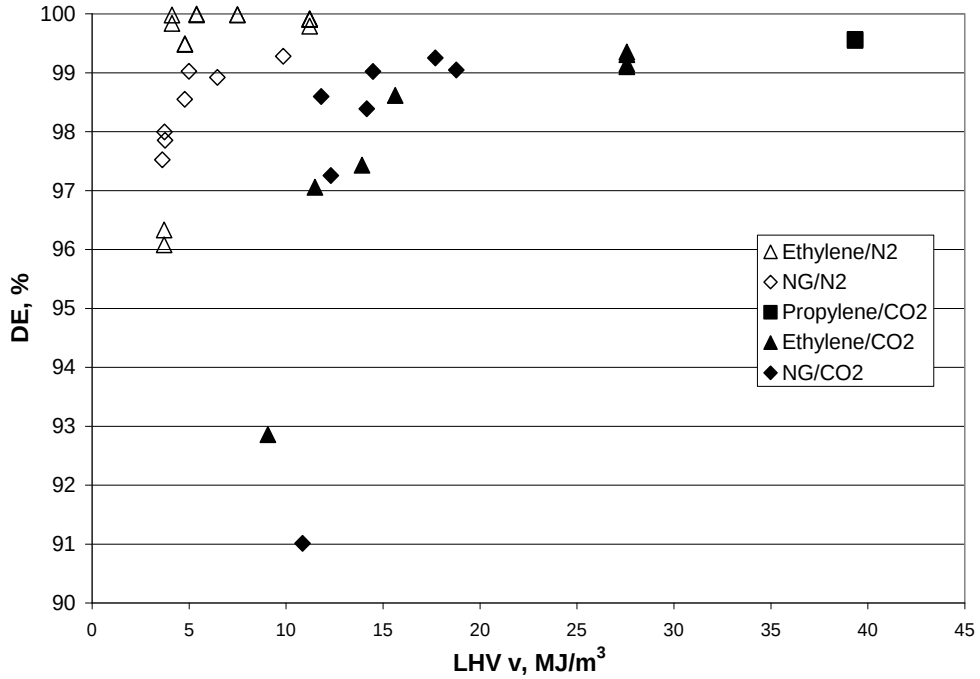

Figure 48 - Destruction efficiency versus heat content, volume basis.

In Figure 49 we have plotted the destruction efficiency against the energy content on a mass basis. Carbon dioxide is denser than nitrogen. This did not turn out to be the case.

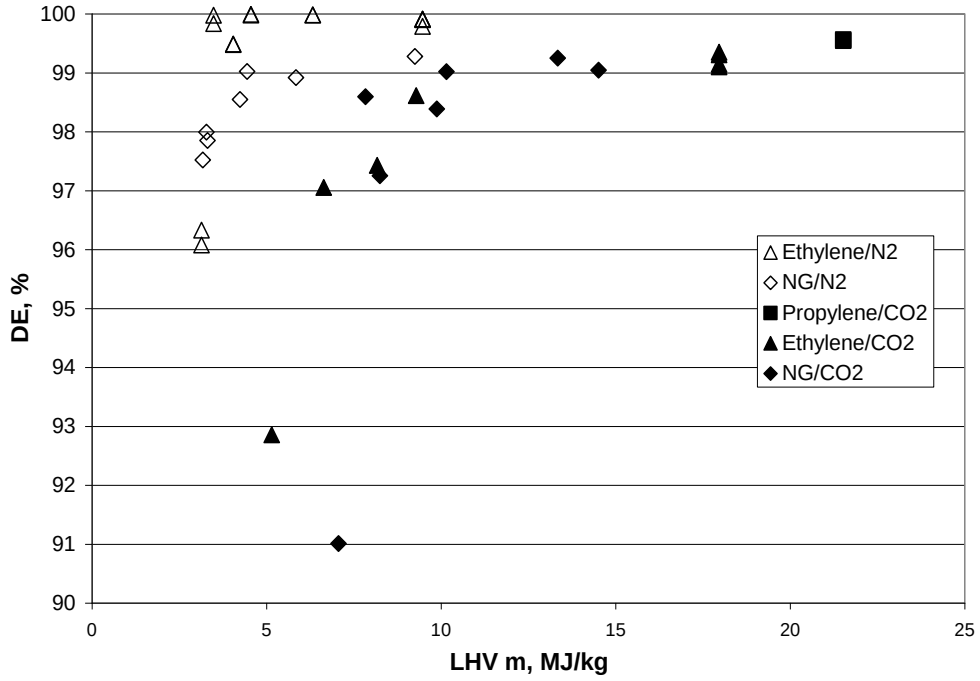

Figure 49 - Destruction efficiency versus heat content, mass basis.

In the Chapter 4 on the steam-assisted flaring, we derived a reduced volume fraction of steam to collapse the efficiency data for the different fuels. The same derivation, with equations 4-1, 4-2, and 4-3, can be applied to these inert gases using I^* values tabulated in the Literature Review (Table 6) [Gogolek et al, 2009a] for nitrogen and carbon dioxide. Table 8 contains the critical volume fractions for the inert gas mixtures for this calculation.

Table 8 - Critical volume fraction for gas mixtures with nitrogen and carbon dioxide.

	I*	λ	Critical volume fraction
N_2 with			
Methane	39	9.55	0.871
Ethylene	45	14.32	0.926
Propylene	40	21.48	0.937
CO_2 with			
Methane	29	9.55	0.812
Ethylene	40	14.32	0.911
Propylene	28	21.48	0.897

The calculated Reduced Volume Fraction Inert, RVFI, is used in Figure 50. The test data for natural gas/CO_2 mixtures shows decrease DE when RVFI is above 0.8. The natural gas/N_2 mixtures have DE > 99% with RVFI above the 'theoretical' maximum of 1. However, the data for ethylene dilution is much closer for both diluting gases. The decrease in DE starts with RVFI around 0.9 for ethylene/CO_2 and around 1 for ethylene /N2. For both fuel gases, the effect of dilution with N_2 is much weaker than dilution with CO_2. For RVFI < 1 the destruction efficiency for dilution with nitrogen is greater than 99%. This has significance for refineries and petrochemical plants where the inert gas is usually nitrogen. Carbon dioxide may be a significant component for biogas flares, production flares, sour gas plants, steam-methane reformers, and gasifiers. Those flares may display lower DE than expected based on heat content.

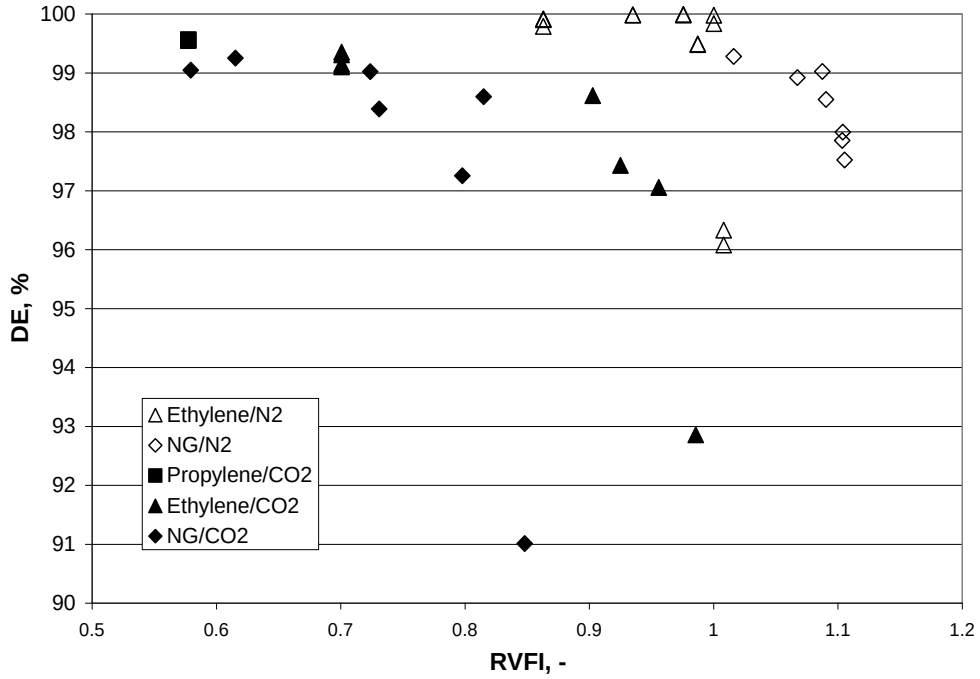

Figure 50 - Destruction efficiency for diluted flare gases versus Reduced Volume Fraction of Inert.

5.4 Conclusion

Tests of dilution of the flare gas with nitrogen or carbon dioxide confirmed the significant difference between the two inert gases. Energy content does not adequately represent the effect of dilution. While nitrogen dilution has very little effect on combustion performance until very close to the extinction limit, carbon dioxide has a much stronger deleterious effect. The estimated energy content to give 98% DE for the mixtures tested here are given in Table 7. Note that the threshold energy content with carbon dioxide dilution is higher than the requirement for assisted flares. The corresponding threshold for nitrogen dilution is much lower, almost half the requirement for unassisted flares.

The RVFI (Reduced Volume Fraction Inert) was introduced to relate the effect of dilution to known combustion properties of the flare gases. The data show that for dilution with nitrogen keeping the RVFI less than 1 (the theoretical maximum) gives DE > 99%. This is important for refineries and chemical plants where nitrogen is the diluting gas. However, for dilution with carbon dioxide the threshold is lower around 0.8 for natural

gas and 0.9 for ethylene, which is similar to the results for the dilution effect observed for steam in Chapter 4.

6.0 TRACE EMISSIONS

6.1 Introduction

In the preceding chapters we have discussed the conversion inefficiency, which is the failure to convert to carbon dioxide, and the destruction efficiency, which is the success in the destruction of the flared hydrocarbon. There remains the discussion of the other species that can be formed in a combustion system and emitted. First among these is carbon monoxide, the primary product of interrupted oxidation of hydrocarbons. In our first chapter with the natural gas baselines and scale-up, we showed that the contribution of methane (fuel) to the inefficiency was in the range from 60% to 80%. This means the carbon monoxide contribution was from 20% to 40%.

Nitrogen oxides, nitric oxide and nitrogen dioxide, are formed in the flame region through the fixing of atmospheric nitrogen at high temperature when there is no fuel-bound nitrogen present. The emissions of these compounds are not related to the conversion of a compound in the flare gas, but need to be related to the flaring process. This can be accomplished through the use of an Emission Factor (EF), which gives the mass emission of the species of interest relative to the energy content of the flare gas. The units for the emission factor are g/MJ or mg/MJ (or lb/Btu). This approach normalizes the emissions to the rate of flaring. Reporting simple stack concentrations biases the results by the dilution of the wind tunnel air flow, which is an artefact of the experimental set-up and has no significance for the flaring process.

The emissions of primary concern to the IFC are the HRVOCs and BTEX. HRVOCs are the highly reactive volatile organic compounds. These are reactive in the atmospheric, particularly urban air-sheds, and contribute to the formation of ozone. BTEX are the simple aromatic compounds benzene, toluene, ethylbenzene and xylenes. These are of concern as toxic or carcinogenic compounds. We had two analysis systems for these groups of organic compounds, described in an earlier report (Caravaggio and Caverly, 2008). These systems have a very low detection limit, 20 ppbv for the HRVOCs and 10 ppbv for the BTEX. The detection limit establishes lower limits for the emissions of these trace compounds.

The emission factor for a species Σ is given by

$$EF_{\Sigma} = \frac{x_{\Sigma}\left(M_{\Sigma} / M_{a}\right)\dot{m}_{air}}{LHV_{m}\dot{m}_{f}} \tag{6-1}$$

The emission factor depends on the air flow rate and the fuel flow rate, as well as the detection limit of the analysis system, and the ratio of the molecular mass of the species of interest to that of air. For example, the emission factor at the detection limit of ethylene, 20 ppbv, ranges from 0.2 mg/MJ to 2 mg/MJ (0.0005 lb/Btu to 0.005 lb/Btu).

6.2 Carbon Monoxide

Carbon monoxide is a product of incomplete or interrupted combustion. It is the other major product in the flare exhaust gas, after carbon dioxide (complete combustion) and the fuel hydrocarbon (no combustion). The emission of carbon monoxide is best calculated as a conversion of the fuel-carbon. Figure 51 gives the conversion of fuel-carbon to carbon monoxide relative to the conversion inefficiency. Note that the conversion to carbon monoxide reaches a maximum of 10% at inefficiency of 30%, with the steam-assisted trials. This indicates that the inefficiency with over-steaming is primarily due to fuel-stripping.

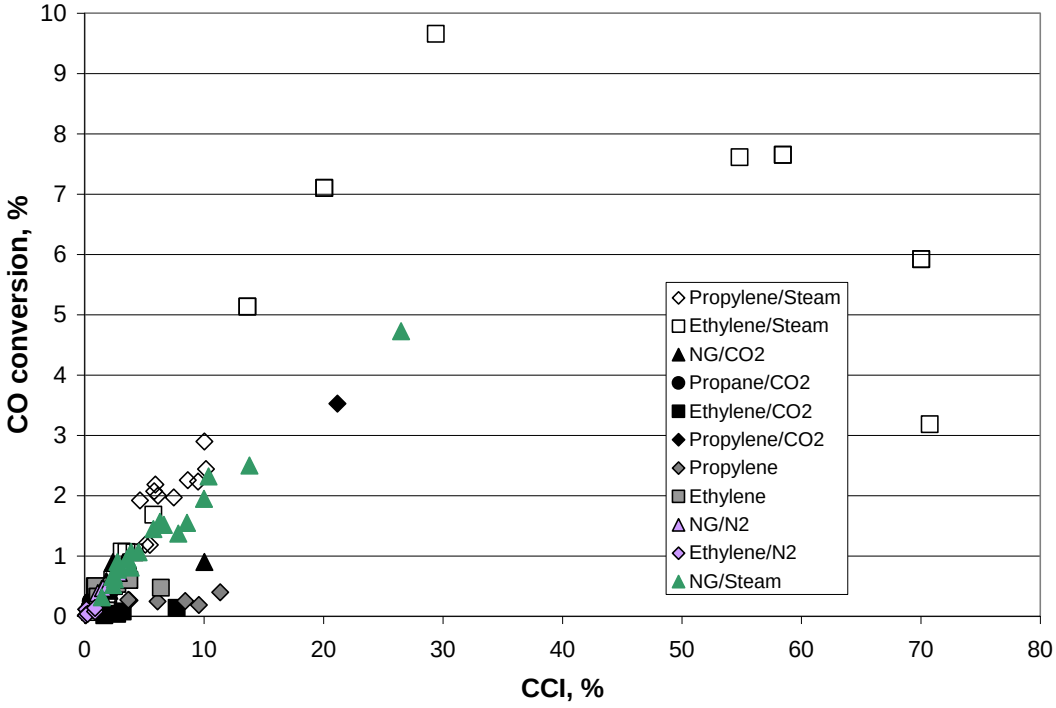

Figure 51- Conversion of fuel-carbon to carbon monoxide for all tests.

The conversion to carbon monoxide as a function of the conversion inefficiency for the natural gas baseline tests (Chapter 2) was shown to be in the range from 20% to 40%[5]. A rough correlation with the power factor was obtained for those tests. Figure 52 shows the correlation of conversion to carbon monoxide with conversion inefficiency. The two simple fuel tests with ethylene and propylene had significant generation of particulate carbon which is a very different chemical mechanism, so the carbon monoxide emissions are affected. The ethylene/carbon dioxide tests display significantly less carbon monoxide generation. No explanation is readily available for that difference.

[5] The inefficiency of those tests is composed of fuel (methane) and carbon monoxide. The fraction of methane is plotted in Fig. 11, and ranges from 60% to 80%. Therefore, the fraction of carbon monoxide is from 20% to 40%.

The remaining runs, including steam-assist and dilution with nitrogen and carbon dioxide, show that carbon monoxide contributes around 25% of the inefficiency. This is in full agreement with the baseline results for natural gas for 7.6 cm, 10.2cm and 15.2 cm (3", 4" and 6") pipe sizes.

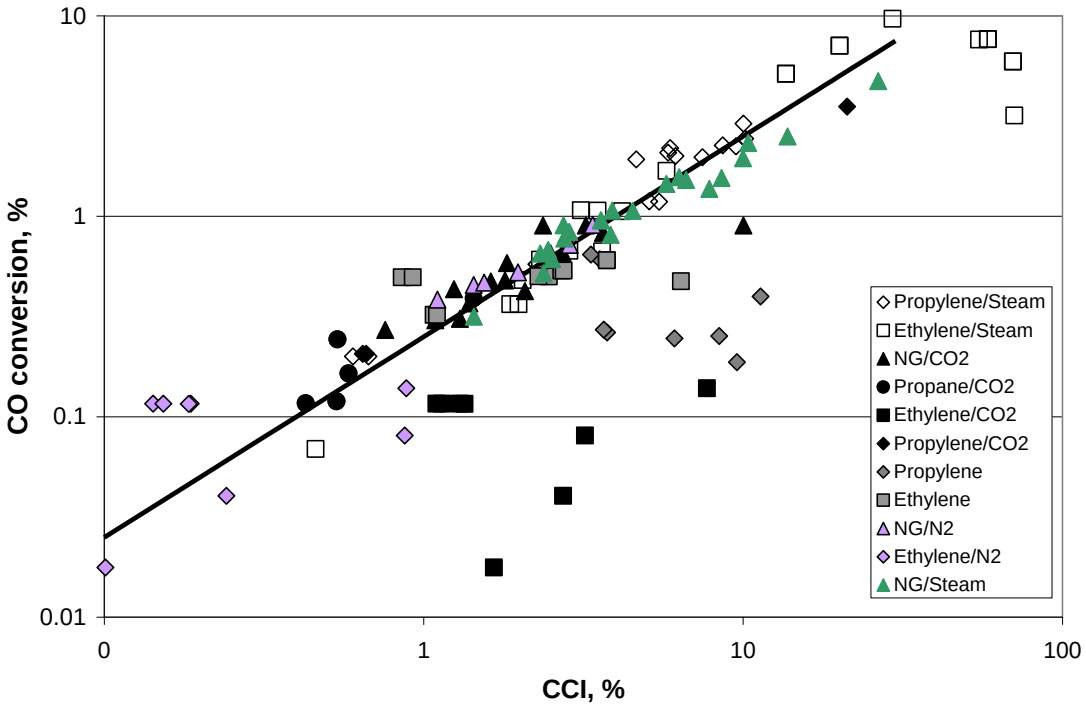

Figure 52 - Log-log plot of the conversion to CO against the conversion inefficiency. The solid line indicates 25% of the inefficiency is due to carbon monoxide.

6.3 Nitrogen Oxides

Unless there are nitrogenous species in the flare gas, the dominant mechanism for generation of nitrogen oxides (NO_x) is thermal fixing of atmospheric nitrogen through the Zeldovich mechanism. Thus NO_x emissions are related to the peak flame temperature, which is a function of several variables. However, the tests did not directly modify those variables nor was flame temperature measured.

The emission factor for NO_x is plotted against conversion inefficiency in Figure 53. The general trend is for the emission factor to decrease with increased inefficiency. This was also found by Pohl and Soelberg (1986). The range of emission factor is from 0.004

g/MJ to 0.04 g/MJ (0.0093 lb/MMBtu and 0.093 lb/MMBtu) which agrees with the range reported by Pohl and Soelberg (1986) for hydrocarbon flare gases.

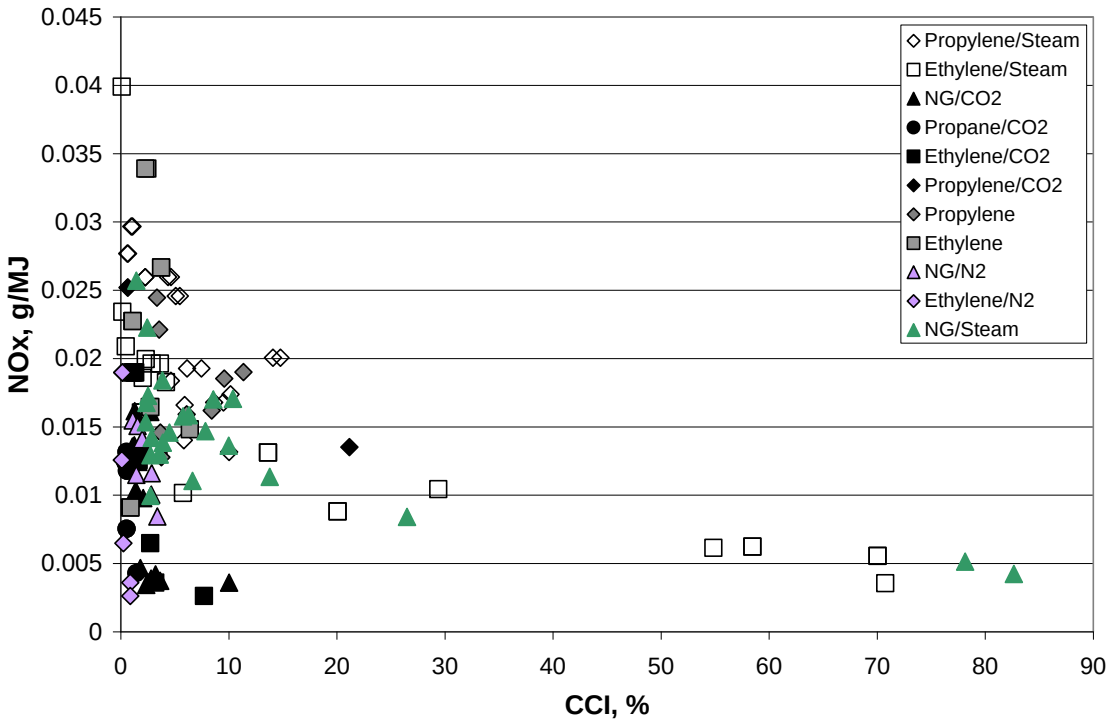

Figure 53 - Emission factor for NO_x plotted against conversion inefficiency for all tests.

The emission factors for NO_x for steam-assisted trials only are presented in Figure 54. The decrease in emission factor with increase SFR is as expected, since the increased steam flow rate will lower the flame temperature. However, the spread of the emission factors for the trials without steam-assist is as wide as the spread for the steam-assisted trials, so it hard to justify detailed analysis of this figure.

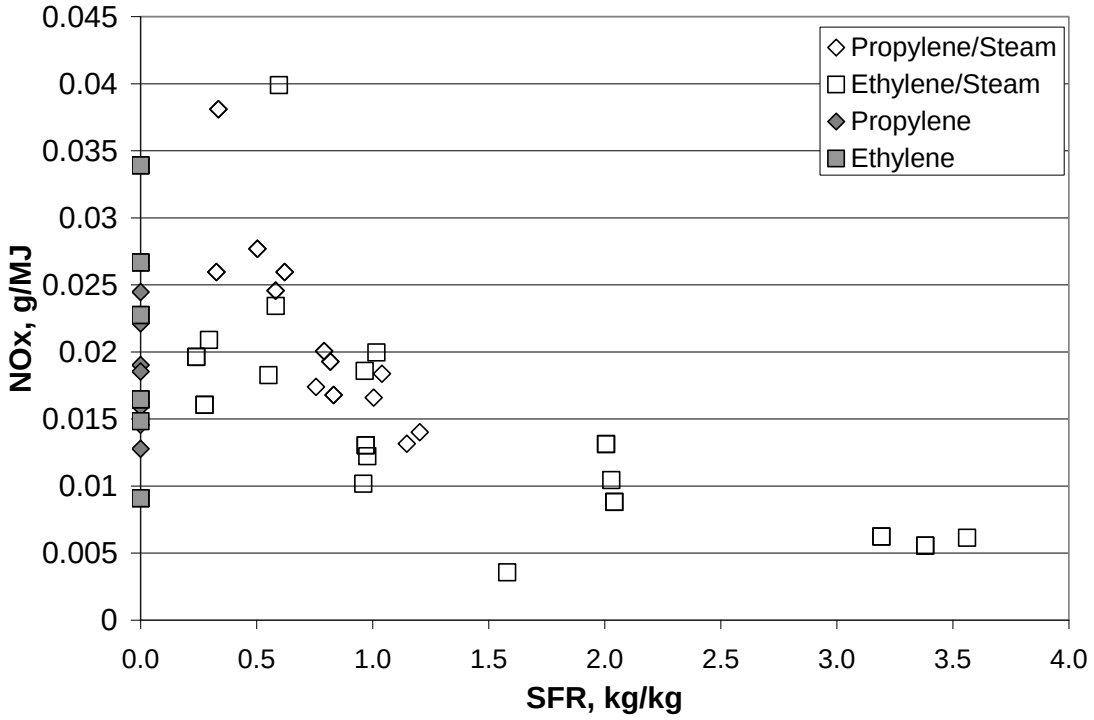

Figure 54 - Emission factor for NO_x for steam-assisted trials.

6.4 Hydrocarbons

The two groups of hydrocarbon emissions are the HRVOCs and the BTEX. There were no detectable emissions of BTEX in any of the tests. The detection limit for the BTEX analysis system is 10 ppbv. This contradicts Pohl and Soelberg (1986) who found approximately 40 ppb of benzene, toluene and xylenes. The HRVOCs measured were ethylene, propylene, the butenes, and 1,3-butadiene. The flare gases tested included ethylene and propylene, simply, steam-assisted, or diluted with nitrogen or carbon dioxide. The fuel stripping mechanism will be responsible for the emission of those compounds when they are present in the flare gas and these results are presented as the destruction efficiency results in previous chapters. This section deals with the HRVOC emissions.

Ethylene was measured in tests with natural gas and propylene. 1-butene was measured in the steam-assisted flaring of propylene. None of the other HRVOCs were detected in these tests.

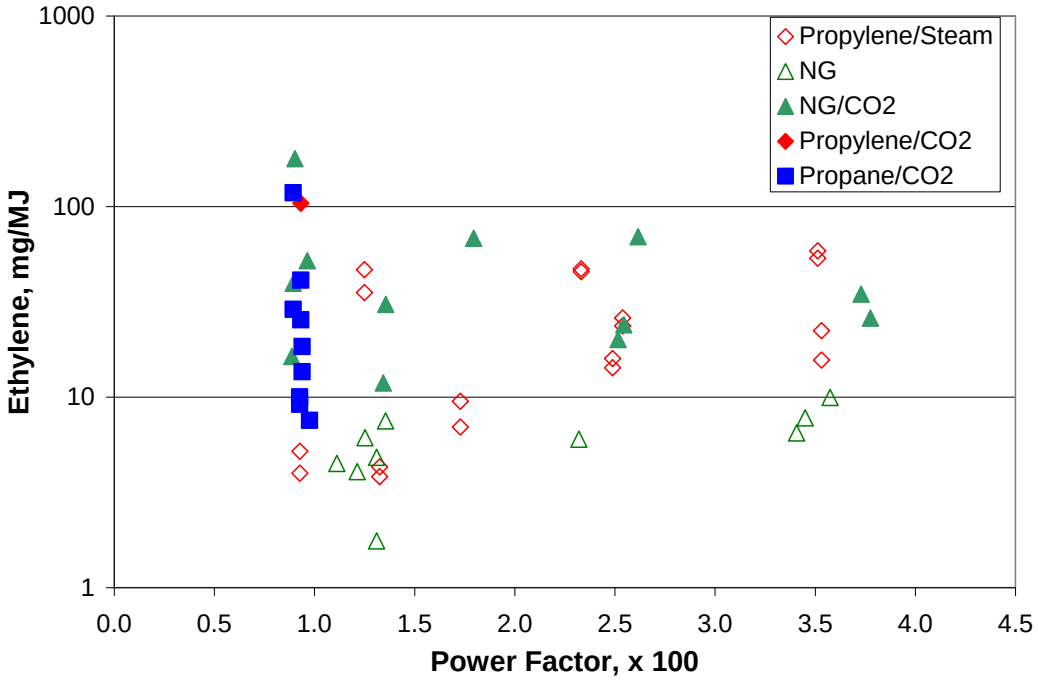

Figure 55 - Emission factors for ethylene plotted against Power Factor for tests with natural gas and propylene.

The emission factors for ethylene are in the range from 5 mg/MJ to 100 mg/MJ (0.012 lb/MMBtu to 0.23 lb/MMBtu) for natural gas and propylene. There is little discernable difference in the emission factors for the two gases being flared. Figure 55 plots the emission factors against the Power Factor, with no evident correlation.

Figure 56 plots the emission factors for ethylene against the steam-to-fuel mass ratio (SFR) for the steam-assisted flaring of natural gas and propylene. There may be an increase of emission factor with SFR.

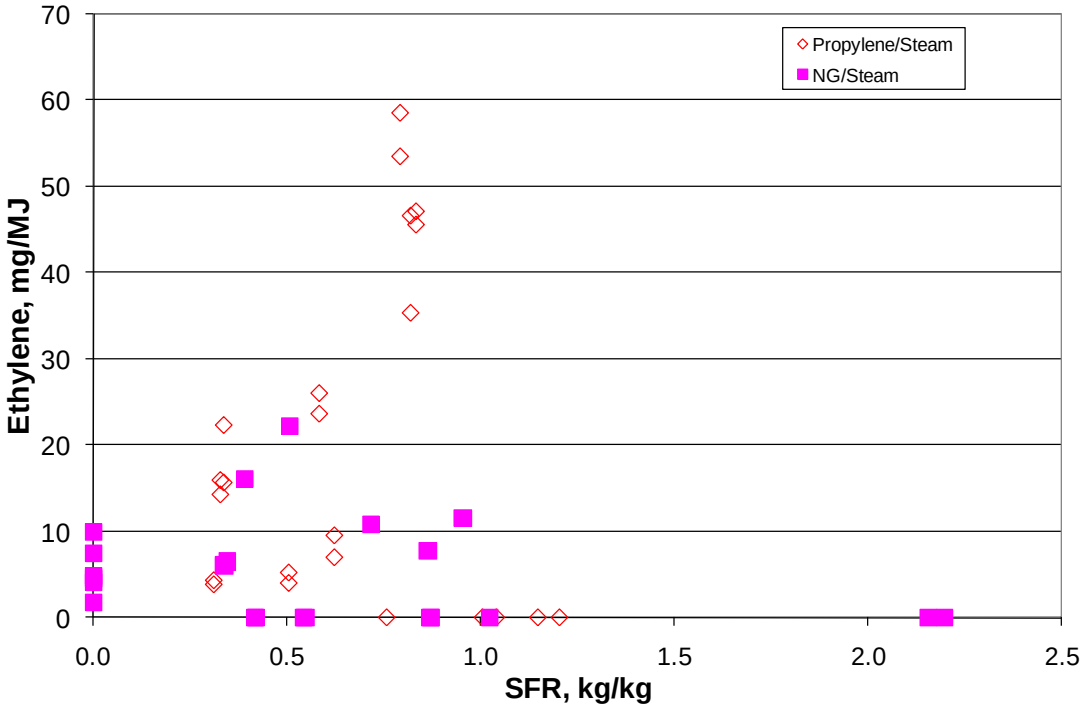

Figure 56 - Emission factors for ethylene plotted against SFR for steam-assisted flaring of natural gas and propylene.

Figure 57 presents the emission factor for ethylene from flaring tests for natural gas, propane, and propylene diluted with carbon dioxide. These are in the same range as for the steam-assisted tests. There does appear to be a correlation with energy content of the flare gas mixture, namely that the emission factor for ethylene decreases with increasing energy content of the flare gas.

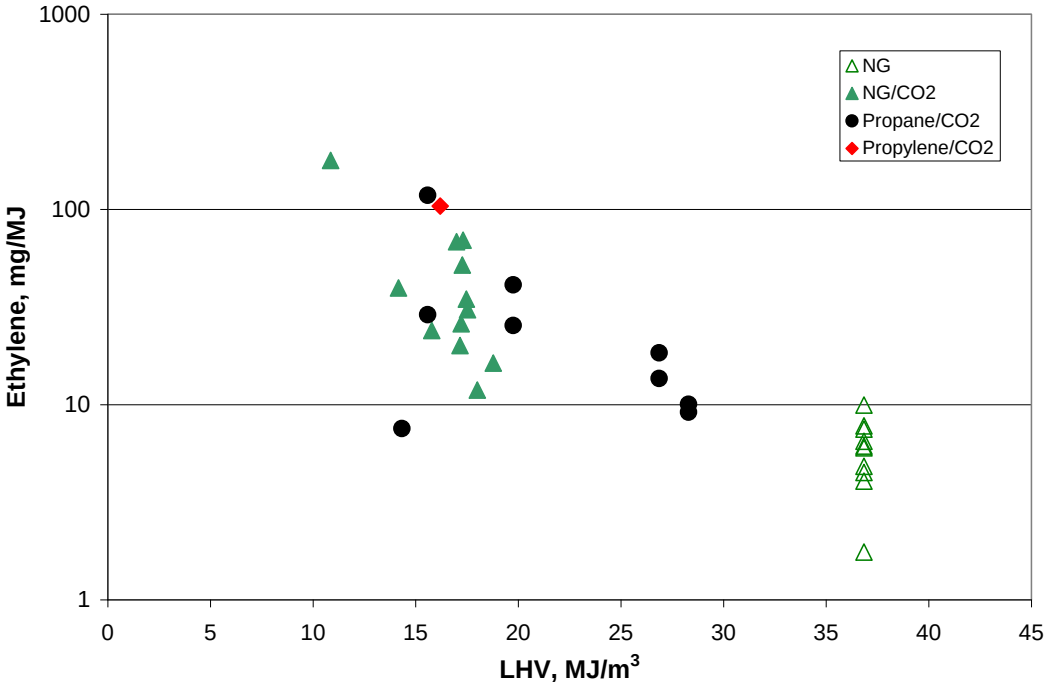

Figure 57 - Emission factor for ethylene for tests with dilution of natural gas, propane and propylene with carbon dioxide.

The only other HRVOC detected was 1-butene, and only for the steam-assisted flaring of propylene. Figure 58 presents the emission factor for 1-butene plotted against the SFR for the steam-assisted flaring of propylene. These emission factors are an order of magnitude smaller than those for ethylene.

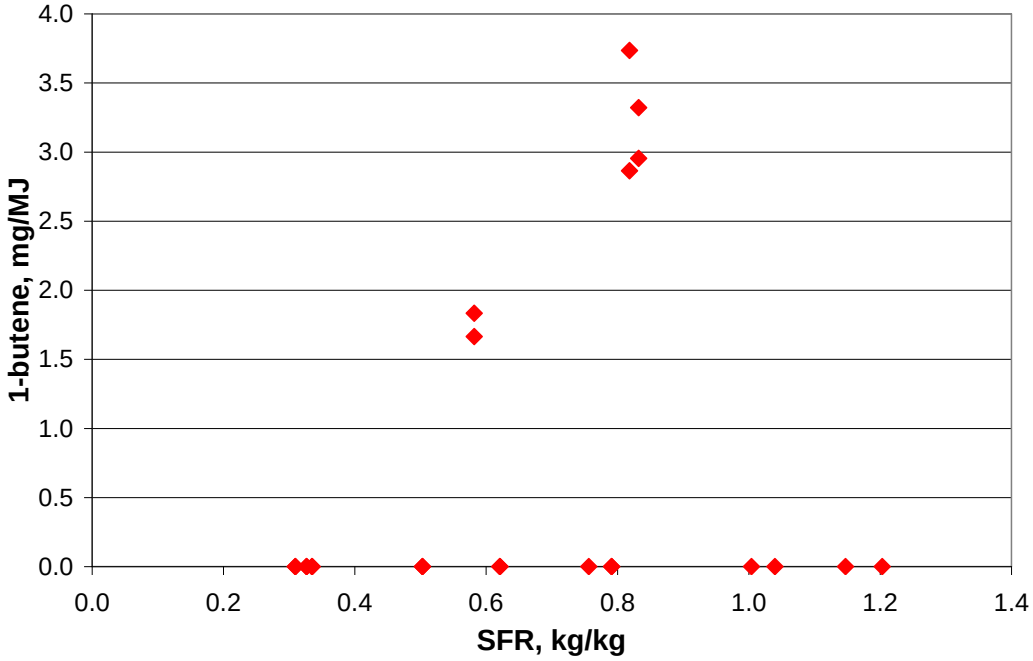

Figure 58 - Emission factor for 1-butene against SFR for steam-assisted flaring of propylene.

The emission factors for 1-butene are plotted against the emission factors for ethylene for the steam-assisted flaring of propylene in Figure 59. This shows that for the detectable levels of 1-butene, these are 0.14 of the emission factor of ethylene. For the two trials with high levels of ethylene emission factors of between 50 and 60 mg/MJ (0.12 lb/MMBtu and 0.14 lb/MMBtu) propylene flared, the expected emissions of 1-butene are at the detection limit of the HRVOC measurement system.

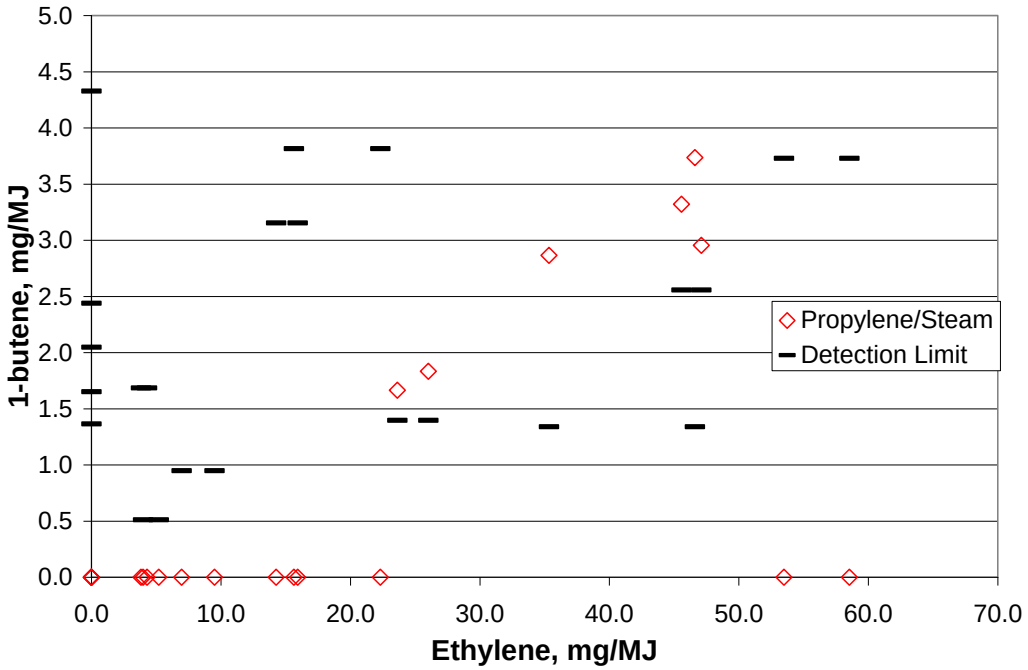

Figure 59 - Emission factor for 1-butene plotted against the emission factor for ethylene for the steam-assisted flaring of propylene. The solid square symbols are the emission factors at the detection limit for these trials.

6.5 Conclusion

The trace emissions from flaring systems are carbon monoxide, nitrogen oxides (NO_x), and hydrocarbons.

The emissions of carbon monoxide are best expressed as a percentage of the conversion inefficiency. The inefficiency due to carbon, in non-sooting systems, is 25% of the total. This is in agreement with the baseline data for natural gas with different diameter flare tips.

The range of emission factor for NO_x is from 0.004 g/MJ to 0.04 g/MJ (0.0093 lb/MMBtu and 0.093 lb/MMBtu), which agrees with the range reported by Pohl and Soelberg (1986) for hydrocarbon flare gases without nitrogenous species.

There were no detectable emissions of BTEX in any of the tests at the detection limit of 10 ppbv. Ethylene was measured in tests with natural gas and propylene. 1-butene was

measured in the steam-assisted flaring of propylene. None of the other HRVOCs were detected in these tests.

The emission factors for ethylene are in the range from 5 mg/MJ to 100 mg/MJ (0.012lb/MMBtu to 0.23 lb/MMBtu) for natural gas and propylene. There is little discernable difference between the two gases.

1-butene was measured in the steam-assisted flaring of propylene. The emission factor for 1-butene is 0.14 of the emission factor for ethylene.

7.0 CONCLUSION

Over 400 test runs were performed in the Flare Test Facility under the auspices of the IFC, covering the conditions of unassisted, steam-assisted, and diluted flaring of natural gas, propylene and ethylene. The results of these tests have provided the information for some of the six gaps in the flaring knowledge base identified in the Introduction, but significant gaps remain. Before getting to the six points, there is one important result that needs to be highlighted.

The question of scale-up of the pilot-scale results in the wind dominated wake-stabilized regime was addressed. Testing was done on pipes of 2.5cm, 5.1cm, 7.6cm, 10.2cm and 15.2 cm (1", 2", 3", 4" and 6") diameter flaring natural gas. The "Three Inch Rule", which states that flaring results with pipes smaller than 7.6 cm (3") do not scale-up to larger flare pipe sizes, was established for the wake-stabilized regime. The "Three Inch Rule" was already established in the literature for the jetting regime [Gogolek et al. 2009]. The results for CCI and DE for natural gas with flare pipes 3, 4 and 6 inches were correlated with the Power Factor (equations 2-2 and 2-4). The Power Factor is used to correlate the results for unassisted and steam-assisted flaring of ethylene and propylene.

It was also shown that the Flame Retention Ring (FRR) has an effect on the efficiency of the flare. The 7.6 cm (3") pipe with FRR has lower efficiency than the 15.2 cm (6") pipe with FRR for a given Power Factor. It was also shown that the FRR affected the ability to scale the CCI from a 7.6 cm (3") flare to a 15.2 cm (6") flare. At the same Power Factor, the efficiency for the 7.6 cm (3") flare with a FRR was lower than the efficiency of the 15.2 cm (6") flare with a FRR. Hence, the CCI data for the 7.6 cm (3") flare with a FRR may be larger than for flares of larger diameter with a FRR. More experimental work is required to determine the minimum scalable flare diameter for flares with a FRR.

Caution is needed in taking the results for simple pipes to full-scale industrial flares. Rigorous scale-up requires matching the structural geometry, fluid mechanics, heat transfer and chemical reactions. In general it is impossible to have a rigorously scaled experiment for combusting flows. That said, pilot-scale testing can provide useful information for full-scale operation as long as the most important features are treated.

7.1 Experimental studies of the flare efficiency in the transition between jetting and wake-stabilized regimes.

These tests were described in Chapter 2. The transition from jetting to wake-stabilized was investigated on a 7.6 cm (3") pipe firing natural gas. The transition is accomplished either by reducing the flare gas rate or by increasing the wind speed. It was found that reducing the flare gas rate has little effect on the efficiency of the flare, while increasing the wind speed decreased the efficiency. The change in efficiency was continuous and almost linear with wind speed, so that there is no sharp change in efficiency with the establishment of the wake-stabilized operation.

7.2 Experimental studies of the effect of wind on steam-assisted flares.

Testing was performed on the 7.6 cm (3") flare tip with FRR (Flame Retention Ring) with steam-assist for natural gas, ethylene and propylene, with cross-wind from 3.5 m/s to 9.5 m/s (11.5 ft/s to 31 ft/s). Previous work, particularly the CMA/EPA study [McDaniel 1983], was done with little or no wind. Steam-assisted flares are more sensitive to the effect of cross-wind than the unassisted flare for all three gases tested. Ethylene is the least affected by the addition of steam, natural gas the most affected. For a given level of Steam to Fuel Ratio (SFR), the effects of varying wind speed and fuel rate is correlated with the Power Factor. The CMA results for flaring propylene are the extrapolation of our results to low values of Power Factor (see Figure 42).

The Reduced Steam Volume Fraction (RSVF) was derived as the ratio of the steam volume fraction to the theoretical maximum steam dilution for continued flammability. This parameter was used to bring together all the steam-assist tests and is proposed as a replacement for the SFR for optimizing the steam-assist rate. The maximum RSVF should be 1; the 'over-steaming' tests in the CMA/EPA study had RSVF slightly larger than 1. Our data indicate that with wind present the maximum RSVF should be 0.8. This translates into maximum SFR = 1.8 for ethylene and maximum SFR = 1.2 for propylene.

With that limit, the data show further that there is a maximum Power Factor to ensure 98% DE – 0.03 for ethylene and 0.02 for propylene. This translates into a minimum exit velocity for the flare gas for a given wind speed. Figure 60 shows the curves for the minimum exit velocity for wind speed up to 10 m/s (32.5 ft/s).

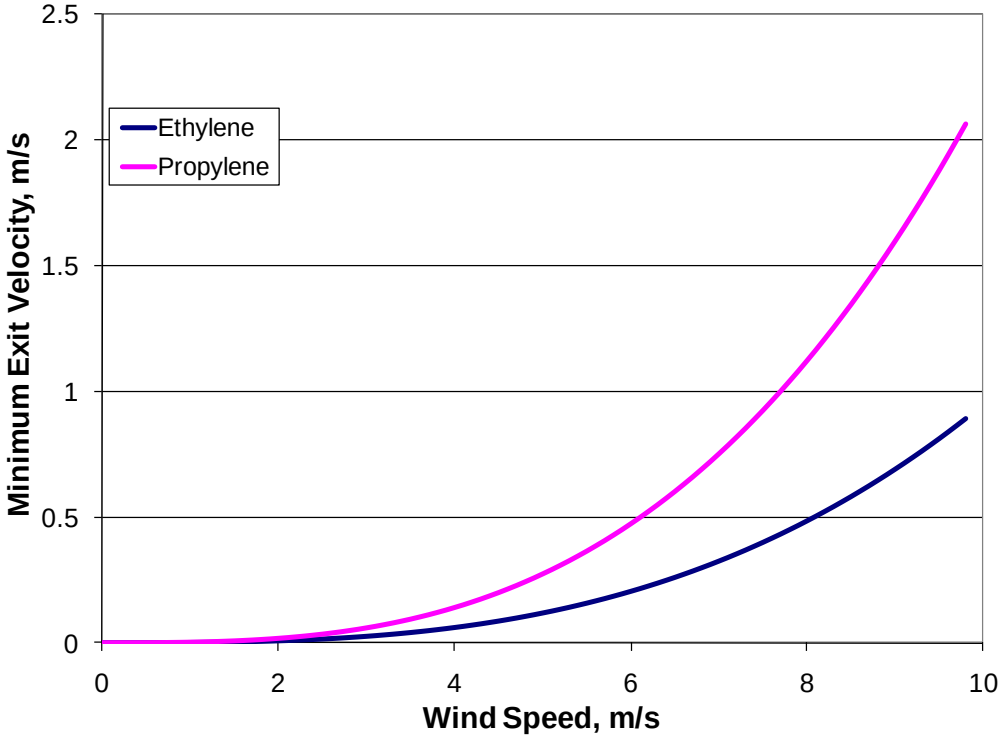

Figure 60 - Minimum exit velocities for steam-assisted flaring of ethylene and propylene based on RSVF<0.8 and maximum Power Factor (x 100) of 2 for propylene and 3 for ethylene.

7.3 Experimental studies on the limiting hydrogen concentration for steam-assisted flares and wind blown flares.

No work was done on this gap.

7.4 Experimental measurements of HRVOC and NOx measurements for flares with and without steam-assist.

Measurements were taken of the various trace emissions, described in detail in Chapter 7. The trace emissions from flaring systems are carbon monoxide, nitrogen oxides (NO_x), and hydrocarbons. There are several quite notable findings:

1. Carbon monoxide is 25% of the CCI (carbon conversion inefficiency), for assisted and unassisted flaring of natural gas, ethylene and propylene.

2. There was no detectable emission of BTEX compounds, or of the HRVOCs 2-butenes, 1-3 butadiene, or of propylene except when it was present in the flare gas.

3. Ethylene was measured during the flaring of natural gas and propylene, although at very low levels. The emission factors for ethylene are in the range from 5 mg/MJ to 100 mg/MJ (0.012 lb/MMBtu to 0.23 lb/MMBtu) for natural gas and propylene. There is little discernable difference between the two gases.

4. 1-butene was measured from the steam-assisted flaring of propylene and the emission factor is 0.14 times the emission factor for ethylene for those tests.

5. The range of emission factor for NO_x is from 0.004 g/MJ to 0.04 g/MJ (0.0093 lb/MMBtu and 0.093 lb/MMBtu), which agrees with the range reported by Pohl and Soelberg (1986) for hydrocarbon flare gases without nitrogenous species.

7.5 Correlation of fuel properties to correlate the flare efficiency with flare gas composition, particularly accounting for the special case of hydrogen, and the inert gases nitrogen and carbon dioxide.

There was only limited success in correlating the flare efficiency results with fuel properties. The Fuel Factor (equation 4-4) does bring together the DE data for steam-assisted flaring of ethylene and propylene (see Figure 46). The Fuel Factor does not work for the data from flaring natural gas. Natural gas is anomalously unreactive hydrocarbon, and this could be the reason. The Fuel Factor may have general applicability because flare gases are generally composed of the more reactive hydrocarbons. We were not successful in finding a factor that can handle the difference between the inert species nitrogen and carbon dioxide.

7.6 Correlation of flare efficiency with steam-assist rate that includes the flare gas composition, perhaps unifying steam with the handling of nitrogen and carbon dioxide dilution.

The Reduced Steam Volume Fraction (RSVF) is put forward as a parameter for correlating the effect of steam-assist on flaring (see Figure 43). The concept behind this

factor is that there is a maximum dilution with steam that a combustible gas can endure and remain flammable. This maximum dilution is used to normalize the steam volume fraction (if the steam was uniformly mixed with the flare gas). RSVF of 1 is the theoretical maximum steam that can be added. Our data shows that RSVF = 0.8 is a practical maximum for flaring in the presence of wind.

We attempted to use the Reduced Volume Fraction Inert (RVFI) for correlating the dilution with nitrogen and carbon dioxide. The test data showed that the dilution of natural gas, ethylene and propylene with nitrogen can proceed to the theoretical maximum (RVFI = 1) with DE above 98%. This means that unassisted flares with nitrogen in the flare gas can have DE greater than 98% with heat content below 7.5 MJ/m^3 (200 Btu/scf). Dilution with carbon dioxide effects a greater decrease in Destruction Efficiency. Our results show that the minimum heat content of 7.5 MJ/m^3 (200 Btu/scf) is too low and does not guarantee 98% DE when the inert gas is carbon dioxide.

7.7 Gaps remaining or identified

A great deal of progress was made in closing the gaps in understanding the dependence of flare efficiency on the operating parameters of wind speed, flare gas rate and composition, and steam-assist rate. However, several gaps remain.

1. The effect of hydrogen: Hydrogen is the most flammable gas and the addition of even small amounts to a gas increases the flammable range, flame speed, and other combustion properties. We did not perform any testing with hydrogen in our flare gas.

2. Scale-up of steam-assisted flare results: Our testing was with a simple pilot-scale flare tip. It may be that this tip is more vulnerable to the effects of cross-wind than a commercial flare tip, with robust pilot burners. Measurements on larger scale flares are needed for confidence in the scalability of the results reported here.

3. A correlating value that reconciles the different fuel gases and inert gases is needed. Some progress has been made and the data reported here can be used to test hypotheses. More data from the flaring of gas mixtures are needed.

8.0 REFERENCES

American Petroleum Institute (API), [1999] "Guide for Pressure-Relieving and Depressuring Systems API RP 521", Feb 15.

Caravaggio, G. and A. Caverly, [2008] "Online Analysis of Flaring Emissions", report to IFC.

Gogolek, P., A. Caverly, J. Pohl, R. Schwartz, J, Seebold [2009]

a) "Emissions from Elevated Flares – A Survey of the Literature", report to IFC.

b) "Flare Test Facility – Equipment and Calculations", report to IFC.

Gogolek, P.E.G., and Hayden, A.C.S. [2003] "Performance of flare flames in a crosswind with nitrogen dilution." Journal of Canadian Petroleum Technology **43** pp. 43-47.

McDaniel, M. [1983] "Flare Efficiency Study." EPA-600/2-83-052.

Pohl, J.H., Payne, R., and Lee, J. [1984] "Evaluation of the Efficiency of Industrial Flares: Test Results." EPA-600 /2-84-095.

Pohl, J.H., and Soelberg, N.R. [1985] "Evaluation of the Efficiency of Industrial Flares: Flare Head Design and Gas Composition". EPA-600/2-85-106.

Pohl, J.H., and Soelberg, N.R. [1986] "Evaluation of the Efficiency of Industrial Flares: H2S Gas Mixtures and Pilot Assisted Flares". EPA-600/2-85-106.

9.0 APPENDIX

Imperial Unit Tables and Figures

Table 9 - Test matrix for tests with FRR firing natural gas.

Pipe Size		Fuel Rate	Exit Velocity	Wind Speed	Number of tests
(Nom. inches)	(Nom. mm)	lb/h	ft/s	ft/s	
3”	80	22 - 66	6.2-18	6.6-39	43
6”	150	22 - 66	1.6-4.9	6.6-39	43

Table 10 - Test matrix for the fuel modification tests, augmented with propane and diluted with nitrogen.

Fuel	Pipe Size		Fuel Rate	Exit Velocity	Wind Speed	Number of tests
	(Nom. Inches)	(Nom. mm)	lb/h	ft/s	ft/s	
NG/propane	3”	80	22 - 66	2.0 – 5.9	11 - 31	20
NG/propane	6”	150	22, 44	0.49, 0.98	11 - 31	9

NG/N_2	3”	80	77 - 231	6.6 - 20	11 - 31	24

Table 11 - Test matrix for the simple fuel flaring tests.

Fuel	Rate	Exit velocity	Wind Speed
	lb/h	ft/s	ft/s
Ethylene	22, 66	3.9, 11	12.5, 23.0, 33.8
Propylene	22, 66	2.4, 7.2	12.5 - 33.8

Table 12 - Overall test matrix for the steam-assisted trials.

Fuel	**Fuel Rate**	**Exit Velocity**	**Wind Speed**	**SFR**
	lb/h	ft/s	ft/s	lb/lb
Natural gas	15 - 66	3.9 - 19	11 - 31	<0.3 – 2.2
Ethylene	22, 66	3.6 - 11	11 - 31	0.24 – 3.4
Propylene	22, 44, 66	2.3, 4.6, 7.2	11 - 31	0.3 – 1.2

Table 13 - Maximum dilution for flammable operation, with energy content and exit velocity.

Mixture	LHV	Fraction inert (Volume basis)	Exit Velocity	Estimated 98% DE Threshold

	Btu/ft^3	%	ft/s	Btu/ft^3
NG/N_2	102.0	89.7	56.1	102.0
NG/CO_2	292.5	70.4	20.3	316.7
$Ethylene/N_2$	99.3	93.4	54.8	104.7
$Ethylene/CO_2$	244.2	83.7	23.6	322.1
$Propylene/CO_2$	434.8	80.1	12.8	536.8

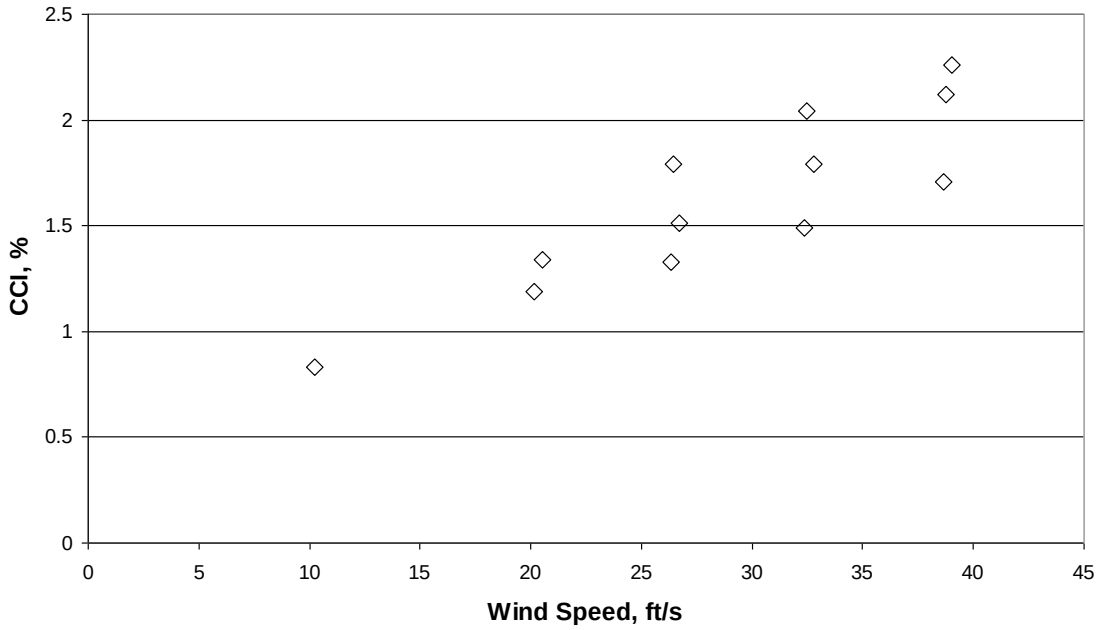

Figure 61 - Baseline testing results for 1" basic pipe firing natural gas.

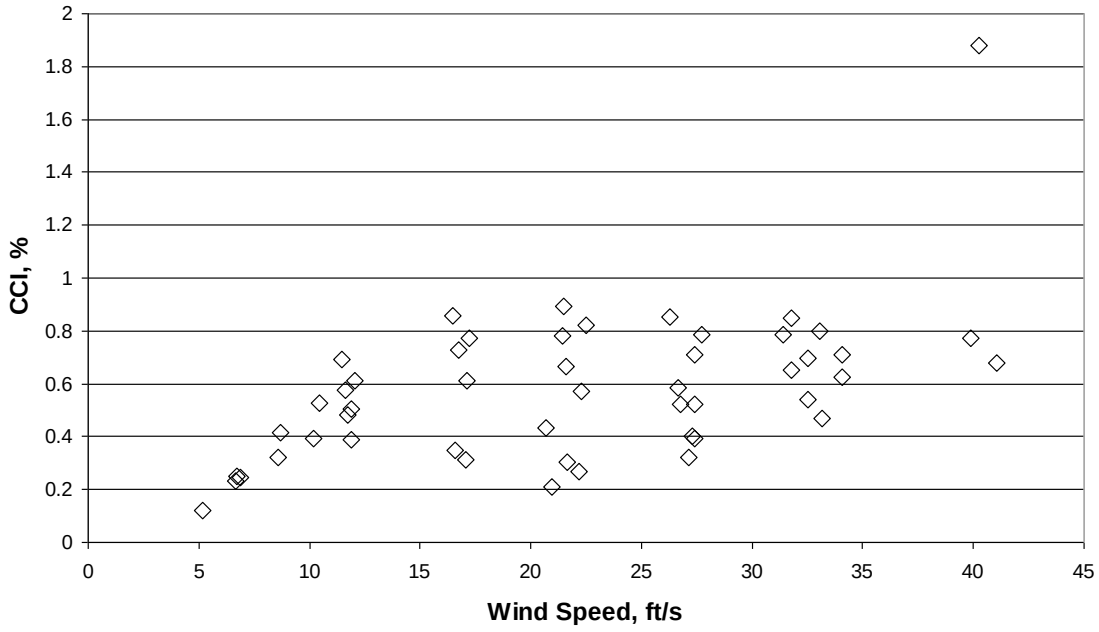

Figure 62- Baseline testing results for 2" basic pipe firing natural gas.

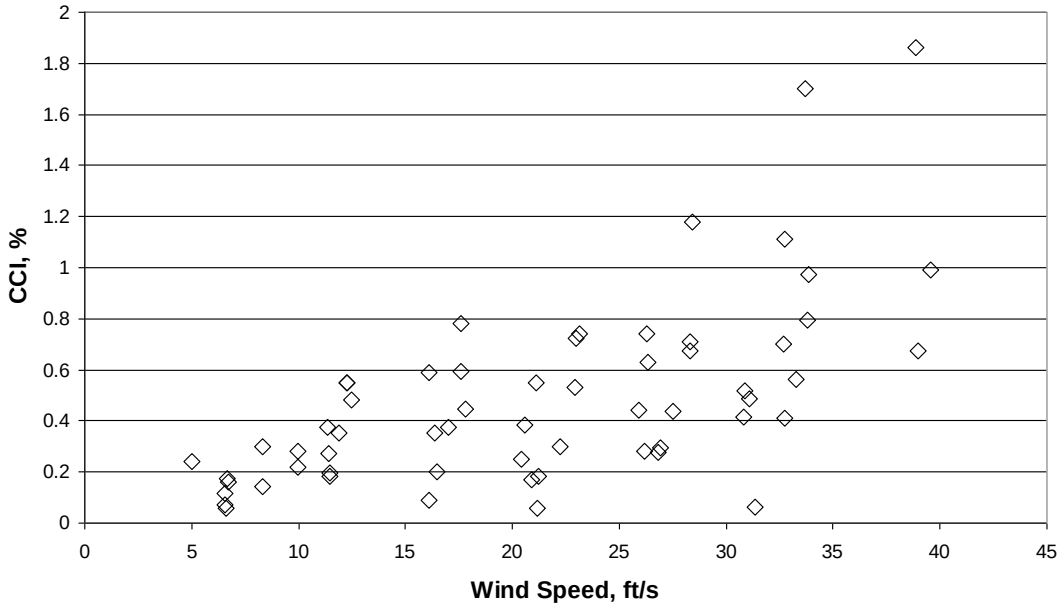

Figure 63 - Baseline testing results for 3" basic pipe firing natural gas.

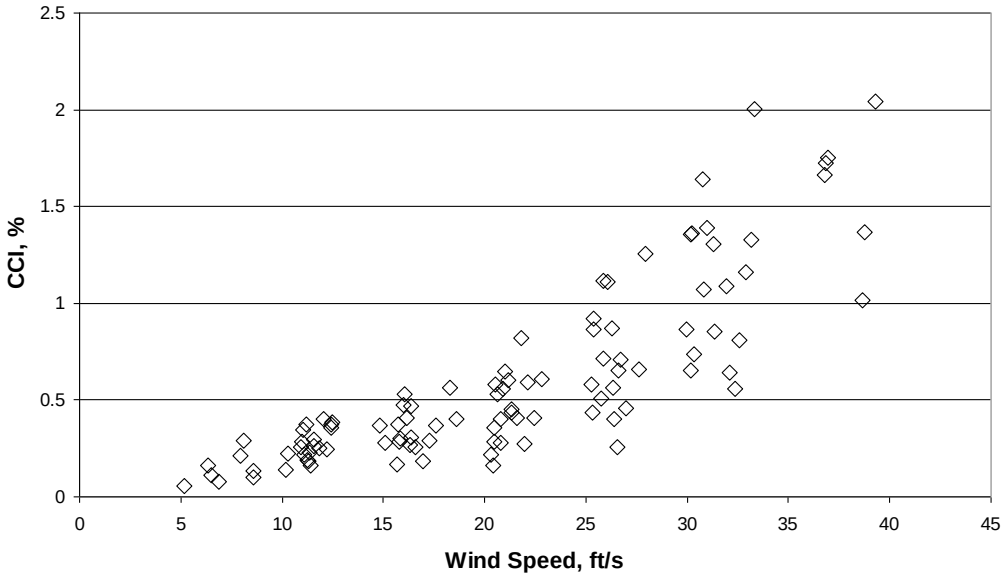

Figure 64 - Baseline testing results for 4" basic pipe firing natural gas.

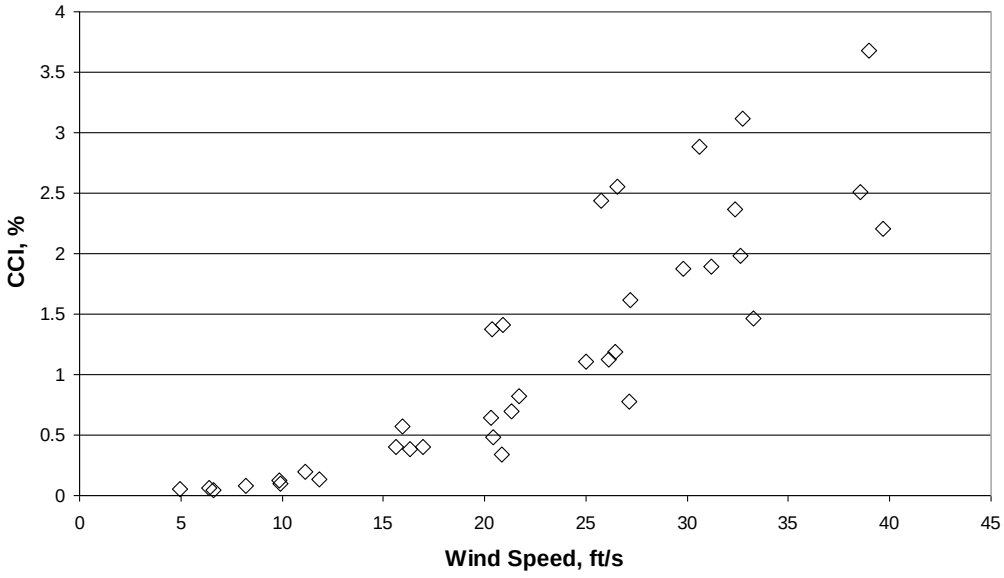

Figure 65 - Baseline testing results for 6" basic pipe firing natural gas.

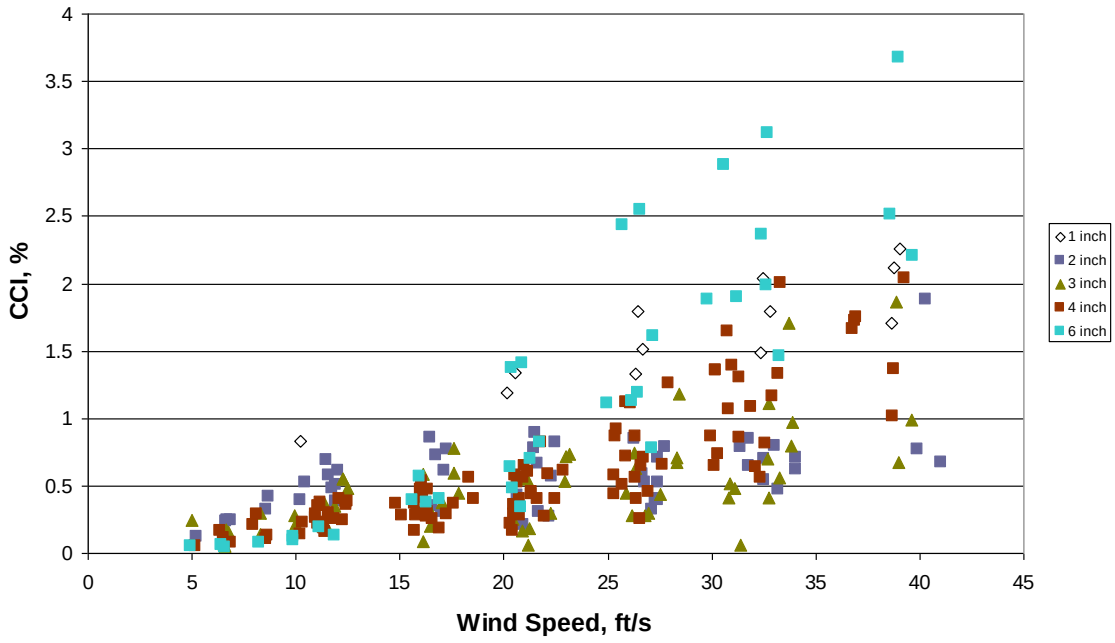

Figure 66 - Results of all baseline tests firing natural gas.

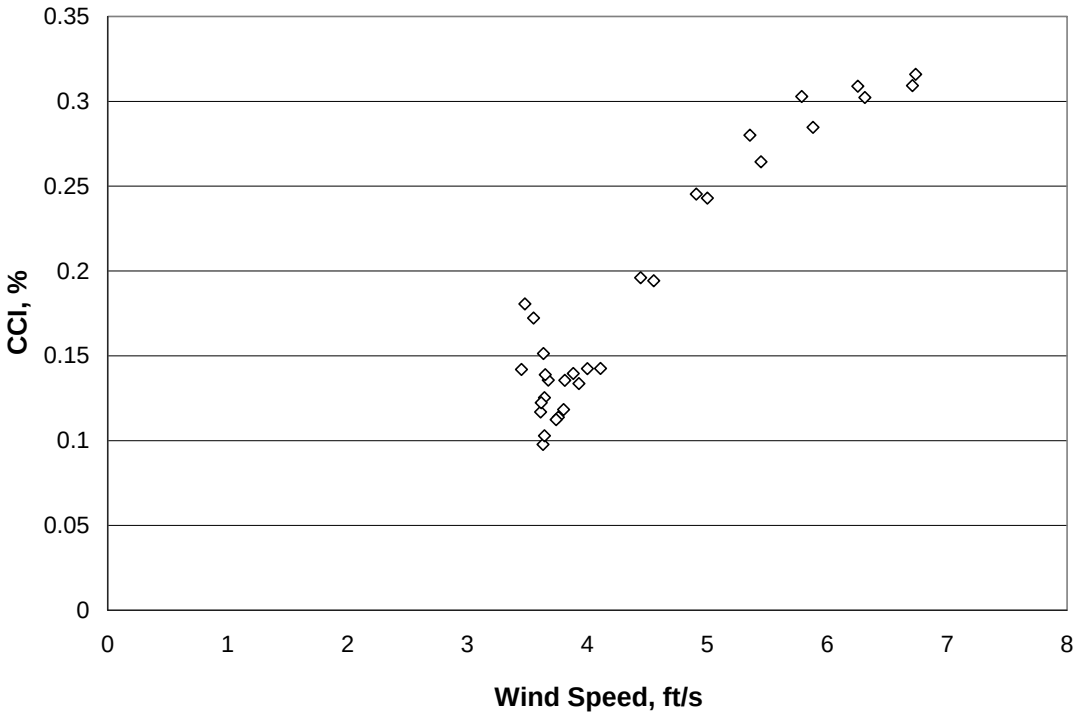

Figure 67 - Results for 3" pipe for transition testing versus wind speed. The change in fuel rate at 2.5 miles/h has a much smaller effect than the increase of wind speed.

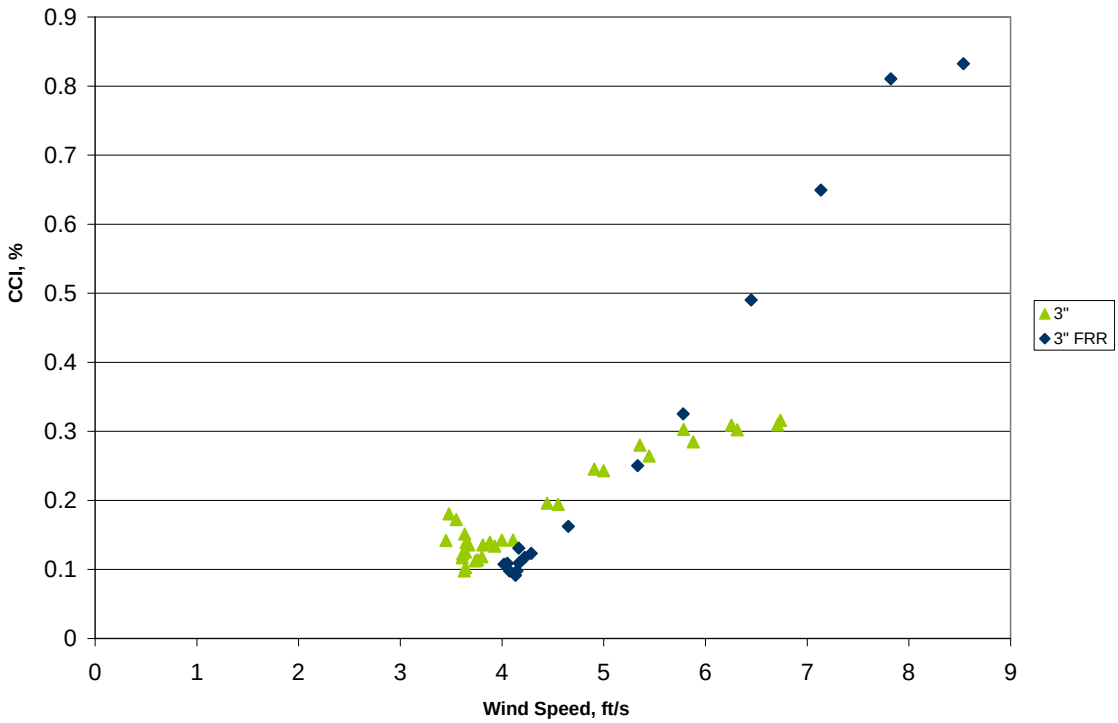

Figure 68 - Transition test results with 3" pipes versus wind speed.

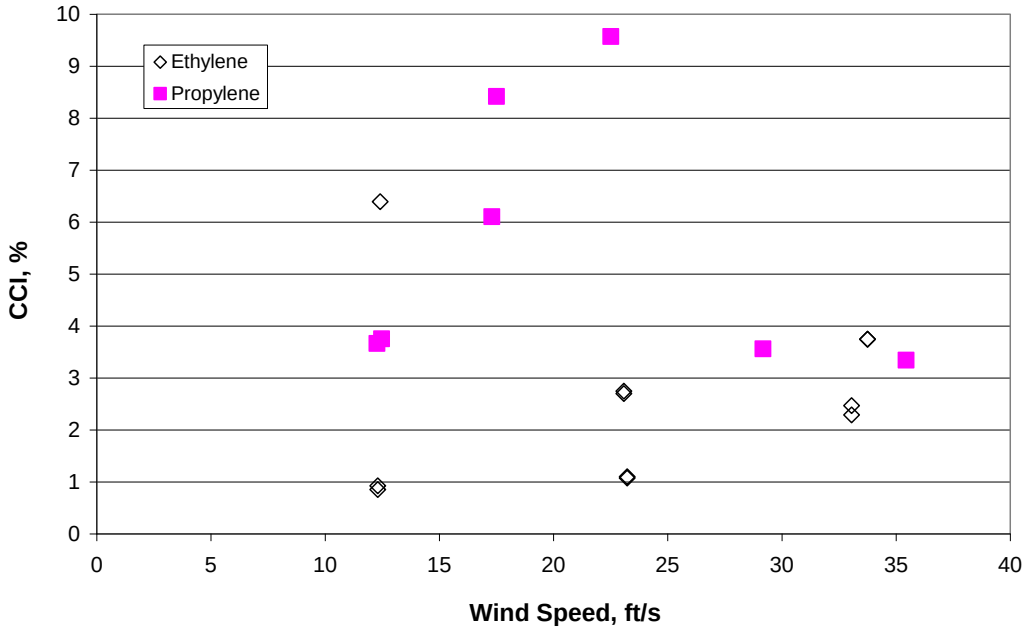

Figure 69 - Conversion inefficiency for unassisted flaring of ethylene and propylene in 3" FRR tip.

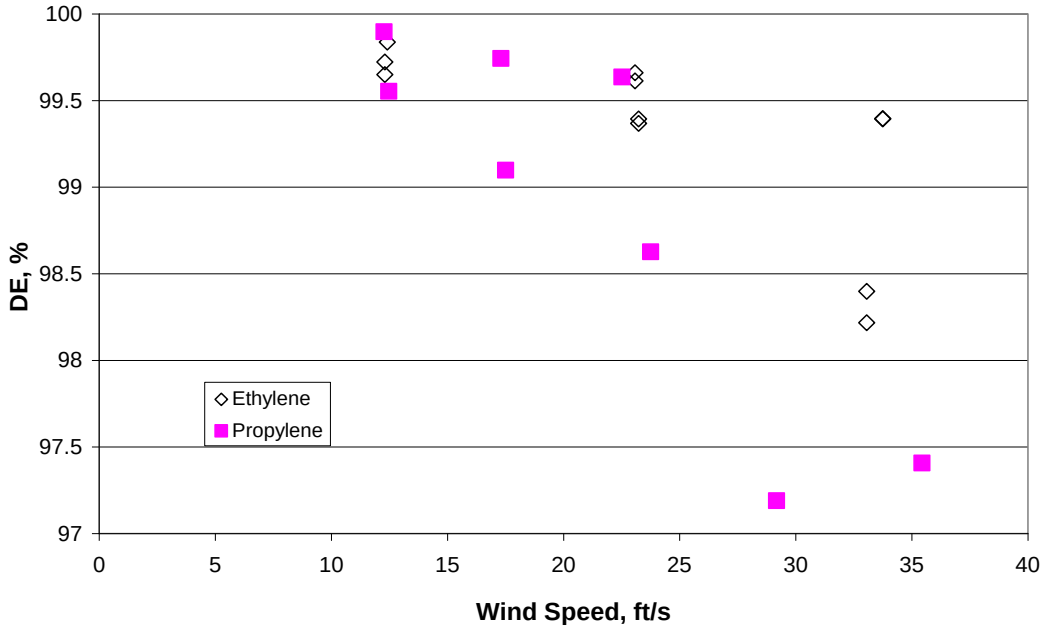

Figure 70 - Destruction efficiency for unassisted flaring of ethylene and propylene in 3" FRR tip.

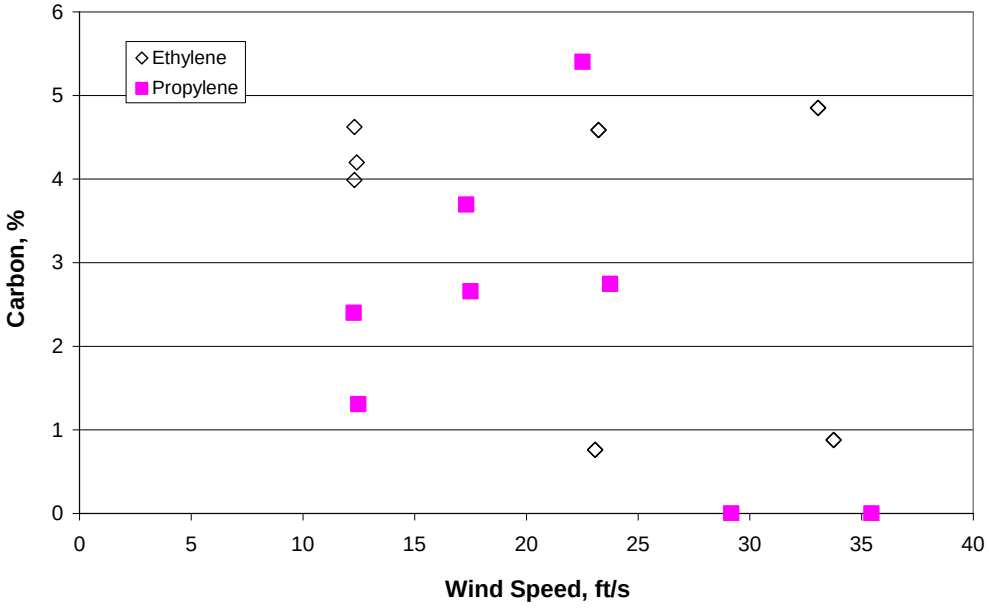

Figure 71 - Solid carbon emission as a percentage of the total carbon for unassisted flaring of ethylene and propylene in 3" FRR flare tip.

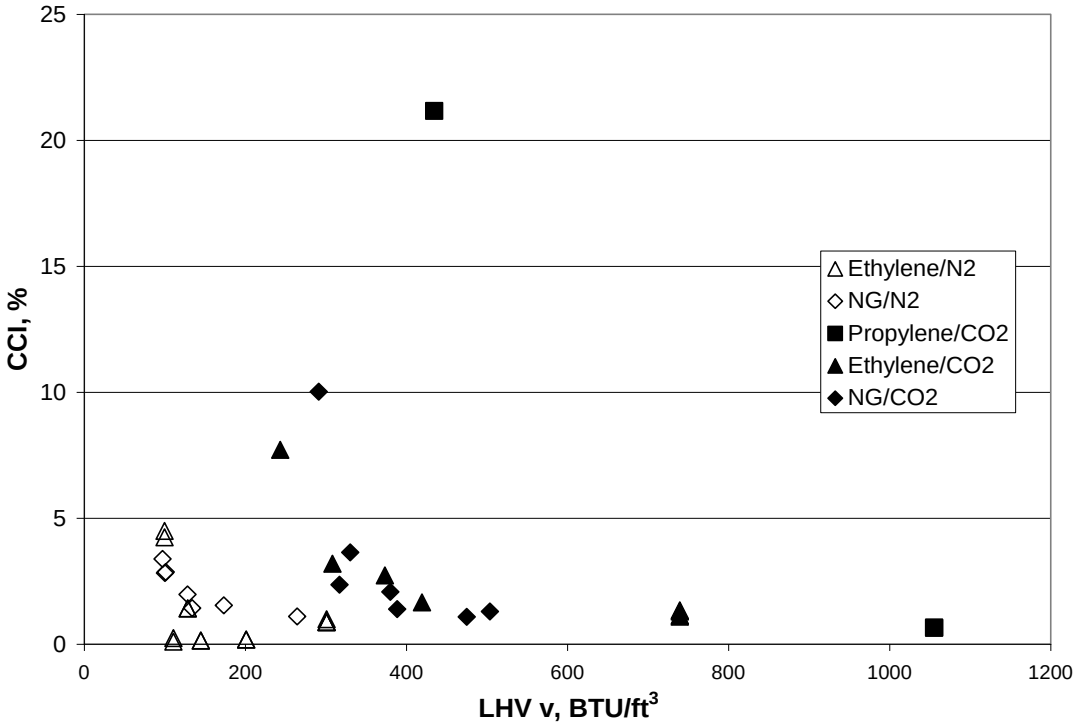

Figure 72 - Conversion inefficiency versus heat content of flare gas.

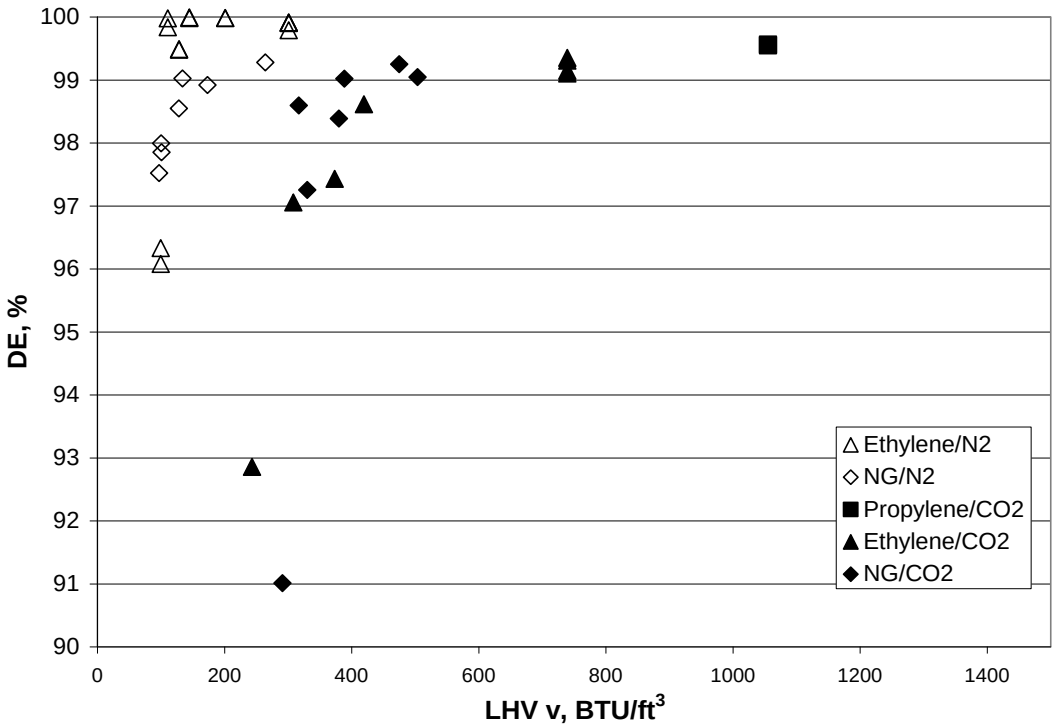

Figure 73 - Destruction efficiency versus heat content, volume basis.

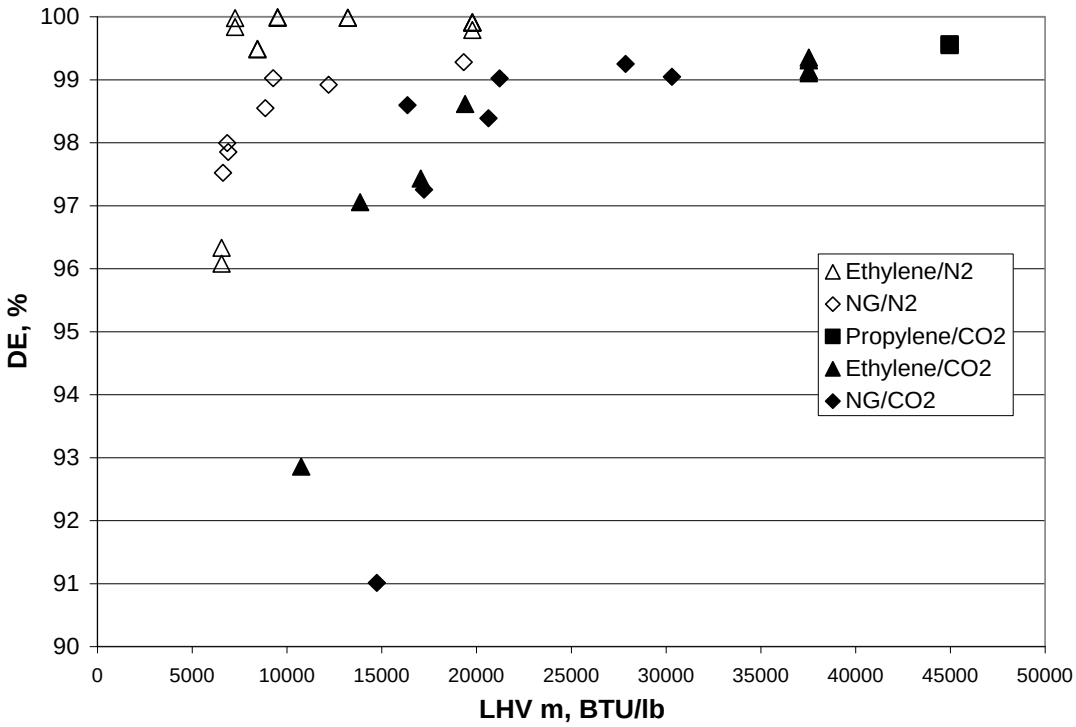

Figure 74 - Destruction efficiency versus heat content, mass basis.

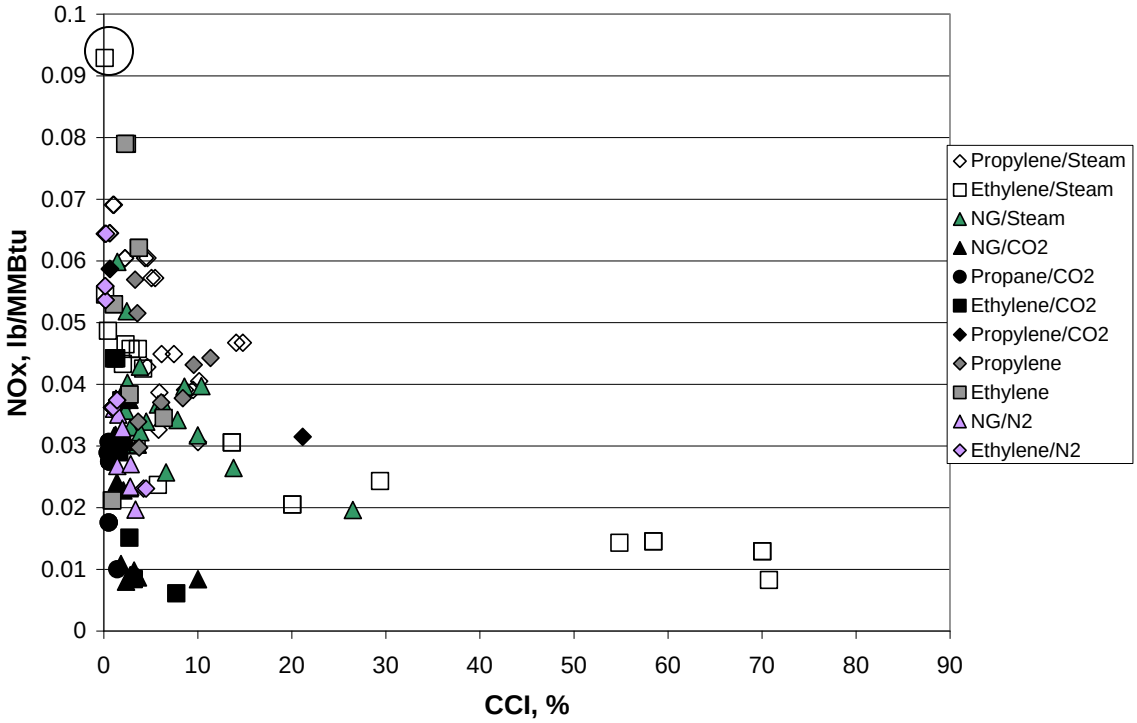

Figure 75 - Emission factor for NO_x plotted against conversion inefficiency for all tests.

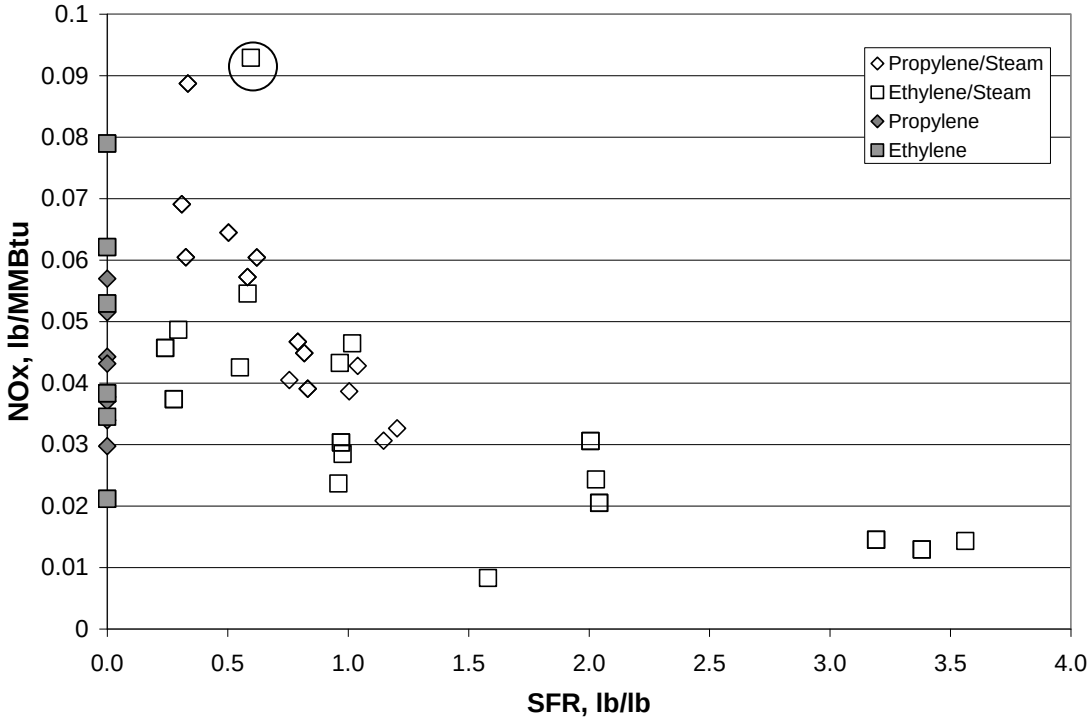

Figure 76 - Emission factor for NO_x for steam-assisted trials.

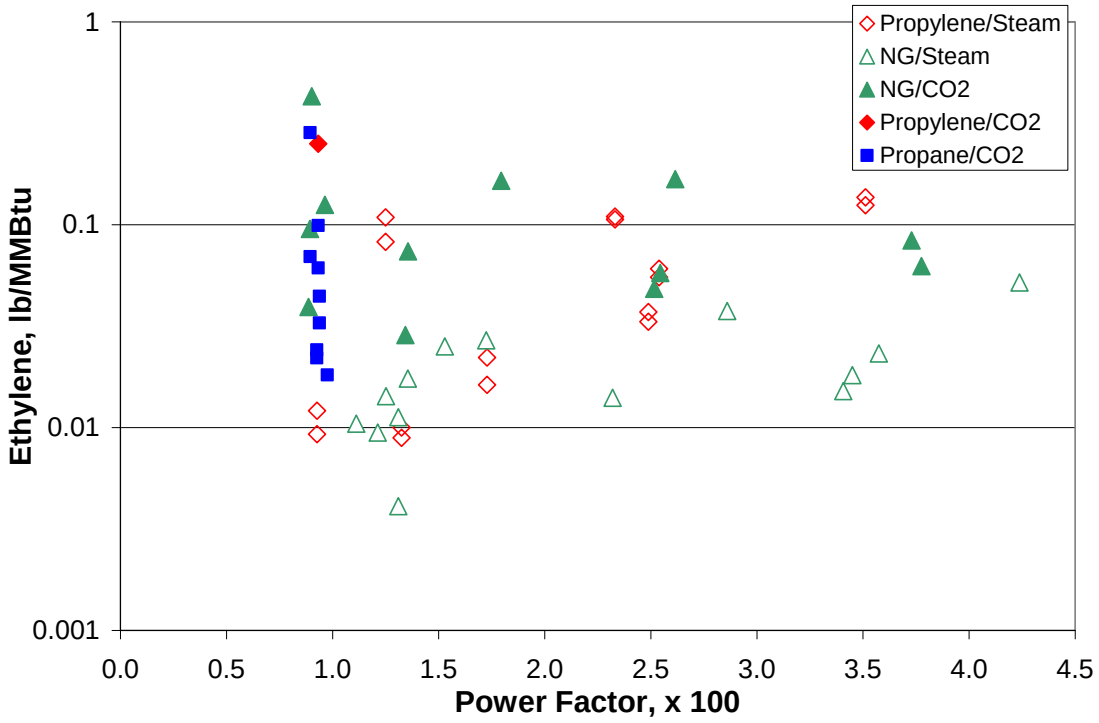

Figure 77 - Emission factors for ethylene plotted against Power Factor for tests with natural gas and propylene.

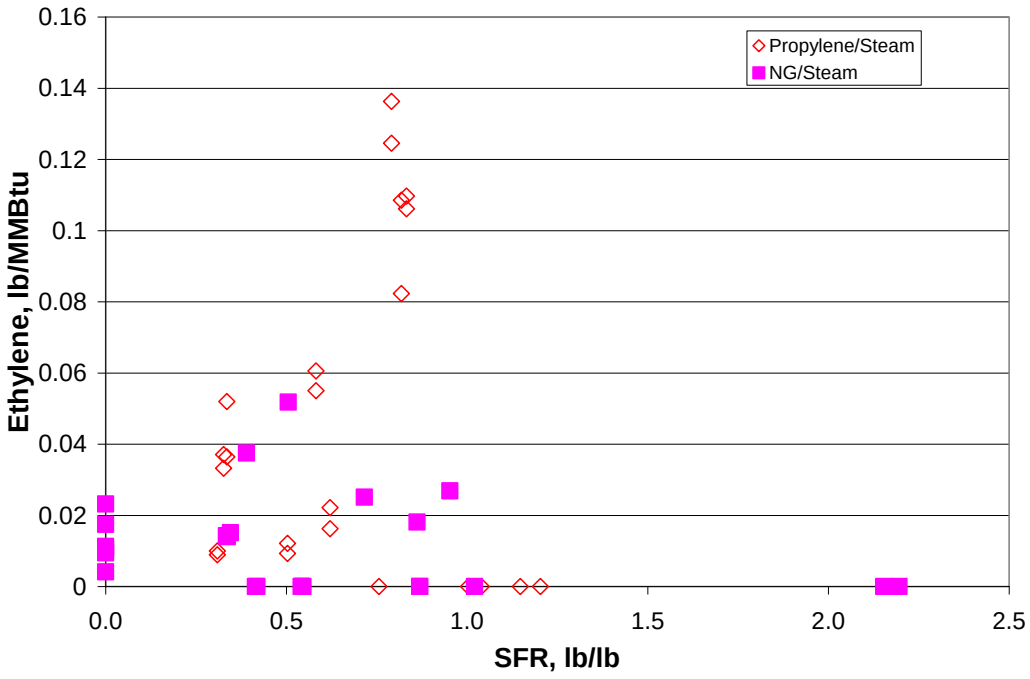

Figure 78 - Emission factors for ethylene plotted against SFR for steam-assisted flaring of natural gas and propylene.

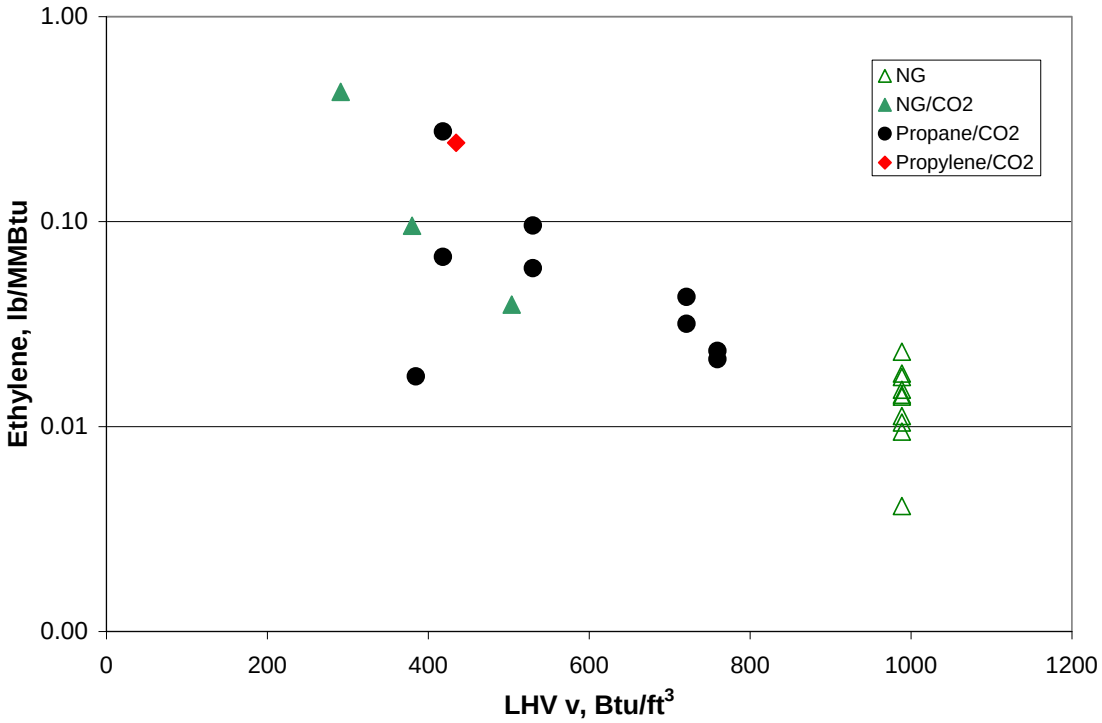

Figure 79 - Emission factor for ethylene for tests with dilution of natural gas, propane and propylene with carbon dioxide.

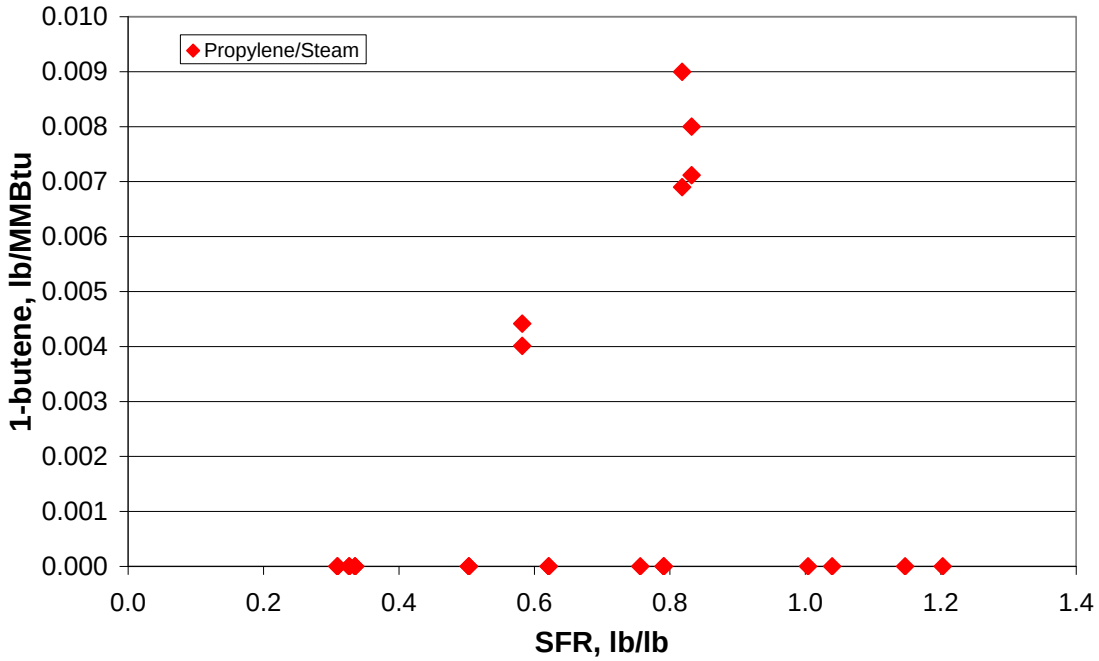

Figure 80 - Emission factor for 1-butene against SFR for steam-assisted flaring of propylene.

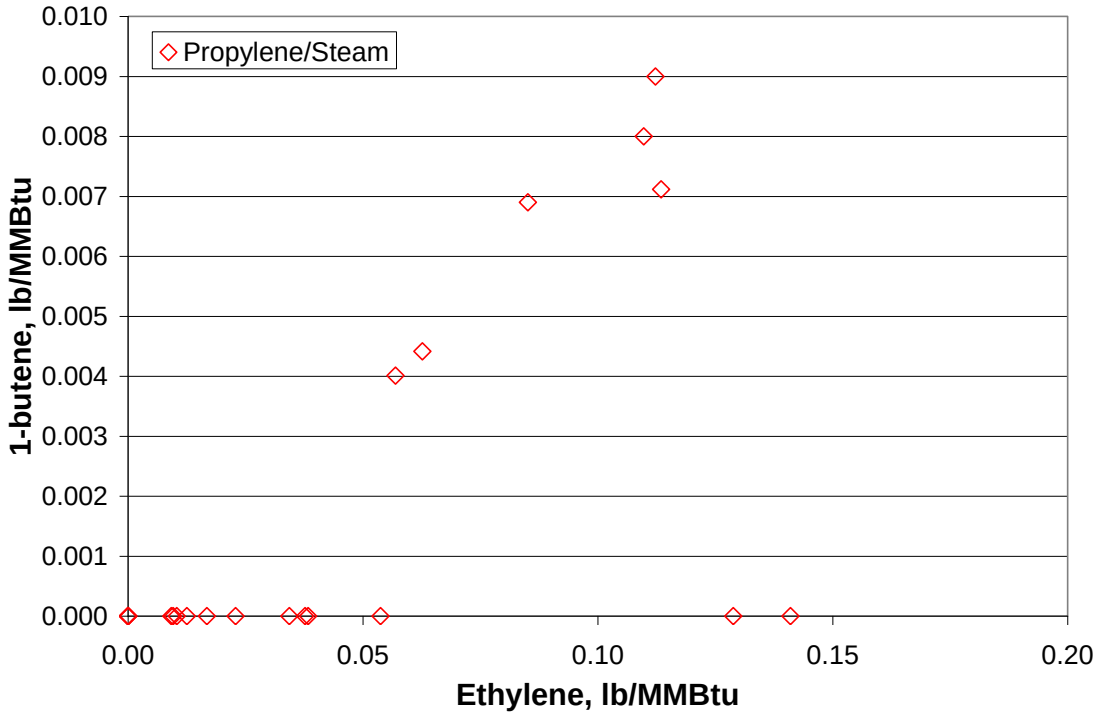

Figure 81 - Emission factor for 1-butene plotted against the emission factor for ethylene for the steam-assisted flaring of propylene. The solid square symbols are the emission factors at the detection limit for these trials.

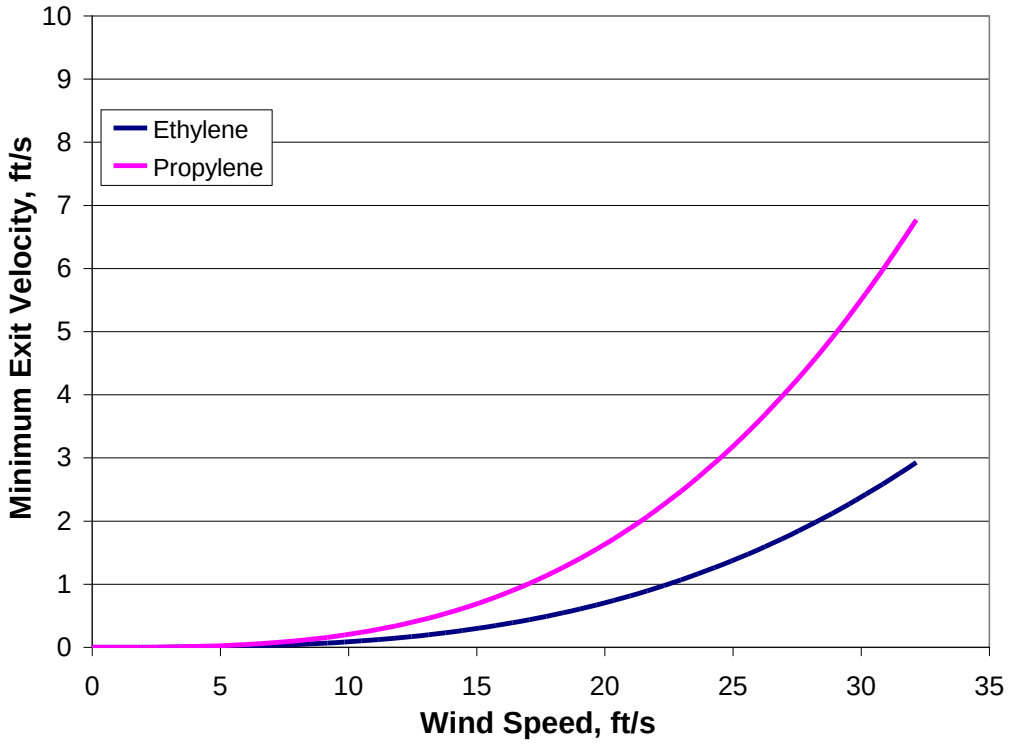

Figure 82 - Minimum exit velocities for steam-assisted flaring of ethylene and propylene based on RSVF<0.8 and maximum Power Factor (x 100) of 2 for propylene and 3 for ethylene.

Natural Resources Canada | Ressources naturelles Canada

CanmetENERGY

Leadership in ecoInnovation

Flare Test Facility – Equipment and Calculations

P. Gogolek, Andrea Caverly, Cory Balderson

CanmetENERGY - Ottawa

J. Pohl

Energy International

R. Schwartz

John Zink

J. Seebold

Consultant

Prepared for the International Flaring Consortium

April 2010

Funding provided by members of the International Flaring Consortium

Canada

DISCLAIMER

This report was prepared by CanmetENERGY as an account of work funded by the International Flaring Consortium (IFC). CanmetENERGY has made all reasonable efforts to ensure the exactness of the information provided in this report and the opinions expressed herein are those of CanmetENERGY solely. However, neither CanmetENERGY, the International Flaring Consortium, nor any person acting on behalf of them;

a. Makes any warranty or representation, expressed or implied with respect to the accuracy, completeness, or usefulness of the information contained in this report, or that the use of any information, apparatus, method, or process disclosed in this report may not infringe privately-owned rights, or

b. Assumes any liability with respect to the use of, or for damages resulting from the use of, any information, apparatus, method, or process disclosed in this report.

Reference to specific commercial products in this report does not represent or constitute an endorsement, recommendation, or favoring by CanmetENERGY, the International Flaring Consortium, nor any person acting on behalf of them, of the specific manufacturer or commercial product. The involvement by CanmetENERGY in this project is not to be used for promotional purposes beyond being identified as an independent third party evaluator.

TABLE OF CONTENTS

1.0 Introduction 1

2.0 The Air Supply, Cold Duct Section and Test Section 4

2.1 The Flare Pipe and Fuel System 6

2.2 Steam-assist Flare Tip 7

2.3 Steam Supply System 8

2.4 Pilot Burners 8

2.5 Gas Sampling 11

2.6 Particulate Sampling 16

2.7 Instrumentation 17

3.0 Testing of Sampling System 18

3.1 Bias Testing of Sampling System 18

4.0 Standard Procedure for Flare Start-up 20

5.0 Calculations 22

5.1 Calculation of Performance Measures 22

5.2 Analytical test cases for flaring calculations 23

5.3 Sensitivity of Calculations 25

5.4 Estimating Uncertainty 30

6.0 Conclusion 37

7.0 References 39

8.0 Appendix 40

A. Imperial Figures and Graphs 41

B. Analyzer Descriptions and Specifications 43

C. Correlations 56

LIST OF FIGURES

Figure 1 - Schematic of Flare Test Facility. 4

Figure 2 - Photo of steam ring with pilot burners 9

Figure 3- Schematics of steam ring and pilot burners 10

Figure 4 – Steam ring and pilots in operation with ethylene fuel (10kg/h ethylene and 20 kg/h steam). 11

Figure 5 – Photo of new sample conditioning system. 12

Figure 6 - Velocity profiles in stack at the sampling location. 13

Figure 7 - Concentration profiles for CO_2 in stack, with the probe value indicated by the line 13

Figure 8 - Concentration profiles for CO in stack, with the probe value indicated by the line 14

Figure 9 - Concentration profiles for CH_4 in the stack, with the probe value indicated by the line. 14

Figure 10 - Division of stack cross-section for averaging point probe. 16

Figure 11 - Uncertainty curves for carbon conversion efficiency (CCE). 35

Figure 12 - Uncertainty curves for the destruction efficiency (DE). 36

Figure 7 - Concentration profiles for CO_2 in stack, with the probe value indicated by the line 41

Figure 8 - Concentration profiles for CO in stack, with the probe value indicated by the line 41

Figure 9 - Concentration profiles for CH_4 in the stack, with the probe value indicated by the line. 42

LIST OF TABLES

Table 1 - Summary of results of segregation study showing averaging properties of the sample probe. 15

Table 2 - Bias test results with old and new conditioning unit in line. 18

Table 3 - Results of bias testing of the new sample conditioning system with methane and propane span gas. 19

Table 4 - Sensitivity of main performance indicators to changes in input variables. Low dilution case with low wind and high fuel flow. 27

Table 5 - Sensitivity of main performance indicators to changes in input variables. High dilution case with high wind and low fuel flow. 29

Table 6 - Uncertainty values for measurements for estimation of uncertainty of CCE and DE. 34

NOMENCLATURE

NOMENCLATURE

α	The dimensionless value of the destruction efficiency as defined in equation 5-9
ε_{CH_4}	Error in stack methane concentration, ppm
ε_{CO}	Error in stack carbon monoxide concentration, ppm
$\varepsilon_{CO_2,in}$	Error in inlet carbon dioxide concentration, ppm
$\varepsilon_{CO_2,out}$	Error in stack carbon dioxide concentration, ppm
η	Carbon conversion efficiency.
σ_c	Reciprocal of increase of carbon in stack gas, summed over all species, equation (5-23), ppm^{-1}.
x	Number of moles of Oxygen used to calculate extent of the reaction (equation 5-10)
$x^c_{CO_2,f}$	Mole fraction of carbon in carbon dioxide in fuel.
$x^c_{CO_2,out}$	Mole fraction of carbon in carbon dioxide in stack gas.
$\{x_i\}_{allcompounds}$	Composition of gas, the mole fraction of all species.
BMS	Burner Management System
BTEX	Benzene, toluene, ethylbenzene, xylenes.
CB	Carbon Balance, %.
CCE	Carbon Conversion Efficiency, the mass

	percentage of carbon in the flare gas converted to carbon dioxide, %.
DE	Destruction Efficiency, the percentage of a species in the flare gas that is converted into any other species. DE = 100% - FS.
FS	Fuel Slip, =100% - DE.
FTF	Flare Test Facility
HRVOC	Highly reactive volatile organic compounds (eg. Ethylene, propylene, 1-butene, cis/trans-2-butene, 1,3-butadiene)
IFC	International Flaring Consortium
$\dot{m}_a$	Mass flow of air, kg/h.
$\dot{m}_{bucket}$	Mass flow of steam measured by the bucket, kg/h.
$\Delta\dot{m}^c{}_{CO}$	Net mass flow of carbon as carbon monoxide, kg/h.
$\Delta\dot{m}^c{}_{CO_2}$	Net mass flow of carbon as carbon dioxide, kg/h.
$\dot{m}_f$	Mass flow of fuel, kg/h.
$\Delta\dot{m}^c{}_{HC}$	Net mass flow of carbon as hydrocarbon, kg/h.
$\dot{m}_{meter}$	Mass flow of steam as measured by the steam flow meter, kg/h.
P	Pressure, kPa.
RH	% Relative Humidity
SDE	Specific Destruction Efficiency, %.
T	Temperature, ºC.
X_i	Place holder variable for input value *i*.

$y_{CO_2,out}$	Mole fraction of carbon dioxide in stack gas, ppm
$y_{CO_2,in}$	Mole fraction of carbon dioxide in inlet air, ppm

1.0 INTRODUCTION

Flares are the primary technology used for the safe and economical disposal of combustible gases at production sites and refineries. Flare performance and associated emissions are current environmental issues in some jurisdictions. This is partly because of genuine gaps in the flare research literature, as identified in a recent literature review (Gogolek et al., 2009). Also, there is confusion about the applicability of some published results to industrial scale flares. The literature review provides some structure and clarity regarding applicability of the various published data. Firstly, we distinguish the jetting and wake-stabilized regimes as distinct limiting modes of operation for flares. The research results from one regime may not be applicable to flares operating in other regimes. For example, the continuous decrease of efficiency with increasing cross-wind speed, which is well-established for the wake-stabilized production flares, may not apply to jetting refinery flares. Secondly, there is a minimum flare pipe size, around 7.5 cm (3 inches), for results to be scalable to industrial-scale flares. This means that some results in the literature are not representative of full-scale operating flares.

The International Flaring Consortium (IFC) was formed to review and address crucial gaps in the science of flares. The first objective of the IFC is to produce a method of predicting flare efficiency from operating variables: flare gas composition and flow rate; steam-assist rate; and wind speed. The method developed will rely upon original experimental work as well as published data. The second objective is to measure the emissions of: NO_x; the most important HRVOCs (ethylene, propylene, 1-3 butadiene, and the butenes) and BTEX (benzene, toluene, ethylbenzene, and the xylenes); and to attempt to predict emission factors for these species based on the same set of operating variables. The third objective is to identify optimal operating conditions and identify the operating envelope for flares.

Based upon the literature review, the following six areas of flare performance need to be addressed:

1. Experimental studies of the flare efficiency in the transition between jetting and wake-stabilized regimes.

2. Experimental studies of the effect of wind on steam-assisted flares.
3. Experimental studies on the limiting hydrogen concentration for steam-assisted flares, pilots, and wind blown flares.
4. Experimental studies of HRVOC and NO_x emissions, with and without steam-assist.
5. Correlation of flare efficiency with fuel properties and flare gas composition, particularly the inert gases nitrogen and carbon dioxide, and the impact of hydrogen.
6. Correlation of flare efficiency with steam-assist rate that considers flare gas composition, perhaps unifying steam with the approach used for correlating the effect of nitrogen and carbon dioxide dilution.

These are specific research areas that formed the general objectives of the IFC.

This report describes the experimental equipment and methods used in the program of the IFC. The experiments are conducted at the Flare Test Facility of CanmetENERGY at Bells Corners in Ottawa. This facility is a single-pass wind tunnel originally constructed for testing full-sized solution gas flares (10 cm and 15 cm) firing mixtures of natural gas and propane. Its capabilities have been expanded to fire different gases, and to provide steam-assist and pilots. The high-precision GC-based analysers for HRVOCs and BTEX are described in a separate report (Caravaggio and Caverly, 2008).

Note on terminology: We use the following definitions of performance measures.

- **Carbon Conversion Efficiency (CCE)**:= the conversion of fuel-bound carbon to carbon dioxide, expressed as a percentage of the mass of carbon as carbon dioxide in the stack gas relative to mass of fuel-bound carbon.
- **Carbon Conversion Inefficiency (CCI)**:= the failure to convert fuel-bound carbon to carbon dioxide, CCI = 100% - CCE.
- **Fuel Slip (FS)**:= percentage of mass of carbon as original fuel species in stack gas relative to the mass of fuel-bound carbon.

- **Destruction Efficiency (DE)**:= the destruction of a particular combustible species, expressed as percentage of 100% minus the mass of carbon of the combustible species in the stack gas relative to the mass of fuel-bound carbon of that combustible species. For a single hydrocarbon species, DE = 100% - FS.

2.0 THE AIR SUPPLY, COLD DUCT SECTION AND TEST SECTION

The flare test facility is shown schematically in Fig. 1. The combustion air is provided by a tubular acoustofoil fan with a rating of 1416 m^3/min at 15.2cm WC (50,000 cfm at 6".WC). Its inlet is equipped with a silencer and it is powered by a 56 kW (75 hp) electric motor with a variable frequency drive. The fan is located outside the building, sheltered from the weather by a tent. The cold duct section, 1.2 m wide and 1.8 m high (4 ft wide and 6 ft high) leads from the fan through the building wall to the upstream end of the test section. This section has a series of narrow gage wire mesh screens to flatten the velocity profile and dampen flow turbulence from the fan.

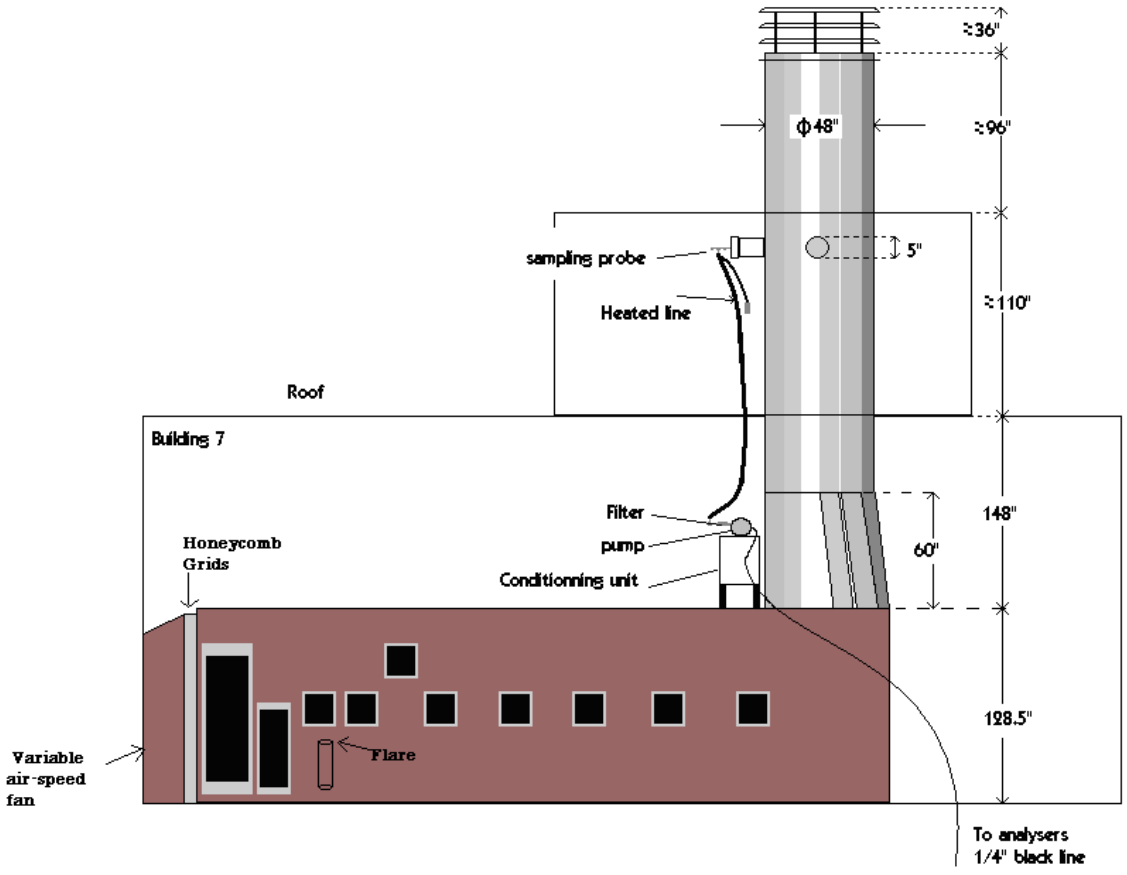

Figure 1 - Schematic of Flare Test Facility.

The airflow measuring station (AFMS) is a fixed array of 56 static and total pressure ports. The array covers the cross-section of the air duct. The average of the pressure measurements is fed to a pressure transmitter with readout in kg/h. Combustion airflow is corrected for barometric pressure, temperature and relative humidity. The temperature is determined by a thermocouple array in the measuring grid. The relative humidity is measured at a local weather station.

Inside dimensions of the test section are 3m high, 1.2m wide and 8.2 m long (10 ft high, 4 ft wide and 27 ft long). At the upstream end is a final flow straightener consisting of a metal honeycomb section 7.6 cm (3") thick. The cold duct from the fan expands to the full size of the flow straightener, but within the expansion an adjustable plate confines the airflow to whatever ceiling height prevails in the test section.

The test section itself has an adjustable ceiling. Channels to support the ceiling along each side of the test section are located at heights of 1.5, 1.8, 2.1 and 2.6 m (5, 6, 7 and 8.5 ft) from the floor. Four modules comprise the ceiling; each is 119cm (47") wide, 140cm (55") long and 7.6 cm (3") thick. The sidewalls, floor and rear end wall of the test section are double-walled, the inner walls being of Type 304 stainless steel, the outer walls of carbon steel. The hollow walls and floor accommodate cooling air, and the ceiling modules are likewise air-cooled, by means of flexible ducting. The floor has four parallel longitudinal cooling passages, with air entering at the rear and discharging sideways at the front. Each sidewall has four cooling sections, each having four passes, with air entering from the top and discharging from the bottom. The ceiling modules also have four passes of cooling air. A blower rated at 340 m^3/min at 25.4 cm WC (12,000 cfm at 10 in. WC), is located on the roof of the building, providing the cooling air. Cooling the walls reduces back radiation to the flame, which could artificially stabilize combustion.

An access door into the test section is located next to the flow straightener. In it is a window almost the full size of the door. There are nine other windows of varying size along the accessible side of the test section, plus two windows in the rear wall, under the transition to the stack, plus four windows in the roof above the flare pipe. Thus, the flare pipe and flare flame can be viewed and photographed from several angles. Each window

has two layers: high-temperature tempered glass on the inside and scratch-resistant Lexan on the outside.

There are eight sampling ports in the sidewall of the test section; three are at 1.2 m another three are at 3 m and two more are at 4.3 m (4 ft, 10 ft, and 14 ft respectively) all located downstream from the flare pipe. There are also two ports in the rear wall and three ports at two levels in the stack. The ports are all 5.1 cm or 10.2 cm (2" or 4") pipe.

A stack, fabricated from Type 304 stainless steel, 1.2 m (4 ft) in diameter and 7.3 m (24 ft) tall, is connected to the downstream end of the test section by a transition section 1.5 m (5 ft) long, also made of Type 304 stainless steel. At the stack outlet is a perforated plate with 51 % opening, above that are a weather cap and two tiers of rain gussets. All these combine to reduce chimney effect and wind effects on draft, and thus improve uniformity of flow in the stack. The cap and rain gussets also serve to keep precipitation out of the stack. An access slot has been provided between the transition section and the base of the stack, by means of which screens or baffles can be inserted, if required, to accomplish more uniform flow in the stack. The primary sampling point is in the stack, 3.7 m (12 ft) above the end of the transition section.

2.1 The Flare Pipe and Fuel System

The flare pipe was located on the centerline of the test section, 2.4 m (8 ft) downstream from the flow straightener. The unassisted flare tips are called "basic pipe". Basic pipe flare tips were made from nominal 2.5 cm to 15.2 cm (1" to 6") diameter Schedule 40 carbon steel pipe. These were fitted to a 5.1 cm (2") threaded coupling in the floor. This coupling comprises the terminal of the fuel supply system.

The main test fuels are natural gas, propane, ethylene, and propylene. Two lines are used for the fuel gases. One line is dedicated to natural gas. The other line is used for one of propane, propylene, or ethylene. There is a third line for carbon dioxide or nitrogen. Propane is supplied in liquid form from a 3785 L (1000 gallon) storage tank through a train which includes a vaporiser, pressure control valve, flow control valve, and a mass flow meter with safety shutoff features. Natural gas comes from the utility mains and flows through a similar train. The compositions of the local natural gas and propane are

given in Table A-1. The propylene and ethylene were supplied from 8 gas cylinders coupled with a manifold equipped with a two-stage pressure regulator. The ethylene manifold and regulator were wrapped with electrical heating tap to protect the piping from the cooling due to the expansion of the ethylene.

The two trains feed into a common 3.8 cm (1.5") pipe, from which a 1.9 cm (0.75") line branches off through a further flow control train to supply the flare igniter. The igniter is fully retractable. The main 3.8 cm (1.5") flare gas line continues through another train measuring and controlling flow and runs 4 m (13 ft) to the coupling where the flare pipe is connected. The flare gas temperature is measured with a K-type thermocouple. Each line has a thermal mass flow meter calibrated for the specific gas. Table A 2 has the correction factors (K values) supplied by the vendor to be applied the flow meter reading when flowing propane, ethylene or propylene.

Carbon dioxide or nitrogen joins the main flare gas line just downstream from its final flow control train. There is a mass flow meter and flow control valve for the diluent gas. The flow meter specifications are given in Table A 3.

2.2 Steam-assist Flare Tip

The steam-assist flare tip comprises the flare pipe, the steam manifold and nozzles, and the pilot burners.

The flare tip used with steam assist is Nominal 7.6 cm (3"), Schedule 80 stainless steel, with a Flare Retention Ring (FRR). The FRR is composed of a number of s-shaped tabs welded inside the pipe. It is a common appurtenance in industrial flares. The open area of the pipe with the FRR is equivalent to a 5.1 cm (2") pipe (21.7 cm^2 or 3.36 in^2). In this case, the tip with the FRR will consume less gas for a given exit velocity. This configuration is more representative of the actual operating equipment than a simple pipe. This tip was also run unassisted, without the steam manifold in place. A Nominal 15.2 cm (6"), Schedule 80, stainless steel pipe with a FRR was also used for some unassisted tests. It is a direct two times scale-up of the 7.6 cm (3") tip and has open area equivalent to a 10.2 cm (4") pipe (81.1 cm^2 or 12.73 in^2).

The assist steam is provided through 12 nozzles, mounted on risers attached to a single manifold. The risers are in groups of four equally spaced around the circumference. The three gaps allow the placement of the pilot burners at the top of the flare pipe. The nozzles inject the steam at the top of the flare pipe. There are two nozzle openings; one large, one small.

2.3 Steam Supply System

The steam is generated by an electric boiler, rated to 50 kg/h (110 lb/h) at 100 psig saturated steam. It is delivered in 1/2" pipe. The flow is controlled by a flow control valve and measured with a mass flow meter. It passes through a superheater (Chromalox MTX-250A, 5 kW (6.7 hp)) to give a temperature boost to minimize condensation in the steam manifold and risers, particularly during the cold winter months. Condensation would produce droplets that intermittently plug the steam nozzles and degrade flare performance. There are three steam traps, with one placed as the steam line enters the wind tunnel. The steam pipe enters the wind tunnel through the wall near the floor, 0.3 m (1 ft) downwind of the flare pipe. It is insulated inside the wind tunnel, from the wall to the manifold.

2.4 Pilot Burners

The pilot burners have three heads off a ring manifold as shown in Figure 2.

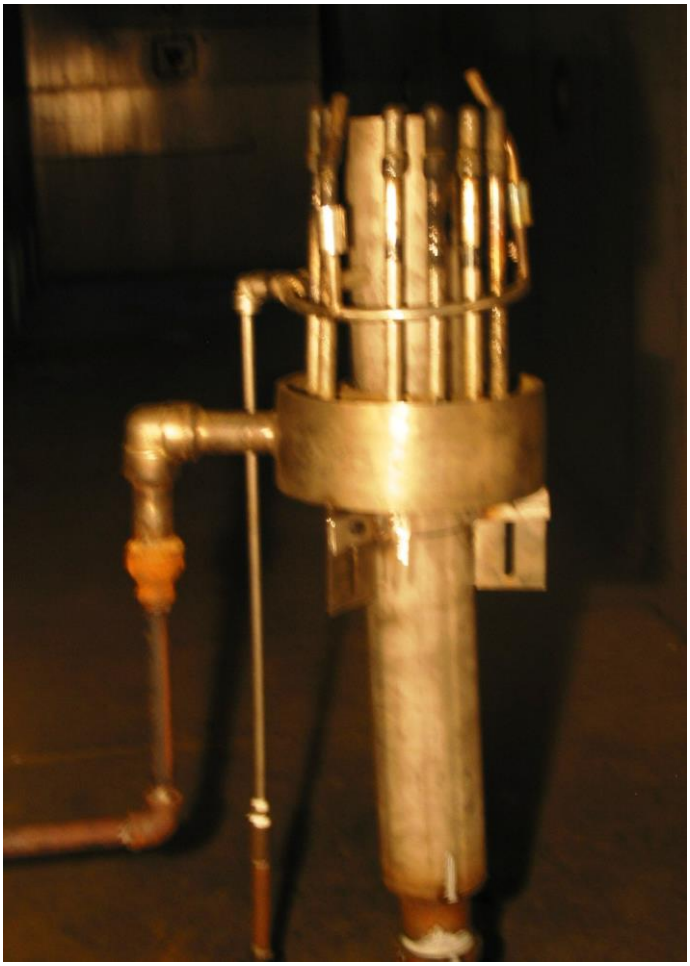

Figure 2 - Photo of steam ring with pilot burners

They are evenly spaced around the perimeter of the flare pipe, one burner directly upwind of the flare pipe, the remaining two downstream as seen in Figure 3.

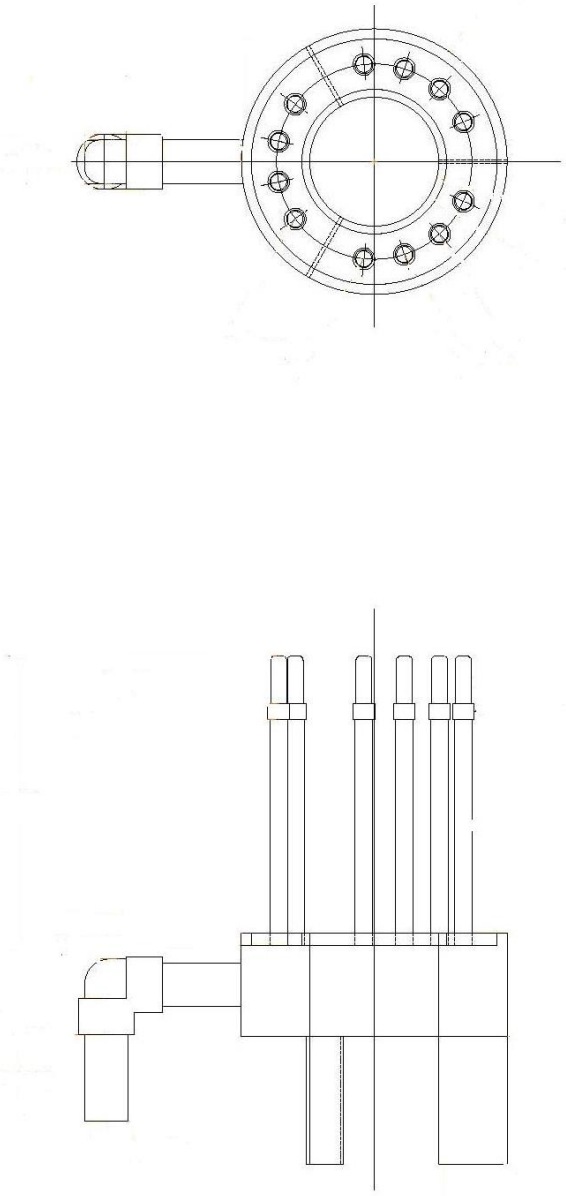

Figure 3- Schematics of steam ring and pilot burners

The pilot burner heads are modified commercial propane torch heads. The total heat input from the pilot burners is 5.3 MJ/h (5000 Btu/h). The fuel is entrained via an eductor operating with compressed air and the air orifice is designed to provide air at approximately a stoichiometric combustion ratio. A flow control valve controls the fuel flow to the eductor. There is a flow meter for the fuel to the pilot burners, and this flow is continuously recorded by computer. The burners receive a controlled stoichiometric air-fuel mixture. The pilot burner and steam ring in operation can be in seen in Figure 4.

Figure 4 – Steam ring and pilots in operation with ethylene fuel (10kg/h ethylene and 20 kg/h steam).

2.5 Gas Sampling

The gas sampling probe consists of a sintered stainless steel tube, 2.5 cm (1") diameter and 18 in. long, that has been installed in the stack, three diameters (3.7 m or 12 ft) from the last disturbance, i.e., from the end of the transition section. By means of a heated-head pump, this probe extracts a sample from a 45.7 cm (18").-long strip across the centreline of the stack and passes it through a heat-traced sample line (Teflon™ 0.64 cm diameter (0.25 inch), 15.2 m (50 ft.) long) to a conditioning system that removes moisture

and particulates. The specifications for the conditioning system can be found in section A-9 and Figure 5 is a photo of the system.

Figure 5 – Photo of new sample conditioning system.

The clean, dry sample is then passed to the analysers which are described in section 2.7.

The sample probe filters particulate matter from the gas stream. It also provides an average sample from the stack, reducing the effect of segregation. A segregation study of the stack was performed. Figure 6 shows the vertical velocity profile measured with a pitot-probe. Figures 7, 8 and 9 show the concentration profiles for CO_2, CO and CH_4.

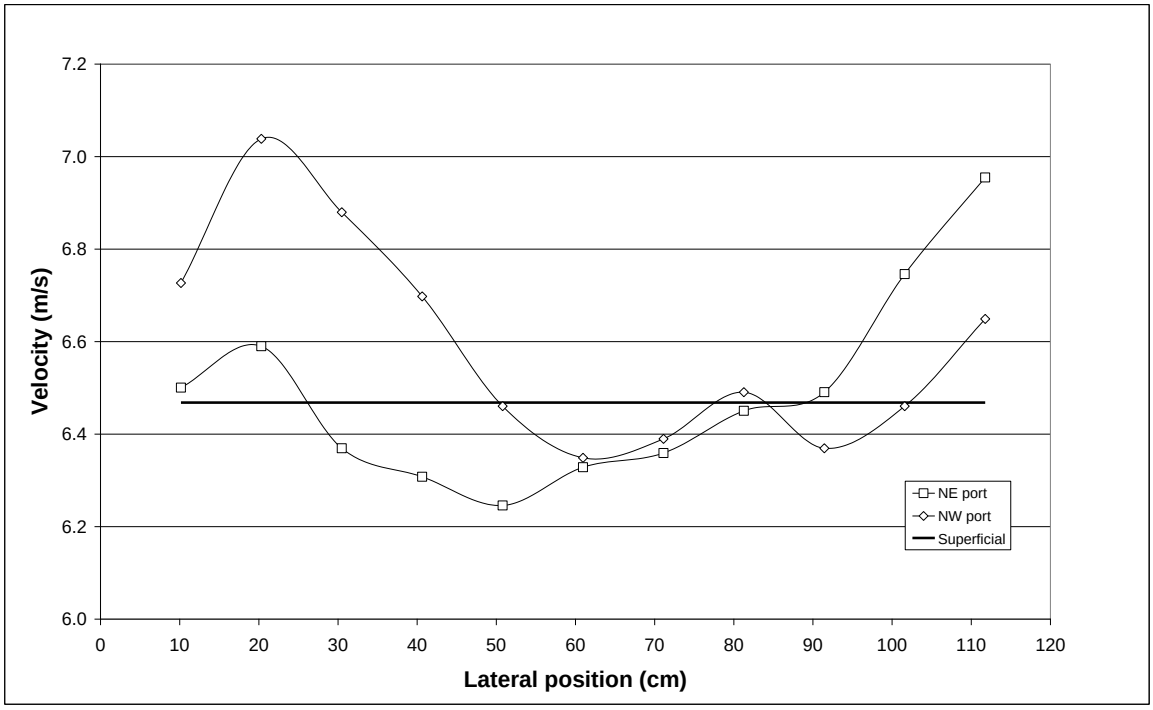

Figure 6 - Velocity profiles in stack at the sampling location.

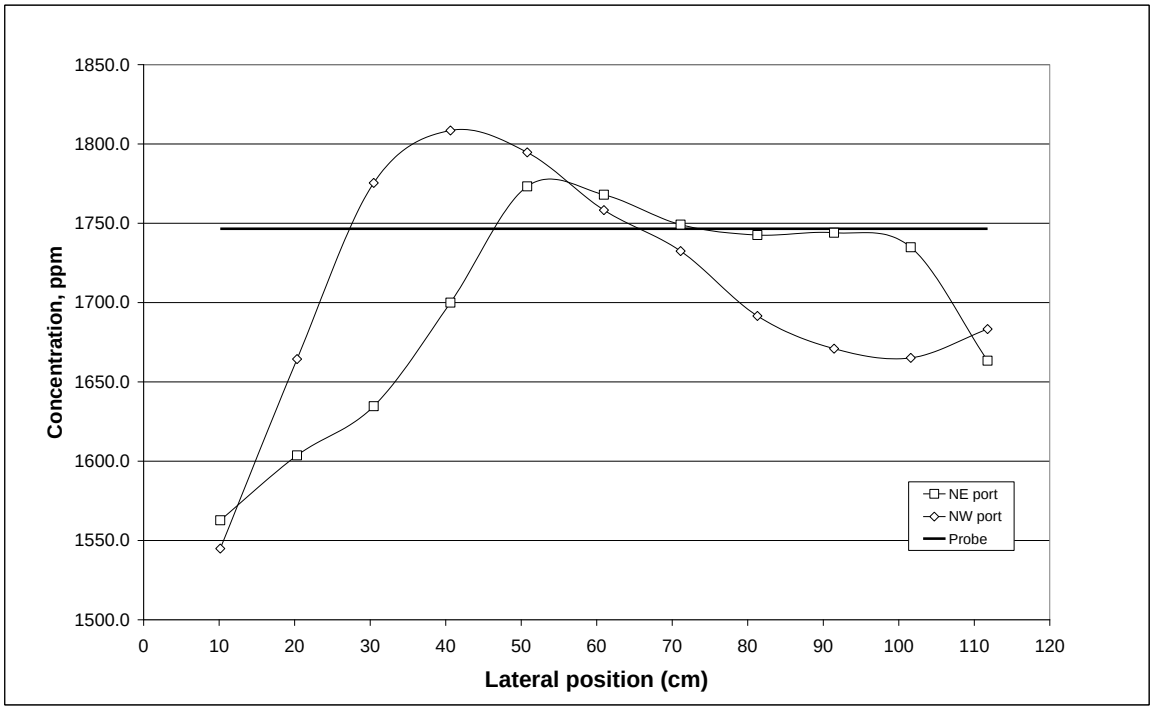

Figure 7 - Concentration profiles for CO_2 in stack, with the probe value indicated by the line.

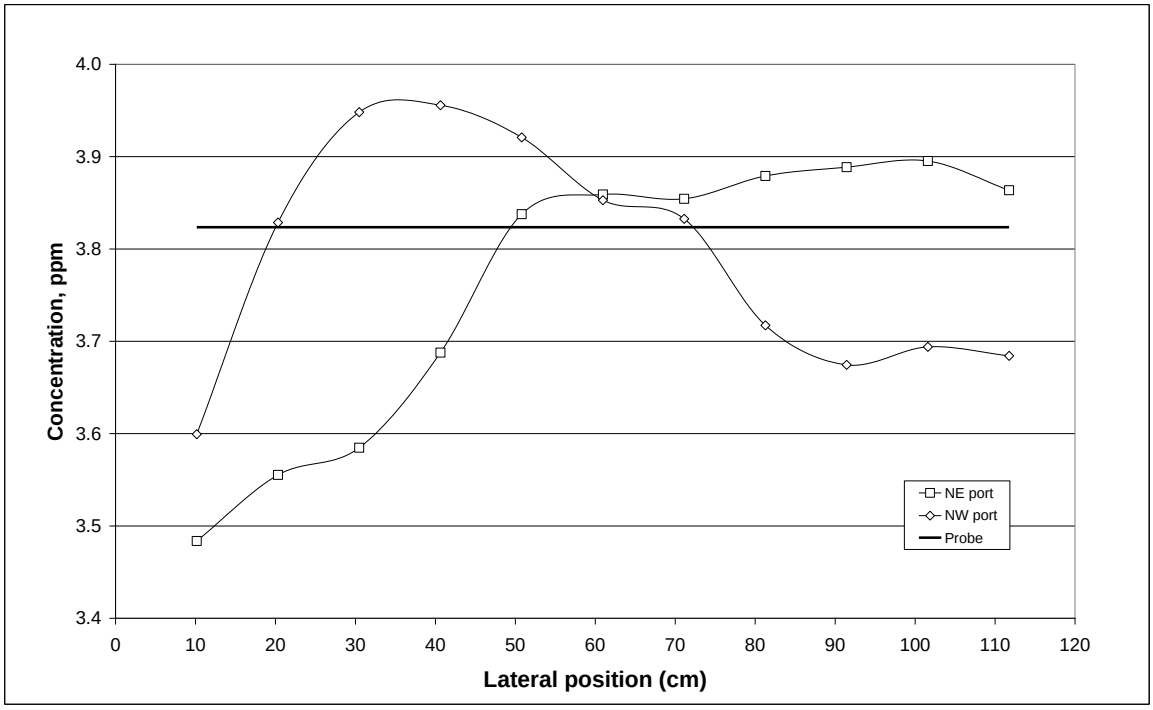

Figure 8 - Concentration profiles for CO in stack, with the probe value indicated by the line.

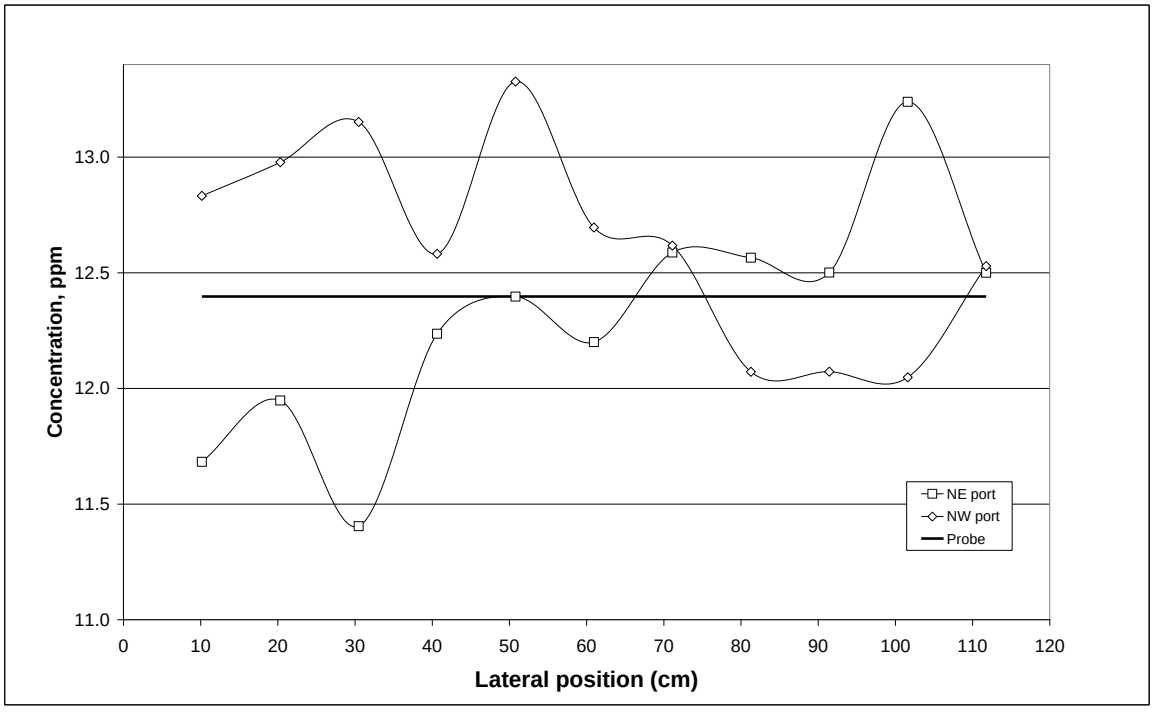

Figure 9 - Concentration profiles for CH_4 in the stack, with the probe value indicated by the line.

The traverses were performed through the two sampling ports in the stack, at 10.2 cm (4 inch) intervals. The gas was sampled through a stainless-steel goose-neck probe. The conditions for the test were: 10 kg/h (22 lb/h) natural gas to the flare and 453 m^3/min (16000 cfm) air flow. The air flow translates into a superficial velocity of 6.5 m/s (21 ft/s) in the stack. The results of the study are summarized in Table 1.

Table 1 - Summary of results of segregation study showing averaging properties of the sample probe.

	Velocity	Velocity	CO_2	CO	CH_4
	m/s	ft/s	ppm	ppm	ppm
Average	6.61	21.69	1663	3.73	12.43
Probe/Superficial	6.47	21.23	1747	3.82	12.40
Difference	-0.14	-0.46	83.22	0.10	-0.04
% Deviation	2.19	2.19	4.76	2.52	-0.28

The averages are calculated using annular slices shown in Figure 10. Each slice is assumed to have the flow of the value of point sample it contains. The average velocity using the point samples is thus the sum of the point velocity multiplied by the slice area divided by the total area. The average velocity compares well with the superficial velocity calculated from the volumetric flow of air. The average concentrations are weighted using the volumetric flow at each sample point. The averages are compared to the value measured by the probe, using the arithmetic average of the central traverse points on the NE port (Fig 10) that cover the probe.

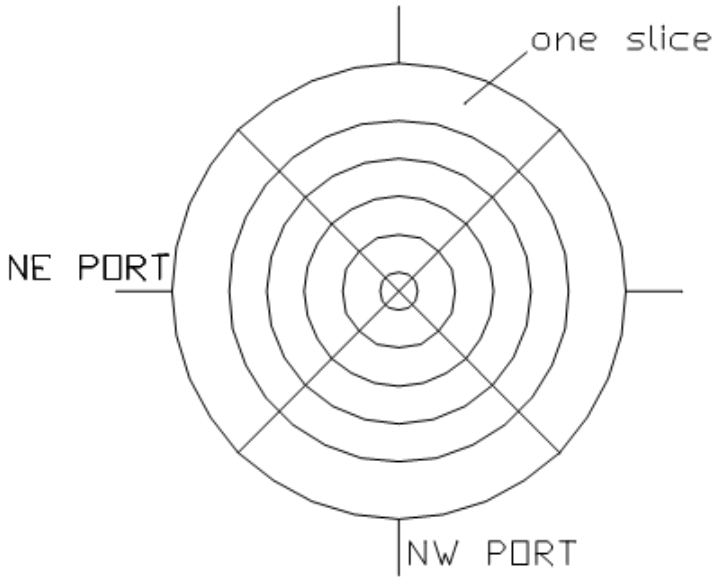

Figure 10 - Division of stack cross-section for averaging point probe.

The carbon dioxide concentration showed the largest difference between the traverse and the probe, but the deviation was still less than 5%.

2.6 Particulate Sampling

A particulate sample is drawn isokinetically from the same sampling location from where the gas sample is drawn. This means gas sampling is interrupted while a particulate sample is being taken. The probe is a gooseneck suction probe, the tip of which can be changed, depending on the gas suction velocity required at the tip. The probe is operated at a suction rate that provides an isokinetic sample. The velocity is determined by a pitot-tube measurement. The suction is controlled by a constant volume vacuum pump. The sample is drawn through a glass-fibre filter, 47 mm (1.9") in diameter, supported on a stainless steel mesh. The predetermined volume of gas is drawn through the filter which has a pore size of 1 μm. The filter is weighed before and after sampling. The weigh scale has 0.0001 g (0.000004 oz) precision. The sampling rate matches the velocity of the gas in the stack. The sampling time is calculated for given air flow and fuel supply rate such that a 0.1% conversion of fuel-carbon to particulate matter would produce 1 mg (0.00004 oz) mass capture on the filter paper. This gives ten times the minimum reading on the scale with this low conversion. If more soot is produced, the sample size will be

correspondingly larger. Samples were weighed immediately after collection, and not dried.

2.7 Instrumentation

The test section is fitted with numerous thermocouples to measure temperature of the inner skin of the enclosure, and temperature of the cooling air. These values are continuously recorded by an automated data logging system. Temperature and flow from the combustion air fan are also logged continuously. Likewise monitored are temperature, pressure, relative humidity and flow rate of the fuel gas and dilution gases. The facility is equipped with a Burner Management System (BMS) to control the air and fuel flows, and maintains safe operations of the system through the flame scanner and automatic shutdown.

The data acquisition system is a National Instruments SCXI 1100, with LabView software running on a PC. The calibration data and run data are logged to a file at 8 second intervals.

Continuous gas analysis is provided by infrared analysers for CO_2, CO, and SO_2, a paramagnetic analyzer for O_2, and a chemiluminescence analyzer for NO_x. There are two analyzers each for CO_2 and CO, with one set having very low ranges (0 to 500 ppm for CO_2, 0 to 50 ppm for CO). Unburned hydrocarbons are determined by FID gas chromatography. The full descriptions of the analysers are given in the appendix sections A-4 to A-7. All the foregoing analyser outputs are recorded by the data acquisition system. The two GC-based analysers use column separation for HRVOCs and BTEX compounds are described in a separate report (Caravaggio and Caverly, 2008). The specifications of the GCs are listed in A-8.

3.0 TESTING OF SAMPLING SYSTEM

3.1 Bias Testing of Sampling System

Bias testing involves putting standard gas through the sampling system to verify that the analysers achieve the same readings. The gas conditioning system was changed during the testing. The first system, a chiller, was failing and caused problems closing the carbon balance. It was replaced with the Nafion membrane based system. The results of the bias testing of the two systems are shown in Table 2.

Table 2 - Bias test results with old and new conditioning unit in line.

	CO_2	CO
Bottle Concentration, ppm	2540	39.6
Old Conditioning Unit, Reading, ppm	2042	30.7
Deviation, %	-19.6	-22.4
New Conditioning Unit, ppm	2579	40.2
Deviation, %	1.5	1.4

There is a loss of 20% of the carbon dioxide and carbon monoxide when using the old conditioning unit. This is sufficient to account for the problem with the carbon balance. It indicates also that tests with the old gas conditioning unit should have significant deficit in the carbon balance.

The slight elevation in the reading for the new unit can be attributed to the slightly elevated pressure in the sample line from the compressed gas cylinder. Exact matching of the pressures in the line was difficult to obtain.

The new sample conditioning unit was also tested with the hydrocarbon span gas. The methane/nonmethane hydrocarbon analyser is self-calibrating. It accepts a deviation of 5% on the span before it re-calibrates. Therefore, these readings show that there is accurate measurement with respect to hydrocarbons with the new conditioning system.

Table 3 - Results of bias testing of the new sample conditioning system with methane and propane span gas.

	CH_4	C_3H_8
Bottle Concentration, ppm	20.5	9.9
New Conditioning Unit, ppm	20.3	9.6
Deviation, %	-0.8	-3.4

4.0 STANDARD PROCEDURE FOR FLARE START-UP

Each analyser is given a zero (N_2) and span (full-scale) twice except for the hydrocarbon analyser which has its own calibration and will recalibrate itself until the % error is less than 2%. The zero and span are left running through the analysers until they settle out and are then corrected to either the span gas or zeroed if necessary. The analysers were also put through a zero and span at the end of the day, but no drift was detected. So this practice was stopped. Typically it takes 30-45 min to zero and span each analyser twice. The analysers take ambient samples for at least 30 min before warm up is started.

The morning start-up before a run consists of opening the manual air valve for the actuators/controls and any fuel valves that are to be used. If steam is to be used the boiler is turned on and the warm-up line opened to get as much condensate out of the system as possible before runs start. The igniter is pushed into the tunnel for light up after an ambient sample is taken.

To light the flare, the fan is started and left at a flow rate of 20,000 kg/h (44,080 lb/h) in manual and local position on the control of the Burner Management System (BMS) while a sample of the ambient air is taken. After the ambient sample is taken the fan speed is increased to 24,000 kg/h (52,896 lb/h) and placed in automatic and remote on the BMS control. The local and remote positions are part of the BMS and are used to prevent accidental lighting of the flare. The flare can only be lit when the fan control is in the remote position and then the fan control is moved back to the local position so that flow rates can be changed.

NG is always used as the warm-up fuel and is always set at a level of 10 kg/h (22 lb/h) for every warm up. The NG valve setting must be placed at 15% open for lighting, which is part of the internal program of BMS. This setting prevents ignition with a high firing rate which could damage the facility or cause it to fill with gas. If the pilots are being used the valve is opened to 62% because the existing pilots work best at this setting. The start button is depressed and the BMS increases fan speed to its maximum speed as a pre-purge. The air is then slowly decreased until it returns to 24,000 kg/h (52,896 lb/h).

At this point the igniter will start and ignition will be verified by the flame scanner and then the BMS will open the main gas valve. Once the flare tip is lit, the fan is restored to the local setting but left in automatic and increased to 35,000 kg/h (77,140 lb/h) (warm up speed) and the fuel valve is opened to 22-23% which gives the 10 kg/h (22 lb/h) required for warm up. If steam is to be used during testing the warm up line is closed and the steam is allowed to enter the line which feeds the steam ring and tips. Warm-up occurs for at least 45 min before the first test is started.

5.0 CALCULATIONS

5.1 Calculation of Performance Measures

The following quantities are measured:

- Air flow into the wind tunnel.
- Air composition (dry basis) into the wind tunnel.
- Fuel flow and composition into the flare tip.
- Assist flow to the flare tip.
- Fuel and air flow into the pilots.
- Composition of the stack gas (dry basis).

There are three main measures of flare performance calculated from these data. The first is the Carbon Conversion Efficiency (CCE). This is sometimes called the combustion efficiency, and is calculated in the following steps:

- Calculate the mass flow of C as CO_2 in the air.
- Calculate the total mass flow of C in the fuel gas and in the pilot burners.
- Calculate the mass flow of nitrogen in the air, assuming nitrogen is the balance from the air composition (nitrogen-tie).
- Calculate the total mass flow of dry gas in the stack using the nitrogen-tie and the composition of the stack gas.
- Calculate the mass flow of C in carbon containing species CO_2, CO, CH_4, and NMHC (as C_3H_8).
- Calculate the net mass flow of C as CO_2 in the stack, which is the total mass flow of C as CO_2 less the mass flow of C as CO_2 in the air.
- Calculate the net mass flow of C in all other carbon-containing species in the stack.

The CCE is given by

$$CCE = 100\% \times \frac{\dot{m}_{CasCO2net}}{\sum \dot{m}_{Cnet}} \tag{5-1}$$

which is the measure of the conversion of fuel carbon to carbon dioxide. The summation sign indicates summation over all species.

The Carbon Balance (CB) is the mass balance of all carbon entering and leaving the FTF and is given by the ratio of the mass flow of carbon over all species in the stack to the mass flow of carbon in all species in the air and fuel.

$$CB = 100\% \times \frac{\sum \dot{m}_{Cstack}}{\sum \dot{m}_{Cair} + \sum \dot{m}_{Cfuel}} \tag{5-2}$$

The Specific Destruction Efficiency of a single hydrocarbon fuel gas species, not found in the air, is given as

$$SDE = 100\% \times \left(1 - \frac{\dot{m}_{CasXinstack}}{\sum \dot{m}_{Cnet}} \right) \tag{5-3}$$

5.2 Analytical test cases for flaring calculations

It is a useful exercise to take a simplified situation for which the results can be calculated and feed these results into the spreadsheet as a validation and a tool for estimating the sensitivity of the calculations to perturbations of the inputs. Here we describe the solution of the simple test cases used for the validation and sensitivity analysis.

The given data is:

- Air flow rate, $\dot{m}_a$.
- Air temperature, pressure, and relative humidity, $T, P, \%RH$.
- Composition of dry air, $\{x_i\}_{allcompounds}$.
- Fuel flow rate, pure compound, $\dot{m}_f$.
- Destruction efficiency, $\%DE$.
- Carbon conversion efficiency, $\%CCE$.

- The reaction is $C_nH_m + xO_2 \rightarrow aCO_2 + bCO + cH_2O$

From these data, the dry gas composition can be calculated. This will give the necessary data to check the flaring calculations.

The following conditions were considered for testing the flaring calculations:

1. Fuels are methane, ethylene, propylene.
2. Air flow is 35,000 kg/h (77,140 lb/h) and fuel flow 30 kg/h (66 lb/h); Air flow is 95,000 kg/h (209,380 lb/h) and fuel flow is 10 kg/h (22 lb/h). These give the extreme combinations of stack concentrations.
3. Relative humidity of 0% and 100%. These check the humidity calculations.
4. Destruction efficiency, carbon conversion efficiency both 100%; destruction efficiency 95%, carbon conversion efficiency 90%. These test the efficiency calculations.

These conditions give a total of 24 test cases, 8 for each fuel.

The calculations proceed as follows:

1. Convert fuel flow from mass to moles. $\dot{C}_f = \frac{\dot{m}_f}{MW_f}$ (5-4)

2. Calculate dry air molecular weight. $MW_{dry} = \sum_i x_i MW_i$ (5-5)

3. Calculate water fraction in air.

4. Calculate wet air molecular weight. $MW_{wet} = x_{H_2O} MW_{H_2O} + (1 - x_{H_2O}) MW_{dry}$ (5-6)

5. Calculate molar flow of wet air. $\dot{C}_{wet} = \frac{\dot{m}_a}{MW_{wet}}$ (5-7)

6. Calculate molar flow of each species in air. $\dot{C}_{weti} = (1 - x_{H_2O}) x_i \dot{C}_{wet}$,

$$\dot{C}_{H_2O} = x_{H_2O} \dot{C}_{wet} \quad (5\text{-}8)$$

7. Calculate chemical reaction coefficients, using destruction efficiency and combustion efficiency.

$$\alpha = \%DE/100; \lambda = \frac{100 - \%CCE}{\%CCE}; a = \frac{n}{1+\lambda}; b = \lambda a; c = \frac{m}{2}; x = a + \frac{(b+c)}{2} \quad (5\text{-}9)$$

8. Apply chemical reaction to molar flows – 1 mole of fuel uses x moles of O_2, produces a moles of CO_2, b moles of CO, and c moles of H_2O.

$$\dot{C}_p = \dot{C}_{wet} + (a + b + c - x)(1 - \alpha)\dot{C}_f + \alpha \dot{C}_f; \quad \dot{C}_{pO2} = \dot{C}_{wetO2} - x(1 - \alpha)\dot{C}_f;$$

$$\dot{C}_{pCO2} = \dot{C}_{wetCO2} + a(1 - \alpha)\dot{C}_f; \dot{C}_{pCO} = \dot{C}_{wetCO} + b(1 - \alpha)\dot{C}_f;$$

$$\dot{C}_{pH2O} = \dot{C}_{wetH2O} + c(1 - \alpha)\dot{C}_f; \quad \dot{C}_{pf} = \alpha \dot{C}_f \quad (5\text{-}10)$$

9. Calculate dry gas composition from molar flows. $x_{pi} = \dfrac{\dot{C}_{pi}}{\dot{C}_p - \dot{C}_{H_2O}}$ (5-11)

5.3 Sensitivity of Calculations

The calculations of the performance indicators – carbon balance, conversion efficiency, and destruction efficiency - include many measured variables and many steps. The errors in the measured variables propagate through the calculations to the performance indicators. The effect of these measurement errors on the performance indicators is not obvious. Of particular interest is whether the error is amplified by the calculations.

The sensitivity of the calculations to these errors is most easily estimated using the calculated test cases. A specified change is applied to an input variable in the test case. This produces a change in the calculated performance indicators. The magnitude of the change indicates the sensitivity of the calculations to errors in the reading for that input variable.

The sensitivity of the calculations was estimated for the following input variables:

- Air flow
- Fuel flow
- Inlet carbon dioxide
- Stack carbon dioxide
- Stack methane
- Relative humidity

Two test cases were used, both with natural gas for fuel. The two cases represent the extremes of dilution: low dilution with low air flow and high fuel flow; high dilution with high air flow and low fuel flow. The air temperature was measured to be 25ºC (77ºF) and relative humidity was 50%.

The errors were taken as the quoted accuracy of the flow meters and analysers in use at the Flare Test Facility. The flow meters have a relative accuracy of 1.5% and 1% of reading for the air and fuel mass flows. The analysers have an absolute accuracy of 1% of full scale. The absolute error for relative humidity was selected to be 2%.

Table 4 shows the sensitivities for the low dilution case, with the low air flow of 35,000 kg/h (77,140 lb/h) and high fuel (natural gas) flow of 30 kg/h (66 lb/h). This case gives the highest concentration of combustion products in the stack gas. The error of 1.5% in the air flow gives a change of 1.2% in the carbon balance. The calculation of carbon balance is only slightly sensitive to the errors in fuel flow rate and relative humidity. The conversion efficiency and destruction efficiency are insensitive to these three variables.

The errors in the stack gas compositions do have an effect on the efficiency calculations, though the effect is small in all cases. A change in stack carbon dioxide measurement of 50 ppm produces a change of 2.5% in the carbon balance. The stack carbon dioxide measurement is the most sensitive variable. Or correctly stated, the accuracy of the carbon dioxide analyser is the most significant part of the system.

All the errors can be combined to produce a maximum change in the performance indicators. For this low dilution case, the maximum change is a little over 5% for the

carbon balance, but less than 0.25% for the efficiencies. The changes are roughly symmetrical in this case, equal in magnitude for both positive and negative changes.

Table 4 - Sensitivity of main performance indicators to changes in input variables. Low dilution case with low wind and high fuel flow.

Sensitivity Table - Low Wind of 35,000 kg/h (77,140 lb/h) and High Fuel of 30 kg/h (66 lb/h)							
Input Variable	Change	Dependent Variable					
		Carbon Balance		Conversion		Destruction Efficiency	
		%	diff	%	diff	%	diff
Base Case	0	101.73		90		95	
Air Flow	+1.5%	102.95	1.22	90	0	95	0
	-1.5%	100.5	-1.23	90	0	95	0
Fuel Flow	+1%	101.92	0.19	90	0	95	0
	-1%	102.54	0.81	90	0	95	0
Inlet CO_2	+ 5 ppm	101.47	-0.26	89.97	-0.03	94.98	-0.02
	- 5 ppm	101.98	0.25	90.03	0.03	95.01	0.01
Stack CO_2	+ 50 ppm	104.24	2.51	90.29	0.29	95.15	0.15
	- 50 ppm	99.22	-2.51	89.68	-0.32	94.84	-0.16
Stack CH_4	+ 1 ppm	101.78	0.05	89.94	-0.06	94.94	-0.06
	- 1 ppm	101.68	-0.05	90.05	0.05	95.06	0.06
Relative Humidity	+2	101.47	-0.26	90	0	95	0
	-2	101.98	0.25	90	0	95	0
Maximum Change	+	106.98	5.25	90.23	0.23	95.11	0.11
	-	96.68	-5.05	89.75	-0.25	94.88	-0.12

Table 5 shows the high dilution case, with high air flow of 95,000 kg/h (209, 380 lb/h) and low fuel rate of 10 kg/h (22 lb/h). This case gives the lowest concentrations of combustion products in the stack. The rest of the conditions of the test case were unchanged.

The inlet flow variable, air flow rate, fuel flow rate, and relative humidity have little effect on the carbon balance and no effect on the conversion efficiency and destruction efficiency.

The errors in the inlet carbon dioxide concentration and the stack methane concentration have relatively little effect on any of the three performance indicators. However, all three performance indicators are sensitive to the stack carbon dioxide measurement. The carbon balance is particularly sensitive, producing a change of 8.5%. Note that the change in the conversion efficiency and destruction efficiency is not symmetric. The positive change from over-estimating the carbon dioxide is smaller than the negative change from under-estimating. This means that when the carbon balance is low due to error in the carbon dioxide measurement, the efficiencies will be significantly lower as well.

The maximum error, due to the combined errors, is around 10% in the carbon balance, around 3% for the conversion efficiency and around 1.25% for the destruction efficiency.

This sensitivity analysis indicated that the carbon balance can be expected to vary by up to 10% due simply to the combined effect of small errors. We could conclude that runs with carbon balance in the range from 90% to 110% have good carbon balance and the results are reliable. The errors in the conversion efficiency and destruction efficiency are smaller and in the same direction as the carbon balance. That is, when there is a low carbon balance, the efficiencies are underestimated.

Table 5 - Sensitivity of main performance indicators to changes in input variables. High dilution case with high wind and low fuel flow.

Sensitivity Table - High Wind of 95,000 kg/h (209, 380 lb/h) and Low Fuel of 10 kg/h (22 lb/h)							
Input Variable	Change	Dependent Variables					
		Carbon		Conversion		Destruction	
		%	diff	%	diff	%	diff
Base Case		100.72		90		95	
Air Flow	+1.5%	101.22	0.5	90	0	95	0
	-1.5%	100.22	-0.5	90	0	95	0
Fuel Flow	+1%	100.38	-0.34	90	0	95	0
	-1%	101.6	0.88	90	0	95	0
Inlet CO_2	+ 5 ppm	99.89	-0.83	89.74	-0.26	94.87	-0.13
	- 5 ppm	101.59	0.87	90.24	0.24	95.12	0.12
Stack CO_2	+50 ppm	109.24	8.52	91.99	1.99	95.99	0.99
	- 50 ppm	92.2	-8.52	86.68	-3.32	93.34	-1.66
Stack CH_4	+ 1 ppm	100.89	0.17	89.55	-0.45	94.53	-0.47
	- 1 ppm	100.55	-0.17	90.44	0.44	95.47	0.47
Relative Humidity	+2	100.61	-0.11	90	0	95	0
	-2	100.83	0.11	90	0	95	0
Maximum Change	+	110.65	9.93	91.78	1.78	95.7	0.7
	-	91.01	-9.71	86.82	-3.18	93.76	-1.24

5.4 Estimating Uncertainty

There are several methods for estimating the uncertainty of a number calculated from experimental data. Here we use the recommendation of Kline and McClintock [1953]. This method was also used in Bourguinon et al. [1999] to estimate the uncertainty of the combustion inefficiency at two different conditions.

We are interested in the uncertainty of the two performance measures: carbon conversion efficiency (CCE) and destruction efficiency (DE). The performance measures are calculated from our data measurements. We can write the relationship as

$$CCE = f(X_i) \tag{5-12}$$

for example. We have the uncertainty ε_i for each measured value X_i. The uncertainty of the calculated *CCE* is estimated by

$$\varepsilon_{CCE} = \left[\sum_i \left(\frac{\partial f}{\partial X_i} \varepsilon_i \right)^2 \right]^{1/2} \tag{5-13}$$

We now derive, through some minor simplifications, an explicit form of the uncertainty for *CCE* and *DE* described in the previous section.

We start with a single hydrocarbon species in the flare gas with no carbon dioxide. This is only for simplicity of notation. We repeat the calculation with carbon dioxide included in the flare gas in Appendix B-3. We will also neglect the flux of particulate carbon. The expression for the *CCE* is

$$CCE = \frac{\Delta \dot{m}^c_{CO_2}}{\Delta \dot{m}^c_{CO_2} + \Delta \dot{m}^c_{CO} + \Delta \dot{m}^c_{HC}} \tag{5-14}$$

$$DE = 1 - \frac{\Delta \dot{m}^c_{HC}}{\Delta \dot{m}^c_{CO_2} + \Delta \dot{m}^c_{CO} + \Delta \dot{m}^c_{HC}} \tag{5-15}$$

The total mass efflux from the system is the sum of the mass flows for inlet air and flare gas. The specific carbon fluxes are

$$\dot{m}^c_{i,in} = \dot{m}_a x^c_{i,in} \tag{5-16}$$

$$\dot{m}^c_{i,out} = (\dot{m}_a + \dot{m}_f)x^c_{i,out}$$

and the change is

$$\Delta\dot{m}^c_i = \dot{m}_a\left(x^c_{i,out} - x^c_{i,in}\right) + \dot{m}_f x^c_{i,out} \tag{5-17}$$

We can neglect $\dot{m}_f$ when

$$\frac{x^c_{i,out} - x^c_{i,in}}{x^c_{i,out}} >> \frac{\dot{m}_f}{\dot{m}_a} \tag{5-18}$$

For our situation, the mass flow of flare gas is in the range of 10 to 30 kg/h (22 to 66 lb/h), while that of air is from 35,000 to 95,000 kg/h (77,140 to 209,380 lb/h). The ratio is smaller than 0.001. The condition above shows that the mass flow of fuel can be neglected when the relative change of mass fraction is greater than 0.1%. Since our instrument accuracy is on the order of 1%, this condition is always met.

The measurements are taken in volume fraction units. These are related to the mass fractions by

$$\dot{x}^c_i = \frac{N_c y_i M_c}{\sum_j y_j M_j} \tag{5-19}$$

The denominator is the average molar mass. The specific carbon flux can be written as

$$\Delta\dot{m}^c_i = \dot{m}_a \frac{N_{ci} M_c}{\overline{M}_{in}}\left(\frac{\overline{M}_{in}}{\overline{M}_{out}} y_{i,out} - y_{i,in}\right)$$

(5-20)

With the very high dilution in our situation, the average molecular weight changes very little and the ratio can be taken to be unity. Substituting the expression for specific carbon flux into the expressions for *CCE* and *DE* gives

$$CCE = \eta = \frac{\Delta y_{CO_2}}{\Delta y_{CO_2} + \Delta y_{CO} + N_c \Delta y_{HC}} \tag{5-21}$$

$$DE = 1 - \frac{N_c \Delta y_{HC}}{\Delta y_{CO_2} + \Delta y_{CO} + N_c \Delta y_{HC}} \tag{5-22}$$

The very high dilution has allowed us to derive an explicit expression for the performance measures *CCE* and *DE* in terms of measured concentrations of CO_2, *CO* and *HC* in the inlet air and stack gas. Note particularly that the air and fuel flow rates do not appear. This is in agreement with the sensitivity analysis that showed very little sensitivity of the full calculation to these variables.

With this formulation we can calculate the partial derivatives needed for the uncertainty estimate. Let

$$\sigma_c = \left(\Delta y_{CO_2} + \Delta y_{CO} + N_c \Delta y_{HC}\right)^{-1} \tag{5-23}$$

Then

$$\frac{\partial \eta}{\partial y_{CO_2,out}} = \sigma_c (1 - \eta) \tag{5-24}$$

$$\frac{\partial \eta}{\partial y_{CO_2,in}} = -\sigma_c (1 - \eta)$$

$$\frac{\partial \eta}{\partial y_{CO,out}} = -\sigma_c \eta$$

$$\frac{\partial \eta}{\partial y_{CO,in}} = \sigma_c \eta$$

$$\frac{\partial \eta}{\partial y_{HC,out}} = -N_c \sigma_c \eta$$

$$\frac{\partial \eta}{\partial y_{HC,in}} = N_c \sigma_c \eta$$

Substituting these into the formula for uncertainty gives

$$\varepsilon_\eta = \sigma_c \left[(1-\eta)^2 \left(\varepsilon^2_{CO_2,out} + \varepsilon^2_{CO_2,in}\right) + \eta^2 \left(\varepsilon^2_{CO,out} + \varepsilon^2_{CO,in}\right) + N_c^2 \eta^2 \left(\varepsilon^2_{HC,out} + \varepsilon^2_{HC,in}\right)\right]^{1/2} \tag{5-25}$$

Thus the uncertainty is expressed in terms of the uncertainties in the measurements, the conversion efficiency, and the total net carbon efflux, which is the same as the total carbon input in the flare gas. In a similar manner, the uncertainty for the destruction efficiency is

$$\varepsilon_{DE} = \sigma_c \left[(1-DE)^2 \left(\varepsilon_{HC,out}^2 + \varepsilon_{HC,in}^2 \right) + DE^2 \left(\varepsilon_{CO_2,out}^2 + \varepsilon_{CO_2,in}^2 + \varepsilon_{CO,out}^2 + \varepsilon_{CO,in}^2 \right) \right]^{1/2} \tag{5-26}$$

These expressions are easily programmed into a spreadsheet along with the experimental data.

The magnitude of the uncertainty and the range is shown by considering the extremes of dilution. The best case is the lowest dilution, meaning lowest air flow and the highest fuel flow. The worst case is the highest dilution, with lowest fuel flow and high air flow. The analytical solution presented above was used to calculate the uncertainty for these extremes. The values used in the calculations are given in Table 6.

Table 6 - Uncertainty values for measurements for estimation of uncertainty of CCE and DE.

Variable		Low Dilution	High Dilution
$y_{CO_2,out}$	ppm	1940	580
$y_{CO_2,in}$	ppm	390	
σ_c	ppm^{-1}	0.000645	0.00526
$\varepsilon_{CO_2,out}$	ppm	50	10
$\varepsilon_{CO_2,in}$	ppm	5	
ε_{CO}	ppm	0.5	
ε_{CH_4}	ppm	1	

The example is for methane. The uncertainty for the inlet CO_2 and for CO and CH_4 are 1% of full-range (500 ppm, 50 ppm and 100 ppm respectively). The uncertainty for outlet CO_2 is also 1% of full-scale, which is 5000 ppm for the low dilution case and 1000 ppm in the high dilution case.

The estimated uncertainty is plotted in Fig. 10 for *CCE* and in Fig. 11 for *DE*. The uncertainty increases with decreasing efficiency. The uncertainty is almost the same for each measure. In the worst case, the high dilution case, the uncertainty is less than 2% even at 70% efficiency. At the threshold level of 98%, the uncertainty is ±0.12% in the low dilution case, ±0.82% in the high dilution case.

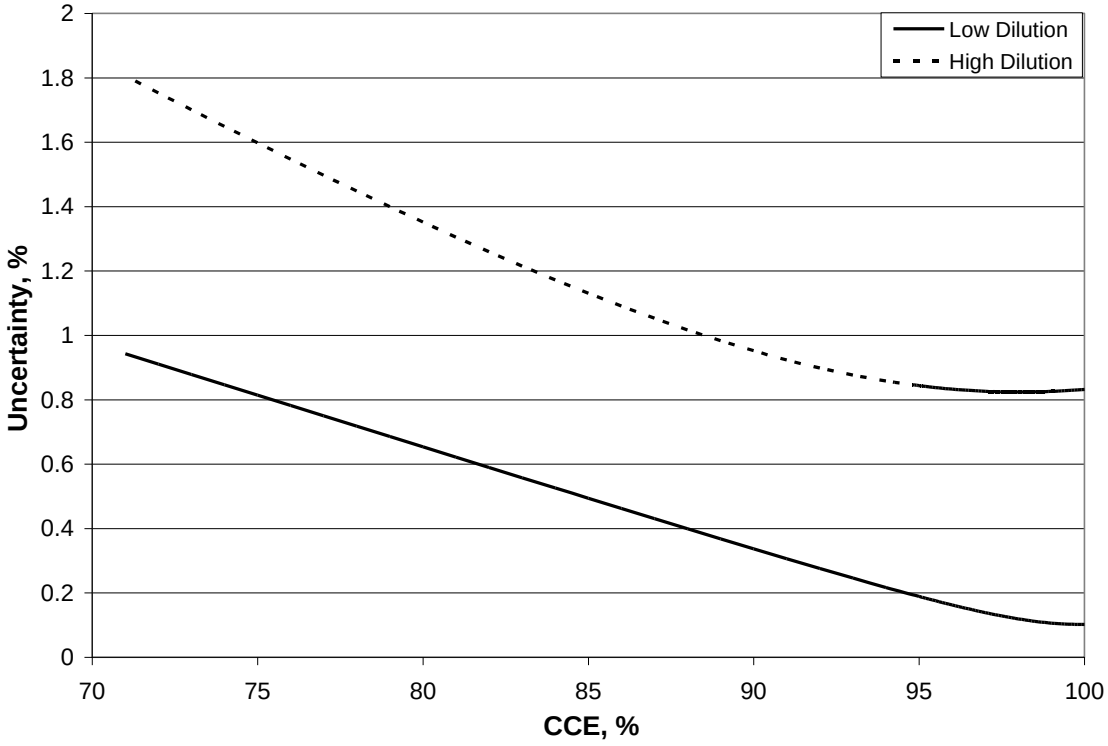

Figure 11 - Uncertainty curves for carbon conversion efficiency (CCE).

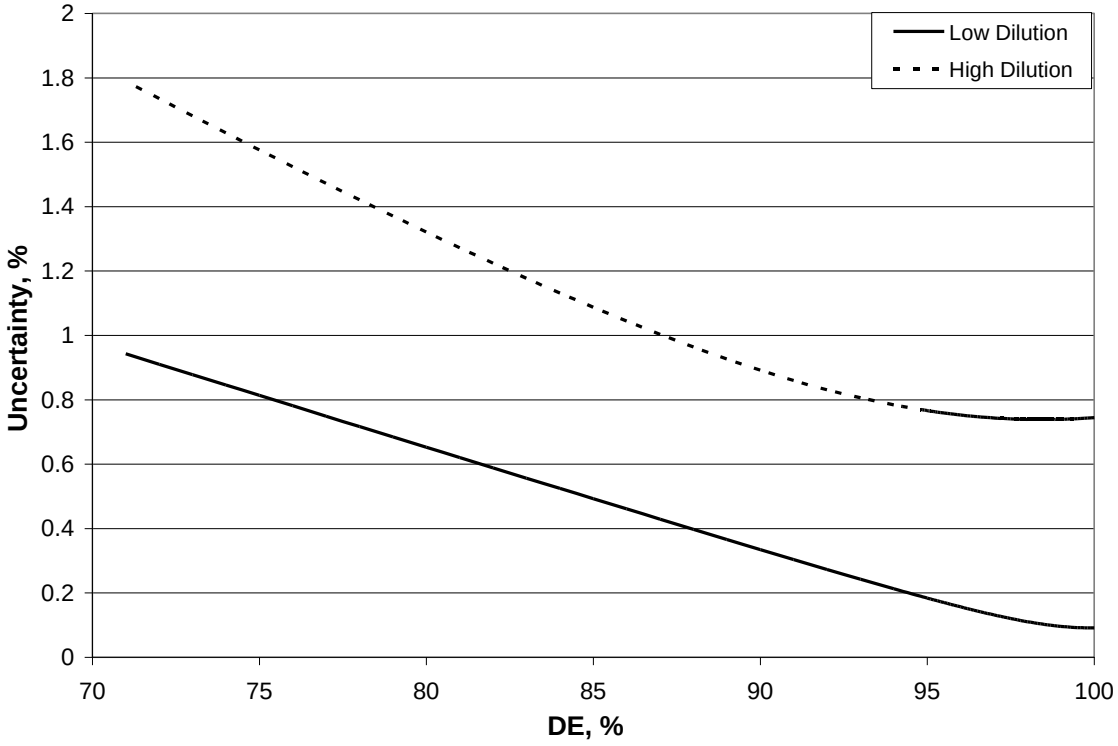

Figure 12 - Uncertainty curves for the destruction efficiency (DE).

6.0 CONCLUSION

The Flare Test Facility at CanmetENERGY has been designed and proven for the experimental program of the International Flaring Consortium. It has the following capabilities:

- It can fire a gas mixture composed of natural gas, propane, ethylene or propylene, and nitrogen or carbon dioxide, with total hydrocarbon flow from 5 kg/h to 30 kg/h (11 lb/h to 66 lb/h) and inert gas flow up to 150 kg/h (331 lb/h).
- The wind speed can be varied from 5 km/h to 35 km/h (3.1 miles/h to 22 miles/h).
- Steam-assisted flare tip has 7.5 cm (3 inch) outside diameter flare gas pipe, with a flame retention ring (open area 21.7 cm^2 or 3.36 in^2), with 12 steam-nozzles and three pilot-burners. The steam supply system can deliver from 5 kg/h to 30 kg/h (11 lb/h to 66 lb/h).
- On-line analysis of gas samples was performed for O_2, CO_2, CO, CH_4 and non-methane hydrocarbons, NO_x, HRVOCs, and BTEX compounds.

The performance measures, carbon conversion efficiency (CCE) and destruction efficiency (DE), are calculated from the measurements. Due to the high dilution of the combustion products in the wind tunnel, these measures are most sensitive to the accuracy of the CO_2 measurement, both upstream and downstream of the flare.

The uncertainty of these measures is shown to increase with decreasing efficiency. The uncertainty also depends upon the dilution level, where there is higher uncertainty with higher dilution. At maximum dilution, the worst case, the uncertainty of the DE is ±0.82% at 98% DE, increasing to ±2% at 70% DE. At minimum dilution, the uncertainty is ±0.12% at 98% DE.

7.0 REFERENCES

Bourguignon, E., M.R. Johnson, and L.W. Kostiuk, [1999] "The use of a closed-loop wind tunnel for measuring the combustion efficiency of flames in a cross flow." *Combustion and Flame,* **119,** pp.319-334.

Caravaggio, G. and A. Caverly, [2008] "Online Analysis of Flaring Emissions", report to IFC.

Gogolek, P., A. Caverly, J. Pohl, R. Schwartz, and J. Seebold [2009] "Emissions from Elevated Flares – A Survey of the Literature", report to IFC.

Kline, S.J. and F.A. McClintock, [1953] "Describing Uncertainties in Single-Sample Experiments, Journal of Mechanical Engineering", pp. 3-8.

8.0 APPENDIX

A. Imperial Figures and Graphs

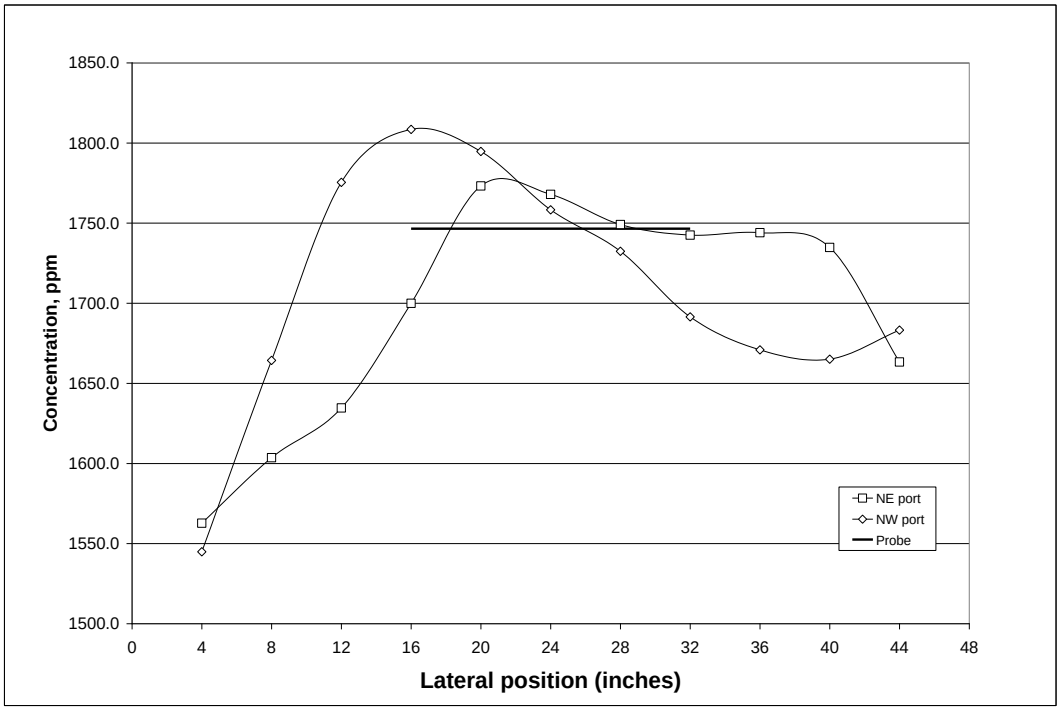

Figure 13 - Concentration profiles for CO_2 in stack, with the probe value indicated by the line.

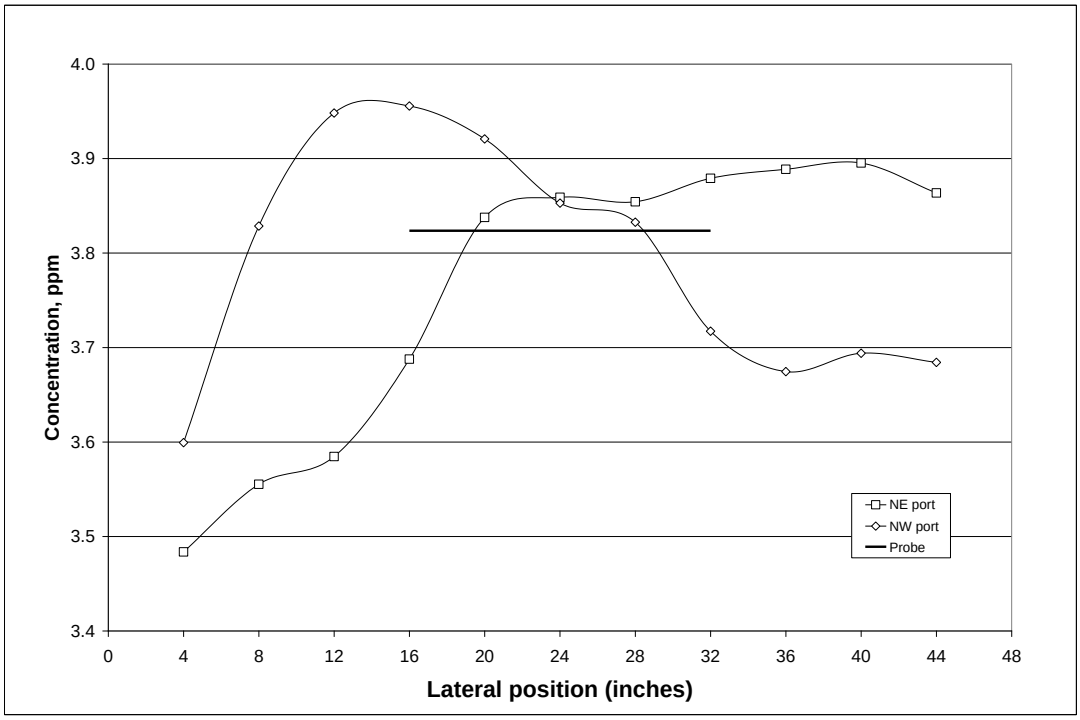

Figure 14 - Concentration profiles for CO in stack, with the probe value indicated by the line.

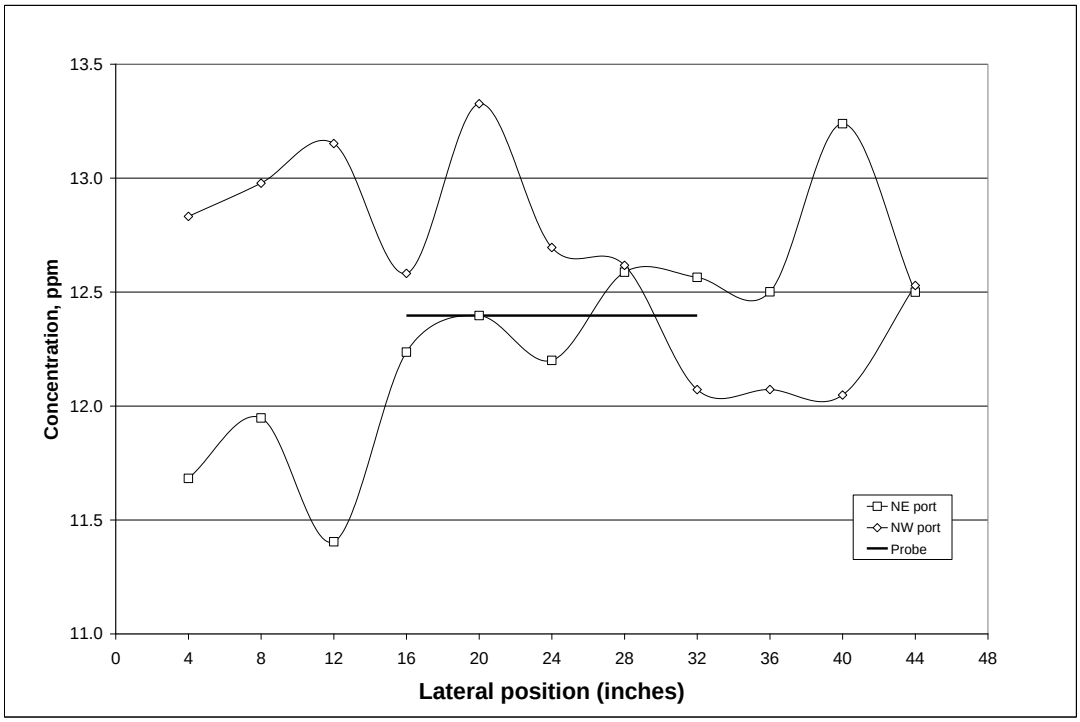

Figure 15 - Concentration profiles for CH_4 in the stack, with the probe value indicated by the line.

B. Analyzer Descriptions and Specifications

1. Composition of NG and Propane

Table A 1 – Composition of NG and propane

	Vol % for NG	Vol % for Propane
CH_4	95.330	0
C_2H_6	2.100	2.0
C_3H_8	0.130	97.2
C_4H_{10}	0.020	0.8
C_5H_{12}	0.000	0
C_6H_{14}	0.000	0
N_2	1.800	0
CO_2	0.620	0
Total	100.000	100.0

2. K Factors

Table A 2 – K correction factor

Gas	Correction factor
Propane	1.01716
Ethylene	1.01983
Propylene	1.066722

3. Flow Meter Specifications

Table A 3 – Flow meter specifications

Location	Manufacturer	Principle	Range	Accuracy
CO_2/Nitrogen line	Endress and Hauser	Thermal mass	Gas and process condition dependent	±0.6% of reading
Propane/Propylene/Ethylene line	Endress and Hauser	Thermal mass	Gas and process condition dependent	±0.6% of reading
Natural Gas line	Endress and Hauser	Thermal mass	Gas and process condition dependent	±0.6% of reading
Pilot line	Sierra Instruments	Thermal mass	Gas dependent	±1.0 % of full scale
Steam line	McCrometer	Pressure difference	Gas dependent	±0.5% of reading

4. Direct Methane, Non-methane Hydrocarbon Analyzer

Manufacturer: Thermo Environmental Instruments Inc.

Model: 55C

Description:

- A back-flush gas chromatography (GC) system designed for automated measurement of methane and non-methane hydrocarbons
- Back-flush GC method permits direct measurement of non-methane hydrocarbons resulting in precise and accurate measurement of low levels of non-methane hydrocarbons (NMHC), even in the presence of high concentration methane
- An automated batch analyzer repeatedly collects and analyzes small amounts of sample stream drawn in by the pump

- An eight port, two position, rotary valve is used to introduce the gas sample into the analyzer and to control the flow of gases through the chromatographic column

Specifications:

Measurement Ranges	0-20 ppm
(Methane and NMHC set independently)	0-200 ppm
(Other ranges optional)	0-2000 ppm
Recorder Ranges (User selectable)	1-2000 ppm
Limits of Detection	20 ppb methane, 50 ppb NMHC as propane
Analysis Time of 1 Sample	70 seconds (approximate)
Accuracy	±2% of measured value
Precision	±2% of measured value
Drift (without auto calibration)	±2% of span
Ambient Operating Temperature	15ºC to 35ºC
Sample Temperature	Ambient to 80ºC (standard) (higher temperatures optional)
Analog Outputs	Separate outputs for Methane, NMHC, THC and chromatogram. Current outputs optional.
Digital Outputs	RS-232
Alarm Systems	Methane Concentration, NMHC Concentration, Calibration Failure, System Failure
Sample Flow Rate	0.5 L/min minimum
Power Requirements	90-110 VAC @ 50/60 Hz 105-125 VAC @ 50/60 Hz 210-250 VAC @ 50/50 Hz
Support Gases (From AL/BOC or Linde)	HC free air (200-300 cc/min) N_2 carrier (35 cc/min) H_2 fuel (25 cc/min)

	Span mix (2-litre/calibration)
Physical Dimensions	42.5 cm (W) x 21.9 cm (H) x 58.4 cm (D)
Weight	27.2 kg

5. NO-NO_2-NO_x Analyzer

Manufacturer: Thermo Electron Corporation

Model: 42C

Description:

- Basis is that nitric oxide (NO) and ozone (O_3) react to produce a characteristic luminescence (chemiluminescence)
- The intensity of the luminescence is linearly proportional to the concentration of NO
- Ambient air sample enters through sample bulkhead and flows through particulate filter and capillary to solenoid valve
- In NO mode the solenoid valve sends sample directly to reaction chamber
- In NO_X mode the solenoid valve sends sample through NO_2 to NO converter and then to reaction chamber
- A flow sensor for measurement of sample flow is located directly before the reaction chamber
- Dry air enters through the dry air bulkhead and flows through a flow sensor and then a silent discharge ozonator
- Ozone reacts with NO from ambient air sample to produce electronically excited NO_2 molecules
- Photomultiplier tube in thermoelectric cooler detects NO_2 luminescence
- Outputs of NO, NO_2, and NO_X concentrations to front panel display and analog outputs

Specifications:

Preset Ranges	0-0.05, 0.1, 0.2, 0.5, 1, 2, 5, 10, 20, 50, and 100 ppm
	0-0.1, 0.2, 0.5, 1, 2, 5, 10, 20, 50, 100, and 150 mg/m^3
Extended Ranges	0-0.2, 0.5, 1, 2, 5, 10, 20, 50, and 100 ppm
	0-0.5, 1, 2, 5, 10, 20, 50, 100, and 150 mg/m^3
Custom Ranges	0-0.05 to 100 ppm for NO, NO_2, and NO_X
	0-0.1 to 150 mg/m^3
Zero Noise	0.20 ppb RMS (60 second averaging time)
Lower Detectable Limit	0.40 ppb (60 second averaging time)
Zero Drift (24 hour)	<0.40 ppb
Span Drift (24 hour)	±1% full scale
Response Time	40 sec (10 second averaging time)
(in automatic mode)	80 sec (60 second averaging time)
	300 sec (300 second averaging time)

Precision	±0.4 ppb (500 ppb range)
Linearity	±1% full scale
Sample Flow Rate	0.6 L/min
Operating Temperature	15ºC to 35ºC
	(may be safely operated over the range of 0 to 45 ºC in non-condensing environment)
Power Requirements	90-110 VAC @ 50/60 Hz
	105-125 VAC @ 50/60 Hz
	210-250 VAC @ 50/50 Hz
	300 Watts
Physical Dimensions	42.5 cm (W) x 21.9 cm (H) x 58.4 cm (D)
Weight	24 kg
Outputs	NO, NO_2, and NO_X, selectable voltage, 4-20 mA, RS-232, RS-485

6. Upstream and Downstream CO_2 Analyzers

Manufacturer: HORIBA Instruments Inc

Model: VIS-510

Description:

- Basis is non-dispersive infrared (IR) analysis method
- Continuously measures components in sample gas, for IFC tests, this was CO_2
- IR rays pass through sample and are absorbed by sample gas
- This causes detection cell membrane to vibrate which generates an electric output
- The electric output corresponds to changes in the capacity between electrodes
- Detection is of IR absorption in the particular wavelength bad for a component
- Changes in the IR absorption of the measured component result in changes in the concentration of the component
- Outputs measured concentration to digital panel display

Specifications:

Ranges

Table A 4 – Analyte measurement ranges

Standard		Option [*1]	
Constituent	Min. Range	Max. Range	Min. Range
CO	0-100 ppm	0-100 vol%	0-50 ppm
CO_2	0-100 ppm	0-100 vol%	0-50 ppm
NO	0-200 ppm	0-100 vol%	0-100 ppm
SO_2	0-100 ppm	0-100 vol%	0-50 ppm
CH_4	0-100 ppm	0-100 vol%	0-50 ppm
C_2H_4	0-200 ppm	0-100 vol%	0-100 ppm

Within the above concentration ranges, up to 4 ranges can be selected with the maximum range ration being 10.

Reproducibility

±0.5% full scale

(However, ±1.0% of full scale when CO, CO_2, SO_2, CH_4, C_2H_4 are less than 100 ppm or NO is less than 200 ppm.)

Zero Drift (24 hour)	±1.0% of full scale
	Note: =2.0%/d in full scale for *1
Span Drift (24 hour)	±1.0% full scale
	Note: =2.0%/d in full scale for *1
Response Speed	Within 30 s for 90% response from analyzer inlet.
Display	LED digital (4 digits effective)
Flow Rate of Sample Gas	Approx. 500 ml/min
Ambient Temperature	0 to 40 ºC
Output Signal	Insulated output: DC 0-16 mA or 4-20 mA
	DC 0-1 V
	DC 0-10 V
Power Requirements	100 VAC @ 50/60 Hz
	115 VAC @ 50/60 Hz
	240 VAC @ 50/50 Hz
Weight	Approx. 15 kg

7. Paramagnetic Oxygen Analyzer

Manufacturer: California Analytical Instruments Inc

Model: 100P

Description:

- Basis is that analyzer measure paramagnetic susceptibility of sample gas with a magneto-dynamic type cell
- Measuring cell consists of a dumbbell made of diamagnetic material and the temperature is electronically controlled to 50 ºC
- As oxygen concentration increases the dumbbell is deflected from rest position
- An increase in oxygen concentration increases the displacement of the dumbbell
- Deflection is detected by optical system connected to an amplifier
- Coil of wire surrounds dumbbell
- Current passed through the coil returns the dumbbell to the original rest position
- The current applied is linearly proportional to the %oxygen concentration in the sample gas at the set temperature
- Outputs %oxygen concentration to a digital panel display

Specifications:

Sample Contact Material	Platinum, glass, stainless steel, vitron
Ranges (Standard fixed ranges, choose A, B, or C)	A) Range 1: 0-1%, Range 2: 0-15%, Range 3: 0-25% B) Range 1: 0-5%, Range 2: 0-10%, Range 3: 0-25% C) Range 1: 0-25%, Range 2: 0-40%, Range 3: 0-100%
Response Time	90% full scale in 2 seconds
Linearity	Better than 1% full scale
Repeatability	Better than 1% full scale
Sample flow rate	1 L/min
Noise	< 1% full scale
Zero Spin Drift	< 1% full scale in 24 hours
Zero & Span Adjustment	Ten turn potentiometer
Display	3 ½ digit panel meter (eg. 100.5)
Outputs	0-10 VDC and 4-20 mA (0-20 mA)
Ambient Temperature	5 to 45 ºC
Sample Temperature	0 to 50 ºC
Sample Condition	Clean, dry gas

Fittings	¼” tube
Power Requirements	115/230 (±10%) VAC, 50/60 Hz, 70 watts/channel
Relative Humidity	less than 90% RH (non-condensing)
Dimensions	13.3 cm (H) x 48.3 cm (W) x 38.1 cm (D)
Weight	4.5 kg

8. Gas Chromatograph with Peltier trap, FID and PID

Manufacturer: SRI Instruments

Model: 8610C

Description:

- Gas chromatograph (GC) is equipped with a Peltier cool trap, a small vacuum pump, Peltier trap, a flame ionization and a photo ionization detector connected in series
- A Nafion dryer is connected to the inlet of the GC to eliminate water from the sample stream
- The sampling pump, Peltier trap and sampling valve are activated using the programmed events function in the Peak Simple 3.29 software
- The separation chromatography is done with a GS GasPro capillary column under the following conditions: sampling time: 0.5 min, temperature program: initial temperature: 40°C, hold for 9 minutes, final temperature: 110°C with a ramp of 10°C/min and the final temperature is held for 20 minutes
- The carrier gas is helium
- Data collection and GC temperature programming are controlled by the Peak Simple 3.29 software
- Plots can be seen in "Online Analysis of Flaring Emissions" [Caravaggio and Caverly, 2008]

Specifications:

Detectors	FID and PID
Gas Sample Inlet	1/8" tube
Fittings	
Gas Sample Outlet	1/8" tube
Fittings	
Column Dimensions	0.32 mm x 60 m
Column Flow Rate	3.58 ml/min
Column Temperature	-80 ºC to 260 ºC
Sampling Pump	91.5 ml/min
Flow Rate	
GC Operating Temperature	-15 ºC to 250 ºC
(with Peltier trap and above column)	
Electrical Requirements	110 VAC, 50/60 Hz, 1150 VA max
Display	LED digital (2 digit effective)
Dimensions	47.0 cm (W) x 31.8 cm (H) x 36.8 cm (D)
Weight	Approx 27 kg

9. Sample Conditioning Unit

Manufacturer: Perma Pure

Model: Mini-GASS

Description:

- Prepare gas samples for the analysis by removing particulates, mists and water vapour without removing the monitored compounds from the gas phase
- Based on a shell and tube model
- Sample passes through a 1 µ filter to remove particulates and aerosols
- Downstream of filter is a Nafion membrane dryer which selectively removes water vapour from the sample through permeation distillation
- Water is continually removed as sample passes from inlet to outlet which reduces the sample dew point as the sample travels through the dryer
- Dry purge gas enters the dryer at the sample outlet end to provide a medium for water vapour to be carried away and creates a temperature gradient along the dryer length
- Ambient purge air enters dryer at sample outlet to cool that portion of the dryer
- This counter flow produces a temperature gradient along the dryer length
- The temperature of the purge gas exhaust is monitored and controlled by an electronic temperature controller to maintain the gradient
- Purge gas passes through the dryer and is heated to the desired sample inlet temperature
- The temperature gradient permits both rapid vapour removal and decreases the final dew point
- If the purge gas temperature falls below the programmed temperature an aluminum heating block conducts energy from the system backplate to the dryer's shell tube.
- This causes purge gas traveling through the dryer's shell to acquire heat from the shell
- It is therefore possible to closely control the final temperature of the purge gas so that a consistent temperature gradient can be maintained
- The sample pump draws the sample and supplies it to the analyzer at up to 5 L/min of sample
- Head of pump is in heated section of system, motor is in control section to keep pump head temperature above dew point of sample to prevent condensation formation

Specifications:

Maximum Sample Flow Rate 0-10 L/min

Maximum Inlet	121 ºC W/SST filter	
Sample Temperature	110 ºC W/KYNAR filter	
Maximum Gas Sample	30%	
Water vapour content		
Outlet Sample Dew Point	-4 ºC at 10 L/min	
	-12 ºC at 5 L/min	
	-25 ºC at 2 L/min	
Soluble Gas Removal	NO, NO2	0% losses
Rates	SO2	0% losses
	CO, CO2	0% losses
	H2S, HCl	0% losses

Maximum Gas Sample	20 psig
Inlet pressure	
Minimum gas sample inlet	5” H2O Vacuum
Pressure (without purge educator option)	
Gas Sample Inlet Fittings	¼” or 3/8” tube
Gas sample Outlet Fittings	¼” or 3/8” tube
Air Requirements	Purge air -40 ºC dew point maximum one CFM
Electrical Requirements	110/220 VAC, 50/60 Hz, 5.0 A/2.5 A, 475 watts
Fuse	5 AMP buss type AGC or equivalent
Enclosure	NEMA 4x, fibreglass with polycarbonate cover
Dimensions	30.5 cm (W) x 50.8 cm (H) x 17.8 cm (D)
Operating Environment	-20 ºC to 40 ºC ambient temp.
	0-95% R.H.

C. Correlations

1. Steam Flow Correction

Bucket tests were performed to check the mass flow meter for steam. The flow meter is a Micrometer V-cone, working on the differential pressure principle.

The 45 gallon plastic barrel was filled with water and ice and placed on an electronic scale. The steam nozzles were submerged into the ice water. The steam flow was turned on. Once steady flow was obtained, the scale was zeroed and timer started. At the allotted time, the scale reading was logged. The steam flow rate is directly calculated from the weight increase and time. The testing had to end when the ice was melted. The steam flow from the flow meter was logged and the average over the sampling time was calculated. Table B1 has the results of the tests. The plot of the bucket flow against the logged average flow is shown in Fig. B1.

Table B 1 – Steam flow bucket test results

Test Number	Nominal Flow	Logged Average	StdDev	Bucket Flow
	kg/h	kg/h		kg/h
1	5	5.812962406	0.381529738	3.4
2	10	9.687420635	0.346938942	9.4
3	15	14.56892308	0.507615695	16.5
4	20	20.47219149	0.910547724	22.2
5	25	25.05207692	0.982680485	29
6	30	31.69609091	0.965781833	38

There is a clear linear relationship between the bucket flow rate and the flow meter reading. The equation is

$$\dot{m}_{bucket} = 1.3066\dot{m}_{meter} - 3.6144$$

This has a significant offset and slope different from unity. It shows that the flow meter underestimates the flow at the high flow rates and overestimates the flow at the lowest flow rates.

Subsequent investigation of the set-up of the flow meter showed that the thermocouple setting was incorrect (J-type for K-type) and the meter configured for super-heated steam whereas it has saturated steam.

The linear correction can be used to adjust the measured flow rates for earlier trials. The correction of the set-up of the flow meter is being discussed with the vendor.

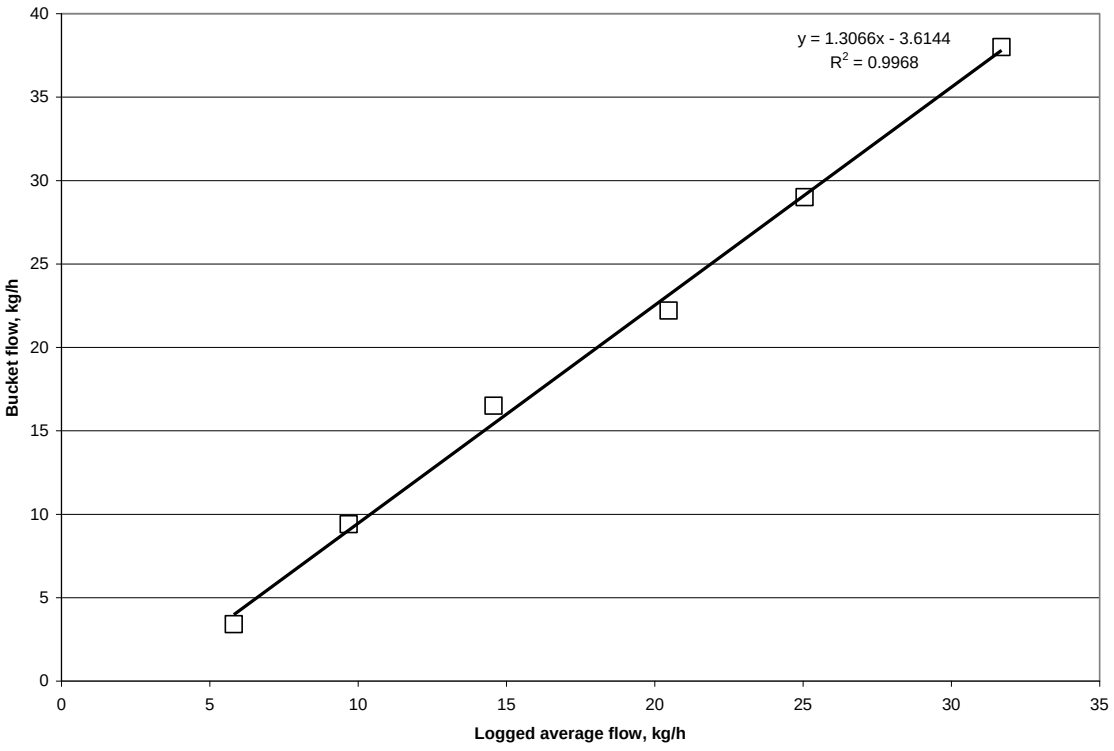

Figure B 1 – Linear relationship of steam flow measured during the bucket tests (bucket flow) and the average of the logged flow.

2. Air Flow Humidity Correction

The mass flow of air is measured from differential pressure across a rake of pitot probes with mass flow calculated using the measured static pressure and temperature at the rake. The air is assumed to have 0%-vol. water content. The actual air can have significant humidity, particularly during the summer months. A correction is needed to account for the humidity.

The vendor (Air Monitor Corp.) provided a spreadsheet giving the calculations performed by the flow meter transmitted to give the mass flow reading. These calculations were done for the range of water content from 0 %-vol to 30 %-vol. This gives the values as if the flow meter was given the water content of the air. The ratio of the moist air flow to the reading (as if dry) flow is plotted against the water content of the air in Fig. B2. The relationship is linear. The water content of air is easily calculated from the measured relative humidity and the calculated vapor pressure of water using Antoine's equation.[1]

[1] $\text{Vapour Pressure } H_2O = e^{(18.3036 - 3816.44/(273.15 + T_a - 46.13))}$ mm Hg

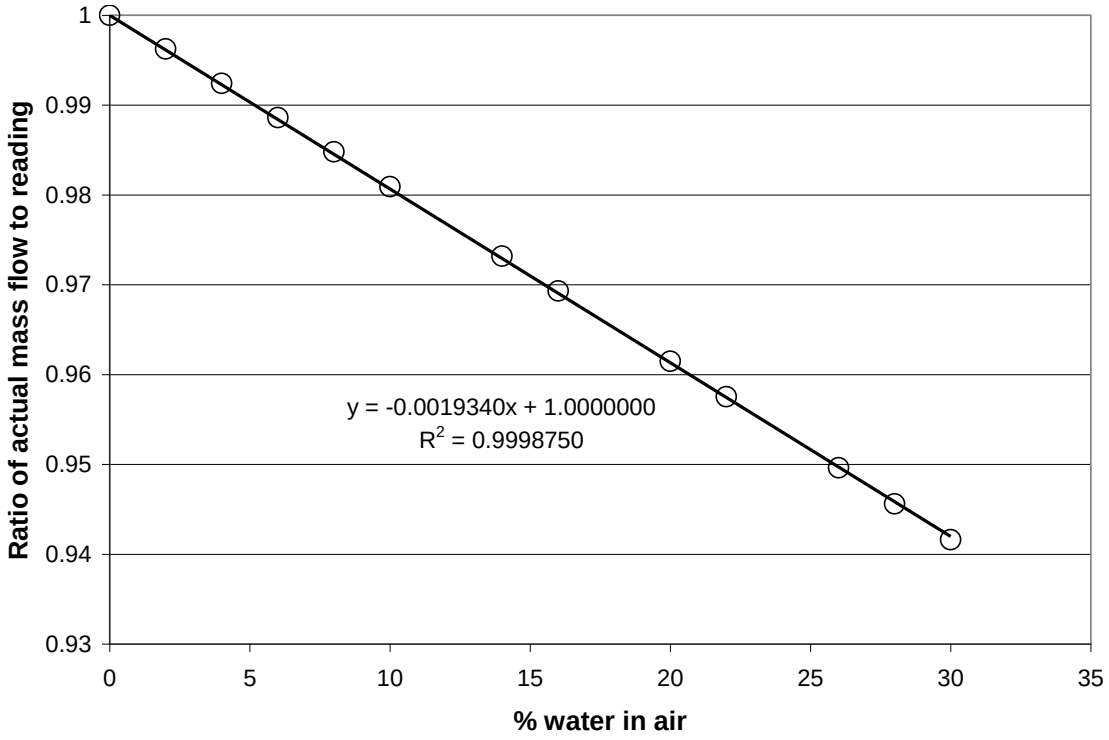

Figure B 2 – Correction of the air flow reading for humidity.

3. Uncertainty Estimation with CO_2 in the Flare Gas

The possibility of CO_2 in the flare gas (in fuel) was neglected in the analysis of uncertainty presented in the main text. In our experiments, CO_2 can appear in the flare gas either as part of the fuel gas or as a separately controlled diluent. In the former case the amount is relatively small, though there are two uncertainties introduced: the fuel flow rate and the actual fraction of CO_2 in the fuel gas. In the second case the CO_2 flow rate is of the same order or larger than the hydrocarbon flow rate. This means that the stack CO_2 is primarily from the inert diluent. Failing to account for this exaggerates the conversion efficiency to CO_2.

We start with the definition of CCE

$$CCE = \frac{\Delta \dot{m}^c_{CO_2}}{\Delta \dot{m}^c_{CO_2} + \Delta \dot{m}^c_{CO} + \Delta \dot{m}^c_{HC}}$$

The only term affected is the mass flux change of carbon as CO_2 in air. It is

$$\Delta\dot{m}^c_{CO_2} = \left(\dot{m}_a + \dot{m}_f\right)x^c_{CO_2,out} - \dot{m}_a x^c_{CO_2,in} - \dot{m}_f x^c_{CO_2,f}$$

A slight rearrangement gives two terms, the first the same as in the earlier derivation. The second term is no longer negligible.

$$\Delta\dot{m}^c_{CO_2} = \dot{m}_a\left(x^c_{CO_2,out} - x^c_{CO_2,in}\right) + \dot{m}_f\left(x^c_{CO_2,out} - x^c_{CO_2,f}\right)$$

The concentration $x^c_{CO_2,out}$ is on the order of 10^{-3} while $x^c_{CO_2,f}$ is two orders of magnitude bigger. Therefore $x^c_{CO_2,out}$ can be neglected in the second term, giving

$$\Delta\dot{m}^c_{CO_2} = \dot{m}_a\left(x^c_{CO_2,out} - x^c_{CO_2,in}\right) - \dot{m}_f x^c_{CO_2,f}$$

Continuing as in the main text by converting to molar concentration, and writing $\dot{m}_f x^c_{CO_2,f} = \dot{m}_{CO_2}$, gives

$$\Delta\dot{m}^c_{CO_2} = \left(y_{CO_2,out} - y_{CO_2,in}\right) - \frac{\overline{M}_{in}}{M_c}\frac{\dot{m}_f}{\dot{m}_a} = \Delta y_{CO_2} - \varphi_{CO_2}$$

The second term is on the order of 10^{-3} on the same order as the change in concentration and therefore errors in each term can be increased in the subtraction. Two additional variables, $\dot{m}_{air}$ and $\dot{m}_f$, are brought into the calculation, with the attendant uncertainties for the measurements. The final forms for the efficiencies are

$$CCE = \eta = \frac{\Delta y_{CO_2} - \varphi_{CO_2}}{\Delta y_{CO_2} - \varphi_{CO_2} + \Delta y_{CO} + N_c\Delta y_{HC}}$$

and similarly

$$DE = 1 - \frac{N_c\Delta y_{HC}}{\Delta y_{CO_2} - \varphi_{CO_2} + \Delta y_{CO} + N_c\Delta y_{HC}}$$

The calculation of the partial derivatives for the uncertainty estimate is a little tedious. There are two additional terms corresponding to $\dot{m}_a$ and $\dot{m}_f$. The total carbon out is

$$\sigma_c = \Delta y_{CO_2} - \varphi_{CO_2} + \Delta y_{CO} + N_c\Delta y_{HC}$$

When using η, δ, and σ_c, the terms from the main text are unchanged. The partial derivatives for the additional terms are

$$\frac{\partial \eta}{\partial \dot{m}_{CO_2}} = -\frac{\varphi_{CO_2}}{\dot{m}_{CO_2}} \sigma_c (1-\eta)$$

$$\frac{\partial \eta}{\partial \dot{m}_{air}} = \frac{\varphi_{CO_2}}{\dot{m}_{air}} \sigma_c (1-\eta)$$

This gives the full expression for the uncertainty

$$\varepsilon_\eta = \sigma_c \left[(1-\eta)^2 \left(\varepsilon_{CO_2,out}^2 + \varepsilon_{CO_2,in}^2 \right) + \eta^2 \left(\varepsilon_{CO,out}^2 + \varepsilon_{CO,in}^2 \right) + N_c^2 \eta^2 \left(\varepsilon_{HC,out}^2 + \varepsilon_{HC,in}^2 \right) + \varphi_{CO_2}^2 (1-\eta)^2 \left(\frac{\varepsilon_{\dot{m}_{CO_2}}^2}{\dot{m}_{CO_2}^2} + \frac{\varepsilon_{\dot{m}_{air}}^2}{\dot{m}_{air}^2} \right) \right]^{1/2}$$

This formula is still easily implemented in a spreadsheet. However, it is too complex to permit simple analysis as in the main text.

I&EC research
Industrial & Engineering Chemistry Research

Article

pubs.acs.org/IECR

Emissions of Nitrogen Oxides from Flares Operating at Low Flow Conditions

Vincent M. Torres,[†] Scott Herndon,[‡] Ezra Wood,[‡,§] Fahad M. Al-Fadhli,[†] and David T. Allen*[,†]

[†]Center for Energy and Environmental Resources, The University of Texas at Austin, 10100 Burnet Road, Building 133, M.S. R7100, Austin, Texas 78758, United States

[‡]Aerodyne Research, Inc., 45 Manning Road, Billerica, Massachusetts 01821-3976, United States

[§]Department of Public Health, University of Massachusetts, Amherst, Massachusetts 01003, United States

ABSTRACT: Full scale flare tests have been conducted to test the impacts of flare operating conditions on the fraction of flared gases that are converted to carbon dioxide and water (combustion efficiency, CE) for flares combusting low heating value gases (~350−600 BTU/scf) at low flow rates (~0.1−0.25% of maximum flow). Flares produce lower flame temperatures when operating with low heating value gases at low combustion efficiencies than when operating with high heating value gases at high combustion efficiencies. This leads to reduced formation of nitrogen oxides (NOx) in the flame. For a series of tests conducted under low flow conditions, with low heating value gases, NOx emission factors ranged between 10 and 120% of the NOx emission factor reported in AP-42. Emissions of NOx were highest for air assisted flares operating at high CE and lowest for steam assisted flares operating at low CE. In general, emissions were lower in steam assisted flare tests than in air assisted flare tests conducted under similar conditions. Photochemical modeling simulations indicated that these reductions in NOx emissions had relatively small impacts on the ozone formation potential of flares operating at low CE.

INTRODUCTION

Flares destroy waste organic gases through combustion at high temperature, producing carbon dioxide and steam. Oxides of nitrogen (NOx, the sum of NO and NO_2) are formed as a byproduct of combustion, and since NOx is a precursor for tropospheric ozone production, emissions of NOx are inventoried in regions where ozone concentrations are of concern. Typically, NOx emissions from flares are estimated using methods outlined by the U.S. Environmental Protection Agency (EPA) in the AP-42 series of documents.[1] Emissions are estimated by multiplying an emission factor by an activity parameter:

$$E = A \cdot \mathrm{EF} \quad (1)$$

where E is the emissions rate, A is the activity rate, and EF is the emission factor.

For estimating NOx emissions from flares, current practice, based on information documented in Section 13.5-1 of AP-42,[1] is to assume a constant emission factor of 0.068 lb of NOx per million BTU of heating value (lower heating value, LHV) of gases sent to the flare. A slightly different set of emission factors is suggested in documentation from the State of Texas.[2] The Texas Commission on Environmental Quality (TCEQ) suggests the use of one of four emission factors: two for low heating value gases (0.068 and 0.064 lb of NOx per million BTU of heating value for steam and air assisted flares, respectively) and two for high heating value gases (0.049 and 0.14 lb of NOx per million BTU of heating value for steam and air assisted flares, respectively). The emission factors suggested by the TCEQ for low heating value gases are very similar to the AP-42 emission factor.

The activity factor in eq 1 is the flow rate of gases fed to the flare, multiplied by their lower heating value. Emissions are estimated, as indicated in eq 1, by multiplying the activity factor by the emission factor. This approach to estimating NOx emissions from flares, and the emission factors, is based largely on data collected during full scale flare tests conducted in 1983,[3] with flares generally operating at high flow rates, with high heating value gases. During these tests, combustion efficiencies (fraction of the feed gases converted to CO_2 and water) were high.

Data presented in other papers in this special issue[4,5] indicate that if too much steam or air is added to flared gases (steam and air assist), particularly at low flow conditions and with low heating value gases being flared, combustion efficiencies can be lower than the targeted values of 98−99%. Since less heat of combustion is generated with low heating value gases, combustion temperatures are lower than for high heating value gases, and production of NOx may be reduced. Further, if too much air or steam is added to the flared gases, destruction efficiencies and combustion temperatures can be reduced, and NOx emissions may be reduced. This paper presents NOx emission data for the steam assisted and air assisted flare tests reported by Torres et al.[4,5] These tests were conducted at low flow rates (0.1−0.25% of maximum flow), and with low heating value gases (300−650 BTU LHV/scf). The NOx emission rates from the tests are compared to emissions calculated using existing procedures, and the potential implications for region-wide NOx

Special Issue: Industrial Flares

Received: January 19, 2012
Revised: March 9, 2012
Accepted: March 21, 2012

   dx.doi.org/10.1021/ie300179x | *Ind. Eng. Chem. Res.* XXXX, XXX, XXX−XXX

emission estimates and ozone formation in the Houston area are quantified.

METHODS

The flare tests used to develop the NOx emission rates reported here have been described in detail in other papers in this special issue and in the Quality Assurance Project Plan and Final Report for the flare tests, reported by the University of Texas.[4−8] The flare tests were conducted with flare gases that were 1:4, by volume, mixtures of natural gas and either propane or propylene, diluted with nitrogen to generate targeted values of heating value for the flared gases. The composition of the flared gases was measured during each test using gas chromatography, and the gases in the flare plume were extracted, using a sampler described in detail elsewhere,[4−8] at a point after the plume had cooled and combustion was no longer occurring. Detailed descriptions of the analytical instrumentation are provided by Knighton et al.[9] For this work, the focus is on the measurements of nitrogen oxides and their ratio to total carbon in the plume. The measurement methods for these species are summarized in Table 1. For these tests, combined nitrogen oxides (NO plus NO_2) were measured using a ThermoElectron Model 42i chemiluminescence monitor. Details of the operation of the chemiluminescence monitor and calibration methods have been previously described.[10] The NOx measurements have been corrected for the quenching of electronically excited NO_2 by water vapor. NO_2 was converted to NO in the monitor with a molybdenum converter. The measurements were designed to provide rapid response measurements (1−10 s). Detection limits, precision, and accuracy of the instrumentation are reported in Table 1.

Table 1. Measurements Performed on the Samples Extracted from the Flare Plume

measurement	instrument	detection limit	precision	accuracy (%)
CO	QC-TILDAS	600 ppt (1 s)	300 ppt (1 s)	4
NOx	ThermoElectron 42i chemiluminescence	0.4 ppb (1 s)	0.2 ppb (1 s)	5
CO_2	LiCor absorption 6262	0.7 ppm (1 s)	350 ppb (1 s)	5
total non-methane hydrocarbons	TECO 55C	3 ppb	15%	20

This work focuses on the flare tests done with propane, since olefin chemiluminescence on reaction with ozone interfered with the NOx chemiluminescence in the NOx monitor during the propylene tests. The experiments done with propane, which were analyzed for NOx emissions, are listed in Tables 2 and 3. Table 2 lists the experiments performed using the steam assisted flare, and Table 3 describes the experiments performed using the air assisted flare. These flares are described in more detail by Torres et al.[5] Test identifiers are the same identifiers used by Torres et al.[5] Individual tests are indicated by a number, such as S12.3R2, which represents steam flare test series number 12 (S12, see Table 2), steam-to-vent gas flow ratio number 3 (S12.3), and replicate number 2 (S12.3R2); similarly A7.3R2 indicates air assisted flare test series 7, air-assist-to-vent gas ratio 3, and replicate number 2 (see Table 3).

Test series S12−S14 were conducted with flare test gases with a targeted lower heating value (LHV) of 350 BTU/scf. For the steam assisted flare, steam could be added either with the vent gas (center steam) or at the rim of the flare tip (upper steam). For each steam flare test series a target value of center steam flow (500, 300, and 0 lb/h) and upper steam flow (500 lb/h for all tests) was selected. For each steam setting, vent gas flow was varied between ∼900 and ∼2400 lb/h. Table 2 summarizes flare operating conditions for the tests performed. Values shown in Table 2 represent time-averaged values of flare operating conditions over the course of each test (typically 7−10 min per test).

Table 2. Operating Conditions for Steam Assisted Flare Tests

flare test no.	flare gas flow (lb/h)	LHV of flared gases (BTU/scf)	steam flow (lb/h) (center/upper)	CE[a] (%)
Test Series 12 (Propane/Natural Gas Mix)				
S12.1R1	2363	364	504/545	97.4
S12.1R2	2368	366	493/548	96.9
S12.2R1	1847	357	500/553	91.0
S12.2R2	1865	364	486/566	92.4
S12.3R1	1394	344	498/540	77.3
S12.3R2	1406	360	483/577	75.5
S12.4R1	940	350	500/548	38.0
Test Series 13 (Propane/Natural Gas Mix)				
S13.1R1	2394	375	300/546	98.0
S13.2R1	1874	365	307/525	94.6
S13.3R1	1404	359	298/555	87.8
S13.4R1	919	331	310/539	42.5
S13.4R2	922	336	321/534	46.9
S13.4R3	947	368	310/446	60.2
S13.5R1	1207	357	313/517	83.1
Test Series 14 (Propane/Natural Gas Mix)				
S14.1R1	2370	385	0/540	98.9
S14.4R1	942	377	0/533	95.3

[a]Combustion efficiency.

Table 3. Operating Conditions for Air Assisted Flare Tests

flare test no.	flare gas flow (lb/h)	LHV of flared gases (BTU/scf)	air flow (scfm/lb·h)	CE (%)
Test Series 7 (Propane/Natural Gas Mix)				
A7.1R1	370	376	2 020/9 110	98.6
A7.1R2	365	356	1 580/7 120	99.8
A7.2R1	364	357	5 010/22 600	93.0
A7.2R2	364	356	4 340/19 600	91.7
A7.3R1	364	355	9 050/40 800	81.6
A7.3R2	365	356	8 050/36 300	77.4
A7.4R1	365	356	14 900/67 300	61.4
A7.5R1	366	356	6 330/28 600	87.2

Test series A7 was the only test series using propane conducted with the air assisted flare. The tests were conducted with flare test gases with a targeted lower heating value (LHV) of 350−370 BTU/scf. For a vent gas flow of 360−370 lb/h, air assist was varied between 7000 and 67 000 lb/h. Table 3 summarizes flare operating conditions for the tests performed. Values shown in Table 3 represent time-averaged values of flare operating conditions over the course of each test (typically 7−10 min per test).

Because the extractive sampling of the flare plume did not collect all of the combustion gases, plume average parameters such as combustion efficiency and NOx emissions were calculated using ratios of concentrations, as described by Herndon et al.[7] For example, measurements of carbon dioxide

dx.doi.org/10.1021/ie300179x | Ind. Eng. Chem. Res. XXXX, XXX, XXX−XXX

in the plume (background corrected), CO in the plume, and propane and methane in the flare feed (vent gas) allow the combustion efficiency (CE, fraction of carbon in flared gases converted to CO_2) to be calculated as

$$\mathrm{CE} = \frac{\text{background corrected } CO_2 \text{ (ppm C) in plume}}{\text{background corrected sum of carbon in unreacted methane and propane, } CO_2, \text{ CO, and products of incomplete combustion}} \quad (2)$$

As described by Herndon et al.,[7] by dividing the numerator and denominator of eq 2 by the concentration of a species such as CO or CO_2, the combustion efficiency can be calculated based on a localized measurement in the plume of concentration ratios.

Similarly, the ratio of NOx to CO_2 (ppb/ppb) or the ratio of NOx to total carbon content (ppb/ppb C) can be used to calculate a plume average emission factor for NOx. The transformation of a concentration ratio to an emission factor is performed by noting that in a 4:1 (by volume) ratio mix of propane and natural gas, fed to the flare, 12/13 of the carbon in combustion gases comes from propane and 1/13 of the carbon comes from methane. Using lower heating values of 21 450 BTU/lb of methane and 19 884 BTU/lb of propane leads to an estimated heating value of 296 000 BTU/lb mol of carbon that is combusted. In this work, two emission factors are estimated. Both emission factors have the form of lb of NOx (as NO_2) per million BTU of heating value. The first emission factor uses the current practice in estimating emissions and assumes that all of the gases fed to the flare are combusted. The second emission factor is based on the heat released by flared gases that are actually combusted. As demonstrated under Results and Discussion, the heat released in the formation of products of incomplete combustion, such as CO, is small; therefore this second emission factor will be equivalent to lb of NOx per million BTU released due to combustion to CO_2 and water.

Based on the heating values for methane and propane, releasing 10^6 BTU due to combustion of flare gases (4:1 by volume propane to methane) requires 3.38 lb mol of carbon. An emission factor of the form reported in AP-42,[1] in units of lb of NOx as NO_2 per million BTU of flared gases, assuming all flared gases are combusted, can be calculated using eq 3:

$$\begin{aligned} &EF_{CE100} \text{ (lb of NOx/}10^6\text{ BTU)} \\ &= (\text{NOx (lb mol)/total carbon (lb mol)}) \\ &\times (3.38 \text{ lb mol C/}10^6\text{ BTU})(46 \text{ lb of } NO_2\text{/lb mol NOx}) \end{aligned} \quad (3)$$

where EF_{CE100} is the emission factor assuming a combustion efficiency of 100%.

An emission factor of the form reported in AP-42,[1] in units of lb of NOx as NO_2 per million BTU of flared gases, accounting only for flared gases that are actually completely combusted, can be calculated using eq 4:

$$\begin{aligned} &EF_{CEact} \text{ (lb of NOx/}10^6\text{ BTU)} \\ &= (\text{NOx (lb mol)/}CO_2\text{ (lb mol)})(3.38 \text{ lb mol C/}10^6\text{ BTU}) \\ &\times (46 \text{ lb of } NO_2\text{/lb mol NOx}) \end{aligned} \quad (4)$$

where EF_{CEact} is the emission factor assuming the actual combustion efficiency observed in the test.

Equations 3 and 4 assume that the sample extracted from the plume is representative of the entire plume. Herndon et al.[7] provide a variety of evidence supporting this assumption. For this work, the assumption is best supported by noting that the ratio of NOx/CO_2, measured throughout any single flare test, was constant as the extractive sampler drew combustion gases in from a variety of locations in the plume. Figure 1 shows representative data from test S13.4R3. Time series for the measurements of CO_2, NOx, CO, formaldehyde (HCHO), ethene (C_2H_4), and ethyne (C_2H_2) in the plume are all highly correlated, indicating that the ratio of NOx/CO_2, on which the emission factors are based, is consistent throughout a 7−10 min flare test in which the extractive sampler drew samples from parts of the plume with varying degrees of dilution by ambient air. Figure 2 shows values of the ratio throughout a 5 min experiment. More details concerning the extractive sampling analysis are available in Herndon et al.[7]

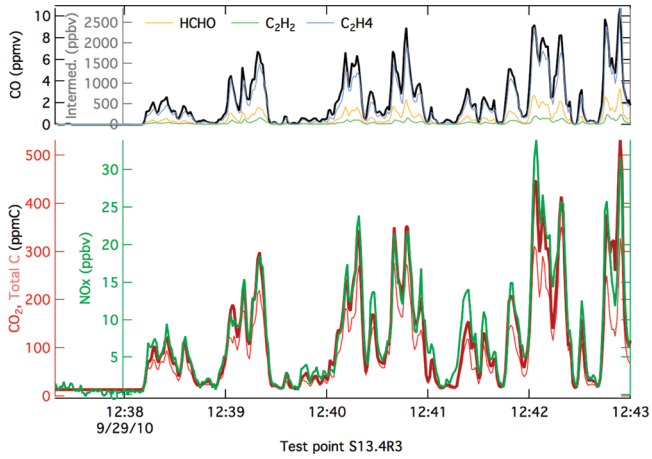

Figure 1. Time series for the S13.4R3 test. The time series for the measurements of CO_2, NOx, CO, formaldehyde (HCHO), ethene (C_2H_4), and ethyne (C_2H_2) are depicted from bottom to top. The dark red trace (total C) is the sum of all forms of carbon detected in the flare plume in units of ppm C and plotted on the same scale as the CO_2 measurement.

RESULTS AND DISCUSSION

Emission Factors. Tables 4 and 5 report NOx emission factors for the steam and air assisted flares, along with average CO/CO_2 molar ratios in the flare plume. The average CO/CO_2 ratio in the plumes in any individual test in these test series exceeded 0.04 in only one experiment (A7.4R1, where CO/CO_2 was 0.0762). Since the heat released by forming CO is less than the heat released by forming CO_2, the fraction of heat released due to the formation of CO is less than 3% of the heat released due to the formation of CO_2 in all but one experiment.

dx.doi.org/10.1021/ie300179x | Ind. Eng. Chem. Res. XXXX, XXX, XXX−XXX

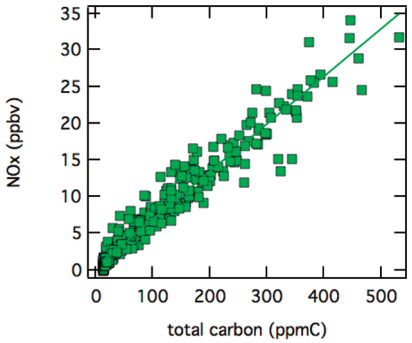

Figure 2. Correlation plot for the determination of NOx emission ratio. The NOx measurement data are plotted vs the total ppm C for the S13.4R3 test point. The slope of the line is 0.065 ± 0.002 ppbv NOx/ppmv total C.

Because this heat release is small and because CO was the dominant product of incomplete combustion, the emission factors reported in Tables 4 and 5 as EF_{CEact} account for only heat release due to CO_2 formation (as described in eq 4).

The observed ratios of NOx/total carbon range from 40 × 10^{-6} to 530 × 10^{-6} ppb NOx/ppb C (molar ratio), corresponding to emission factors ranging from roughly 10% of the AP-42 emission factor to 120% of the AP-42 emission factor. The air assisted flare had generally higher emissions than the steam assisted flares. These results are generally consistent with the emission factors reported by the TCEQ for high BTU gases where the emissions reported for air assisted flares are more than double those for steam assisted flares (0.14 vs 0.049 lb of NOx per million BTU of heating value). However, the TCEQ reports virtually identical emission factors for low heating value gases for air and steam assisted flares (0.064 and 0.068 lb of NOx per million BTU of heating value). The results reported here suggest that, for low heating value gases, air assisted flares should have higher NOx emission rates than steam assisted flares.

As expected, for both the air assisted and steam assisted flares, the highest NOx emission ratios (and emission factors) were observed at the highest values of CE. As shown in Figures 3 and 4, for both types of flares, NOx emission factors decreased by roughly a factor of 2 as CE dropped from roughly 1 to 0.9, and then remained relatively constant as CE continued to decrease to 0.8.

Implications for Emissions in the Houston Area. The emission factors reported in Tables 4 and 5 suggest that, under low flow conditions, NOx emissions from flares may range between 10 and 120% of the average emission factors suggested in AP-42. The impact of these uncertainties in emission factors on air quality can be roughly assessed by comparing flaring emissions to total region-wide NOx emissions. Pavlovic et al.[11] report a special inventory of vent gas fed to flares in the Houston area for 2006 and demonstrate that, for many flares, the majority of the vent gas fed to flares is associated with low flow conditions. Using the standard emission factor of 0.068 lb of NOx/10^6 BTU leads to an estimate of 1.4 tons/day of NOx from flaring. This is roughly 0.9% of the total industrial NOx emissions in 2009 (157 tons/day) and 0.3% of the total NOx emissions for the Houston region in 2009 (444 tons/day).[12]

While these emissions, on average, are a small percentage of total NOx emissions in the Houston area, they are not constant. Figure 5 shows hourly NOx emissions from a single flare in the Houston area. This single flare can have emissions of up to 0.8 ton/day (based on the lower heating value of the gases sent to the flare and the AP-42 emission factor). Since this NOx can be co-emitted with reactive volatile organic compounds (VOCs), the ozone formation potential of these emissions can be large.[13]

Al-Fadhli et al.[13] have used photochemical modeling to examine the impact, on ozone formation, of increased VOC emissions associated with low flare CE. They found that, for certain large flares in the Houston area, ozone concentrations could be enhanced by up to 15 ppb under some conditions. For one large flare located at a petroleum refinery/petrochemical complex, increases in ozone concentrations of up to 40 ppb

Table 4. NOx Emissions and Emission Factors for Steam Assisted Flare Tests

flare test no.	CE (%)	NOx/total C molar ratio (×10^6)	EF_{CE100} (lb of NOx/10^6 BTU)	NOx/CO_2 molar ratio (×10^6)	CO/CO_2 molar ratio	EF_{CEact} (lb of NOx/10^6 BTU)[a,b]
			Test Series 12 (Propane/Natural Gas Mix)			
S12.1R1	97.4	114 ± 2.5	0.018	119 ± 5.3	0.0087	0.019
S12.1R2	96.9	100 ± 2.1	0.016	102 ± 4.3	0.0059	0.016
S12.2R1	91.0	90 ± 1.0	0.014	96 ± 2.1	0.0103	0.015
S12.2R2	92.4	57 ± 11.1	0.009	60 ± 24	0.0114	0.009
S12.3R1	77.3	57 ± 3.0	0.009	70 ± 7.5	0.0222	0.011
S12.3R2	75.5	53 ± 1.8	0.008	66 ± 4.4	0.0228	0.010
S12.4R1	38.0	43 ± 0.7	0.007	108 ± 1.8	0.0349	0.017
			Test Series 13 (Propane/Natural Gas Mix)			
S13.1R1	98.0	144 ± 1.1	0.022	146 ± 2.1	0.0036	0.023
S13.2R1	94.6	105 ± 0.7	0.016	109 ± 1.4	0.0081	0.017
S13.3R1	87.8	87 ± 4.1	0.014	92 ± 9.1	0.0127	0.014
S13.4R1	42.5	69 ± 3.5	0.011	135 ± 14.5	0.0344	0.021
S13.4R2	46.9	55 ± 0.8	0.009	98 ± 2.7	0.0380	0.015
S13.4R3	60.2	65 ± 0.8	0.010	91 ± 2.4	0.0292	0.014
S13.5R1	83.1	72 ± 0.7	0.011	82 ± 1.7	0.0212	0.013
			Test Series 14 (Propane/Natural Gas Mix)			
S14.1R1	98.9	212 ± 2.3	0.033	214 ± 4.7	0.0023	0.033
S14.4R1	95.3	181 ± 3.9	0.028	186 ± 8.0	0.0071	0.028

[a]AP-42 reported the emission factor is 0.068 lb of NOx per million BTU of heating value. [b]TCEQ reported the emission factors for air assisted flares are 0.14 and 0.064 lb of NOx per million BTU of heating value for high and low heating value gases, respectively. TCEQ reported the emission factors for steam assisted flares are 0.049 and 0.068 lb of NOx per million BTU of heating value for high and low heating value gases, respectively.

dx.doi.org/10.1021/ie300179x | Ind. Eng. Chem. Res. XXXX, XXX, XXX−XXX

Table 5. NOx Emissions and Emission Factors for Air Assisted Flare Tests

flare test no.	CE (%)	NOx/total C molar ratio ($\times 10^6$)	EF_{CE100} (lb of NOx/10^6 BTU)	NOx/CO_2 molar ratio ($\times 10^6$)	CO/CO_2 molar ratio	EF_{CEact} (lb of NOx/10^6 BTU)[a,b]
			Test Series 7 (Propane/Natural Gas Mix)			
A7.1R1	98.6	473 ± 6.0	0.074	475 ± 11.9	0.0010	0.074
A7.1R2	99.8	533 ± 9.0	0.083	534 ± 18.0	0.0009	0.083
A7.2R1	93.0	357 ± 5.9	0.056	377 ± 12.3	0.0133	0.059
A7.2R2	91.7	298 ± 8.2	0.046	317 ± 16.9	0.0124	0.049
A7.3R1	81.6	209 ± 2.6	0.032	240 ± 5.9	0.0287	0.037
A7.3R2	77.4	213 ± 1.5	0.033	257 ± 3.8	0.0400	0.040
A7.4R1	61.4	210 ± 4.4	0.033	417 ± 33.9	0.0762	0.065
A7.5R1	87.2	259 ± 3.7	0.040	283 ± 7.3	0.0190	0.044

[a]AP-42 reported the emission factor is 0.068 lb of NOx per million BTU of heating value. [b]TCEQ reported the emission factors for air assisted flares are 0.14 and 0.064 lb of NOx per million BTU of heating value for high and low heating value gases, respectively. TCEQ reported the emission factors for steam assisted flares are 0.049 and 0.068 lb of NOx per million BTU of heating value for high and low heating value gases, respectively.

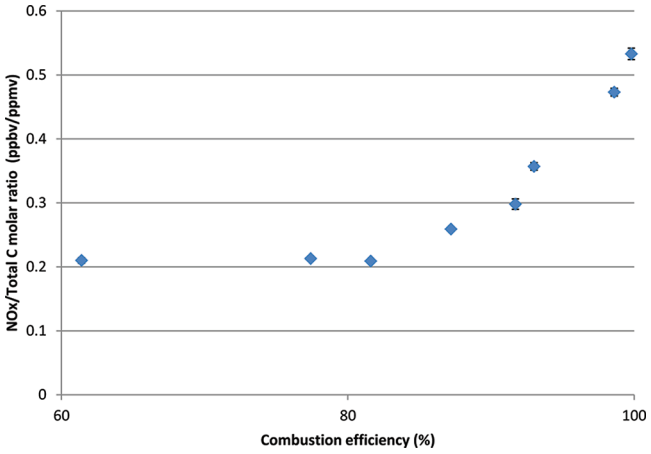

Figure 3. NOx emission ratio plotted vs propane combustion efficiency.

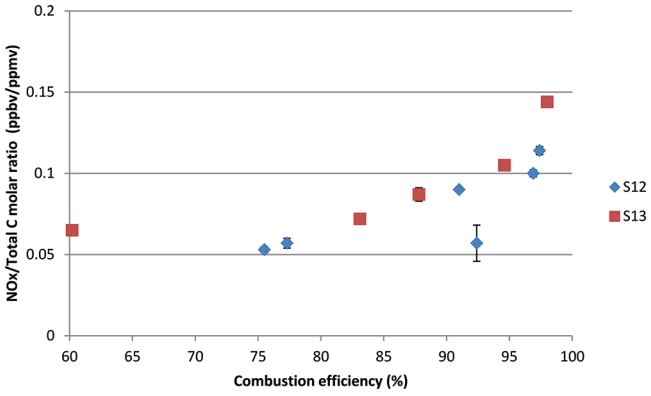

Figure 4. NOx emission ratio (relative to total carbon) plotted vs propane combustion efficiency.

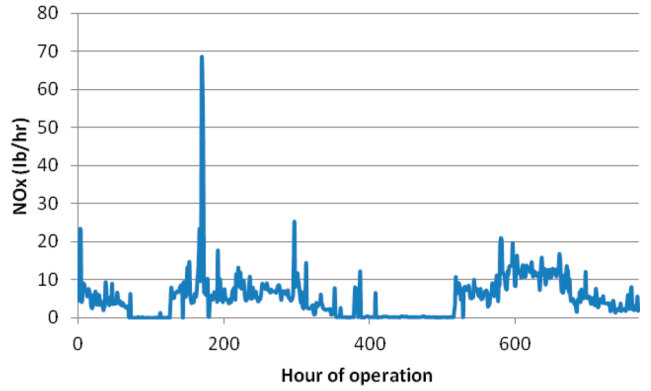

Figure 5. Temporal distribution of NOx emissions for a flare in the Houston area during a month-long period (768 h) in 2006.[11]

were predicted. These analyses all used NOx emissions based on the AP-42 emission factors. Applying the same photochemical modeling tools as employed by Al-Fadhli et al.,[13] the changes in ozone production due to reduced NOx emissions were estimated. Since it is not possible to precisely estimate NOx emissions of flares operating in Houston based on the work reported here (key parameters such as air assist rates and steaming rates are not reported for the flares in Houston), it was assumed in the photochemical modeling that the NOx emissions could be 50% of the AP-42 value for steam-assisted flares operating at 98% CE (see Table 4). For 75 and 90% CE, it was assumed in the photochemical modeling that NOx emissions could be 25% of the AP-42 value (see Table 4). For the flare that produced the largest changes in ozone concentrations, changing the NOx emissions at 75 and 90% CE resulted in small changes in ozone concentrations relative to the changes in ozone concentrations associated with the enhanced hydrocarbon emissions associated with lower CE. For example, at 75% CE, the maximum increase in ozone concentration compared to an assumed 98% CE efficiency (DRE) is 21 ppb, using AP-42 emission factors. This value is unchanged if NOx emissions in the flare are lowered to 25% of the AP-42 value. At 90% CE, the maximum increase in ozone concentration compared to an assumed 98% CE is 8.3 ppb, using AP-42 emission factors. This value increases to 9.4 ppb if NOx emissions in the flare are lowered to 25% of the AP-42 value. There are some localized changes of ozone very close to the flare, but in general, the impacts of reduced NOx emissions from flaring at low CE had a smaller impact on ozone formation than the increased hydrocarbon emissions associated with flaring at low CE. This result is partially due to the fact that changes in CE have a greater impact on hydrocarbon emissions than NOx emissions. Decreasing CE from 98 to 75% increases hydrocarbon emissions by more than an order of magnitude. In contrast, NOx emissions are reduced by only a factor of 4 when reduced to 25% of their AP-42 value. In addition, the flares are generally located in facilities that have many other NOx emission sources, and the hydrocarbons from the flare can react with either NOx from the flare or NOx from other sources in the complex.

dx.doi.org/10.1021/ie300179x | Ind. Eng. Chem. Res. XXXX, XXX, XXX−XXX

CONCLUSION

Operating with low heating value gases, with potentially low combustion efficiencies, flares produce lower flame temperatures than when operating with high heating value gases at high combustion efficiencies. This can lead to reduced formation of NOx in the flame. For a series of tests conducted under low flow conditions, with low heating value gases, NOx emission factors ranged between 10 and 120% of the NOx emission factor reported in AP-42. Emissions were lower in steam assisted flare tests than in air assisted flare tests, and NOx emissions fell as CE decreased. Photochemical modeling simulations indicated that these reductions in NOx emissions had relatively small impacts on the ozone formation potential of flares operating at low CE.

AUTHOR INFORMATION

Corresponding Author

*E-mail: allen@che.utexas.edu. Tel.: (512) 475-7842.

Notes

The authors declare no competing financial interest.

REFERENCES

(1) U.S. Environmental Protection Agency (EPA). AP-42 Emissions Factors "Chapter 13: Miscellaneous Sources". http://www.epa.gov/ttn/chief/ap42/index.html (accessed December 2011).

(2) Texas Commission on Environmental Quality, Air Permits Division. Air Permit Technical Guidance for Chemical Sources: Flares and Vapor Oxidizers, RG-109 (Draft), October 2000.

(3) McDaniel, M. *Flare Efficiency Study*; EPA-600/2-83-052, July 1983. Available at http://www.epa.gov/ttn/chief/ap42/ch13/index.html (accessed December 2011).

(4) Torres, V. M.; Herndon, S.; Kodesh, Z.; Allen, D. T. Industrial flare performance at low flow conditions. 1. Study overview. *Ind. Eng. Chem. Res.* **2012**, DOI: 10.1021/ie202674t.

(5) Torres, V. M.; Herndon, S.; Allen, D. T. Industrial flare performance at low flow conditions. 2. Steam- and Air-assisted flares. *Ind. Eng. Chem. Res.* **2012**, DOI: 10.1021/ie202675f.

(6) Allen, D. T.; Torres, V. M. *2010 TCEQ Flare Study Project, Final Report*; Available at http://www.tceq.texas.gov/assets/public/implementation/air/rules/Flare/TCEQ2010FlareStudyDraftFinalReport.pdf (accessed December 2011).

(7) Herndon, S. C.; Nelson, D. D.; Wood, E. C.; Knighton, W. B.; Kolb, C. E.; Kodesh, D. T.; Torres, V. M.; Allen, D. T. Application of the carbon balance method to flare emissions characteristics. *Ind. Eng. Chem. Res.* **2012** (submitted to this Special Issue); also available from corresponding author.

(8) Texas Commission on Environmental Quality. 2010 Flare Study Quality Assurance Project Plan. Available at http://www.tceq.texas.gov/assets/public/implementation/air/rules/Flare/QAPP.pdf (accessed July 2011).

(9) Knighton, W. B.; Herndon, S. C.; Franklin, J. F.; Wood, E. C.; Wormhoudt, J.; Brooks, W.; Fortner, E. C.; Allen, D. T. Direct measurement of volatile organic compound emissions from industrial flares using real-time on-line techniques: Proton Transfer Reaction Mass Spectrometry and Tunable Infrared Laser Differential Absorption Spectroscopy. *Ind. Eng. Chem. Res.* **2012**, DOI: 10.1021/ie202695v.

(10) Wood, E. C.; Herndon, S. C.; Onasch, T. B.; Kroll, J. H.; Canagaratna, M. R.; Kolb, C. E.; Worsnop, D. R.; Neuman, J. A.; Seila, R.; Zavala, M.; Knighton, W. B. A case study of ozone production, nitrogen oxides, and the radical budget in Mexico City. *Atmos. Chem. Phys.* **2009**, *9* (7), 2499−2516.

(11) Pavlovic, R. T.; Allen, D. T.; McDonald-Buller, E. C. Temporal Variability in Flaring Emissions in the Houston-Galveston Area. *Ind. Eng. Chem. Res.* **2012**, DOI: 10.1021/ie2013357.

(12) Texas Commission on Environmental Quality. Revisions to the State Implementation Plan for the Control of Ozone Air Pollution, Houston-Galveston-Brazoria Eight-Hour Ozone Nonattainment Area, Adopted May 23, 2007, Docket No. 2006-1874-SIP. Available at http://www.tceq.texas.gov/airquality/sip/may2007hgb.html#narratives.

(13) Al-Fadhli, F. M.; Kimura, Y.; McDonald-Buller, E. C.; Allen, D. T. Impact of flare destruction efficiency and products of incomplete combustion on ozone formation in Houston, Texas. *Ind. Eng. Chem. Res.* **2012**, DOI: 10.1021/ie201400z.

Atmos. Chem. Phys., 9, 2499–2517, 2009
www.atmos-chem-phys.net/9/2499/2009/

Atmospheric Chemistry and Physics

A case study of ozone production, nitrogen oxides, and the radical budget in Mexico City

E. C. Wood[1], S. C. Herndon[1], T. B. Onasch[1], J. H. Kroll[1], M. R. Canagaratna[1], C. E. Kolb[1], D. R. Worsnop[1], J. A. Neuman[2], R. Seila[3], M. Zavala[4], and W. B. Knighton[5]

[1]Aerodyne Research, Inc., Billerica, Massachusetts, USA
[2]Earth System Research Laboratory, NOAA, Boulder, Colorado, USA
[3]National Exposure Research Laboratory, Environmental Protection Agency, Research Triangle Park, North Carolina, USA
[4]Molina Center for Energy and the Environment, La Jolla, California, USA
[5]Department of Chemistry and Biochemistry, Montana State University, Bozeman, Montana, USA

Received: 14 July 2008 – Published in Atmos. Chem. Phys. Discuss.: 19 August 2008
Revised: 25 March 2009 – Accepted: 31 March 2009 – Published: 7 April 2009

Abstract. Observations at a mountain-top site within the Mexico City basin are used to characterize ozone production and destruction, nitrogen oxide speciation and chemistry, and the radical budget, with an emphasis on a stagnant air mass observed on one afternoon. The observations compare well with the results of recent photochemical models. An ozone production rate of ∼50 ppbv/h was observed in a stagnant air mass during the afternoon of 12 March 2006, which is among the highest observed anywhere in the world. Approximately half of the ozone destruction was due to the oxidation of NO_2. During this time period ozone production was VOC-limited, deduced by a comparison of the radical production rates and the formation rate of NO_x oxidation products (NO_z). For $[NO_x]/[NO_y]$ values between 0.2 and 0.8, gas-phase HNO_3 typically accounted for less than 10% of NO_z and accumulation-mode particulate nitrate ($NO^-_{3(PM1)}$) accounted for 20%–70% of NO_z, consistent with high ambient NH_3 concentrations. The fraction of NO_z accounted for by the sum of $HNO_{3(g)}$ and $NO^-_{3(PM1)}$ decreased with photochemical processing. This decrease is apparent even when dry deposition of HNO_3 is accounted for, and indicates that HNO_3 formation decreased relative to other NO_x "sink" processes during the first 12 h of photochemistry and/or a significant fraction of the nitrate was associated with the coarse aerosol size mode. The ozone production efficiency of NO_x on 11 and 12 March 2006 was approximately 7 on a time scale of one day. A new metric for ozone production efficiency that relates the dilution-adjusted ozone mixing ratio to cumulative OH exposure is proposed.

Correspondence to: E. C. Wood
(ezrawood@aerodyne.com)

1 Introduction

1.1 Megacities and air pollution

Urban areas are often characterized by the presence of large emissions of pollutants, including volatile organic compounds (VOCs), nitrogen oxides ($NO_x \equiv NO+NO_2$), sulfur dioxide (SO_2), and particulate matter (PM). Many of these compounds (e.g., benzene and diesel PM) are directly toxic to humans (Khan, 2007; McCreanor et al., 2007; Yauk et al., 2008). These primary pollutants react in the atmosphere, forming secondary pollutants such as ozone, formaldehyde, nitric acid, and secondary PM. The spatial distribution of secondary pollutants and their direct effect on public health, vegetation, and the Earth's radiative balance can be quite different than that of their precursor primary pollutants. Ozone (O_3), in particular, plays a central role in tropospheric chemistry, as it is both a product and initiator of photochemistry as well as a potent greenhouse gas. Ozone is one of the US EPA's six criteria air pollutants subject to national ambient air quality standards (NAAQS) created to protect public health. Numerous air basins across the world, spanning urban, suburban, and rural areas, have difficulty meeting relevant air quality standards for O_3. Understanding the formation of O_3 and the transformations of its precursors (VOCs and NO_x) is

Published by Copernicus Publications on behalf of the European Geosciences Union.

crucial for reducing air pollution on both urban and regional scales. Over the past several decades great effort has been focused on characterizing air pollution and atmospheric photochemistry in the US and Europe (Carslaw et al., 2001; Emmerson et al., 2007; Kleinman, 2005; Nunnermacker et al., 1998; Ryerson et al., 2001; Tressol et al., 2008). However, there are few studies of tropospheric photochemistry in developing megacities – where much of the projected increases in population and pollutant emissions over the next several decades are expected to occur (Molina et al., 2004).

During the 2006 MILAGRO (Megacity Initiative: Local And Global Research Observations) campaign, Mexico City was used as a test case for developing megacities. Mexico City is currently the third most populous urban agglomeration in the world, with a population of 19 million (UN, 2008). Although the air quality in Mexico City has improved greatly over the past 10 years (de Foy et al., 2008), it remains highly polluted, with ozone concentrations frequently exceeding 100 ppbv. The motor vehicle fleet, consisting of over 4 million cars and trucks, is older than the US fleet, and approximately 30% of light-duty gasoline vehicles do not have functioning 3-way catalytic converters (CAM, 2008). The latitude (19° 24° N) and altitude of the Mexico City plateau (2.2 km above sea level) leads to elevated actinic flux levels throughout the year. The high altitude also tends to cause fuel-rich combustion in the vehicle fleet.

Inferences about tropospheric photochemistry based on measurements from stationary sites are often complicated by the fact that the observed changes in pollutant concentrations over time are a function of not just chemistry but also meteorology and emissions patterns. Additionally, the air masses observed usually contain a range of aged and fresh pollutants, since primary emission sources of NO_x, VOCs, and PM continue to impact most stationary sites throughout the day. Measurements on board instrumented aircraft are often better suited for tracking the evolution of an air mass over time (Ryerson et al., 2001), though the first 3–7 h of atmospheric oxidation following sunrise usually occur in a shallow boundary layer near the urban surface where it may be unfeasible to fly. Smog chamber studies have provided insight into numerous atmospheric processes, but are challenged by wall interactions and the difficulty in realistically mimicking atmospheric parameters such as actinic flux, low pollutant concentrations, and total atmospheric composition. Some atmospheric processes have not been adequately characterized by laboratory studies, e.g. secondary organic aerosol formation (de Gouw et al., 2005; Volkamer et al., 2006). This emphasizes the importance in quantifying such processes using atmospheric measurements.

In this paper, we present measurements from Pico de Tres Padres, a unique mountain-top stationary site that is situated within the Mexico City basin but is minimally impacted by nearby emissions. The air masses observed on 12 March 2006 were stagnant in the afternoon and provided an excellent opportunity to study ozone chemistry without the confounding influence of transport. Secondary organic aerosol formation at this site is analyzed and described in two related manuscripts (Wood et al., 2009; Herndon et al., 2008). The observations and inferences regarding tropospheric chemistry are compared to the predictions of several photochemical models (Lei et al., 2007; Madronich, 2006; Tie et al., 2007). Such observational-based characterizations of photochemistry, even if focused on a short period of time, are crucial for testing our understanding of the underlying photochemical processes that control secondary air pollution.

1.2 Urban photochemistry overview

Tropospheric ozone is produced by the oxidation of VOCs (volatile organic compounds) in the presence of nitrogen oxides ($NO_x \equiv NO+NO_2$) and sunlight. Central to understanding ozone production is the photostationary state formed between NO, NO_2, and O_3 in sunlight:

$$NO + O_3 \longrightarrow NO_2 + O_2 \quad \text{(R1)}$$

$$NO_2 + h\nu(\lambda < 400\,\text{nm}) \longrightarrow NO + O(^3P) \quad \text{(R2)}$$

$$O(^3P) + O_2 + M \longrightarrow O_3 + M \quad \text{(R3)}$$

Net reaction: null

NO can also be oxidized to NO_2 by compounds other than O_3, most importantly hydroperoxy radicals (HO_2) and organic peroxy radicals (RO_2, where "R" represents an organic group):

$$HO_2 + NO \longrightarrow OH + NO_2 \quad \text{(R4)}$$

$$RO_2 + NO \longrightarrow RO + NO_2 \quad \text{(R5a)}$$

During the day, most of the NO_2 formed from R4 and R5a undergoes photolysis, leading to the creation of ozone (R2 and R3). When discussing ozone production quantitatively, it is useful to use the concept of O_x ("odd-oxygen"), which in the troposphere is often defined as the sum of O_3 and NO_2 ($[O_x] \equiv [O_3]+[NO_2]$). NO_2 is included because it acts as a reservoir of O_3, formed by R1 or as a source of O_3 (R4 and R5a). The sum of the rates of R4 and R5a is therefore equated to the instantaneous production rate of O_x:

$$P(O_x) = \sum_i k_{5ai}[R_iO_2][NO] + k_4[HO_2][NO] \quad (1)$$

Although the right-hand side of Eq. (1) is often defined as $P(O_3)$ (i.e., the instantaneous production rate of O_3 rather than O_x), by defining it as $P(O_x)$ instead there is no need to account for reactions of NO_2 subsequent to its formation, and the expression holds true at all light levels. We note that during the day, typically over 95% of the NO_2 will undergo photolysis to form O_3 (the remainder reacts to form HNO_3 or other compounds), and thus the terms "O_x production" and "ozone production" are often nearly equivalent. However, in the presence of large concentrations of NO, photochemically formed O_x may appear mainly in the form of

NO_2, underscoring the advantage of considering O_x rather than O_3. A more inclusive definition of $[O_x]$ includes $O(^1D)$, $O(^3P)$, NO_3, and N_2O_5, but these compounds are reasonably assumed to be minor contributors to O_x concentrations compared to O_3 and NO_2 during daytime.

In fresh urban plumes with active photochemistry, the production rate of O_x is often much greater than the total rate of the O_x losses, and thus ozone can accumulate in high concentrations (>100 ppbv). O_x is fairly long-lived, with a lifetime range of about a day to weeks.

The sum of NO_x and its oxidation products are known as "reactive nitrogen" or NO_y ($NO_y \equiv NO+NO_2+HNO_3+NO^-_{3(PM1)}$+organic nitrates+$NO_3+2N_2O_5+$ HONO+...), and the oxidation products alone are known as NO_z ($NO_z \equiv NO_y - NO_x$). All NO_z compounds, with the exception of HONO, NO_3, and N_2O_5, are the result of three categories of $RO_x - NO_x$ reactions:

$$RO_2 + NO + M \longrightarrow RONO_2 + M \quad \text{(R5b)}$$

$$NO_2 + OH + M \longrightarrow HNO_3 + M \quad \text{(R6)}$$

$$RO_2 + NO_2 + M \longleftrightarrow RO_2NO_2 + M \quad \text{(R7)}$$

Aerosol nitrate is mainly formed as ammonium nitrate following reaction of HNO_3 with NH_3. In this paper, the products of R5b and R7 are collectively referred to as "organic nitrates", and comprise peroxyacyl nitrates formed from R7 (most commonly peroxyacetyl nitrate, PAN) and multi-functional alkyl nitrates formed from R5b. Partitioning of organic nitrates can form aerosol nitrate as well (Lim and Ziemann, 2005), though the extent to which this occurs in the atmosphere is currently not well quantified.

2 Experimental section

Measurements were made aboard the Aerodyne mobile laboratory, a panel truck outfitted with a suite of real-time instrumentation for gaseous and fine-particulate measurements (Herndon et al., 2005; Kolb et al., 2004). The mobile laboratory was deployed during the MAX/MEX portion of the MILAGRO-2006 campaign to various sites throughout the Mexico City Metropolitan Area (MCMA). Sites were chosen based on the 2–5 day weather forecast and knowledge of how synoptic scale weather patterns typically produce prevailing basin flow archetypes (de Foy et al., 2005; de Foy et al., 2008; Fast et al., 2007). The goal of these deployments was to sample the urban outflow. Some of the mobile laboratory deployment locations are depicted in Fig. 1. Most of the data presented in this manuscript were recorded at Pico de Tres Padres (PTP), which is the highest point in the Sierra de Guadalupe range in the northern section of the MCMA. The sampling altitude at PTP was 720 m above the MCMA valley elevation of 2.2 km. PTP is situated between "T0" and "T1", two of the MAX/MEX supersites

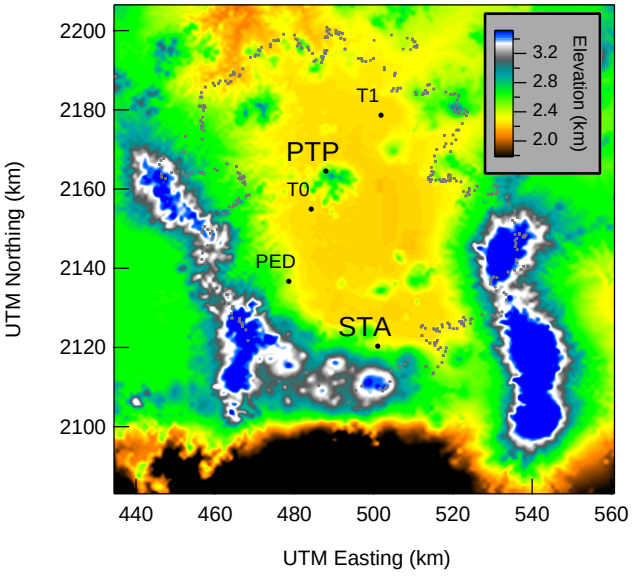

Fig. 1. Selected deployment locations for the mobile laboratory during MILAGRO-2006. The figure is a topographical representation of the Mexico City Metropolitan Area. The sites "T0" and "T1" are the campaign supersites. This work focuses on measurements from Pico de Tres Padres (PTP). Santa Ana (STA) and Pedregal (PED) are the sites of two additional mobile laboratory deployments in the south of the city. The urban core of the federal district is encompassed by T0, PED, and STA. UTM=universal transverse mercator. The border of the *Distrito Federal* is depicted by the grey dots.

(http://www.asp.bnl.gov/MAX-Mex.html) that were hosted by the Instituto Nacional de Petroleo and the Universidad Tecamac, respectively. PTP is ~10 km northeast of T0 and ~19 km southwest of T1.

Nitric oxide (NO) and total reactive nitrogen (NO_y) were measured with a ThermoElectron model 42C chemiluminescence sensor in conjunction with an external molybdenum (Mo) converter that was mounted to the roof of the mobile lab. Measurements of NO were also made with an ECO Physics model CLD 88Y chemiluminescence sensor. Both instruments were periodically calibrated with a standard tank of NO (Scott Specialty gases), diluted with NO_x-free zero air using a ThermoElectron dynamic gas calibrator. The efficiency of the Mo converter for NO_y was quantified by calibrations with NO_2 and n-propyl nitrate. Particulate nitrate was assumed to be converted with the same efficiency as gas-phase species given the high surface area mesh design of the molybdenum converter (Williams et al., 1998). The 1σ uncertainty of the NO 1-min data is the greater of 7% or 0.5 ppbv (NO), and the uncertainty of the NO_y data is estimated as the greater of 15% or 1.5 ppbv. NO_z concentrations were calculated using the NO_y, NO, and NO_2 measurements (i.e., $[NO_z]=[NO_y]-[NO]-[NO_2]$).

Two dual-laser Aerodyne tunable infrared laser differential absorption spectrometers (TILDAS) using pulsed

quantum cascade lasers (Herndon et al., 2007; Nelson et al., 2004) were used to measure NO_2 (at 1606 cm^{-1}), CO (at 2100 cm^{-1}), HCHO (at 1722 cm^{-1}), HNO_3 (at 1721 cm^{-1}), and NH_3 (at 965 cm^{-1}). The inlet for these two instruments consisted of 1 m of heated 1/4" OD PFA tubing followed by a heated teflon-coated cyclone (URG-2000-30ED; aerosol diameter size cut-off of 0.8 μm at a flow rate of 8 liters per minute) and a siloxyl-coated glass orifice to reduce the sampling pressure. The estimated uncertainties for the NO_2, CO, and HCHO measurements are 8%. In order to assess the inlet transmission for $NH_{3(g)}$ and HNO_3, small flows of both gases from permeation tube sources were introduced into the inlet four times. The ambient aerosol loadings (measured with the aerosol mass spectrometer) during these standard additions were in the range 10 to 30 $\mu g/m^3$. The ambient temperature ranged from 16° to 22°C and the relative humidity ranged from 28% to 45%. For comparison, the range of conditions observed between 06:00 and 20:00 LT at PTP was 10° to 27°C and 12% to 75% relative humidity. Inlet losses of NH_3 and HNO_3 were on order 28% and 45% respectively; the measurements have been proportionally corrected. Given the size of the inlet losses and the limited range of ambient conditions under which standard additions were performed, we estimate an uncertainty of 50% for the HNO_3 measurements (the NH_3 measurements are not used quantitatively in this analysis). Only NH_3 and HNO_3 measurements from PTP are included in the analysis.

Ozone (O_3) was measured with a dual-beam absorbance photometer at 254 nm (2B Tech model 205), with an accuracy of 2%. Acetaldehyde, acetone, acetonitrile, benzene, and C3-benzene compounds (sum of C_9H_{12} isomers and C_8H_8O isomers) were measured with a proton-transfer mass spectrometer (Rogers et al., 2006). With the exception of acetonitrile, concentrations were derived from response factors determined from a calibrated gas standard with an accuracy of 25%. Acetonitrile concentrations were determined from transmission corrected ion intensities and equations derived from standard reactions kinetics (Lindinger et al., 1998) assuming a reaction rate constant of 4.74×10^{-9} ml molecule^{-1} s^{-1} (Zhao and Zhang, 2004).

Particulate nitrate (vacuum aerodynamic diameters between 60 and 800 nm–50% cut points) was measured with an Aerodyne compact time-of-flight aerosol mass spectrometer (C-ToF-AMS) with an accuracy of 20% (Canagaratna et al., 2007; Drewnick et al., 2005; Liu et al., 2007). A collection efficiency due to particle bounce of 0.5 was used for all species during the MILAGRO study based on comparisons with other aerosol instrumentation, including a co-located Scanning Mobility Particle Sizer (SMPS; TSI model 3080) and recent laboratory studies (Canagaratna et al., 2007;Matthew et al., 2008). Size distribution measurements from both the AMS and SMPS from this study and previous measurements in Mexico City (Salcedo et al., 2006) indicate that the particulate measurements discussed here represent PM_1 mass loadings.

Thirty-one alkenes were quantified using GC-FID from whole air samples collected in stainless steel canisters (Seila et al., 2001). The alkenes were ethene, propene, 1-butene, trans-2-butene, cis-2-butene, 1-pentene, trans-2-pentene, cis-2-pentene, 1-hexene, 1-heptene, t-3-hexene, 1-octene, t-4-octene, 1-decene, isobutene, 3-methyl-1-butene, 2-methyl-1-butene, 2,4,4-trimethyl-1-pentene, 2-methyl-2-butene, 2,4-dimethyl-1-pentene, 2-methyl-2-pentene, 1,3-butadiene, cyclopentene, cyclooctene, cyclohexene, isoprene, limonene, camphene, beta pinene, and alpha pinene.

Photolysis rate constants for O_3, HCHO, acetaldehyde, and acetone were determined by a combination of measurement and model results. The photolysis rates calculated from the Scanning Actinic Flux Spectroradiometer operated by B. Lefer and J. Flynn at the T1 site were used in conjunction with the NCAR tropospheric ultraviolet and visible radiation model (TUV). Equation (2) was used to estimate photolysis rates: $j_{PTP} = \frac{j_{PTP}(TUV)}{j_{T1}(TUV)} \times j_{T1}$(measured) (2)where j_{PTP}(TUV) and j_{T1}(TUV) are the model results and j(measured) is from the T1 measurement. This approach uses TUV to account for the difference in elevation between PTP and T1 (850 m), for which aerosol and absorbing gases affect the optical transmission. The hourly vertical profiles of ozone used in the model were generated from the measurements at T0 and PTP. Although no information regarding the NO_2 and O_3 column above the convective mixing layer was included, the systematic errors associated with this are expected to cancel in the first factor of the right-hand side of Eq. (2). The total ozone column is characterized by the T1 measurements. The ratio of j_{PTP}(TUV)/j_{T1}(TUV) depends on the specific molecular photolysis rate, but for all of the compounds discussed in this work, the altitude correction is less than 16%.

The largest source of uncertainty in the photolysis rate constants by this approach lies in the fact that PTP is ~19 km away from T1 and the cloud cover was not spatially identical. A comparison of the measured radiometer data at T1 and an Eppley UV photometer used aboard the mobile laboratory suggests qualitative agreement when cloud patches moved above the region. For the periods in which the photolysis rates were analyzed, there was minimal cloud cover (i.e., it was not cloudy).

A second source of uncertainty in this approach stems from the differences in albedo and upwelling/downwelling radiation associated with the elevation and topographical differences between T1 and PTP. The T1 measurement data is based on the downwelling radiation, however at PTP the photolysis rate in the sampled air had a contribution from reflected light. We estimate that this contributes an uncertainty of 4% in the calculated photolysis rates, based on the average Mexico City albedo.

Additional sources of error in this approach are due to the absence of modeled absorbers in the 850 m elevation distance between T1 and PTP. Hourly profiles of ozone and NO_2 were used in the model, though SO_2, HONO, HCHO

and acetaldehyde were ignored. The bias introduced by neglecting these absorbers would result in an underestimate of the photolysis rates at PTP since such absorption leads to higher photolysis frequencies at higher altitudes. This underestimate is likely most pronounced in the early morning when the convective mixing layer height is below the altitude of PTP.

The combined uncertainties in the photolysis rates (accounting for the altitude, cloud coverage, albedo, and unknown absorbers) is estimated as 25%.

All stated accuracies reflect 1σ uncertainty. All reaction rate constants used are those from the latest JPL recommendations (Sander et al., 2006). One-minute averages are used for all measurements presented, with the exception of the VOC canister measurements which were 30 min averages. The NO_2 data are one minute averages recorded every three minutes, thereby affecting the O_x and NO_z values too. All linear correlation fits were calculated using a least-squares algorithm that accounts for the uncertainty in both variables.

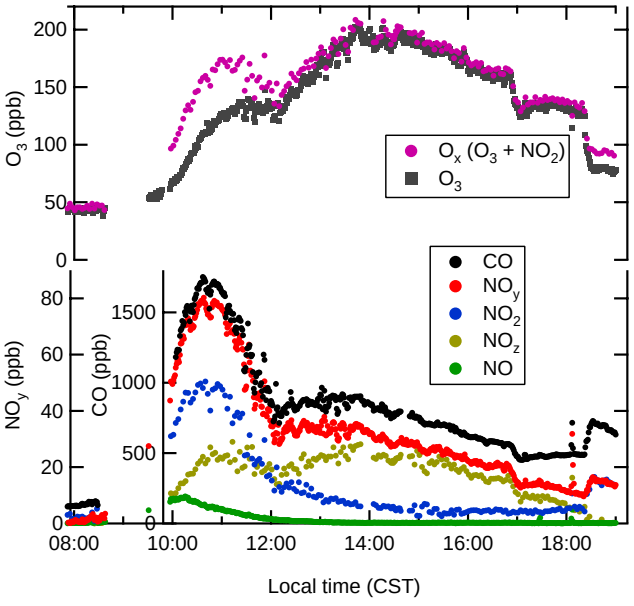

Fig. 2. Time series of several species at PTP on March 12, 2006. The time period between 12:15 and 13:15 was characterized by stagnant air and is used to infer the production rates of O_x and NO_z. The gap in the data between 08:30 and 10:00 is due to instrument maintenance.

3 Results and discussion

3.1 Air masses observed at PTP

Because the mobile laboratory payload did not include any direct measurements of the vertical structure of the atmosphere, the measurements of the convective mixing layer heights at T0 and T1 (Shaw et al., 2007) have been examined as a proxy. Typically, during clear-sky insolation, the mixed layer grew to a height of ∼1 km above T0 by 11:30 local time (LT). CO mixing ratios increased sharply at PTP near 09:30. That pollution reached PTP before the mixing layer height reached the elevation of PTP (as measured at T0 and T1) is most likely due to differential heating and upslope winds.

The altitude and horizontal location within the city and the lack of short "spikes" in the time series of all species indicate that PTP was not greatly affected by nearby emissions, and thus was a near-ideal stationary measurement location for sampling mixed urban emissions during their first 2 to 12 h of photochemistry. This is in contrast to most ground sites within cities, which are usually close (within 100 m) to traffic and other pollution sources. Based on the measured wind speeds, the emissions from the closest neighborhood (∼4 km to the south) would have had on the order of 15–60 min to mix into the urban plume. On 12 March 2006 (the day highlighted in this work), the transport time from other parts of the city was on the order of 1–5 h, whereas vertical mixing time scales in the afternoon are typically less than 30 minutes (Stull, 1988). Therefore, as the mixing layer grew above PTP, the sampled air masses were typically an accumulation of pollutants from many sectors of the city mixed both vertically and horizontally over several hours. Multi-day accumulation of pollutants is rare in Mexico City due to efficient venting (de Foy et al., 2006).

PTP was above the nocturnal boundary layer during most of each night. With the exception of a few episodes in which fresh emissions were brought to the site by strong winds or when trapped residual layers advected past the site, the nighttime measurements were indicative of a clean residual boundary layer. For example, the mean nighttime mixing ratios of CO, O_3, NO_y and CH_3CN (acetonitrile) between 02:00 and 06:00 on 12 March were 132, 44, 0.6, and 0.2 ppbv, respectively. The organic aerosol loading at night was 1.1 $\mu g\,m^{-3}$ (STP, 273 K and 1 atm) and was highly oxidized.

Much of this work focuses on data from 12 March 2006, in which there was a one-hour pause in the rise of the mixing layer in the afternoon. Figure 2 shows a time series of CO, O_3, O_x, NO_y, NO, NO_2, and NO_z concentrations observed at PTP on Sunday, 12 March 2006. Concentrations of all species rose sharply starting at ∼09:00 CST, as upslope winds transported pollutants from below the sampling elevation to PTP. Concentrations of CO (which is relatively photochemically inactive) reached an initial peak at 10:40 due to upslope winds, though the mixing layer depth at T0 did not reach the elevation of PTP (720 m above the city elevation) until ∼11:30 as described earlier. [CO] decreased between 11:00 and 12:00 as the mixing layer rose above PTP and the effect of dilution overweighed the flux of CO from below.

The measurements of the convective mixing depth above T0 show no increase between 12:00 and 13:00 on 12 March 2006 (Shaw et al., 2007). The urban emission inventory (CAM, 2008), which apportions on-road emissions by hour of day, indicates that the amount of CO emitted between 12:00 and 13:00 is equal to 15% of the amount emitted between 05:00 and 12:00. This should lead to an increase of [CO] by approximately 15% above the background mixing ratio if there is no mixing with the residual layer aloft caused by a rising boundary layer. The observed enhancement in [CO] between 12:15 and 13:15 was 14% (calculated as $([CO]_{13:15}-130\,ppbv)/([CO]_{12:15}-130\,ppbv)$ to account for the background CO mixing ratio of 130 ppbv). The favorable comparison between the observed and predicted increase in [CO] complements the T0 measurements showing a pause in the rise of the mixing layer between 12:15 and 13:15. This analysis is not sensitive to inaccuracies in the absolute magnitude of CO emissions; it is sensitive only to the reported *timing* of CO emissions between the early morning and afternoon, since the quantity used is the relative increase in [CO] rather than the absolute mixing ratios. This time period was unlike most other days at PTP, when boundary layer dynamics and advection played much greater roles in determining changes in pollutant concentrations.

A comparison of the ratios of several primary pollutants at PTP and T0 (a site greatly impacted by fresh urban emissions) indicates that the air observed at PTP was representative of mainly urban emissions and was not greatly affected by biomass burning, biogenic VOCs, or other non-urban pollutants. The $\Delta[NO_y]/\Delta[CO]$, Δ[benzene]/Δ[CO], and $\Delta[CH_3CN]/\Delta[CO]$ ratios were deduced from linear fits of the correlation graphs of 1-min data. The $\Delta[NO_y]/\Delta[CO]$ ratio was 0.050 ppbv/ppbv (R = 0.99) on 11 and 12 March, 0.054 ppbv/ppbv (R=0.95) for the entire PTP dataset, and between 0.04 and 0.07 ppbv/ppbv at T0. The Δ[benzene]/Δ[CO] ratio was 1.8 pptv/ppbv (R=0.93) on 11 and 12 March 2006, 1.67 pptv/ppbv (R=0.87) for the entire PTP dataset, and 1.1 to 1.8 at T0. The $\Delta[CH_3CN]/\Delta[CO]$ ratio on 12 March 2006 was between 0.2 to 0.5 pptv/ppbv. Other measurements in urban air have been in the range 0.1–0.3 (Kleinman et al., 2008; Knighton et al., 2007), while the ratios observed in air impacted by biomass burning are between 1 and 7 (de Gouw et al., 2006). This suggests that biomass burning probably did not have a significant impact on the air on 12 March until 18:00, when a biomass burning PM plume was observed. Isoprene (canister) and other biogenic VOCs (e.g., terpenes) typically accounted for less than 10% of the calculated VOC reactivity over the entire PTP dataset, indicating there was only a small influence from biogenic emissions.

3.2 O_x production and loss rates

Given the well-characterized, stagnant meteorology of 12 March 2006, the measurements are used to characterize numerous aspects of tropospheric chemistry. The average wind speed during this time period was 1.5 m/s from the southeast, so the air sampled spanned less than a 6 km horizontal range – most of which is unpopulated land along the mountain slope, with no urban emission sources. For comparison, the distance between T0 and PTP is ~10 km. Other days were excluded from this analysis because of at least one of the following two filtering criteria: 1) the wind speeds were greater than 2 m/s, and 2) [CO] did not show a gradual increase of less than 100 ppbv/h in the afternoon as observed on 12 March. On most other days, [CO] steadily decreased in the afternoon as the mixing depth grew above PTP.

Table 1. Quantification of the destruction (loss) rate of O_x between 12:15 and 13:15 on 12 March 2006. Mixing ratios used for these calculations: $[O_3]$=160 ppb (measured), $[H_2O]$=7 ppth (measured), $[HO_2]$=40 ppt (estimated), $[OH]=6\times10^6$ molec/cm^3 (estimated). A boundary layer height of 0.9 km and a deposition velocity of 0.4 cm/s were used to calculate the dry deposition rate of O_3. The oxidation rate of NO_2 was calculated as $0.8\times P(NO_z)$.

Reaction	Rate (ppbv/h)
$O(^1D)+H_2O$	1.0
HO_2+O_3	0.8
$OH+O_3$	0.2
$NO_2\rightarrow NO_z$	6.0
O_3+VOCs	0.7
O_3 dry deposition	2.6
$NO_3+h\nu\rightarrow NO+O_2$	0.3
Total	11.6

We assume that concentrations of O_x and NO_z were both vertically homogeneous within the mixing layer and horizontally homogeneous within the ~5.4 km air mass sampled during this hour. From 12:15 to 13:15 we interpret the observed increases in $[O_x]$ and $[NO_z]$ to be mainly due to photochemistry, with an estimated uncertainty of 25% due to the coarse level of knowledge regarding the mixing layer depth and the assumption of horizontal homogeneity for $[O_x]$ and $[NO_z]$.

Given these assumptions, the average O_x production rate $P(O_x)$ during this time is estimated using the observed time rate of change of O_x ($\Delta[O_x]/\Delta t$; t ≡ time) and the calculated O_x loss (destruction) rate $L(O_x)$ according to Eq. (2):

$$\Delta[O_x]/\Delta t = P(O_x) - L(O_x) \quad (2)$$

where the sign of $L(O_x)$ is positive. The value of $\Delta[O_x]/\Delta t$ is 37 ppbv/h, calculated from the time series data. $L(O_x)$ is calculated from R6–R7 and R8–R15 as summarized in Table 1:

$$L(O_x) = \Sigma \text{ Rates (R6, R7, R8 to R15)} \quad (3)$$

$$O_3 + h\nu \longrightarrow O(^1D) + O_2 \quad \text{(R8)}$$

$$O(^1D) + H_2O \longrightarrow 2OH \quad \text{(R9)}$$

$$HO_2 + O_3 \longrightarrow OH + 2O_2 \quad \text{(R10)}$$

$$OH + O_3 \longrightarrow HO_2 + O_2 \quad \text{(R11)}$$

$$O_3 + \text{VOCs} \longrightarrow \text{products} \quad \text{(R12)}$$

$$NO_2 + O_3 \longrightarrow NO_3 + O_2 \quad \text{(R13)}$$

$$NO_3 + h\nu \longrightarrow NO + O_2 \quad \text{(R14)}$$

O_3 dry deposition (R15)

The NO_z production rate is used to quantify O_x losses from R6 and R7 because the products of these two reactions form observable NO_z species. Because these two reactions account for approximately 80% of total NO_z production (based on the NO_y speciation observed at the T1 site (Farmer et al., 2009), O_x loss by R6 and R7 is calculated from the observed NO_z production rate (Sect. 3.3.1) multiplied by 0.8. The rates of R10 and R11 are calculated assuming an HO_2 mixing ratio of 40 pptv and an OH concentration of 6×10^6 molecules cm^{-3} (as estimated later in this section and in section 3.3.3). Alkene measurements were not available on the afternoon of 12 March, and so the rate of alkene ozonolysis (R12) is based on measurements from other afternoons at PTP that had similar concentrations of CO, O_3, and aromatic VOCs (which were measured continuously by the PTR-MS). O_x destruction via the minor NO-yielding branch of NO_3 photolysis was calculated assuming that NO, NO_2, and NO_3 were in a photostationary state (Geyer et al., 2003). Dry deposition of O_3 was estimated using the boundary layer height of 0.9 km and a deposition velocity of 0.4 cm s^{-1} (Wesely and Hicks, 2000).

As seen in Table 1, the single greatest loss mechanism of O_x was the conversion of NO_2 into NO_z compounds, which accounted for approximately 50% of O_x destruction. The importance of NO_2 oxidation as an indirect O_3 sink likely decreased after one day of photochemistry, since most NO_x is converted to NO_z on this time scale. The other O_x destruction mechanisms are not expected to change as greatly after one day. The relative importance of ozone photolysis (R8 and R9) as an O_x sink during the entire 11-day PTP data set depended greatly on the meteorology, since the rate is proportional to the mixing ratio of water vapor.

With the value of 12 ppbv/h for $L(O_x)$ as described above, the O_x production rate is calculated using Eq. (3) as 49±15 ppbv/h, in which the uncertainty is based on the uncertainty in the fit of the slope of the time series data as well as uncertainty in the mixing layer depth.

Primary emissions of NO_2 are estimated to account for less than 1% of observed O_x at all times at PTP as estimated by the quantity $0.04[NO_y]/[O_x]$, where the average NO_2/NO_x emission ratio in Mexico City is assumed to be 4%. This emission ratio is an upper limit based on early-morning measurements of NO, NO_2, and O_3 at the T0 site (near urban emissions) and previously published literature values (Shorter et al., 2005). Net thermal decomposition of peroxyacyl nitrates would act as a source of O_x as well, but it is not evident from our measurements whether there was net formation or decomposition of peroxyacyl nitrates during the afternoon at PTP. We estimate that an upper limit to the contribution of peroxyacyl nitrate thermal decomposition to O_x production during the stagnant period was 2 ppbv/h.

The inferred $P(O_x)$ value of 49±15 ppbv/h agrees within 50% with $P(O_x)$ calculations based on the VOC reactivity and estimated OH concentrations (Wood et al., 2009). Ozone production rates calculated using measurements of HO_2 and NO and Eq. (1) reached even higher values of up to 100 ppbv/h in the afternoon at more centrally-located urban site in Mexico City (Dusanter et al., 2009; Shirley et al., 2006). These values are among the highest observed anywhere in North America. A comparison of ozone production rates in Phoenix, Philadelphia, and Houston (Kleinman et al., 2002) indicated peak ozone production rates of approximately 5, 16, and 20 ppbv/h, respectively, with elevated rates of over 50 ppbv/h observed in petrochemical plumes in Houston. Peak instantaneous ozone production rates of 30–36 ppbv/h have been observed in Nashville (Daum et al., 2000; Thornton et al., 2002). The VOC reactivity at PTP calculated as $\Sigma k_{OH+VOC}[VOC]$ was extremely high compared to the other locations – measurements from the afternoon of 11 and 12 March ranged from 13 s^{-1} to 20 s^{-1}. In comparison, the 90th percentile VOC reactivities in Nashville, Phoenix, and Houston were 6 s^{-1}, 5 s^{-1}, and 22 s^{-1}, respectively (Kleinman et al., 2002). The calculated VOC reactivities at PTP are in rough agreement with measurements of the total OH loss rate in Mexico City in 2003 (Shirley et al., 2006) of ~25 s^{-1} in the afternoon – approximately 80% of which was due to reaction with VOCs and CO (i.e., the VOC reactivity was approximately 20 s^{-1}). A quantitative discussion of the speciated VOC reactivity at PTP and T0 is presented in Wood et al. (2009).

Given the NO mixing ratio of 1.0±0.5 ppbv between 12:15 and 13:15, we estimate that the sum of $[HO_2]$ and $[RO_2]$ was 95±50 pptv using Eq. (1) and the rate constant of R4 (8.1×10^{-12} cm^3 $molecule^{-1}$ s^{-1}) for oxidation of NO by RO_2. Observations aboard the C-130 aircraft at comparable NO_x concentrations (>10 ppbv) have shown that HO_2 comprised slightly less than 50% of the sum of HO_2 and RO_2 (Cantrell et al., 2007). This value is useful for estimating the rate of the HO_2 self-reaction and the rate of HO_2+O_3. The large uncertainties do not affect the conclusions of this paper.

3.3 Nitrogen oxides

3.3.1 Production rateof NO_z

The value of $P(NO_z)$ can be inferred using a method similar to that used to infer $P(O_x)$ in Sect. 3.2 (i.e. $\Delta[NO_z]/\Delta t = P(NO_z) - L(NO_z)$). The value of $\Delta[NO_z]/\Delta t$

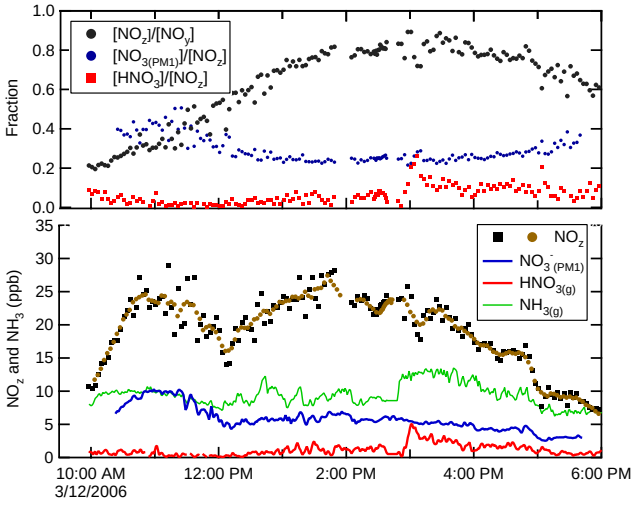

Fig. 3. Partial speciation of NO_y at PTP. The NO_z data are depicted both as 3 minute averages (black squares) and as smoothed, 12 minute running averages (brown circles). Particulate nitrate ($NO^-_{3(PM1)}$) accounts for 20-40% of NO_z during the day, and $HNO_{3(g)}$ accounts for less than 10%. Gaseous NH_3 is included for comparison, though is not a part of NO_y or NO_z.

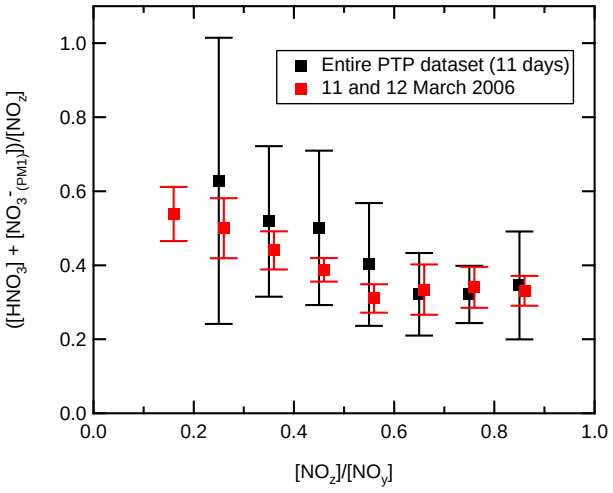

Fig. 4. Speciation of NO_z as a function of $[NO_z]/[NO_y]$. Mean values of $([HNO_3] + [NO^-_{3(PM1)}])/[NO_z]$ using the entire PTP dataset and 11-12 March 2006 between 8:00 and 20:00 are displayed in $[NO_z]/[NO_y]$ bins of width 0.1 Error bars are ± one standard deviation of the 1-min averaged values.

between 12:15 and 13:15, calculated as $([NO_z]_{12:15}-[NO_z]_{13:15})/1$ h), was 6.8±1.7 ppbv/h. Losses of NO_z during this time period can be constrained by the observed decrease in $\Delta[NO_y]/\Delta[CO]$, calculated as $([NO_y]–0.6)/([CO]–130)$ (i.e., the background-adjusted $[NO_y]$:[CO] ratio). Since CO is relatively unreactive on a time scale of hours, it is useful as a dilution tracer. During the stagnant hour, $\Delta[NO_y]/\Delta[CO]$, decreased by only 6%. If the overall urban $[NO_x]/[CO]$ emission ratio did not change enough to affect the ratio of cumulative (integrated) NO_x and CO emitted, and if the decrease in $[NO_y]/[CO]$ was solely due to NO_z losses rather than NO_x losses, then this 6% decrease in $[NO_y]/[CO]$ would correspond to a 9% decrease in NO_z, since $[NO_z]/[NO_y]$ was on average 0.65. The assumption regarding the changes in the overall urban NO_x/CO emission ratio is supported by the 2006 emission inventory (CAM, 2008) and discussed further in Sect. 3.3.2. Thus we calculate that $P(NO_z)$ is 9% higher than $\Delta[NO_z]/\Delta t$ and equal to 7.4±1.9 ppbv/h.

3.3.2 Speciation of NO_y

Between 12:15 and 13:15, $[NO_x]/[NO_y]$ decreased from 0.5 to 0.2 due to the oxidation of NO_x into NO_z compounds (Fig. 3). The speciation of NO_z can only partially be described since our directly measured individual NO_z species were restricted to accumulation-mode particulate nitrate ($NO^-_{3(PM1)}$) and gas-phase HNO_3. Particulate nitrate comprised 40% of NO_z from 10:00 to 11:00 (Fig. 3) and decreased to approximately 22% by 13:00. Nitric acid accounted for less than 4% of NO_z until 15:00, when it increased to 12%. The sum of $[HNO_{3(g)}]$ and $[NO^-_{3(PM1)}]$, henceforth referred to as ΣNO^-_3, accounted for 43% of NO_z in the morning and decreased to a minimum value of 25% shortly before 15:00.

Since the $NO^-_{3(PM1)}$ measurement only accounts for accumulation mode nitrate (vacuum aerodynamic diameter less than 1 μm), any uptake of NO_y onto coarse-mode PM is not accounted for in this speciation. The dominant mode peak of the $NO^-_{3(PM1)}$ size distribution was 330 nm at 10:00 and increased to 380 nm by 12:00. The same trend was observed in the ammonium aerosol size distributions.

The partitioning of $HNO_{3(g)}$ and $NO^-_{3(PM1)}$ at other ground sites in Mexico City has been described recently (Fountoukis et al., 2007; Hennigan et al., 2008; San Martini et al., 2006; Zheng et al., 2008). The high NH_3 mixing ratios act to drive photochemically formed HNO_3 into particulate ammonium nitrate (NH_4NO_3). As the temperature increases in the afternoon, NH_4NO_3 vaporizes, releasing HNO_3 vapor and increasing the ratio of $HNO_{3(g)}$ to $NO^-_{3(PM1)}$ (Fountoukis et al., 2007; Hennigan et al., 2008; Zheng et al., 2008).

The relative partitioning of NO_z among HNO_3, NO^-_3, and other compounds not measured at PTP (e.g., peroxyacyl nitrates, alkyl nitrates, and coarse-mode nitrate PM) is determined by the net production and loss rates of the main NO_z species (R6 – R7). Figure 4 shows that $[\Sigma NO^-_3]/[NO_z]$ decreases with photochemical processing (i.e., with increasing $[NO_z]/[NO_y]$). Figure 4 shows the means and standard deviations of the 1-minute averaged data from 12 March 2006 and the entire 11-day PTP dataset between 08:00 and 16:00, which spans a range of meteorological conditions. This overall trend agrees with measurements aboard the C-130 aircraft in which the sum of $HNO_{3(g)}$ and $NO^-_{3(PM1)}$ (as measured by an AMS) accounted for 30%–40% of NO_z in aged

air masses ($[NO_z]/[NO_y]>0.7$) (Flocke, personal communication, 2008). Speciated NO_y measurements at the T1 site exhibited similar trends (Farmer et al., 2009).

We discuss three possible factors contributing to the observed decrease in $[\Sigma NO_3^-]/[NO_z]$: 1) Deposition of $HNO_{3(g)}$, 2) A decrease in the role of HNO_3 formation relative to total NO_z formation, and 3) a shift of the nitrate aerosol size distribution from the accumulation mode to the coarse mode (particles greater than 1 μm in diameter), which is not detected by the AMS.

The first possible explanation of the decrease in $[\Sigma NO_3^-]/[NO_z]$ with photochemical age is enhanced deposition of HNO_3 relative to the other NO_z compounds. Gas-phase HNO_3 has a high dry deposition velocity (Wesely and Hicks, 2000), but the fact that the high NH_3 concentrations present in Mexico City convert most HNO_3 into particulate ammonium nitrate (Hennigan et al., 2008) suggests that this effect may not be as important as it is in low NH_3 environments. The extent to which HNO_3 deposition caused the decrease in $[\Sigma NO_3^-]/[NO_z]$ can be constrained by the small decreases observed in $\Delta[NO_y]/\Delta[CO]$ over the course of each day. Over the entire PTP dataset between 08:00 and 18:00, $\Delta[NO_y]/\Delta[CO]$ decreased from a median value of 0.050 at $[NO_z]/[NO_y]$ values less than 0.2 (during the morning) down to 0.045 at $[NO_z]/[NO_y]$ values greater than 0.6 (which occurred on some but not all afternoons). If this decrease in $[NO_y]/[CO]$ is assumed to be due solely to deposition of HNO_3 and $NO_{3(PM1)}^-$, then the observed values of $[\Sigma NO_3^-]/[NO_z]$ can be "corrected" upwards to account for this deposition as described in Sect. 3.3.1. Such a correction is complicated by the fact that the NO_x:CO emission ratio is not constant throughout the day. The key quantity that must be considered is the ratio of *cumulative* NO_x emissions to *cumulative* CO emissions. The emissions inventory (CAM, 2008) indicates that this ratio varies by less than 10% after 09:00. Overall, the value of $[\Sigma NO_3^-]/[NO_z]$ can be increased by at most a factor of 1.2 to account for HNO_3 deposition. This does not explain the overall decreasing trend in $[\Sigma NO_3^-]/[NO_z]$ observed with increasing photochemical age.

The second possible explanation for the decrease in $[\Sigma NO_3^-]/[NO_z]$ over time is that there was a decrease in the HNO_3 production rate relative to that of the other unmeasured NO_z compounds, presumably peroxyacyl nitrates (R7) and multifunctional alkyl nitrates (R5b). The equilibrium constant for R7 for many organic peroxy radicals (such as the peroxyacetyl radical, $CH_3C(O)O_2$) is very sensitive to temperature, and the corresponding peroxyacyl nitrates can either be in a state of net formation or net thermal decomposition depending on temperature and the concentrations of the relevant species. The lack of knowledge of the peroxyacyl nitrate mixing ratios themselves combined with the uncertainties in the mixing ratios of OH, NO, NO_2, and the precursor compounds (e.g., acetaldehyde for peroxyacetyl nitrate) preclude a quantitative assessment of whether peroxyacyl nitrates were undergoing net formation or net decomposition during the stagnant hour. We note that the results of one modeling study (Lei et al., 2007) showed that there was net formation of PAN compounds during the day in Mexico City, though not necessarily under the same conditions observed at PTP. Similarly, a box-model study of the Mexico City outflow indicated that the ratio of the production rate of HNO_3 to the net production rate of total PAN compounds decreases in the early afternoon of the first day of photochemistry (Madronich, 2006), though the temperature was held at 10°C in the model. The thermal decomposition lifetime (1/e) of PAN varies from ~1 h at 24°C to 2 days at 0°C.

The third possible explanation for the observed decrease in $[\Sigma NO_3^-]/[NO_z]$ with increasing $[NO_z]/[NO_y]$ is that there was a shift in the size distribution of aerosol nitrate from the accumulation mode (where it can be detected by the AMS) to the coarse mode (Laskin et al., 2005). The AMS is most sensitive to particles with vacuum aerodynamic diameters between ~60 nm and ~800 nm (Canagaratna et al., 2007), whereas the NO_y (and NO_z) measurements do not have a particle size cut-off. This is a plausible explanation, especially since coarse-mode nitrate has been observed in Mexico City during MILAGRO (Moffet et al., 2008; Querol et al., 2008), however it cannot be quantified using the PTP dataset as there was no measure of the coarse mode particulate nitrate mass. The decrease in the accumulation mode nitrate mass during the morning is consistent with increasing ambient temperature and the associated shift in the ammonium nitrate equilibrium (Zheng et al., 2008). On 11 and 12 March, the AMS (and SMPS) mass distribution data indicated an increase in the particulate nitrate mass mode from 330 nm to 380 nm between 10:00 and 12:00. This shift in the aerosol size distribution increased the fraction of total mass in particles greater than 800 nm to which the AMS is less sensitive, which may also have contributed to the observations.

In summary, the decreasing trend in $[\Sigma NO_3^-]/[NO_z]$ with photochemical age displayed in Fig. 4 cannot be fully explained by deposition of $HNO_{3(g)}$, and was likely caused by some combination of a decrease in the production rate of HNO_3 relative to other NO_z compounds, a shift of the nitrate aerosol mass distribution from the accumulation mode to the coarse mode, and a shift of the accumulation mode mass distribution toward particles greater than 800 nm (vacuum aerodynamic diameter). Similar conclusions regarding the importance of deposition and coarse-mode nitrate were reached in Zheng et al. (2008).

3.3.3 Estimate of OH

The increase in $[\Sigma NO_3^-]$ during the stagnant period can be used to infer the average OH concentration since ΣNO_3^- is the result of R6 and $[NO_2]$ was measured. Between 12:15 and 13:15, $[\Sigma NO_3^-]/\Delta t$ was 1.9±0.5 ppbv/h, which is approximately 30%±8% of the total increase in NO_z. Given

the average NO_2 mixing ratio of 10 ppbv and the rate constant for R6, the average OH concentration during the stagnant period is estimated as 6×10^6 molecules cm^{-3}, which is in line with previous afternoon measurements of OH in Mexico City (Shirley et al., 2006). This value is an underestimate of [OH] if there was an increase in coarse-mode nitrate (and low by a factor of $(HNO_{3(g)}+NO^-_{3total})/(HNO_{3(g)}+NO^-_{3PM1})$). Conversely, this is an overestimate of [OH] if HNO_3 was not the sole source of particulate nitrate (i.e., if there was significant partitioning of organic nitrates to the condensed phase). Besides the comparison to previous measurements of OH in Mexico City, this estimate of [OH] is only used to quantify the rates of R11 and R19. The uncertainty in this estimate does not affect the conclusions presented. For example, this estimate would have to be more than a factor of 6 too low in order for R11 to account for an appreciable fraction (>10%) of the total O_x loss.

3.4 Radical budget and ozone production

The photochemistry of ozone production and atmospheric oxidation in general is driven by RO_x ($RO_x \equiv OH+HO_2+RO_2$) radicals. The design of effective air pollution abatement strategies requires knowledge of whether ozone production is "NO_x-limited" or "VOC-limited" (NO_x-saturated), which is intimately related to reactions between RO_x and NO_x. At low NO_x mixing ratios, self-reactions of RO_x (R16–R19) dominate the removal processes of RO_x, the O_x production rate increases with increasing NO_x concentration, and O_x production is NO_x-limited. At higher NO_x concentrations, reactions with NO_x dominate the RO_x removal processes, the O_x production rate decreases with increasing NO_x concentrations, and O_x production is VOC-limited.

In order to investigate the radical budget and to determine whether ozone production was NO_x-limited or VOC-limited during the afternoon of 12 March, we compare the NO_z production rate described in Sect. 3.3.1 to the production rate of RO_x radicals. The reactions of RO_x with NO_x are the same reactions that form NO_z, i.e. formation of HNO_3, $RONO_2$, and RO_2NO_2 compounds (R5b, R6, R7). Thus the observed NO_z production rate serves as an indicator of the sum of the rates of R5b, R6, and R7. RO_x sinks not accounted for by $P(NO_z)$ are from RO_x self-reactions:

$$HO_2 + HO_2 \longrightarrow H_2O_2 + O_2 \quad \text{(R16)}$$

$$RO_2 + HO_2 \longrightarrow ROOH + O_2 \quad \text{(R17)}$$

$$RO_2 + RO_2 \longrightarrow \text{products} \quad \text{(R18)}$$

$$OH + HO_2 \longrightarrow H_2O + O_2 \quad \text{(R19)}$$

In steady state, the production rate of RO_x ($P(RO_x)$) equals the loss rate of RO_x ($L(RO_x)$). Since all losses of RO_x by reaction with NO_x form observable NO_z species (R5b–R7), $P(RO_x)$ is equal to $P(NO_z)$ when ozone production is strongly VOC-limited (Eq. 3):

$$P(RO_x) = L(RO_x) \approx P(NO_z) \quad (4)$$

whereas $P(NO_z)$ is much less than $P(RO_x)$ when ozone production is NO_x-limited. Thus a comparison of $P(RO_x)$ and $P(NO_z)$ serves as a useful indicator of whether ozone production is NO_x-limited or VOC-limited. Note that $P(NO_z)/P(RO_x)$ is similar to the "L_N/Q" quantity used by Kleinman et al. (2005).

The validity of Eq. (3) assumes that all observable NO_z compounds are formed by RO_x-NO_x reactions. The only observable NO_z species that are not formed by RO_x-NO_x reactions according to the current understanding of NO_y chemistry are NO_3, N_2O_5, and heterogeneously-formed HONO, and it is unlikely that any of these compounds accounts for an appreciable fraction of NO_z during the day.

In order to compare $P(RO_x)$ and $P(NO_z)$, we calculate $P(RO_x)$ from the following RO_x sources for the PTP data set: reaction of $O(^1D)$ with water vapor (R8 and R9); photolysis of the oxygenated VOCs formaldehyde, acetaldehyde, and acetone (R20–R22); and ozonolysis of alkenes (R23):

$$HCHO + h\nu + 2O_2 \longrightarrow CO + 2HO_2 \quad \text{(R20)}$$

$$CH_3CHO + h\nu + 2O_2 \longrightarrow CH_3O_2 + HO_2 + CO \quad \text{(R21)}$$

$$CH_3COCH_3 + h\nu + 2O_2 \longrightarrow CH_3C(O)O_2 + CH_3O_2 \quad \text{(R22)}$$

$$O_3 + \text{alkenes} \longrightarrow \text{products} + RO_2 + OH \quad \text{(R23)}$$

RO_x yields for alkene-ozonolysis reactions are based on the tabulated OH yields of Calvert et al. (2000) and are doubled to account for co-generated peroxy radicals.

The time series of these photolytic RO_x sources for 12 March 2006 is depicted in Fig. 5. The average value of $P(RO_x)$ from the reaction of $O(^1D)$ with water vapor and the photolysis of oxygenated VOCs between 12:15 and 13:15 was 1.3 ± 0.4 pptv/s. VOC canister measurements were not made during this time period, and so the contribution of alkene ozonolysis to $P(RO_x)$ is not accurately known. This quantity is estimated as 0.4 ± 0.2 pptv/s, based on the ozonolysis rates calculated from other afternoon samples at PTP with comparable values of concentrations of O_3, CO, aromatic VOCs, and photochemical age values calculated using a C3-benzene photochemical clock (Herndon et al., 2008). The total calculated $P(RO_x)$ is therefore 1.7 ± 0.5 pptv/s, with the range reflecting the uncertainty in the contribution from alkene ozonolysis and the uncertainty in the photolysis values.

The observed value of $P(NO_z)$, 2.1 ± 0.4 pptv/s, is a lower limit to the true value of $L(RO_x)$ since non-NO_x related RO_x losses (R14-R17) do not form NO_z. We estimate that

the water-assisted self reaction of HO_2 accounts for approximately 0.1 pptv/s, based on an estimated HO_2 mixing ratio of 40 pptv and the measured water vapor concentration. The estimated rate of the reaction between RO_2 and HO_2 using 40 pptv for both species and a rate constant of 10^{-11} molecules cm^{-3} s^{-1} (Atkinson, 1994) is 0.3 pptv/s, though there are strong indications that this rate constant is high by up to an order of magnitude (Lelieveld et al., 2008; Thornton et al., 2002). Heterogeneous loss of HO_2 is possibly the most uncertain RO_x loss process (Emmerson et al., 2007; Thornton et al., 2008).

The comparison of the calculated $P(RO_x)$ value (1.7 ± 0.5 pptv/s) and $L(RO_x)$ inferred from $P(NO_z)$ (2.1 ± 0.4 pptv/s) indicates both that the budget of RO_x sources and sinks is "closed" within the methodological uncertainties (i.e., $P(RO_x)$ has been shown to equal $L(RO_x)$) and that ozone production is indeed VOC-limited since $P(NO_z)$ is roughly equal to $L(RO_x)$. That ozone production is VOC-limited is in agreement with predictions from previous photochemical models (Lei et al., 2007; Tie et al., 2007) and recent measurements (Nunnermacker et al., 2008; Stephens et al., 2008). Although the large uncertainty bars preclude a more quantitative insight into RO_x sources, we note that it is not possible for $P(NO_z)$ to actually exceed $P(RO_x)$, assuming net formation of N_2O_5, NO_3, and HONO was a negligible portion of $P(NO_z)$. Either $P(NO_z)$ has been overestimated or $P(RO_x)$ has been underestimated. The latter possibility is likely, since the calculation of $P(RO_x)$ does not include the net source of RO_x from the photolysis of HONO, H_2O_2, or oxygenated VOCs beyond formaldehyde, acetaldehyde, and acetone. The HONO mixing ratio would have to exceed the calculated photostationary state HONO mixing ratio of $\sim$10 pptv by a factor of 10 to account for a net RO_x source of 0.3 pptv/s. We estimate that photolysis of glyoxal (CHOCHO) contributes at most an additional 0.1 pptv/s, based on the maximum glyoxal concentrations ($\sim$1 ppbv) observed previously in Mexico City (Volkamer et al., 2005). Studies of RO_x production that have utilized the Master Chemical Mechanism (Saunders et al., 2003) have invoked a large source of RO_x from oxygenated VOCs besides the three considered in our calculation of $P(RO_x)$ (Emmerson et al., 2007; Volkamer et al., 2007). It is not unreasonable that some combination of these sources could account for an additional 0.2–0.3 pptv/s. It is unlikely that the reaction of electronically excited NO_2 with water vapor acts as a significant RO_x source during the afternoon due to the small solar zenith angles (Li et al., 2008).

This use of NO_z measurements as a tool for gleaning information on RO_x loss rates may be useful in smog chamber experiments as well as stagnant air masses. The alternative, more common method of quantifying RO_x losses relies on the explicit calculation of the rate of each RO_x loss reaction, which requires accurate knowledge of the reactants OH, HO_2, and speciated RO_2 mixing ratios as well as the relevant rate constants, which are highly uncertain for many RO_2 reactions. We note that this analysis of the calculated RO_x production rate and the inferred RO_x loss rate does not provide information on the *interconversions* between OH, HO_2, and RO_2; actual measurements of those species would be required for that analysis.

In general, $P(O_x)$ increases with increasing RO_x production rates (Kleinman, 2005). The inferred value of $P(O_x)$ of 49 ppbv/h (13 pptv/s) for the observed $P(RO_x)$ rate of 1.7 ± 0.5 pptv/s also agrees well with that predicted by Lei et al. (2007). This agreement is perhaps fortuitous given the uncertainties of both methods.

$P(RO_x)$ exhibits an interesting asymmetry over the course of the day. Due to the elevated concentrations of oxygenated VOCs in the morning, $P(RO_x)$ (excluding alkene ozonolysis) peaks at a value of 1.6 pptv/s at 11:00, whereas peak actinic flux and photolysis frequencies peak more than an hour later. This overall temporal profile was observed during several but not all days at PTP. The peak and mean daytime values of $P(RO_x)$ on 12 March were higher than on any other day at PTP between 8 March and 18 March. The mean value of $P(RO_x)$ between 9:00 and 16:00 during this span of 11 days, under various meteorological conditions, was 0.6 pptv/s, whereas on 12 March it was 1.2 pptv/s.

Another interesting feature of RO_x production on 12 March is that despite extremely high O_3 mixing ratios ($>$150 ppbv), O_3 photolysis accounted for at most 43% of $P(RO_x)$ excluding alkene ozonolysis, similar to observations in the city center in 2003 (Volkamer et al., 2007). The relative humidity was low on 12 March (less than 17% after noon), limiting the rate of reaction between water vapor and $O(^1D)$ produced from the photolysis of ozone. The relative importance of O_3 photolysis as a RO_x source increased later in the month when the relative humidity increased greatly. The oxygenated VOCs (primarily HCHO) that account for the largest fraction of $P(RO_x)$ are both emitted directly in Mexico City at rates higher than in the US and are produced by VOC oxidation (Garcia et al., 2006; Kolb et al., 2004; Zavala et al., 2006).

3.5 Efficiency of ozone production

The efficiency of ozone production can be quantified with regard either to the NO_x catalytic cycle or to the oxidation of VOCs. The number of ozone molecules that are produced per molecule of NO_x before the NO_x is removed from active photochemistry is known as the ozone production efficiency (OPE) of NO_x. Similarly, the amount of ozone that can be produced by the oxidation of individual VOCs has been studied in laboratory studies, yielding quantities such as the ozone creation potential (Derwent et al., 1996) and the maximum incremental reactivity (Carter et al., 1995). We examine ozone production in Mexico City using both the NO_x-based OPE metric and a new VOC-based metric that uses the correlation of the $\Delta[O_x]/\Delta[CO]$ ratio with an aromatic-VOC based photochemical clock.

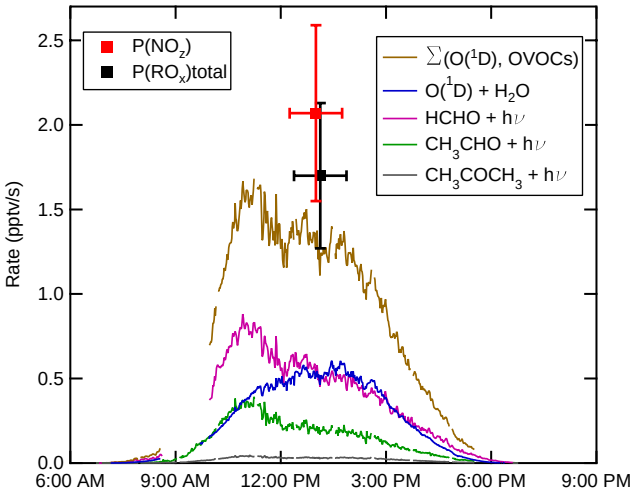

Fig. 5. Comparison of the NO_z production rate with the RO_x production rate during the afternoon of 12 March. RO_x production rates from the photolysis of O_3, HCHO, CH_3CHO, and acetone are depicted as lines, with the sum depicted by the brown line (OVOC = oxygenated volatile organic compound). The total $P(RO_x)$ value (black square) is calculated as the sum of the photolytic RO_x sources and an estimated 0.4 pptv/s from alkene ozonolysis. The red square demarks the average NO_z production rate observed between 12:15 and 13:15.

PTP is an excellent site for examining both of these approaches given the known meteorology, the lack of proximate emission sources, and (for one hour during the afternoon of 12 March 2006) the quantified production and loss rates of both O_x and NO_z.

3.5.1 Ozone production efficiency of NO_x

The OPE of NO_x has been extensively discussed over the last 20 years (Lin et al., 1988; Nunnermacker et al., 2000; Wang et al., 1998). The instantaneous OPE is usually defined as $P(O_x)/P(NO_z)$, whereas the integrated OPE for an observed air mass is usually inferred by the correlation between O_x and NO_z (i.e., $\Delta[O_x]/\Delta[NO_z]$). The instantaneous OPE of an air mass is expected to vary with time, and is affected by the temporal evolution of the partitioning of RO_x among OH, HO_2, and RO_2 and the partitioning of NO_x between NO and NO_2.

Inferred and/or modeled OPE values range from 2–8 in urban (high-NO_x) settings and power plant plumes (Kleinman, 2000;Nunnermacker et al., 2000) up to 46 for the mean OPE of the southern hemisphere (Wang et al., 1998). The large range of values reflects the non-linear dependence of ozone production on its chemical precursors. In general, the OPE increases with the VOC reactivity to NO_x ratio and is highest in chemical environments in which ozone production is NO_x-limited. The interpretation of inferred OPE values using observations of $\Delta[O_x]/\Delta[NO_z]$ is complicated by photochemical and depositional losses of NO_z (Nunnermacker et al., 1998) and O_x. The OPE can also be difficult to interpret if the observed air masses are inhomogeneous – i.e., if the observed ozone is the result of multiple air masses of different histories that have mixed prior to the observations (Liang and Jacobson, 2000).

The role that thermally labile peroxyacyl nitrates (such as PAN) have as a reservoir of both RO_x and NO_x complicates the interpretation of the OPE. Net formation of peroxyacyl nitrates acts as a temporary sink of NO_x (and O_x). Subsequent thermal decomposition of peroxyacyl nitrates releases the NO_x, allowing it to catalyze the production of more O_3 - quite possibly in chemical environments where $OPE_{(Inst)}$ is different than where the NO_x was initially emitted. Thus the number of ozone molecules produced from each NO_x depends on what temporal and spatial scale is considered. Shon et al. (2008) and Nunnermacker et al. (2008) report OPE values (inferred from $\Delta[O_x]/\Delta[NO_z]$) that range from 5 within the boundary layer up to 8.5 in the marine free troposphere outside of Mexico City. The timing of NO_x emissions can also affect OPE values, since at night NO_x emissions can lead to net destruction of O_x through reactions involving NO_3 and N_2O_5 (Brown et al., 2006). The OPE values determined below in Sect. 3.5.2 and 3.5.3 are focused on daytime chemistry on a time scale of less than 10 h.

Between 12:15 and 13:15 on 12 March 2006, the value of $P(O_x)/P(NO_z)$ using the values for $P(O_x)$ and $P(NO_z)$ derived in Sect. 3.1 and 3.2 was 6.4. This value for the OPE reflects the *gross* O_x produced per NO_x. This value is greater than the correlation between the O_x and NO_z concentrations during this hour (5.4), which is more a measure of the *net* O_x produced per NO_x, and is also affected by deposition of NO_z. The correlation is higher when all data between 09:00 and 16:00 on both 12 March and 11 March are included. These two days experienced similar air masses and a comparable range of photochemical ages (as determined by $[NO_z]/[NO_y]$). The slope of the graph of O_x versus NO_z (Fig. 5) for these two days is 6.2±0.2. To infer the gross O_x produced per NO_x, the slope can be "corrected" to account for losses of O_x. Additionally, the NO_z measurements can be corrected to account for cumulative NO_z losses (deposition). As discussed in Sect. 3.3.1, we can infer that between 12:15 and 13:15 on 12 March approximately 9% of the NO_z was removed from the system by a comparison of the $\Delta[NO_y]/\Delta[CO]$ ratio with that expected based on the cumulative emissions of NO_x and CO. If the emission ratio of NO_x/CO were actually a constant value of 0.05 throughout the day, the "corrected" value of $[NO_z]$ (i.e., the value of $[NO_z]$ that would have been measured had there been no NO_z deposition) can be expressed by Eq. (4):

$$[NO_{z(CORRECTED)}] = 0.05 \times ([CO] - 130) - [NO_x] \quad (5)$$

where the NO_y measurements are ignored and instead are simulated by the CO measurements and scaled by the NO_x/CO emission ratio.

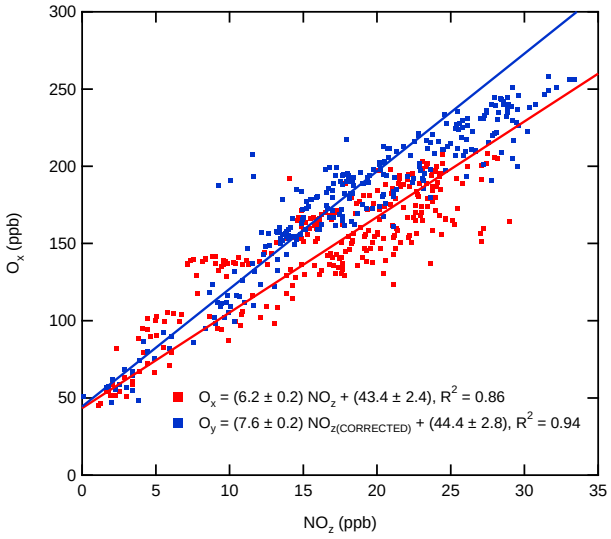

Fig. 6. Inference of the short-term ozone production efficiency (OPE) at PTP on 11 and 12 March 2006 between 08:30 and 18:00. The red points use the raw O_x and NO_z data. Correcting for losses of both species produces the blue points (see text).

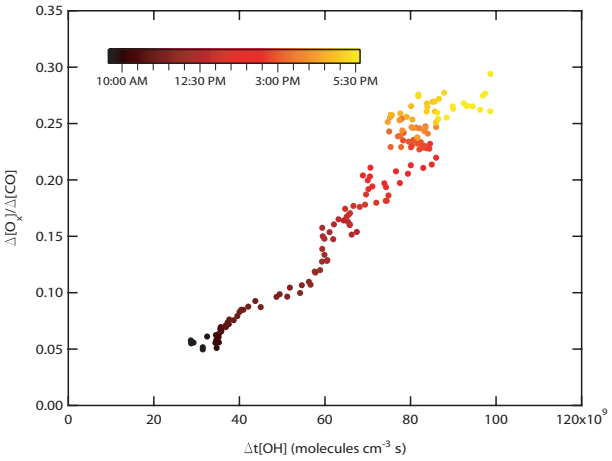

Fig. 7. Correlation of $\Delta[O_x]/\Delta[CO]$ on 12 March 2006 with cumulative OH exposure (Δt[OH]) as inferred by a C9-aromatic photochemical clock.

The total O_x lost is determined by the integrated O_x destruction mechanisms described in Sect. 3.2. We use the quantity "O_y" to represent the total integrated O_x production. In Sect. 3.2 the quantity $0.8\times P(NO_z)$ was used to estimate total O_x loss rate via NO_2 oxidation, which accounted for approximately 50% of the total O_x loss between 12:15 and 13:15. If this value (50%) does not vary greatly over the course of the day, then total integrated O_x losses can be approximated by Eq. (5):

$$[O_Y] = [O_x] + 1.6[NO_z] \quad (6)$$

The true percentage undoubtedly varies over the course of the day, contributing to the uncertainty of this approximation. $[O_y]$ is between 5% and 25% higher than $[O_x]$.

Figure 6 depicts the correlations on 11 and 12 March 2006 between O_x and NO_z, which has a slope of 6.2, and that between O_y and $NO_{z(CORRECTED)}$, which has a higher slope of 7.6. In most other cases where inferred OPE values have been corrected for losses (Nunnermacker et al., 1998), the corrected OPE have been lower than the uncorrected OPE, in contrast to the case here. This is because the correction for O_x losses is greater than the correction for NO_z. This is partially just a difference in approach: by using O_y instead of O_x, the approach used here reflects the integrated ozone production rather than the *net* ozone production per molecule of NO_x oxidized. In the air masses examined, NO_y was mostly conserved; the maximum correction to NO_z was 20%. For more highly aged air masses, the relative magnitude of the O_x and NO_z corrections might be different. The oxidation of NO_2 was the dominant loss of O_x in the young air masses observed, which had undergone less than 10 h of atmospheric oxidation. The contribution of this O_x loss process likely decreased in importance after the NO_x/NO_y decreased to lower values ($\sim$0.1).

The similarity between the corrected slope and the uncorrected slope indicate that the OPE can be reasonably approximated during one day of photochemistry in Mexico City by the correlation of $[O_x]$ with $[NO_z]$. Slightly higher O_x/NO_z correlations were observed elsewhere in the city – for example, our measurements at Santa Ana during an ozone-south meteorological episode (deFoy et al., 2006) on 24 March 2006 yielded an (uncorrected) OPE value of 7.5$\pm$0.3. The values derived here (6–8) are within the range of 4 to 12 calculated by Lei et al. (Lei et al., 2007) for NO_x mixing ratios greater than 10 ppbv.

3.5.2 $\Delta[O_x]/\Delta[CO]$ and a VOC-based photochemical clock

Since CO is a relatively unreactive tracer of dilution, the quantity $\Delta[O_x]/\Delta[CO]$ can be interpreted as the dilution-adjusted measure of integrated ozone production, similar to the use of the ratio of organic aerosol to CO in studies of secondary organic aerosol formation (Kleinman et al., 2008). In the MCMA, on-road vehicles are the largest source of CO by far, accounting for over 99% of total CO emissions (CAM, 2008). VOCs are emitted by on-road vehicles (34% by mass) as well as area sources (46%) and industrial sources (17%), though the most reactive VOCs are emitted by on-road vehicles (CAM, 2008; Velasco et al., 2007). Thus CO and the most important ozone-producing VOCs are co-emitted, and emissions of total VOCs and CO overlap spatially. The CO mixing ratio is in most cases proportional to the total emissions of VOCs, though the proportionality constant (e.g., the VOC/CO emission ratio) depends greatly on the nature of the emission sources .

The increase in $\Delta[O_x]/\Delta[CO]$ can be related to the cumulative OH exposure $\Delta t[OH]$ (photochemical age) of the observed air mass using a C9-aromatic photochemical clock (Herndon et al., 2008; Roberts et al., 1984). The photochemical age we use is based on PTR-MS measurements of benzene and the sum of C9-aromatic compounds, which include C_9H_{12} and C_8H_8O isomers. The calculation is described in Herndon et al. (2008). Since the air masses observed consisted of a combination of fresh emissions and aged emissions and are best described by a distribution of photochemical ages, the single values derived using this photochemical clock are meant only as an estimate of the average OH exposure of the air.

Figure 7 depicts the correlation between $\Delta[O_x]/\Delta[CO]$ and $\Delta t[OH]$ between 09:00 and 17:00 on 12 March 2006, with $\Delta[O_x]/\Delta[CO]$ calculated as $([O_x]–45)/([CO]–130)$. Background values of 45 ppbv for O_x and 130 ppbv for CO are based on observations at night, when PTP was well above the nocturnal boundary layer. As expected, $\Delta[O_x]/\Delta[CO]$ increases with $\Delta t[OH]$, and there is little scatter in the plot ($R^2>0.9$). The slope of a linear fit (not shown) is 3.8×10^{-12} ppbv O_x ppbv^{-1} CO (molecules OH cm^{-3} s)$^{-1}$, though it appears that it may be higher for the afternoon than for the morning data. This is supported by the fact that $\Delta[O_x]/\Delta[CO]$ should equal zero when $\Delta t[OH]$ is zero. Observations on other days were similar, with most slopes within the range of 3.6×10^{-12} to 5.6×10^{-12} ppbv O_x ppbv^{-1} CO (molecules OH cm^{-3} s)$^{-1}$. The correlation was poor when the air masses observed were affected by a range of emission sources within the same day (e.g., biomass burning vs. urban emissions).

Variation in the slopes by time of day could be related to differences in ozone photochemistry between the morning and afternoon. Within the boundary layer, overall concentrations of NO_x and VOCs are highest in the morning because of the shallow mixing depth (typically less than 500 m between 06:00 and 11:00). Additionally, the VOC mixture differs: it consists primarily of unoxidized, primary VOCs in the morning and a mix of primary and secondary VOCs (e.g., oxygenated VOCs) in the afternoon. Thus it is conceivable that for a given amount of OH exposure, the different photochemical conditions could lead to differences in the slope of $\Delta[O_x]/\Delta[CO]$ vs. $\Delta t[OH]$ (e.g., if secondary VOCs are more efficient at producing ozone). Changes in the slope of Fig. 7 could also simply be caused by perturbations to the $\Delta[O_x]/\Delta[CO]$ ratio and the inferred OH exposure ($\Delta t[OH]$) due to changes in the emission ratios of the aromatic VOCs and CO.

A plot of $\Delta[O_x]/\Delta[NO_y]$ vs. $\Delta t[OH]$ (not shown) looks similar to Fig. 7 since NO_y was mostly conserved in the air masses observed. The quantity $\Delta[O_x]/\Delta[NO_y]$ is related to the OPE of NO_x in that it expresses the average number of ozone molecules that have been produced per molecule of NO_x emitted (rather than ozone produced per NO_x oxidized). This quantity is initially zero in fresh emissions that have not undergone photochemical conversion, when $[NO_x]$ and $[NO_y]$ are equal. As the air mass is photochemically processed, O_x is produced, NO_x is converted into NO_z, and there are fresh emissions of NO_x. Ignoring the effects of O_x and NO_y loss/deposition, the value of $\Delta[O_x]/\Delta[NO_y]$ should approach the integrated OPE value of $\Delta[O_x]/\Delta[NO_z]$, since NO_y consists primarily (>90%) of NO_z in highly aged air. On 12 March 2006, the value of $\Delta[O_x]/\Delta[NO_y]$ steadily increased during the day and reached 7 by 17:00, which is comparable to the OPE inferred in Fig. 6. This is expected since $[NO_z]$ and $[NO_y]$ are close in magnitude then, and thus $\Delta[O_x]/\Delta[NO_y]\approx\Delta[O_x]/\Delta[NO_z]$.

Comparison of the correlation of $\Delta[O_x]/\Delta[CO]$ with $\Delta t[OH]$ observed in Mexico City to other locations should be done with the caveat that the values are greatly affected by the VOC/CO emission ratios. This metric may be most useful for comparing ozone production during different times of day or under different meteorological conditions at locations when the VOC/CO ratio does not vary greatly.

4 Conclusions

Measurements of several ambient gas-phase and particulate species from a unique mountain-top site in Mexico City have been used to characterize the chemistry of ozone production, nitrogen oxides, and the RO_x budget, with an emphasis on one hour of data during which the rise of the mixing depth was slow. Overall, the observations agree well with the predictions of photochemical models (Lei et al., 2007; Tie et al., 2007).

The observed time rate of change in the mixing ratios of O_x and NO_z combined with calculations of the O_x loss rates during the case study period (12 March 2006) were used to infer an O_x production rate of 49 ppbv/h and an NO_z production rate of 7.6 ppbv/h. The dominant loss process for O_x was the oxidation of NO_2 to NO_z compounds (e.g., HNO_3); photolysis of O_3 was a minor contributor to O_x loss due to the low relative humidity. A decrease in $([HNO_{3(g)}]+[NO^-_{3(PM1)}])/[NO_z]$ with increasing $[NO_z]/[NO_y]$ was observed. Deposition of HNO_3 was a minor contributor to this trend, whereas a shift of the aerosol nitrate size distribution from the accumulation mode to the coarse mode and possibly a decrease in the HNO_3 production rate relative to total NO_z production are plausible explanations. A comparison of RO_x production rates and the observed increase in NO_z during a period of stagnant air indicates that O_x production was VOC-limited and that the RO_x budget was closed (i.e., $P(RO_x)=L(RO_x)$) to within the methodological uncertainties.

The ozone production efficiency of NO_x on a time scale of one day was approximately 7 as inferred by the correlation of $[O_x]$ to $[NO_z]$. Corrections to this correlation that account for losses of O_x and NO_z increase the inferred value of the ozone production efficiency by less than 30%. A new metric for assessing the efficiency of ozone production has been

proposed and is based on the correlation of the $[O_x]$:[CO] ratio with the average OH exposure as inferred by ratios of aromatic VOCs.

Although this analysis focused on only a short time period, the chemistry characterized is in agreement with previous modeling work and lends confidence to the state of knowledge regarding ozone chemistry, nitrogen oxides, and the underlying fast radical chemistry. A few aspects of the chemistry, however, have not been commonly observed in other locations. For example, gas-phase HNO_3 comprised a small fraction of NO_z (less than 15% usually), whereas particulate nitrate comprised a much larger fraction - mainly due to the high concentrations of NH_3. The photolysis of ozone and subsequent reaction of $O(^1D)$ with water vapor was a minor destruction channel for O_3 during the first $\sim$24 h of atmospheric chemistry, and even during high O_3 events ($[O_3]>150$ ppbv) ozone photolysis accounted for less than half of total RO_x sources in dry air masses. Although rare in the literature, these characteristics are not necessarily unique considering that the atmosphere above most developing megacities remains largely uncharacterized.

Acknowledgements. This work was funded in part by NSF grants (ATM-528227 & ATM-0528170) and DOE grants (DE-FGO2-05ER63982 & DE-FGO2-05ER63980). We gratefully acknowledge Luisa Molina and Linsey Marr for providing the two chemiluminescence analyzers. We thank Manuel Quiñones of Televisa for providing power and on-site support at PTP, Rafael Ramos for logistical assistance, Sasha Madronich of NCAR for assistance with the TUV model, and Delphine Farmer for helpful conversations. The United States Environmental Protection Agency through its Office of Research and Development collaborated in the research described here. It has been subjected to Agency review and approved for publication.

Edited by: S. Madronich

References

Atkinson, R.: Gas-phase tropospheric chemistry of organic compounds, Journal of Physical Chemistry Ref. Data, M2, 1994.

Brown, S. S., Neuman, J. A., Ryerson, T. B., Trainer, M., Dubé, W. P., Holloway, J. S., Warneke, C., De Gouw, J. A., Donnelly, S. G., and Atlas, E.: Nocturnal odd-oxygen budget and its implications for ozone loss in the lower troposphere, Geophys. Res. Lett., 33, doi:10.1029/2006GL025900, 2006.

Calvert, J. G., Atkinson, R., Kerr, J. A., Madronich, S., Moortgat, G. K., Wallington, T. J., and Yarwood, G.: The Mechanisms of Atmospheric Oxidation of the Alkenes, Oxford University Press, Oxford, 277–278, 2000.

CAM: Inventario de emisiones 2006 de la Zona Metropolitana del Valle de Mexico, http://www.sma.df.gob.mx, 2008.

Canagaratna, M. R., Jayne, J. T., Jimenez, J. L., Allan, J. D., Alfarra, M. R., Zhang, Q., Onasch, T. B., Drewnick, F., Coe, H., Middlebrook, A., Delia, A., Williams, L. R., Trimborn, A. M., Northway, M. J., DeCarlo, P. F., Kolb, C. E., Davidovits, P., and Worsnop, D. R.: Chemical and microphysical characaterization of ambient aerosols with the Aerodyne Aerosol Mass Spectrometer, Mass Spectrom. Rev., 26, 185–222, doi:10.1002/mas.20115, 2007.

Cantrell, C., Anderson, R., Mauldin, L., Kociuch, E., McCoy, J., Eisele, F., Apel, E., Reimer, D., Hills, A., Karl, T., Knapp, D., Montzka, D., Fried, A., Weibring, P., Walega, W., Richter, D., Flocke, F., Zheng, W., Emmons, L., Crawford, J., Dunlea, E., DeCarlo, P., Clarke, T., Howell, S., Cohen, R., Shetter, R., Hall, S., Russell, L., Kok, G., Weber, R., Madronich, S., Wennberg, P., Crounse, J., McCabe, D., and Holloway, J.: HO_x Behavor as Observed Aboard the C-130 during MILAGRO, MILAGRO Science Meeting, Mexico City, 2007.

Carslaw, N., Creasey, D. J., Harrison, D., Heard, D. E., Hunter, M. C., Jacobs, P. J., Jenkin, M. E., Lee, J. D., Lewis, A. C., Pilling, M. J., Saunders, S. M., and Seakins, P. W.: OH and HO2 radical chemistry in a forested region of north-western Greece, Atmos. Environ., 35, 4725–4737, 2001.

Carter, W. P. L., Pierce, J. A., Luo, D., and Malkina, I. L.: Environmental chamber study of maximum incremental reactivities of volatile organic compounds, Atmos. Environ., 29, 2499–2511, 1995.

Daum, P. H., Kleinman, L. I., Imre, D., Nunnermacker, L. J., Lee, Y. N., Springston, S. R., Newman, L., Weinstein-Lloyd, J., Valente, R. J., Imhoff, R. E., Tanner, R. L., and Meagher, J. F.: Analysis of O_3 formation during a stagnation episode in central Tennessee in summer 1995, J. Geophys. Res.-Atmos., 105, 9107–9119, 2000.

de Foy, B., Caetano, E., Magaña, V., Zitácuaro, A., Cárdenas, B., Retama, A., Ramos, R., Molina, L. T., and Molina, M. J.: Mexico City basin wind circulation during the MCMA-2003 field campaign, Atmos. Chem. Phys., 5, 2267–2288, 2005, http://www.atmos-chem-phys.net/5/2267/2005/.

de Foy, B., Varela, J. R., Molina, L. T., and Molina, M. J.: Rapid ventilation of the Mexico City basin and regional fate of the urban plume, Atmos. Chem. Phys., 6, 2321–2335, 2006, http://www.atmos-chem-phys.net/6/2321/2006/.

de Foy, B., Fast, J. D., Paech, S. J., Phillips, D., Walters, J. T., Coulter, R. L., Martin, T. J., Pekour, M. S., Shaw, W. J., Kastendeuch, P. P., Marley, N. A., Retama, A., and Molina, L. T.: Basin-scale wind transport during the MILAGRO field campaign and comparison to climatology using cluster analysis, Atmos. Chem. Phys., 8, 1209–1224, 2008, http://www.atmos-chem-phys.net/8/1209/2008/.

de Gouw, J. A., Middlebrook, A. M., Warneke, C., Goldan, P. D., Kuster, W. C., Roberts, J. M., Fehsenfeld, F. C., Worsnop, D. R., Canagaratna, M. R., Pszenny, A. A. P., Keene, W. C., Marchewka, M., Bertman, S. B., and Bates, T. S.: Budget of organic carbon in a polluted atmosphere: Results from the New England Air Quality Study in 2002, J. Geophys. Res.-Atmos., 110, doi:10.1029/2004JD005623, 2005.

de Gouw, J. A., Warneke, C., Stohl, A., Wollny, A. G., Brock, C. A., Cooper, O. R., Holloway, J. S., Trainer, M., Fehsenfeld, F. C., Atlas, E. L., Donnelly, S. G., Stroud, V., and Lueb, A.: Volatile organic compound composition of merged and aged forest fires from Alaska and Western Canada, J. Geophys. Res., 111, doi:10.1029/2005JD006175, 2006.

deFoy, B., Varela, J. R., Molina, L. T., and Molina, M. J.: Rapid ventilation of the Mexico City basin and regional fate of the urban plume, Atmos. Chem. Phys., 6, 2321–2335, 2006, http://www.atmos-chem-phys.net/6/2321/2006/.

Derwent, R. G., Jenkin, M. E., and Saunders, S. M.: Photochemical ozone creation potentials for a large number of reactive hydrocarbons under European conditions, Atmos. Environ., 30, 181–199, 1996.

Drewnick, F., Hings, S. S., DeCarlo, P., Jayne, J. T., Gonin, M., Fuhrer, K., Weimer, S., Jimenez, J. L., Demerjian, K. L., Borrman, S., and Worsnop, D. R.: A New Time-of-Flight Aerosol Mass Spectrometer (TOF-AMS) – Instrument Description and First Field Deployment, Aerosol Sci. Technol., 39, 637–658, 2005.

Dusanter, S., Vimal, D., Stevens, P. S., Volkamer, R., and Molina, L. T.: Measurements of OH and HO_2 concentrations during the MCMA-2006 field campaign Part 1: Deployment of the Indiana University laser-induced fluorescence instrument, Atmos. Chem. Phys., 9, 1665–1685, 2009, http://www.atmos-chem-phys.net/9/1665/2009/.

Emmerson, K. M., Carslaw, N., Carslaw, D. C., Lee, J. D., McFiggans, G., Bloss, W. J., Gravestock, T., Heard, D. E., Hopkins, J., Ingham, T., Pilling, M. J., Smith, S. C., Jacob, M., and Monks, P. S.: Free radical modelling studies during the UK TORCH Campaign in Summer 2003, Atmos. Chem. Phys., 7, 167–181, 2007, http://www.atmos-chem-phys.net/7/167/2007/.

Farmer, D. K., Cohen, R. C., Perring, A. E., et al.: NO_y partitioning and the role of alkyl nitrates in air quality in the Mexico City area, Atmos. Chem. Phys., in preparation, 2009.

Fast, J. D., De Foy, B., Acevedo Rosas, F., Caetano, E., Carmichael, G., Emmons, L., McKenna, D., Mena, M., Skamarock, W., Tie, X., Coulter, R. L., Barnard, J. C., Wiedinmyer, C., and Madronich, S.: A meteorological overview of the MILAGRO field campaigns, Atmos. Chem. Phys., 7, 2233–2257, 2007, http://www.atmos-chem-phys.net/7/2233/2007/.

Fountoukis, C., Nenes, A., Sullivan, A., Weber, R., VanReken, T., Fischer, M., Matias, E., Moya, M., Farmer, D., and Cohen, R. C.: Thermodynamic characterization of Mexico City aerosol during MILAGRO 2006, Atmos. Chem. Phys., 9, 2141–2156, 2009, http://www.atmos-chem-phys.net/9/2141/2009/.

Garcia, A. R., Volkamer, R., Molina, L. T., Molina, M. J., Samuelson, J., Mellqvist, J., Galle, B., Herndon, S. C., and Kolb, C. E.: Separation of emitted and photochemical formaldehyde in Mexico City using a statistical analysis and a new pair of gas-phase tracers, Atmos. Chem. Phys., 6, 4545–4557, 2006, http://www.atmos-chem-phys.net/6/4545/2006/.

Geyer, A., Alicke, B., Ackermann, R., Martinez, M., Harder, H., Brune, W., Di Carlo, P., Williams, E., Jobson, T., Hall, S., Shetter, R., and Stutz, J.: Direct observations of daytime NO_3: Implications for urban boundary layer chemistry, J. Geophys. Res., 108, 4368, doi:4310.1029/2002JD002967, 2003.

Hennigan, C. J., Sullivan, A. P., Fountoukis, C. I., Nenes, A., Hecobian, A., Vargas, O., Peltier, R. E., Case Hanks, A. T., Huey, L. G., Lefer, B. L., Russell, A. G., and Weber, R. J.: On the volatility and production mechanims of newly formed nitrate and water soluble organic aerosol in Mexico City, Atmos. Chem. Phys., 8, 3761–3768, 2008, http://www.atmos-chem-phys.net/8/3761/2008/.

Herndon, S., Onasch, T., Wood, E. C., Kroll, J. H., Canagaratna, M., Jayne, J., Zavala, M., Knighton, W. B., Mazzoleni, C., Dubey, M. K., Ulbrich, I., Jimenez, J. L., Seila, R., de Gouw, J. A., De Foy, B., Fast, J., Molina, L., Kolb, C. E., and Worsnop, D. R.: The correlation of secondary organic aerosol with odd oxygen in Mexico City, Geophys. Res. Lett., 35, doi:10.1029/2008GL034058, 2008.

Herndon, S. C., Jayne, J. T., Zahniser, M. S., Worsnop, D. R., Knighton, B., Alwine, E., Lamb, B. K., Zavala, M., Nelson, D. D., and McManus, J. B.: Characterization of urban pollutant emission fluxes and ambient concentration distributions using a mobile laboratory with rapid response instrumentation, Faraday Discuss, 130, 327–339, 2005.

Herndon, S. C., M. S. Zahniser, D. D. Nelson Jr., J. Shorter, J. B. McManus, R. Jiménez, C. Warneke, and Gouw, J. A. d.: Airborne measurements of HCHO and HCOOH during the New England Air Quality Study 2004 using a pulsed quantum cascade laser spectrometer, J. Geophys. Res., 112, D10S03, doi:10.1029/2006JD007600., 2007.

Khan, H. A.: Benzene's toxicity: a consolidated short review of human and animal studies, Human Exp. Tox., 26, 677–685, 2007.

Kleinman, L. I.: Ozone process insights from field experiments – part II: Observation-based analysis for ozone production, Atmos. Environ., 34, 2023–2033, 2000.

Kleinman, L. I., Daum, P. H., Imre, D., Lee, Y. N., Nunnermacker, L. J., Springston, S. R., Weinstein-Lloyd, J., and Rudolph, J.: Ozone production rate and hydrocarbon reactivity in 5 urban areas: A cause of high ozone concentration in Houston, Geophys. Res. Lett., 29(10), 1467, doi:10.1029/2001GL014569, 2002.

Kleinman, L. I.: The dependence of tropospheric ozone production rate on ozone precursors, Atmos. Environ., 39, 575–586, 2005.

Kleinman, L. I., Springston, S. R., Daum, P. H., Lee, Y. N., Nunnermacker, L. J., Senum, G. I., Wang, J., Weinstein-Lloyd, J., Alexander, M. L., Hubbe, J., Ortega, J., CAnagaratna, M. R., and Jayne, J.: The time evolution of aerosol composition over the Mexico City plateau, Atmos. Chem. Phys., 8, 1559–1575, 2008, http://www.atmos-chem-phys.net/8/1559/2008/.

Knighton, W. B., Fortner, E. C., Herndon, S. C., Wood, E. C., Canagaratna, M., Jayne, J., Kroll, J. H., Onasch, T., Trimborn, A., Worsnop, D., and Kolb, C.: Examination of Biomass Burning Tracer Signatures in Urban Environments, EOS, Transactions, American Geophysical Union, A33D-1569, 2007.

Kolb, C. E., Herndon, S. C., McManus, J. B., Shorter, J. H., Zahniser, M. S., Nelson, D. D., Jayne, J. T., Canagaratna, M. R., and Worsnop, D. R.: Mobile Laboratory with Rapid Response Instruments for Real-Time Measurements of Urban and Regional Trace Gas and Particulate Distributions and Emission Source Characteristics, Environ. Sci. Technol., 38, 5694–5703, 2004.

Laskin, A., Wietsma, T. W., Krueger, B. J., and Grassian, V. H.: Heterogenous chemistry of individual mineral dust particles with nitric acid: A combined CCSEM/EDX, ESEM, and ICP-MS study, J. Geophys. Res.-Atmos., 110(D10), doi:10.1029/2004JD005206, 2005.

Lei, W., de Foy, B., Zavala, M., Volkamer, R., and Molina, L. T.: Characterizing ozone production in the Mexico City Metropolitan Area: a case study using a chemical transport model, Atmos. Chem. Phys., 7, 1347–1366, 2007, http://www.atmos-chem-phys.net/7/1347/2007/.

Lelieveld, J., Butler, T. M., Crowley, J. N., Dillon, T. J., Fischer, H., Ganzeveld, L., Harder, H., Lawrence, M. G., Martinez, M., Taraborrelli, D., and Williams, J.: Atmospheric oxidation capacity sustained by a tropical forest, Nature, 452, 737–740, 2008.

Li, S., Matthews, J., and Sinha, A.: Atmospheric Hydroxyl Radical Production from Electronically Excited NO_2 and H_2O, Science,

319, 1657–1660, 2008.

Liang, J. and Jacobson, M. Z.: Effects of subgrid segregation on ozone production efficiency in a chemical model, Atmos. Environ., 34, 2975–2982, 2000.

Lim, Y. B. and Ziemann, P. J.: Products and mechanism of secondary organic aerosol formation from reactions of n-alkanes with OH radicals in the presence of NO_x, Environ. Sci. Technol., 39, 9229–9236, 2005.

Lin, X., Trainer, M., and Liu, S. C.: On the Nonlinearity of the Tropospheric Ozone Production, J. Geophys. Res., 93, 15879–15888, 1988.

Lindinger, W., Hansel, A., and Jordan, A.: Proton-transfer-reaction mass spectrometry (PTR-MS): on-line monitoring of volatile organic compounds at pptv levels, Chemical Society Reviews, 27, 347, 1998.

Liu, P. S. K., Deng, R., Smith, K. A., Williams, L. R., Jayne, J. T., Canagaratna, M. R., Moore, K., Onasch, T. B., Worsnop, D. R., and Deshler, T.: Transmission Efficiency of an Aerodynamic Focusing Lens System: Comparison of Model Calculations and Laboratory Measurements for the Aerodyne Aerosol Mass Spectrometer, Aerosol Sci. Technol., 41, 721–733, 2007.

Madronich, S.: Chemical Evolution of gaseous air pollutants downwind of tropical megacities: Mexico City case study, Atmos. Environ., 40, 6012–6018, 2006.

Matthew, B. M., Middlebrook, A. M., and Onasch, T. B.: Collection Efficiencies in an Aerodyne Aerosol Mass Spectrometer as a Function of Particle Phase for Laboratory Generated Aerosols, Aerosol Sci. Technol., 42, 884–898, 2008.

McCreanor, J., Cullinan, P., Nieuwenhuijsen, M. J., Stewart-Evans, J., Malliarou, E., Jarup, L., Harrington, R., Svartengren, M., Han, I., Ohman-Strickland, P., Chung, K. F., and Zhang, J.: Respiratory Effects of Exposure to Diesel Traffic in Persons with Asthma, The New England Journal of Medicine, 357, 2348-2358, 2007.

Moffet, R. C., de Foy, B., Molina, L. T., Molina, M. J., and Prather, K. A.: Measurement of ambient aerosols in northern Mexico City by single particle mass spectrometry, Atmos. Chem. Phys., 8, 4499–4516, 2008, http://www.atmos-chem-phys.net/8/4499/2008/.

Molina, L. T., Molina, M. J., Slott, R. S., Kolb, C. E., Gbor, P. K., Meng, F., Singh, R. B., Galvez, O., Sloan, J. J., Anderson, W. P., Tang, X., Hu, M., Xie, S., Shao, M., Zhu, T., Zhang, Y. H., Gurjar, B. R., Artaxo, P. E., Oyola, P., Gramsch, E., Hidalgo, D., and Gertler, A. W.: Air Quality in Selected Megacities, J. Air Waste Manage. Assoc., 55, 1–73, 2004.

Nelson, D. D., McManus, B., Urbanski, S., Herndon, S., and Zahniser, M. S.: High precision measurements of atmospheric nitrous oxide and methane using thermoelectrically cooled mid-infrared quantum cascade lasers and detectors, Spectroc. Acta Pt. A-Molec. Biomolec. Spectrom., 60, 3325–3335, 2004.

Nunnermacker, L. J., Imre, D., Daum, P. H., Kleinman, L., Lee, Y. N., Springston, S. R., Newman, L., Weinstein-Lloyd, J., Luke, W. T., Banta, R., Alvarez, R., Senff, C., Sillman, S., Holdren, M., Keigley, G. W., and Zhou, X.: Characterization of the Nashville urban plume on July 3 and July 18, 1995, J. Geophys. Res., 103, 28129–28148, 1998.

Nunnermacker, L. J., Kleinman, L. I., Imre, D., Daum, P. H., Lee, Y. N., Lee, J. H., Springston, S. R., Newman, L., and Gillani, N.: NO_y lifetimes and O_3 production efficiencies in urban and power plant plumes: Analysis of field data, J. Geophys. Res.-Atmos., 105, 9165–9176, 2000.

Nunnermacker, L. J., Weinstein-Lloyd, J. B., Hillery, B., Giebel, B., Kleinman, L. I., Springston, S. R., Daum, P. H., Gaffney, J., Marley, N., and Huey, G.: Aircraft and ground-based measurements of hydroperoxides during the 2006 MILAGRO field campaign, Atmos. Chem. Phys., 8, 7619–7636, 2008, http://www.atmos-chem-phys.net/8/7619/2008/.

Querol, X., Pey, J., Minguillon, M. C., Perez, N., Alastuey, A., Viana, M., Moreno, T., Bernabe, R. M., Blanco, S., Cardenas, B., Vega, E., Sosa, G., Escalona, S., Ruiz, H., and Artinano, B.: PM speciation and sources in Mexico during the MILAGRO-2006 Campaign, Atmos. Chem. Phys., 8, 111–128, 2008, http://www.atmos-chem-phys.net/8/111/2008/.

Roberts, J. M., Fehsenfeld, F. C., Liu, S. C., Bollinger, M. J., Hahn, C., Albritton, D. L., and Sievers, R. E.: Measurements of aromatic hydrocarbon ratios and NO_x concentrations in the rural troposphere: Estimates of air mass photochemical age and NO_x removal rate, Atmos. Environ., 18, 2421–2432, 1984.

Rogers, T. M., Grimsrud, E. P., Herndon, S. C., Jayne, J. T., Kolb, C. E., Allwine, E., Westberg, H., Lamb, B. K., Zavala, M., Molina, L. T., Molina, M. J., and Knighton, W. B.: On-road measurements of volatile organic compounds in the Mexico City metropolitan area using proton transfer reaction mass spectrometry, Int. J. Mass Spectrom., 252, 26–37, 2006.

Ryerson, T. B., Trainer, M., Holloway, J. S., Parrish, D. D., Huey, L. G., Sueper, D. T., Frost, G. J., Donnelly, S. G., Schauffler, S., Atlas, E. L., Kuster, W. C., Goldan, P. D., Hubler, G., Meagher, J. F., and Fehsenfeld, F. C.: Observations of ozone formation in power plant plumes and implications for ozone control strategies, Science, 292, 719–723, 2001.

Salcedo, D., Onasch, T. B., Dzepina, K., Canagaratna, M. R., Zhang, Q., Huffman, J. A., DeCarlo, P. F., Jayne, J. T., Mortimer, P., Worsnop, D. R., Kolb, C. E., Johnson, K. S., Zuberi, B., Marr, L. C., Volkamer, R. M., Molina, L. T., Molina, M. J., Cardenas, B., Bernabe, R. M., Marquez, C., Gaffney, J. S., Marley, N. A., Laskin, A., Shutthanandan, V., Xie, Y., Brune, W., Lesher, R., Shirley, T., and Jimenez, J. L.: Characterization of ambient aerosols in Mexico City during the MCMA-2003 campaign with aerosol mass spectrometry: results from the CENICA Supersite., Atmos. Chem. Phys., 6, 925–946, www.atmos-chem-phys.net/6/925/2006/, 2006.

San Martini, F. M., Dunlea, E. J., Grutter, M., Onasch, T. B., Jayne, J. T., Canagaratna, M. R., Worsnop, D. R., Kolb, C. E., Shorter, J. H., Herndon, S. C., Zahniser, M. S., Ortega, J. M., McRae, G. J., Molina, L. T., and Molina, M. J.: Implementation of a Markov Chain Monte Carlo method to inorganic aerosol modeling of observations from the MCMA-2003 campaign - Part I: Model description and application to the La Merced site, Atmos. Chem. Phys, 6, 4867–4888, 2006.

Sander, S. P., Friedl, R. R., Golden, D. M., Kurylo, M. J., Moortgat, G. K., Wine, P. H., Ravishankara, A. R., Kolb, C. E., Molina, M. J., Finlayson-Pitts, B. J., Huie, R. E., and Orkin, V. L.: Chemical Kinetics and Photochemical Data for Use in Atmospheric Studies: Evaluation Number 15, Jet Propulsion LaboratoryJPL Publication 06-2, 2006.

Saunders, S. M., Jenkin, M. E., Derwent, R. G., and Pilling, M. J.: Protocol for the development of the Master Chemical Mechanism, MCM v3 (Part A): tropospheric degradation of non-

aromatic volatile organic compounds, Atmos. Chem. Phys., 3, 161–180, 2003, http://www.atmos-chem-phys.net/3/161/2003/.

Seila, R. L., Main, H. H., Arriaga, J. L., Martinez, G., and Ramadan, A. B.: Atmospheric volatile organic compound measurements during the 1996 Paso del Norte Study, The Science of the Total Environment, 276, 153–169, 2001.

Shaw, W. J., Pekour, M. S., Coulter, R. L., Martin, T. J., and Walters, J. T.: The daytime mixing layer observed by radiosonde, profiler and lidar during MILAGRO, Atmos. Chem. Phys. Discuss., 15025–15065, 2007.

Shirley, T. R., Brune, W. H., Ren, X., Mao, J., Lesher, R., Cardenas, B., Volkamer, R., Molina, L. T., Molina, M. J., Lamb, B., Velasco, E., Jobson, T., and Alexander, M.: Atmospheric oxidation in the Mexico City Metropolitan Area (MCMA) during April 2003, Atmos. Chem. Phys., 6, 2753-2765, 2006, http://www.atmos-chem-phys.net/6/2753/2006/.

Shon, Z. H., Madronich, S., Song, S. K., Flocke, F. M., Knapp, D. J., Anderson, R. S., Shetter, R. E., Cantrell, C. A., Hall, S. R., and Tie, X.: Characteristics of the NO-NO_2-O_3 system in different chemical regimes during the MIRAGE-Mex field campaign, Atmos. Chem. Phys., 8, 7153–7164, 2008, http://www.atmos-chem-phys.net/8/7153/2008/.

Shorter, J. H., Herndon, S., Zahniser, M. S., Nelson, D. D., Wormhoudt, J., Demerjian, K. L., and Kolb, C. E.: Real-time Measurements of Nitrogen Oxide Emissions from In-use New York City Transit Buses using a Chase Vehicle, Environ. Sci. Technol, 39, 7991–8000, 2005.

Stephens, S., Madronich, S., Wu, F., Olson, J. B., Ramos, R., Retama, A., and Munoz, R.: Weekly patterns of Mexico City's surface concentrations of CO, NO_x, PM_{10} and O_3 during 1986–2007, Atmos. Chem. Phys., 8, 5313–5325, 2008, http://www.atmos-chem-phys.net/8/5313/2008/.

Stull, R. B.: An Introduction to Boundary Layer Meteorology, Kluwer Academic Publishers, The Netherlands, 1988.

Thornton, J. A., Wooldridge, P. J., Cohen, R. C., Martinez, M., Harder, H., Brune, W. H., Williams, E. J., Roberts, J. M., Fehsenfeld, F. C., Hall, S. R., Shetter, R. E., Wert, B. P., and Fried, A.: Ozone production rates as a function of NO_x abundances and HO_x production rates in the Nashville urban plume, J. Geophys. Res.-Atmos., 107, 4146, 2002.

Thornton, J. A., Jaegle, L., and McNeill, V. F.: Assessing known pathways for HO_2 loss in aqueous atmospheric aerosols: Regional and global impacts on tropospheric oxidants, J. Geophys. Res., 113, 113, D05303, doi:10.1029/2007JD009236, 2008.

Tie, X., Madronich, S., Li, G., Ying, Z., Zhang, R., Garcia, A. R., Lee-Taylor, J., and Liu, Y.: Characterizations of chemical oxidants in Mexico City: A regional chemical dynamical model (WRF-Chem) study, Atmos. Environ., 41, 1989–2008, 2007.

Tressol, M., Ordonez, C., Zbinden, R., Brioude, J., Thouret, V., Mari, C., Nedelec, P., Cammas, J. P., Smit, H., Patz, H. W., and Volz-Thomas, A.: Air pollution during the 2003 European heat wave as seen by MOZAIC airliners, Atmos. Chem. Phys., 8, 2133–2150, 2008, http://www.atmos-chem-phys.net/8/2133/2008/.

UN: World Urbanization Prospects: The 2007 Revision, United Nations, New York, USA, 2008.

Velasco, E., Lamb, B., Westberg, H., Allwine, E., Sosa, G., Arriaga-Colina, J. L., Jobson, B. T., Alexander, M. L., Prazeller, P., Knighton, W. B., Rogers, T. M., Grutter, M., Herndon, S. C., Kolb, C. E., Zavala, M., De Foy, B., Volkamer, R., Molina, L. T., and Molina, M. J.: Distribution, magnitudes, reactivities, ratios and diurnal patterns of volatile organic compounds in the Valley of Mexico during the MCMA 2002 & 2003 field campaigns, Atmos. Chem. Phys., 7, 329–353, 2007, http://www.atmos-chem-phys.net/7/329/2007/.

Volkamer, R., Molina, L. T., Molina, M. J., Shirley, T., and Brune, W. H.: DOAS measurement of glyoxal as an indicator for fast VOC chemistry in urban air, Geophys. Res. Lett., 32, L08806,, doi:10.1029/2005GL022616, 2005.

Volkamer, R., Jimenez, J. L., San Martini, F., Dzepina, K., Zhang, Q., Salcedo, D., Molina, L. T., Worsnop, D. R., and Molina, M. J.: Secondary organic aerosol formation from anthropogenic air pollution: Rapid and higher than expected, Geophys. Res. Lett., 33, L17811, doi:10.1029/2006GL026899, 2006.

Volkamer, R., Sheehy, P., Molina, L., and Molina, M.: Oxidative capacity of the Mexico City atmosphere –Part 1: A radical source perspective, Atmos. Chem. Phys. Discuss., 7, 5365–5412, 2007, http://www.atmos-chem-phys-discuss.net/7/5365/2007/.

Wang, Y. H., Logan, J. A., and Jacob, D. J.: Global simulation of tropospheric O_3-NO_x-hydrocarbon chemistry 2. Model evaluation and global ozone budget, J. Geophys. Res.-Atmospheres, 103, 10727–10755, 1998.

Wesely, M. L. and Hicks, B. B.: A review of the current status of knowledge on dry deposition, Atmos. Environ., 34, 2261–2282, 2000.

Williams, E. J., Baumann, K., Roberts, J. M., Bertman, S. B., Norton, R. B., Fehsenfeld, F. C., Springston, S. R., Nunnermacker, L. J., Newman, L., Olszyna, K., Meagher, J., Hartsell, B., Edgerton, E., Pearson, J. R., and Rodgers, M. O.: Intercomparison of ground-based NO_y measurement techniques, J. Geophys. Res.-Atmos., 103, 22261–22280, 1998.

Wood, E. C., Canagaratna, M., and Herndon, S.: Investigation of the correlation between odd-oxygen and secondary organic aerosol in Mexico City and Houston, in preparation, 2009.

Yauk, C., Polyzos, A., Rowan-Carroll, A., Somers, C. M., Godschalk, R. W., Van Schooten, F. J., Berndt, M. L., Pogribny, I. P., Koturbash, I., Williams, A., Douglas, G. R., and Kovalchuk, O.: Germ-line mutations, DNA damage, and global hypermethylation in mice exposed to particulate air pollution in an urban/industrial location, Proceedings of the National Academy of Science, 105, 605–610, 2008.

Zavala, M., Herndon, S. C., Slott, R. S., Dunlea, E. J., Marr, L. C., Shorter, J. H., Zahniser, M., Knighton, W. B., Rogers, T. M., and Kolb, C. E.: Characterization of on-road vehicle emissions in the Mexico City Metropolitan Area using a mobile laboratory in chase and fleet average measurement modes during the MCMA-2003 field campaign, Atmos. Chem. Phys., 6, 5129–5142, 2006, http://www.atmos-chem-phys.net/6/5129/2006/.

Zhao, J. and Zhang, R.: Proton transfer reaction rate constants between hydronium ion (H3O+) and volatile organic compounds (VOCs), Atmos. Environ., 38, 2177–2185, 2004.

Zheng, J., Zhang, R., Fortner, E. C., Volkamer, R. M., Molina, L., Aiken, A. C., Jimenez, J. L., Gaggeler, K., Dommen, J., Dusanter, S., Stevens, P. S., and Tie, X.: Measurements of HNO_3 and N_2O_5 using Ion drift – Chemical Ionization Mass Spectrometry during the MCMA – 2006 Campaign, Atmos. Chem. Phys., 8, 6823–6838, 2008, http://www.atmos-chem-phys.net/8/6823/2008/.